Westinghouse Non-Proprietary Class 3

[redacted]

Westinghouse Energy Systems

[redacted]

Westinghouse Non-Proprietary Class 3

[redacted]

Westinghouse Energy Systems

WCAP-14255

AP600 SPES-2
TEST ANALYSIS REPORT

May 1995

by

J. P. Cunningham
M. T. Friend
L. E. Hochreiter
R. Hundal
V. Merritt
M. Ogrinsh
R. F. Wright

WESTINGHOUSE ELECTRIC CORPORATION
Energy Systems Business Unit
Nuclear Technology Division
P.O. Box 355
Pittsburgh, Pennsylvania 15230-0355

TABLE OF CONTENTS

TABLE OF CONTENTS (Cont.)

TABLE OF CONTENTS (Cont.)

TABLE OF CONTENTS (Cont.)

LIST OF TABLES

LIST OF TABLES (Cont.)

LIST OF FIGURES

LIST OF FIGURES

SUMMARY

The SPES-2 facility is a full-height, full-pressure, and 1/395th power and volume scale simulation of the AP600 nuclear steam supply system and the AP600 passive safety features. A series of twelve design basis events were simulated at SPES-2 to obtain data for verification and validation of the computer models used for the safety analysis of the AP600. The results of these tests were presented in the *SPES-2 Final Data Report*[1] that was issued in March 1995.

The purpose of this report is to describe the analysis of the test data which was performed to provide additional information, and to demonstrate, through mass and energy balances, the applicability of the SPES-2 tests for computer model verification and validation.

The SPES-2 test program was performed as part of the Advanced Light Water Reactor (ALWR) program sponsored by the U.S. Department of Energy (DOE) and the Electric Power Research Institute (EPRI). Westinghouse conducted this test program in cooperation with SIET (Società Informazioni Esperienze Termoidrauliche), ENEL (Ente Nazionale per l'Energia Elettrica), ENEA (Ente per Le Nuove Technologie, l'Energia e l'ambiente), and Sopren-Ansaldo.

ACKNOWLEDGEMENTS

The authors wish to acknowledge Mr. Tim Andreychek and Mr. Brian Alsop for their initial work on the SPES-2 data analysis software, and especially Mr. James Thomas for his invaluable assistance in developing and maintaining the SPESAN computer code. Also, Bill Brown for reviewing the methodology.

The authors wish to thank to Ms. Patti Todaro and Ms. Becky Jung for their editing skills, and Ms. Ruth Flanders and the Word Processing Center operators for their skill in producing this document under tight time and resource constraints. Also, Mr. Mike Mankowski for his help in creating the graphics in this document, and Ms. Rita Ozolniece for her project management skill.

1.0 INTRODUCTION

This report describes the analysis of the SPES-2 test data that will be used to validate the AP600 safety analysis computer codes. The test data report for the SPES-2 test is given in WCAP-14309, *Final Data Report*,[1] which describes the test facility, the valid instrumentation, and the test facility performance for the different experiments. This report will examine, in additional detail, the thermal-hydraulic behavior of the test facility and the phenomenon observed in the experiments, and as identified in the PIRT. This analysis will aid the computer code validation activities.

SPES-2 is a full-height, full-pressure integral systems simulation of the Westinghouse AP600 reactor design. The SPES-2 test was performed as part of the Advanced Light Water Reactor (ALWR) program sponsored by the U.S. Department of Energy (DOE) and the Electric Power Research Institute (EPRI). Westinghouse, in cooperation with SIET (Società Informazioni Esperienze Termoidrauliche), ENEL (Ente Nazionale per l'Energia Elettrica), ENEA (Ente per le Nuove Technologie, l'Energia e l'ambiente), and Sopren-Ansaldo, performed the SPES-2 tests to obtain data on the integrated behavior and performance of the AP600 passive safety systems to support validation of the computer codes used to perform the licensing safety analyses for the AP600.

1.1 Background

AP600 is a 600 MWe Westinghouse Advanced Reactor designed to enhance plant safety with accident mitigation features that, once actuated, depend only on natural forces, such as gravity and natural circulation, to perform all required safety functions.

The AP600 primary system is a two-loop design. Each loop contains one hot leg, two cold legs, and one steam generator with two canned reactor coolant pumps (RCPs) attached directly to the steam generator outlet channel head. The passive safety systems comprise the following:

- Two full-pressure core makeup tanks (CMTs) that provide borated makeup water to the primary system at any pressure.

- Two accumulators that provide borated water to the reactor vessel when/if primary pressure $\leq$ 700 psia.

- A passive residual heat removal (PRHR) heat exchanger (HX), comprised of a C-shaped tube bundle submerged inside the in-containment refueling water storage tank (IRWST), that can remove heat from the primary system at any pressure.

- The automatic depressurization system (ADS), which is comprised of a set of valves connected to the pressurizer steam space and the two hot legs. These valves are opened sequentially to provide a controlled depressurization of the primary system.

- An IRWST that provides a large source of core cooling water, which drains by gravity after the ADS has actuated.

- A passive containment cooling system (PCS) that utilizes the AP600 steel containment shell to transfer heat to the environment (ultimate heat sink). The PCS was not included in the SPES-2 experiments.

In reviews of the AP600, the U.S. Nuclear Regulatory Commission (NRC) identified several concerns regarding the performance of the AP600 passive safety systems. Those concerns include the following:

- Possible high-pressure passive safety system interactions which could retard cooling to the core.

- Possible active system/passive system interaction which could retard cooling to the core.

- The dependence on small temperature differences resulting in small density differences, which then are responsible for driving heads for recirculating flows.

- The effects of code accuracy in predicting long transients in which the driving heads for the flows in the systems are small.

The SPES-2 test facility was specifically designed to simulate the AP600 transients such that the NRC concerns could be addressed.

The SPES-2 facility was designed to simulate the AP600 plant at full-scale elevation and full pressure, while simulating the full AP600 plant range of power with a volume scaling factor of 1/395. SPES-2 makes use of some major components of the previous facility, SPES-1,[2] such as rod bundle, pressurizer, steam generators and reactor coolant pumps (RCPs). However, the reactor-vessel downcomer, lower plenum, upper plenum, and upper head were all replaced to simulate the AP600 plant components. Also, the SPES RCPs were re-oriented in order to eliminate the cold-leg loop seal that exists in standard Westinghouse pressurized water reactors (PWRs). All of the main coolant loop piping and passive safety systems have been expressly designed and constructed for SPES-2 in order to model the AP600 plant. A complete description of the SPES-2 facility is provided in WCAP-14073, *SPES-2 Facility Description.*[2]

A series of cold, low-pressure and hot, high-pressure pre-operational tests were performed to characterize the SPES-2 facility, to demonstrate proper operation of the facility, to ensure that piping/component parameters properly matched the AP600 plant prior to the performance of matrix tests, and to provide benchmark data on the facility behavior for the computer code analysis. The matrix tests discussed in Section 1.4 were developed to examine the AP600 passive safety system performance in mitigating the effects of design basis events (DBEs). Events that were simulated include loss-of-coolant accidents (LOCAs) ranging from 1-in. diameter equivalent to the double-ended guillotine (DEG) break of an 8-in. direct vessel injection (DVI) line, steam generator tube ruptures (SGTRs), and a large main steam line break (SLB).

1.2 Important Small-Break Loss-of-Coolant Accident Phenomena

The small-break LOCA (SBLOCA) transient can be subdivided into four different periods that characterize thermal-hydraulic phenomena. Those periods include the following:

- Blowdown - The initial depressurization from the plant operating pressure to the steam generator secondary-side pressure, after which the pressure stabilizes.

- Natural Circulation - The time period from the stabilization of the primary pressure with the secondary-side pressure until ADS-1 is activated. The primary reactor system is cooled by different modes of natural circulation; that is, single-phase natural circulation, two-phase natural circulation, and reflux condensation. Each cooling mode is dependent on the system mass inventory. As the mass is lost from the break, the cooling proceeds from single-phase, to two-phase, to reflux condensation cooling.

- ADS Stages 1, 2, and 3 Blowdown - Once the CMTs drain to their setpoint, the ADS stage 1 valve opens and the reactor system is depressurized through the ADS flow path in addition to the break. As the CMT continues to drain into the reactor vessel, additional valves are opened on the pressurizer to enhance the blowdown of the system.

- IRWST Injection - Stable injection from the IRWST indicates the complete depressurization of the primary system down to containment pressure. Also, injection from the IRWST indicates the end of the small-break transient and the beginning of the long-term cooling transient.

Using these different time periods, the important thermal-hydraulic phenomena have been identified and ranked in a Phenomena Identification and Ranking Table (PIRT), as given in Table 1-1. This PIRT table has been updated and made more complete as compared to that which was given in the *NOTRUMP Code Applicability Document.*[3] The individual phenomena were emphasized for the ADS system and other components have been added to the PIRT. The phenomena for each identified phase of the small-break transient relative to the AP600 small break performance is discussed in the following paragraphs.

For the blowdown phase, the reactor is assumed to be operating at normal full-power, steady-state conditions at the start of the blowdown. The break opens at time zero, and the pressurizer pressure begins to fall as mass is lost out the break. This depressurization is largely defined by critical flow through the break. With the break located at the bottom of the cold leg, a mixture flow exits the break for the majority of the transient, since the mixture level stays high in the reactor vessel. The pressurizer pressure falls below the safety signal setpoint, causing the reactor to trip. The safety systems actuation (S) signal follows and results in opening the CMT isolation valves. Once the residual fissions decrease, core power is defined by the decay heat model. The RCPs trip after a short delay. Pump performance both before and after the trip is modeled according to the pump characteristic for curves. After the pumps coast down, the primary reactor coolant system (RCS) is cooled by natural circulation, with energy removed from the primary system by the steam generators via their safety valves and the break. Stored energy from the thick and thin metal in the reactor vessel

and pressurizer is transferred to the coolant. Note that all of these phenomena are essentially the same for AP600 as for conventional PWRs. The liquid in the upper plenum and upper head (depending on the temperature) will flash, and the upper head core start to drain.

Blowdown phase phenomena unique to the AP600 are those associated with the CMT delivery. Once the CMT isolation valves open on an S actuation signal, the CMT injects borated water due to gravity-driven recirculation into the RCS through the DVI lines. The CMT volume injected is replaced with hot liquid from the cold-leg, leaving the CMT which circulates through the cold-leg balance line (CLBL); this hot liquid collects at the top of the CMT. The downcomer fluid stages subcooled through the initial decomposition.

For the natural circulation phase of the transient, the primary system exists in a quasi-steady-state condition with the secondary side, with the decay energy being removed by the steam generator secondary side, as the primary system drains. The steam generator in AP600 plays a more limited role in the natural circulation cooling phase than for conventional plants because the generators drain relatively early in the transient. Since the PRHR is activated on an S signal during an SBLOCA, the IRWST becomes the primary heat sink for the RCS early in the transient; the PRHR will remove energy from the primary system, causing it to depressurize. The steam generator secondary side becomes a heat source once the PRHR reduces the primary pressure to that of the secondary side. The PRHR is ranked high in the PIRT since it becomes a significant heat removal path particularly after the primary pressure is less than the steam generator pressure. Therefore, any condensation in the steam generator tubes during AP600 small-break LOCA transients ceases early. The requirement for detailed models for condensation heat transfer in the steam generator tubes are not as significant for AP600 as for a conventional plant. The importance shifts to the PRHR performance and the IRWST heat sink behavior. The reverse heat transfer path due to the secondary heating of the RCS primary, continues until the generators drain. The CMT continues to deliver in the recirculation mode for a while, but eventually a vapor region forms at the top of the CMT volume and CMT draindown begins. As the CMT drains while injecting, its level falls to the ADS actuation setpoint, which initiates the third phase of the AP600 SBLOCA transient, the ADS blowdown phase. The downcomer and lower plenum are marked medium importance since they provide the driving head for natural circulation.

The ADS blowdown phase continues through ADS-1, ADS-2, ADS-3 and ADS-4 as the primary system completely depressurizes approximately the containment pressure. Table 1-1 relates AP600-specific components, events, and phenomena that occur during the automatic depressurization of the RCS to achieve water injection by gravity from the IRWST. Since ADS-1 creates an opening at the top of the pressurizer, the pressurizer two-phase fluid level increases markedly. Pressurizer tank level and surge line phenomena are significant factors in the depressurization behavior following ADS actuation. Flashing of fluid in the RCS occurs again due to the depressurization caused by the ADS.

Following actuation of ADS-1, ADS-2 and ADS-3 activate via timers. Accumulator injection begins once the pressure drops below 700 psia which reduces the flow delivered from the CMT, and CMT flow may even be stopped temporarily due to pressurization of the DVI line by the accumulator. The CMT drain rate, DVI line, and CLBL behaviors are significant because the ADS-4 actuation is based upon the CMT liquid level decreasing below a low-low setpoint value. Of somewhat less importance

is the condensation of vapor on the CMT walls, since the recirculation has resulted in heating of the CMT.

Critical flow through the ADS stages is the major factor in determining when the RCS has depressurized to the extent that the gravity injection of water from the IRWST can begin. Fourth-stage ADS performance will be particularly affected by the nature of flow in the hot legs. Successful operation of the ADS leads into the IRWST injection cooling phase of the AP600 SBLOCA event.

The final stage of the SBLOCA is IRWST injection. At this point, the primary system is completely depressurized and the transient continues into the long-term cooling phase of the accident. By the time of IRWST injection, the CMT is either completely empty or very nearly empty; therefore, CMT phenomena have become relatively unimportant, whereas the IRWST gravity drain rate through the DVI is important. The hot-leg flow phenomena, together with the ADS-4 flow, is also important. Moreover, the break critical flow behavior is now less important than before because all the ADS flow paths are open, providing a large area through which to vent steam. Maintaining the core covered with liquid or a two-phase mixture becomes a function of the decay heat level and the IRWST flow.

The impact of noncondensible gas released when the accumulators empty of liquid during AP600 SBLOCAs is shown to be of low importance in the SBLOCA PIRT because of the large number of vent paths for the gas.

1.3 Important Phenomena for Steam Generator Tube Rupture and Steam Line Break Transients

The SPES-2 test program also examined SGTR accidents and a SLB transient for LOFTRAN and LOFTR-2 computer code validation. A separate PIRT has been developed for the non-LOCA transients; it is included in the *LOFTRAN Code Applicability Document*[4] and is given in Table 1-2. The key thermal-hydraulic phenomena for the non-LOCA transients are identified in Table 1-2. Columns 3 and 14 identify the phenomena of importance for the SLB and the SGTR transients.

Not all of the phenomena identified for the SLB in Table 1-2 will be addressed in the SPES-2 tests, since neither the neutronic feedback nor boron mixing in the power channel are modeled for the steam line break. However, the thermal-hydraulic systems' effects (such as the fluid flashing in the reactor head and the forced and natural circulation flow in the primary system) are simulated. The steam generator heat transfer, CMT recirculation and the pressure drop and temperature distribution in the balance lines are simulated also. All these items are indicated as high priority in the PIRT table and were simulated in the SPES-2 facility.

The high ranking thermal-hydraulic phenomena identified for the SGTR transients can also be simulated in the SPES-2 test facility. The critical flow through the faulted steam generator tube is simulated. Also simulated are the steam generator secondary-side conditions, the core decay power, and the PRHR (which also acts to depressurize the primary system). The recirculation behavior of the CMTs and the primary system natural circulation behavior are simulated.

Therefore, the thermal-hydraulic phenomena, which has been ranked high in the non-LOCA PIRT, have been simulated successfully in the SPES-2 test facility such that AP600 safety analysis computer codes can be validated.

1.4 Test Objectives

There are two primary objectives of the AP600, SPES-2 Integral Systems Test:

- To simulate the AP600 thermal-hydraulic phenomena and behavior of the passive safety system identified in the PIRT tables for specific SBLOCAs, SGTRs, and an SLB.

- To obtain detailed experimental results for validation of safety analysis computer codes.

1.5 Test Matrix

The SPES-2 test matrix was developed to provide data for the important thermal-hydraulic phenomena identified in the SBLOCA PIRT and the non-LOCA PIRT for the AP600 passive safety systems, for computer code validation. The individual test initial and boundary conditions were selected to range the thermal-hydraulic phenomena, to challenge the passive safety systems, to provide direct comparisons between selected tests, and/or to match the limiting assumptions used in safety analysis computer codes. The resulting test matrix is shown in Table 1-3 and is discussed below.

There were seventeen tests performed at the SPES-2 facility– thirteen of which were successful and are reported as valid tests. Four runs were considered either unsuccessful or inappropriate to report. Table 1-4 lists all seventeen runs from WCAP-14309, *Final Data Report*,[1] the test date, a brief test description, and a comment on the test acceptance.

Three of the SPES-2 matrix tests were designated as "blind" tests. The data for these three tests were reviewed only by the Westinghouse Test Engineering group. However, the initial and boundary conditions were provided to other Westinghouse personnel to allow "blind" computer code predictions of the facility responses to be performed.

1.5.1 Small Break Loss-of-Coolant Accident Transients

The passive safety systems are designed to provide sufficient water for LOCA mitigation over a long period of time; thus CMT draindown, ADS actuation, accumulator delivery, and primary system depressurization to IRWST delivery all must occur. Eight different LOCA simulations with a wide selection of break sizes and locations were tested to observe the integrated operation of the passive system over a wide range of thermal-hydraulic conditions. All LOCA tests, with one exception, were performed without operation of the active, nonsafety pumped injection/heat removal. All tests were initiated from full-power operating conditions and used the minimum pressure setpoints for reactor trip and safety system actuations, as defined in the AP600 *Standard Safety Analysis Report (SSAR)*[5].

Test No. 1 A 1-in. diameter break simulation was selected as the smallest LOCA to be simulated. This was based on analyses that showed that complete heatup of the CMT water occurred prior to ADS actuation, so that any effect of CMT water flashing during depressurization could be observed.

Note that matrix test no. 2 in Table 1-1 was not performed because the AP600 actuation logic for the PRHR HX was revised to initiate PRHR operation whenever the S signal occurs. This test was intended to simulate a LOCA recovery with steam generator startup feedwater (SFW) operating. This would have delayed PRHR HX operation until ADS was actuated, with the prior AP600 actuation logic.

Test No. 3 A 2-inch break simulation in the bottom of a cold-leg loop pipe (which contains a CMT balance line) was performed as the base case LOCA to which other LOCAs would be compared. Analysis showed that this break resulted in the minimum primary system water inventory during passive system mitigation of higher probability, small cold-leg breaks.

This 2-inch diameter, base case break simulation was repeated at the end of the test program to demonstrate the repeatability of the SPES-2 facility operation and passive safety system performance.

Test No. 4 The 2-inch LOCA simulation with operation of the active, nonsafety systems was performed in order to observe passive safety system versus nonsafety system interactions as compared with the base case 2-inch LOCA (test no. 3).

Test Nos. 5 and 7 A 2-inch break simulation in the DVI line and in the cold-leg to CMT balance line were each performed to observe the effect of break location on the passive safety system mitigation capability as compared to the base case 2-inch LOCA (test no. 3).

Test No. 6 A DEG break simulation of one of two DVI lines was performed to minimize the amount of safety injection flow delivered to the reactor vessel (only one of two CMTs, accumulators, and IRWST injection lines deliver).

Test No. 8 A DEG break simulation of one 8-inch cold-leg to CMT balance line was performed to observe the effect on the faulted CMT and to provide a comparison LOCA with the DEG DVI LOCA.

Test No. 13 The 1-inch diameter break simulation (test no. 1) was repeated with the number of PRHR HX tubes increased from one tube to three tubes to maximize the primary system cooling and to better simulate two PRHR HXs in operation in the AP600 plant.

1.5.2 Steam Generator Tube Rupture Transients

Three SGTRs simulations were performed at SPES-2. All these tests modeled a full rupture of a single steam generator tube, and all were initiated from full-power operating conditions and used low-low pressurizer level to initiate reactor trip and safety system actuations.

Test No. 9 An SGTR with operator action and nonsafety systems operating in conjunction with the passive safety systems was performed to observe the combined effect of manual SGTR recovery actions and passive system operation.

Test No. 10 An SGTR without operator actions and without operation of active, nonsafety, pumped injection/heat removal was simulated to observe the capability of the passive systems to terminate the event without intervention and to identify if any different thermal-hydraulic behavior was observed.

Test No. 11 An SGTR without operator actions or nonsafety system operation but with the inadvertent actuation of the ADS was performed to observe the thermal-hydraulic effect of backflow from the faulted steam generator on ADS depressurization capability.

1.5.3 Steam Line Break

This test was a simulation of a large single-ended SLB. It was performed to examine the thermal-hydraulic behavior of a rapid intact primary system cooldown transient and to observe the ability of the CMT to provide primary system mass addition without requiring ADS actuation.

Test No. 12 This test was performed at AP600 hot, zero power conditions, and no core decay heat was used. Also, this test was performed with three PRHR HX tubes to maximize primary system cooling and to better simulate two PRHR HXs in operation in the AP600. The break size was scaled to simulate a [ ]^{a,b,c} AP600 break area (full steam generator outlet area) and was performed with no operator actions or active, nonsafety system operation.

1.6 SPES-2 Atypicalities Relative to the AP600 Plant

The SPES-2 test facility was scaled on a power-to-volume basis with full height being maintained for all components except for the pressurizer vessel.[1] Using this scaling method, there is a distortion of the test facility surface area-to-fluid volume that causes heat loss, which is surface-area dependent, to become significant relative to the full AP600 plant. Similar scaling was used on the semi-scale test facility SBLOCA experiments[2] and the same scaling distortion problem existed. For the semi-scale tests, strip heaters also added additional thermal mass to pipes and vessels. This was not a significant problem for semi-scale tests, since the test facility was not fully depressurized therefore, the excess energy from the heaters did not effect fluid conditions. For the AP600, a different situation exists.

The AP600 fully depressurizes during an SBLOCA transient, so that the pipes, which are initially at high temperatures, transfer heat back to the fluid as the system depressurizes. Since the surface area for the piping is larger per unit fluid volume, metal heat transfer to the coolant will be larger in the SPES-2 facility compared to the AP600 plant.

The approach used to compensate for the larger than nominal heat losses, at full system pressure and temperature, was to increase to the rod bundle power to compensate for the heat losses from the piping and components. Calculations using the RELAP 5 MOD 3 V80 code established the power compensation level that best matched the AP600 transient. Calculations for the AP600 plant transient established a baseline transient that the SPES-2 test facility should simulate. Increasing the power in the rod bundle by 150 kW until ADS-1 occurred compensated for the heat losses. After ADS-1, the compensating power was eliminated and the power curve for the facility became the ANS 1979 decay curve. Pre-test calculations were performed for all the tests simulated in the SPES-2 facility in which the facility response was compared to the expected response for the AP600. The power used for heat loss compensation was verified over the full test matrix. Figures 1-1 to 1-9 show the comparison of the SPES-2 transient results with the calculated results for the AP600. As the figures indicate, using the power compensation results in a similar response as the expected AP600 plant response. In addition, calculations were also performed assuming that the SPES facility was perfectly insulated so that heat losses were zero. For these calculations, the compensating power was not used. Figures 1-10 to 1-13 compare the two calculations and indicate that there is good agreement between the two cases which also supports the use of the compensating power for the experiments. Therefore, the power compensation was used on all SBLOCA experiments.

Scaling distortions result when using the power compensation method, before ADS activation, to account for heat losses in the SPES-2 facility. By increasing rod bundle power to values greater than the scaled amount, the void fraction in the simulated core is larger and additional steam is generated. The additional steam will be condensed in the generators and in the PRHR. As a result, the heat removal rate from the PRHR will be larger before ADS since it will condense more steam. In the original scaling report for the SPES-2 facility,[2] scaling indicated that 1.7 PRHR tubes should be used as scaled to the AP600 PRHR. Two PRHR tubes were planned to be used in the SPES experiments since this would have been closest to the scaled value; however, when pre-test analysis was performed using RELAP 5 MOD 3 V80, it was found that using two PRHR tubes over estimated the PRHR heat exchange by a factor of two. Greater heat exchange was due to the power compensation used in the test bundle which increased the bundle steaming rate. Therefore, the number of PRHR tubes were reduced to a single tube, which gave better agreement with the estimated AP600 PRHR heat exchange.

The original SPES facility used the Wilson[2] bubble rise model for scaling the pressurizer behavior. This resulted in a shorter, larger diameter pressurizer then the ideally scaled pressurizer. Concerns were raised on pressurizer behavior for SBLOCAs when the ADS activates. Additional calculations were performed using the RELAP 5 MOD 3 V80 code to access the difference in the ideally scaled pressurizer and the existing pressurizer in the facility. Figures 1-14 to 1-18 show that there is no significant effect of the shorter pressurizer in the SPES-2 facility so the existing pressurizer is sufficient for the AP600 SBLOCA tests.

The SPES-2 facility did not simulate the containment back pressure, therefore the IRWST was at atmospheric pressure. For the SPES-2 transient to reach IRWST injection the primary system it would have to depressurize to nearly atmospheric pressure. It was anticipated that the SPES-2 facility would have excessive metal heat release to the fluid as the transient would depressurize and the metal would transfer heat to the fluid. The higher metal heat release results in the system pressure being held-up above the IRWST cut-in pressure so that IRWST injection would be delayed relative to the corresponding injection for the AP600. Therefore, the ADS-4 lines and valve sizes were increased to values greater than the scaled values to compensate for the excessive metal heat release from the SPES piping. Sensitivity calculations were performed using the RELAP 5 MOD 3 V 80 code to help determine the sizing of the fourth stage piping and valve areas to insure IRWST injection at about the same time as that estimated for the AP600 plant.

The SPES-2 test facility simulates only two reactor coolant pumps (RCPs). The single pipe from the steam generator exit is connected to a single pump. There is a common portion of pipe downstream of the pump which then splits into two separate cold legs. These cold legs are then connected to the annular downcomer. In the AP600 plant, there are four separate reactor pumps which are individually connected to the cold legs. Every attempt was made to preserve flow resistance and the elevation where the split in the single cold leg occurred relative to the AP600 plant. A divider plate was used in the common portion of the cold leg downstream of the pump to further separate the two cold legs. Changes made to the cold leg in SPES result in a more protypical resistance from the flow from one cold leg to the adjacent cold leg, so that any potential bypass between the two cold legs is minimized. The specific geometry of the SPES-2 configuration was modeled in the NOTRUMP and WCOBRA/TRAC codes to more accurately represent the facility.

The SPES-2 scaling compromises that result from using power-to-volume scaling were effectively dealt with by using pre-test analysis to evaluate options and methods of operating the facility. The use of higher bundle power to mitigate the excessive heat loss, while creating other scaling issues, proved the best method of preserving the overall transient response of the facility to that predicted for the AP600 plant. The enlargement of the ADS-4 valves and piping, also acted to mitigate the steaming from the excessive surface area of the metal components. With the larger ADS-4 and associated piping, stable IRWST injection was achieved for all the SBLOCAs in a time frame which was consistent with the anticipated AP600 plant response. There are geometry differences between the SPES-2 test facility and the AP600, however, these differences can be accommodated in the noding and modeling of the facility.

The SPES-2 tests atypicalities have been minimized so that the resulting data from the experiments is valid for computer assessment and validation for passive safety systems such as those for the AP600 plant.

TABLE 1-1
PHENOMENA IDENTIFICATION RANKING TABLE FOR AP600 SMALL-BREAK LOCA

Component Phenomenon	Blowdown	Natural Circulation	ADS Blowdown	IRWST Injection Cooling
Break				
Critical Flow	H	H	H	M
Subsonic Flow	N/A	N/A	N/A	M
ADS Stages 1 to 3 Critical Flow	H* (inadvertent ADS)	H* (inadvertent ADS)	H	M
Two-Phase Pressure Drop	N/A*	N/A*	H	M
Valve Loss Coefficients	N/A*	N/A*	H	M
Single-Phase Pressure Drop	N/A	N/A	N/A	L
Vessel/Core				
Decay Heat	H	H	H	H
Forced Convection	M	N/A	N/A	N/A
Flashing	M	N/A	M	L
Wall Stored Energy	M	N/A	M	M
Natural Circulation Flow and Heat Transfer	M	M	M	M
Mixture Level Mass Inventory	H	H	H	H
RCP				
RCP Performance	M	N/A	N/A	N/A
Pressurizer				
Pressurizer Fluid Level	M	M	M	L
Wall Stored Heat	M	M	M	L
Pressurizer Surge Line Pressure Drop/Flow Regime	L	L	M	L
Downcomer/Lower Plenum	L	M	M	M
Upper Head/Upper Plenum	L	M	M	M
Cold Legs	L	M	M	M

* The ADS is not normally opened during these phases unless the transient is an inadvertent ADS; for that case, the ADS phenomena would be ranked as high (H).

TABLE 1-1 (Cont.)
PHENOMENA IDENTIFICATION RANKING TABLE FOR AP600 SMALL-BREAK LOCA

Component Phenomenon	Blowdown	Natural Circulation	ADS Blowdown	IRWST Injection Cooling
Steam Generator 2ϕ - Natural Circulation	L	M	L	L
SG Heat Transfer	L	M	L	L
Secondary Conditions	L	M	L	L
Hot Leg Flow Pattern Transition	L	H	H	H
ADS 1-4 Critical Flow	N/A	N/A	H	H
Subsonic Flow	N/A	N/A	L	H
CMT Recirculation Injection	M	M	L	L
Gravity Draining Injection	N/A	M	H	L
Vapor Condensation Rate	N/A	M	M	L
CMT Balance Lines Pressure Drop	M	H	H	L
Flow Composition	M	H	H	L
Accumulators Injection Flow Rate	N/A	M	H	N/A
Noncondensible Gas Entrainment	N/A	N/A	L	L
IRWST Gravity Draining Injection	N/A	N/A	N/A	H
Vapor Condensation Rate	N/A	N/A	M	L
DVI Line Pressure Drop	M	M	M	M
PRHR Natural Circulation Flow and Heat Transfer	L	H	M	L

TABLE 1-2
PHENOMENA IDENTIFICATION RANKING TABLE FOR AP600 NON-LOCA AND STEAM GENERATOR TUBE RUPTURE DESIGN BASIS ANALYSES

Component & System Phenomenon	(1) FW Malf	(2) ELI	(3) SLB	(4) Inad-vertent PRHR	(5) LOL	(6) Loss ac & LONF	(7) FLB	(8) LOSS of RCS Flow	(9) LR & BS	(10) SUIL	(11) RWAP	(12) Inad-vertent CMT or CVS	(13) RCS Dep.	(14) SGTR
Critical Flow	N/A	N/A	H	N/A	N/A	N/A	H	N/A	N/A	N/A	N/A	N/A	M	H
Vessel Mixing	H	L	H	H	L	M	M	L	L	H	L	M	L	M
Flashing in Upper Head	N/A	N/A	M	L	N/A	L	L	N/A	N/A	N/A	N/A	L	L	L
Core Reactivity Feedback	H	M	H	H	M	L	M	M	M	H	M	L	L	L
Reactor Trip	H	L	H	H	H	H	H	H	H	H	H	H	H	H
Decay Heat	L	L	L	H	L	H	H	L	L	L	L	H	L	H
Forced Convection	H	H	H	H	H	H	H	H	H	H	H	M	H	L
Natural Circulation Flow and Heat Transfer	M	L	H	H	L	H	H	L	L	L	L	H	L	M
RCP Coastdown Performance	L	N/A	L	L	L	L	L	H	H	N/A	N/A	L	L	L
Pressurizer Pressurizer Fluid Level	L	L	M	M	L	M	L	L	L	L	L	M	L	M
Surge Line Pressure Drop	L	L	L	L	H	L	L	M	H	L	L	L	L	L
Steam Generator (SG) Heat Transfer	H	H	H	L	H	H	H	L	L	L	M	L	L	M
Secondary Conditions	M	L	H	L	L	M	M	L	L	L	L	L	L	H

TABLE 1-2 (Cont.)
PHENOMENA IDENTIFICATION RANKING TABLE FOR AP600 NON-LOCA AND STEAM GENERATOR TUBE RUPTURE DESIGN BASIS ANALYSES

Component & System Phenomenon	(1) FW Malf	(2) ELI	(3) SLB	(4) Inadvertent PRHR	(5) LOL	(6) Loss ac & LONF	(7) FLB	(8) LOSS of RCS Flow	(9) LR & BS	(10) SUIL	(11) RWAP	(12) Inadvertent CMT or CVS	(13) RCS Dep.	(14) SGTR
RCS Wall Stored Heat	L	L	L	L	N/A	L	L	N/A	N/A	L	N/A	L	L	M
CMT Recirculation Injection	N/A	N/A	H	H	N/A	H	M	N/A	N/A	N/A	N/A	H	N/A	L
Gravity Draining Injection	N/A	N/A	N/A	N/A	N/A	N/A	N/A	N/A	N/A	N/A	N/A	N/A	N/A	N/A
Vapor Condensation Rate	N/A	N/A	N/A	N/A	N/A	N/A	N/A	N/A	N/A	N/A	N/A	N/A	N/A	N/A
Balance Line Pressure Drop	N/A	N/A	H	H	N/A	H	M	N/A	N/A	N/A	N/A	H	N/A	L
Balance Line Initial Temperature Dist.	N/A	N/A	H	H	N/A	H	M	N/A	N/A	N/A	N/A	H	N/A	L
Accumulators Injection Flow Rate	N/A	N/A	M	N/A	N/A	N/A	N/A	N/A	N/A	N/A	N/A	N/A	N/A	N/A
PRHR Flow Rate and Heat Transfer	N/A	N/A	L	H	N/A	H	H	N/A	N/A	N/A	N/A	H	N/A	H

(1) FW Malf - Feedwater malfunction that results in a decrease in feedwater temperature or an increase in feedwater flow
(2) ELI - Excessive increase in secondary steam flow
(3) SLB - Steam line break
(4) Inadvertent PRHR - Inadvertent operation of the PRHR
(5) LOL - Loss of secondary-side load events
(6) Loss ac & LONF - Loss of ac power and loss of normal feedwater
(7) FLB - Feed line break
(8) Loss of RCS Flow - Loss of forced RCS flow
(9) LR & BS - Locked RCP rotor and broken RCP shaft
(10) SUIL - Startup of an inactive reactor coolant pump at an incorrect temperature
(11) RWAP - RCCA withdrawal at power
(12) Inadvertent CMT or CVS - Inadvertent operation of the CMT or chemical and volume control system
(13) RCS Dep. - Inadvertent RCS depressurization
(14) SGTR - Steam generator tube rupture

H = High Importance M = Moderate Importance L = Low Importance N/A = Not Applicable

TABLE 1-3
SPES-2, TEST MATRIX

Test No.	Test Type	Test Description (AP600 Transient Simulated)	Status Nonsafety Systems	AP600 Single Failure Simulated	Comment
1	Small Break LOCA	1-inch cold-leg break (Note 2), bottom of loop B (Note 1)	CVCS, NRHR, and SFWS Off. No operator actions (OAs).	One of two 4th-stage valves on loop B	Maximize CMT heatup prior to ADS actuation.
2	Small Break LOCA	1-inch cold-leg break, bottom of loop B	CVCS, NRHR Off; SFWS On (Note 3). No OAs.	One of two 4th-stage valves on loop B	This test deleted due to AP600 design changes.
3 (Note 4)	Small Break LOCA	2-inch cold-leg break, bottom of loop B	CVCS, NRHR, and SFWS Off. No OAs.	One of two 4th-stage valves on loop B	Reference cold-leg break.
4	Small Break LOCA	2-inch cold-leg break, bottom of loop B	CVCS, NRHR, and SFWS On (Note 3).	One of two 4th-stage valves on loop B	Nonsafety/passive system interactions.
5	Small Break LOCA	2-inch DVI break	CVCS, NRHR and SFWS Off. No OAs.	One of two 4th-stage valves on loop B	Asymmetric CMT performance.
6	Small Break LOCA	DEG break of DVI	CVCS, NRHR, and SFWS Off. No OAs.	One of two stage 1 and stage 3 valves	Complete loss of one-of-two injection flow paths.
7	Small Break LOCA	2-inch break in CL/CMT-B balance line	CVCS, NRHR, and SFWS Off	One of two 4th-stage valves on loop B	Examine effect on CMT drain down.
8	Small Break LOCA	DEG break of a CL/CMT-B balance line	CVCS, NRHR, and SFWS Off. No OAs.	One of two stage 1 and stage 3 ADS valves	No delivery from faulted CMT.
9	SGTR	Design basis SGTR (1 tube)	CVCS, SFWS On; Operator action to isolate SG, subcool, depressurize.	None	Recovery with operator action; show recovery margin.

TABLE 1-3
SPES-2, TEST MATRIX (Cont.)

Test No.	Test Type	Test Description (AP600 Transient Simulated)	Status Nonsafety Systems	Single Failure	Comment
10	SGTR	Design basis SGTR (1 tube)	No CVCS or SFWS. No. OAs.	None.	SGTR recovery with no operator action.
11	SGTR	Design basis SGTR (1 tube) with inadvertent ADS actuation.	No CVCS or SFWS. No OAs.	One of two 4th-stage valves on loop B.	ADS actuated to cause steam generator to primary flow. Observe dilution rate and effect on ADS performance.
12	SLB (with three PRHR HX tubes in service).	SL break at zero power. A 1.388 ft.^{2} single-ended SLB on SG-A discharge.	No CVCS, NRHR, SFWS.	None.	Show CMTs do not drain and no ADS actuation occurs.
13	Small Break LOCA (with three PRHR HX tubes in service).	1-inch cold-leg break on bottom of loop B.	CVCS, NRHR, and SFWS off. No OAs.	One of two 4th-stage valves on loop B.	Show effect of three PRHR tubes, compare with matrix test 1.

Notes:

1. Loop B is the CMT side of plant; loop A is pressurizer and PRHR side of plant.
2. Break sizes are "a broken pipe of the indicated diameter," e.g., 2-inch break is 3.146 in.^{2}
3. SG main feedwater isolated on S signal and SFWS initiated, SFWS on until isolated on HI SG level or LO-Tcold.
4. Selected as repeat test to show facility repeatability.

TABLE 1-4
TEST RUNS AT SPES-2

Test Run Number	Test Date	Test Description	Comments
S00103	2/5/94	SBLOCA - 2-inch cold-leg break at bottom of loop B	Successful, but not included in final report since AP600 ADS valve sizes and setpoints were changed.
S00203	4/9/94	SBLOCA - 2-inch cold-leg break at bottom of loop B	Successful, but not included in final report since pressurizer to CMT balance line was subsequently deleted.
S00303	4/30/94	SBLOCA - 2-inch cold-leg break at bottom of loop B	Successful.
S00401	5/6/94	SBLOCA - 1-inch cold-leg break at bottom of loop B	Successful.
S00504	5/18/94	SBLOCA - 2-inch cold-leg break at bottom of loop B with nonsafety systems	Successful.
S00605	5/27/94	SBLOCA - 2-inch DVI break	Successful.
S00706	6/10/94	SBLOCA - DEG break of DVI	Successful.
S00807	6/12/94	SBLOCA - 2-inch break in CL/CMT balance line	Unsuccessful - due to valve misalignment in break piping to condenser.
S00908 (blind)	6/23/94	SBLOCA - DEG break of CL/CMT balance line	Successful.
S01007	7/7/94	SBLOCA - 2-inch break in CL/CMT balance line	Successful.
S01110	7/14/94	SGTR - 1 tube; passive safety systems only	Successful.
S01211 (blind)	9/7/94	SGTR - 1 tube; inadvertent ADS actuation	Successful.

TABLE 1-4 (Cont.)
TEST RUNS AT SPES-2

Test Run Number	Test Date	Test Description	Comments
S01309	9/22/94	SGTR - 1 tube; nonsafety systems operational with operator action for mitigation	Successful.
S01412	10/7/94	SLB at hot, zero power conditions	Unsuccessful - Leak in several power channel heated rods caused unisolable water loss from facility.
S01512 (blind)	10/11/94	SLB at hot, zero power conditions	Successful.
S01613	10/15/94	SBLOCA - 1-inch cold-leg break at bottom of loop B	Successful.
S01703	11/11/94	SBLOCA - 2-inch cold-leg break at bottom of loop B	Successful.

a,b,c

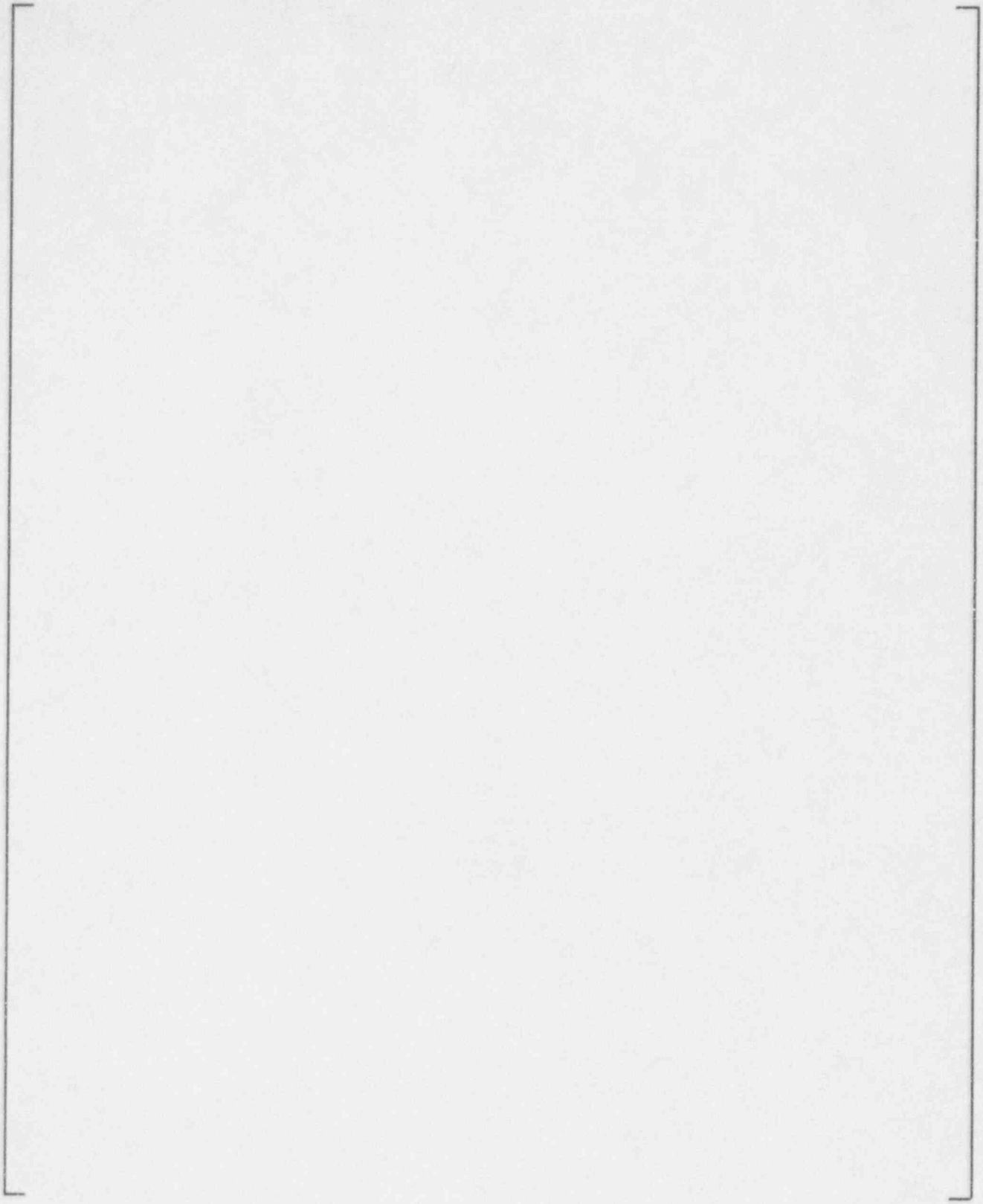

Figure 1-1 Comparison of AP600 to SPES-2 System Pressure

a,b,c

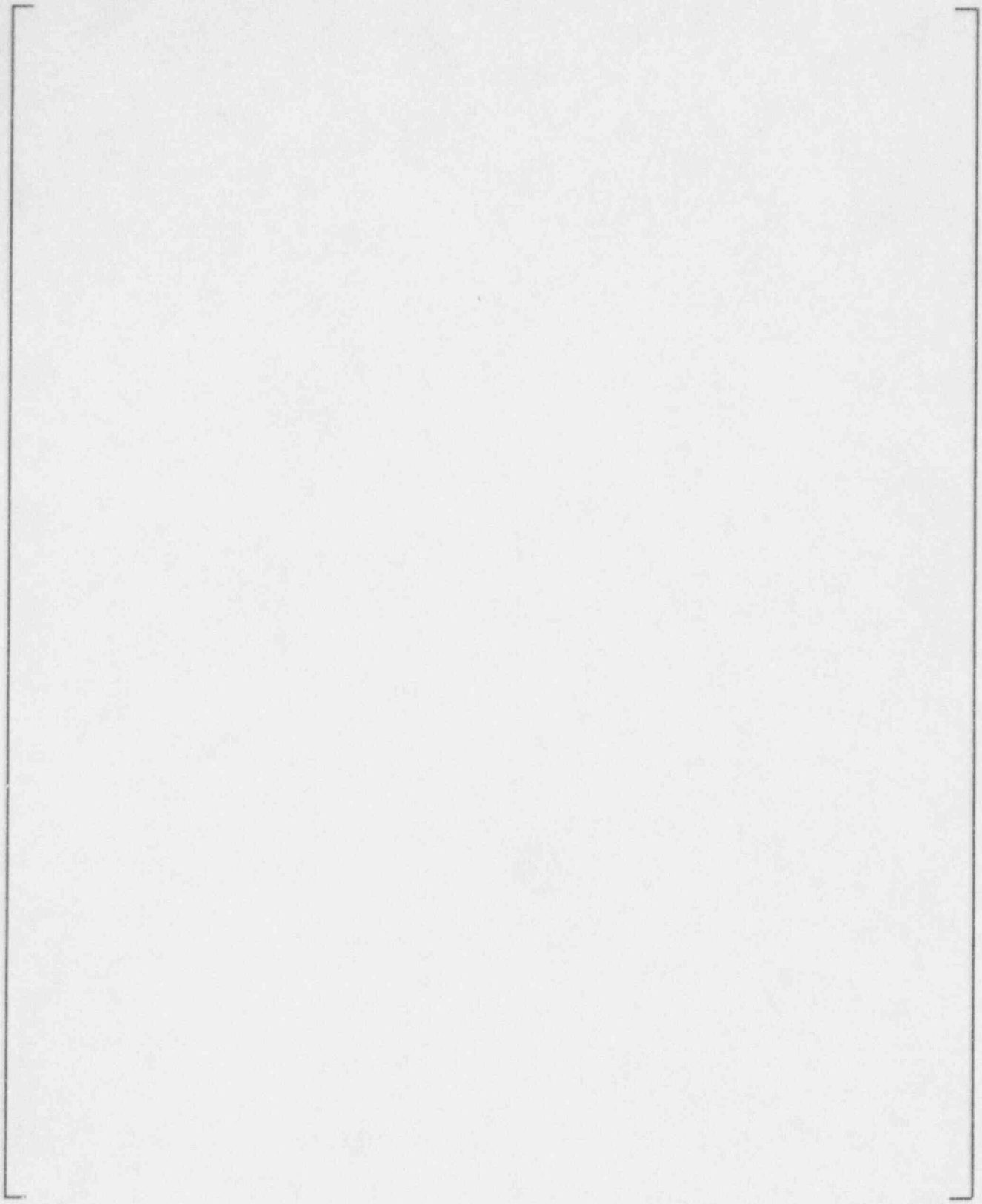

Figure 1-2 Comparison of AP600 and SPES-2 CMT Injection Flows

a,b,c

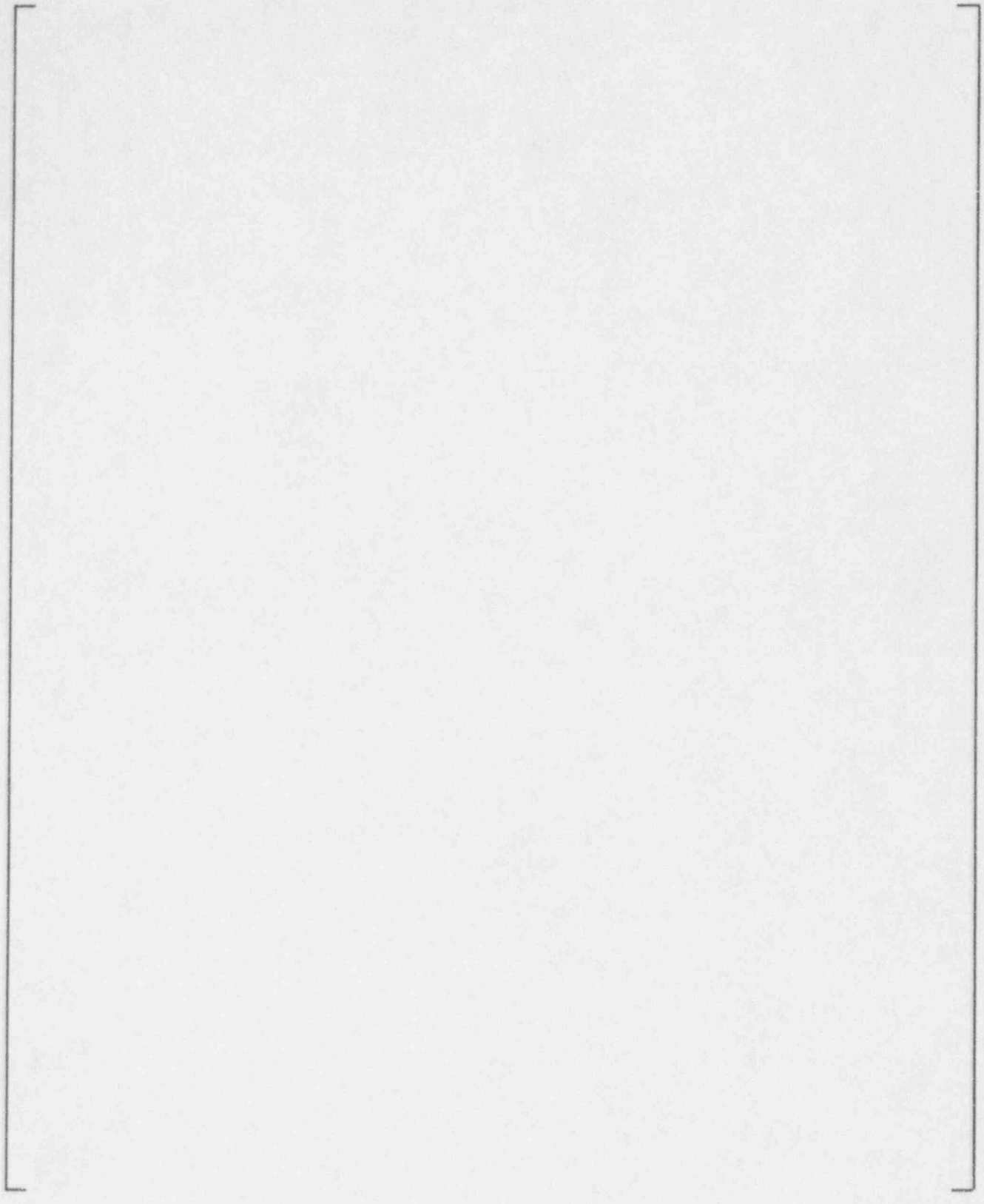

Figure 1-3 Comparison of AP600 and SPES-2 CMT Level

a,b,c

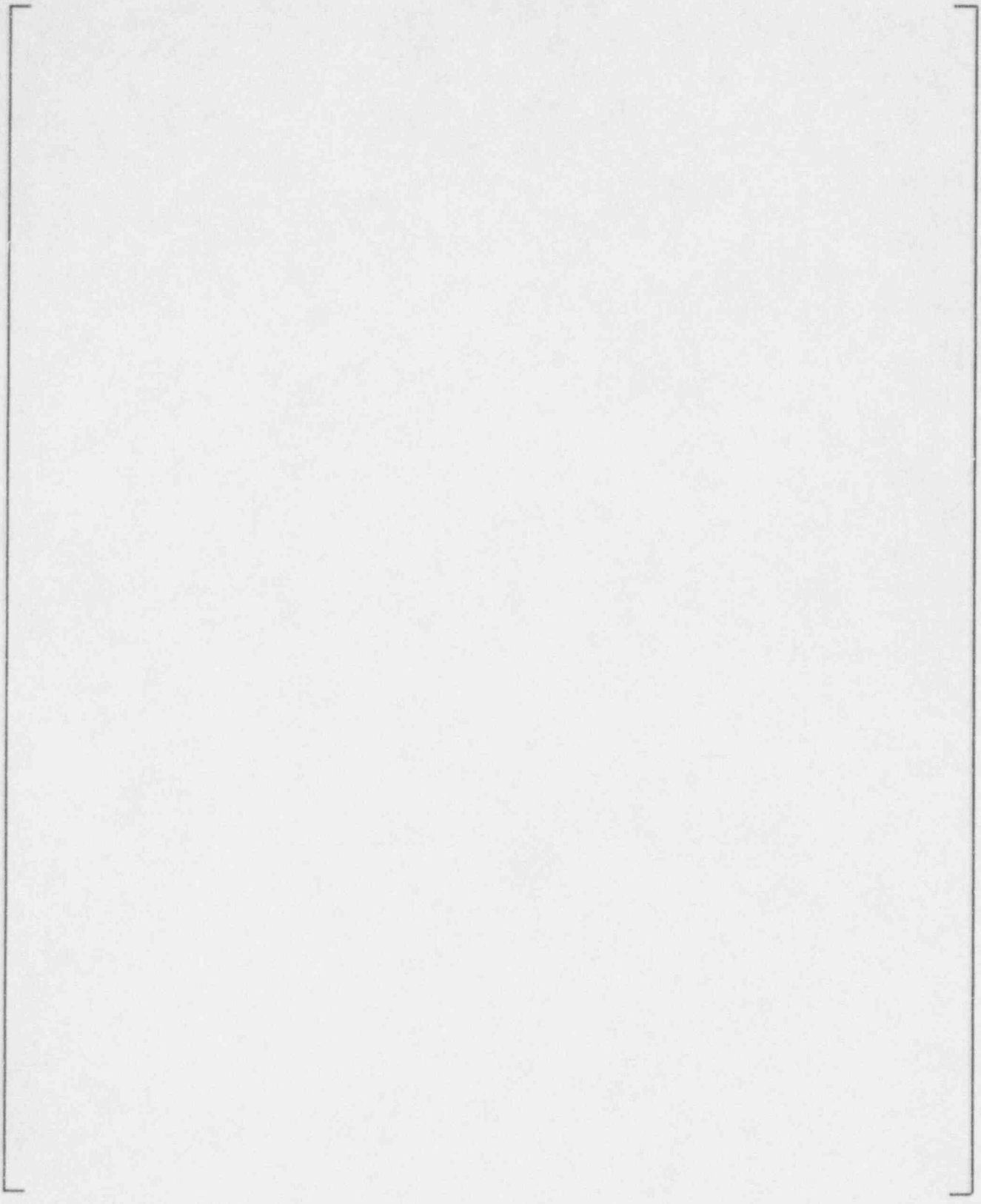

Figure 1-4 Comparison of Pressurizer Level for AP600 and SPES-2

a,b,c

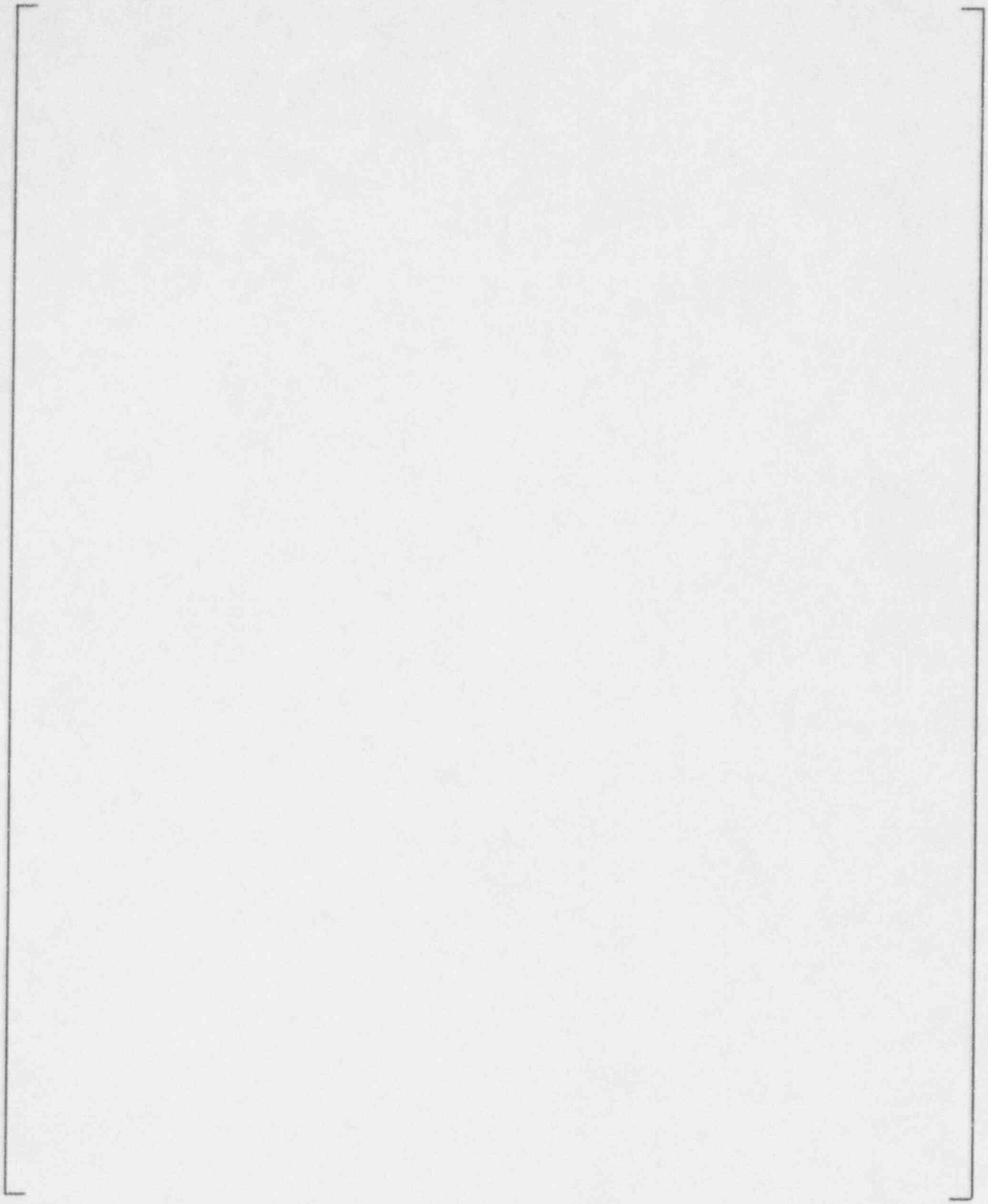

Figure 1-5 Comparison of AP600 to SPES-2 Accumulator Flows

a,b,c

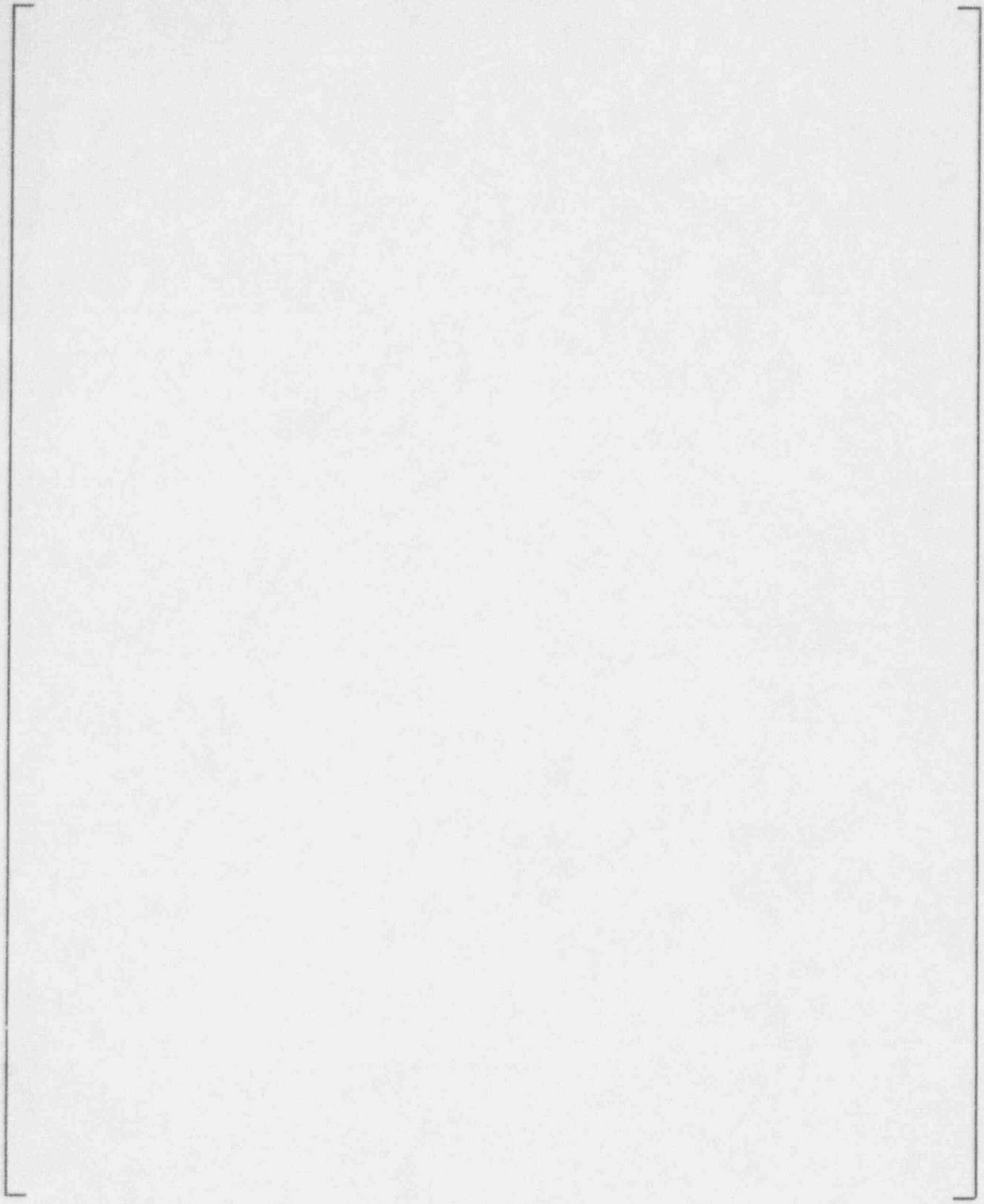

Figure 1-6 Comparison of AP600 and SPES-2 ADS-1 Discharge Flow

a,b,c

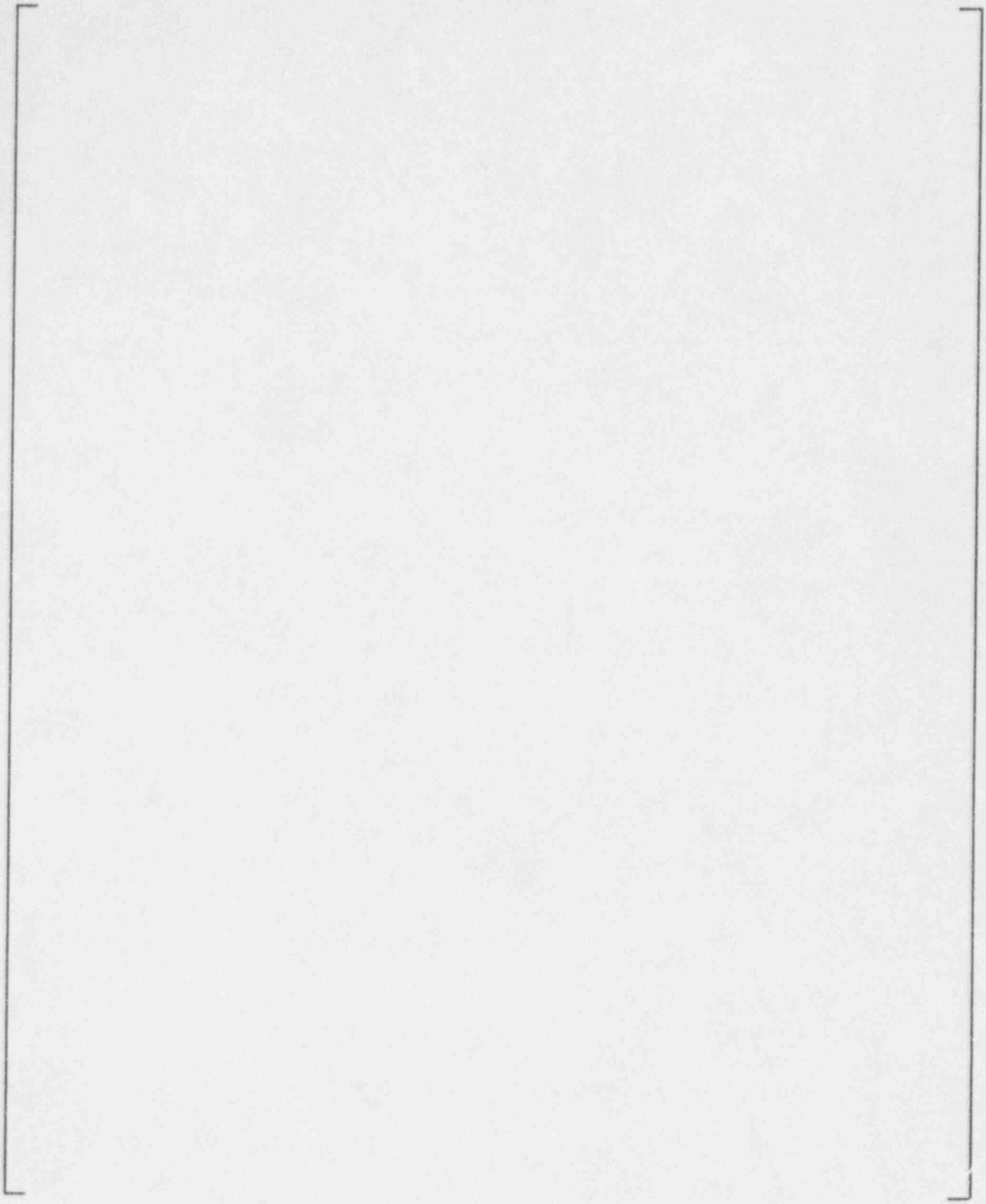

Figure 1-7 Comparison of AP600 and SPES-2 ADS-2 Discharge Flow

a,b,c

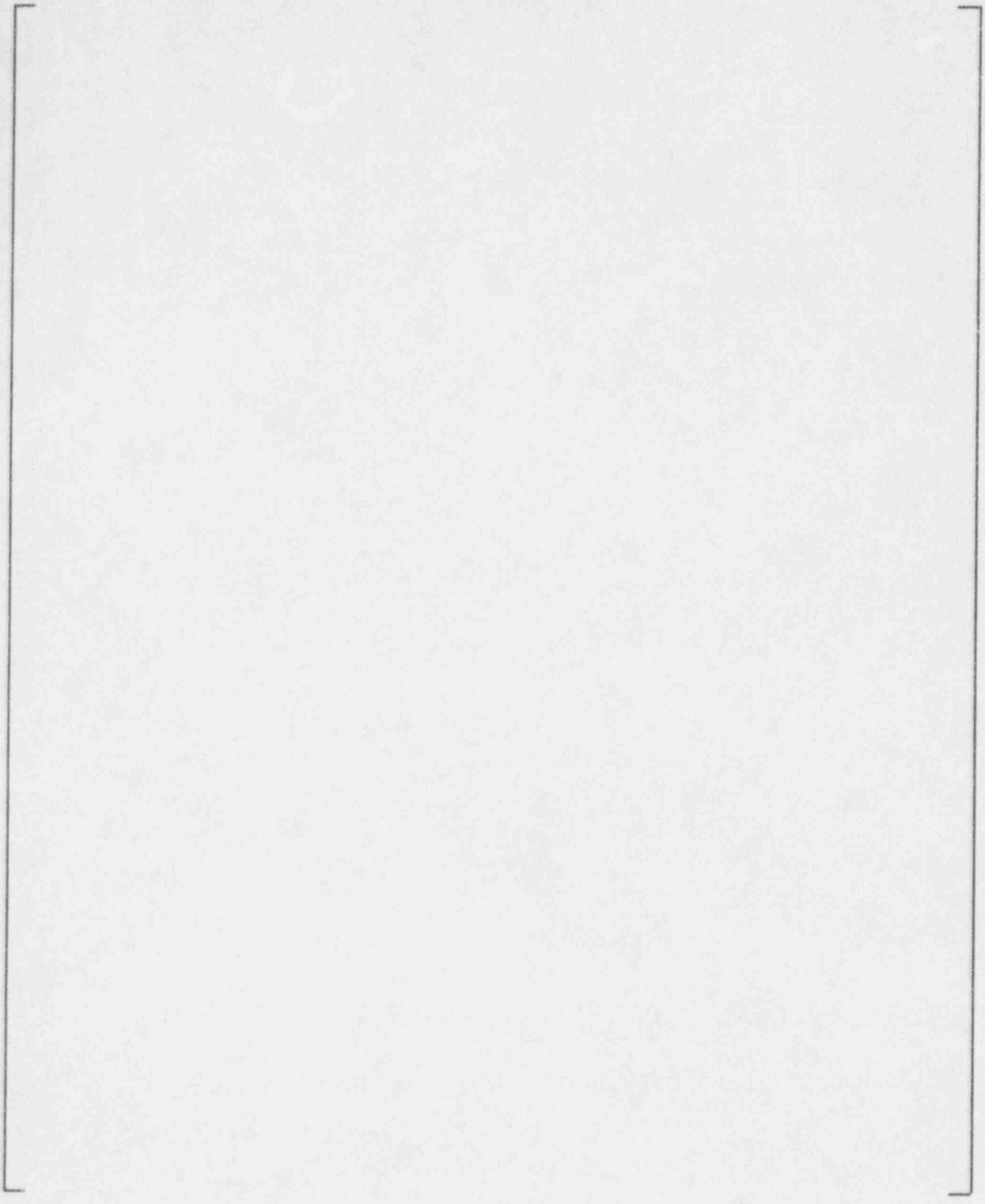

Figure 1-8 Comparison of AP600 and SPES-2 ADS-3 Discharge Flow

a,b,c

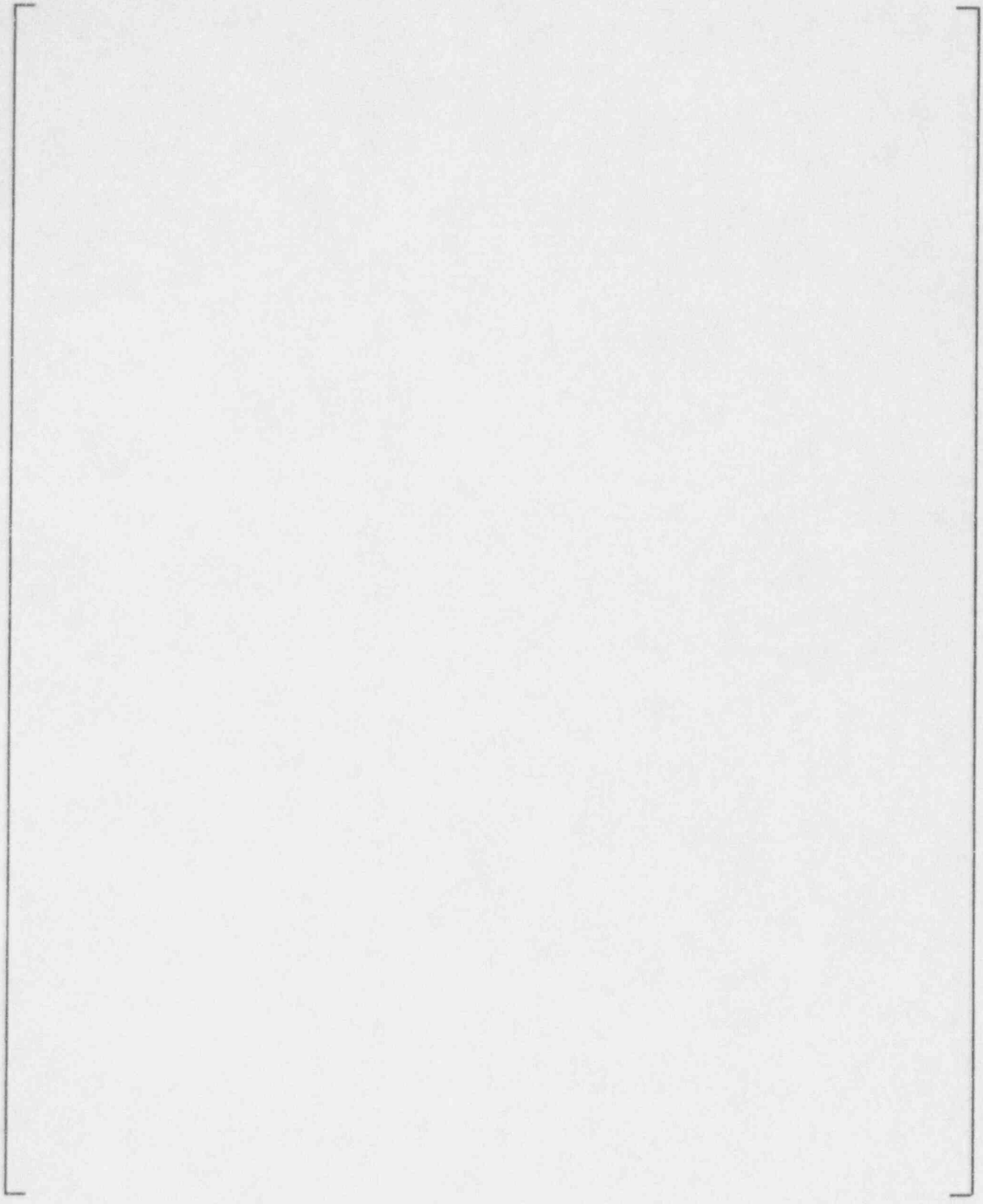

Figure 1-9 Comparison of AP600 and SPES-2 Total Primary System Mass

a,b,c

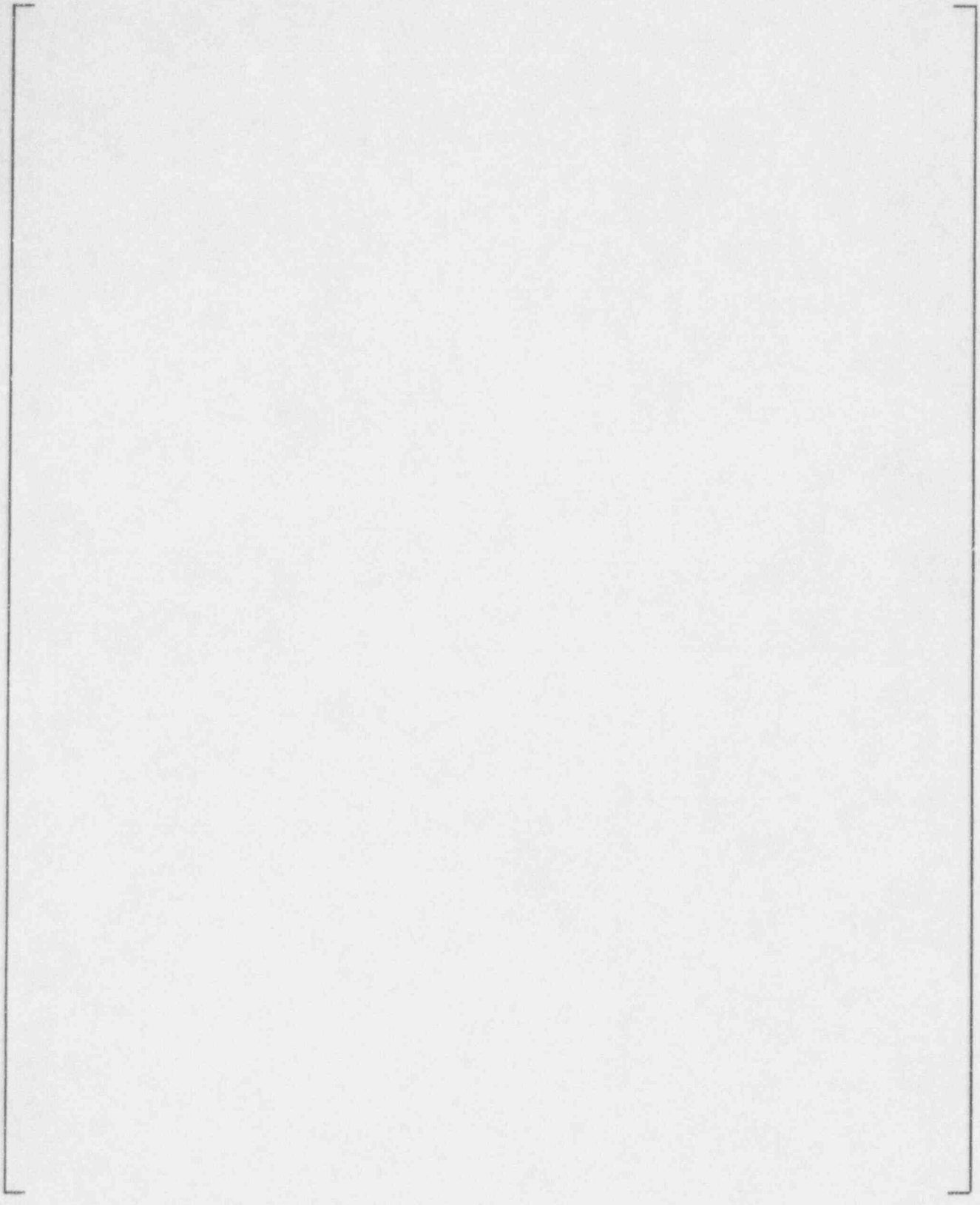

Figure 1-10 Comparison of Ideally Scaled SPES-2 Primary- and Secondary-Side Pressures to SPES-2 with Power Compensation

a,b,c

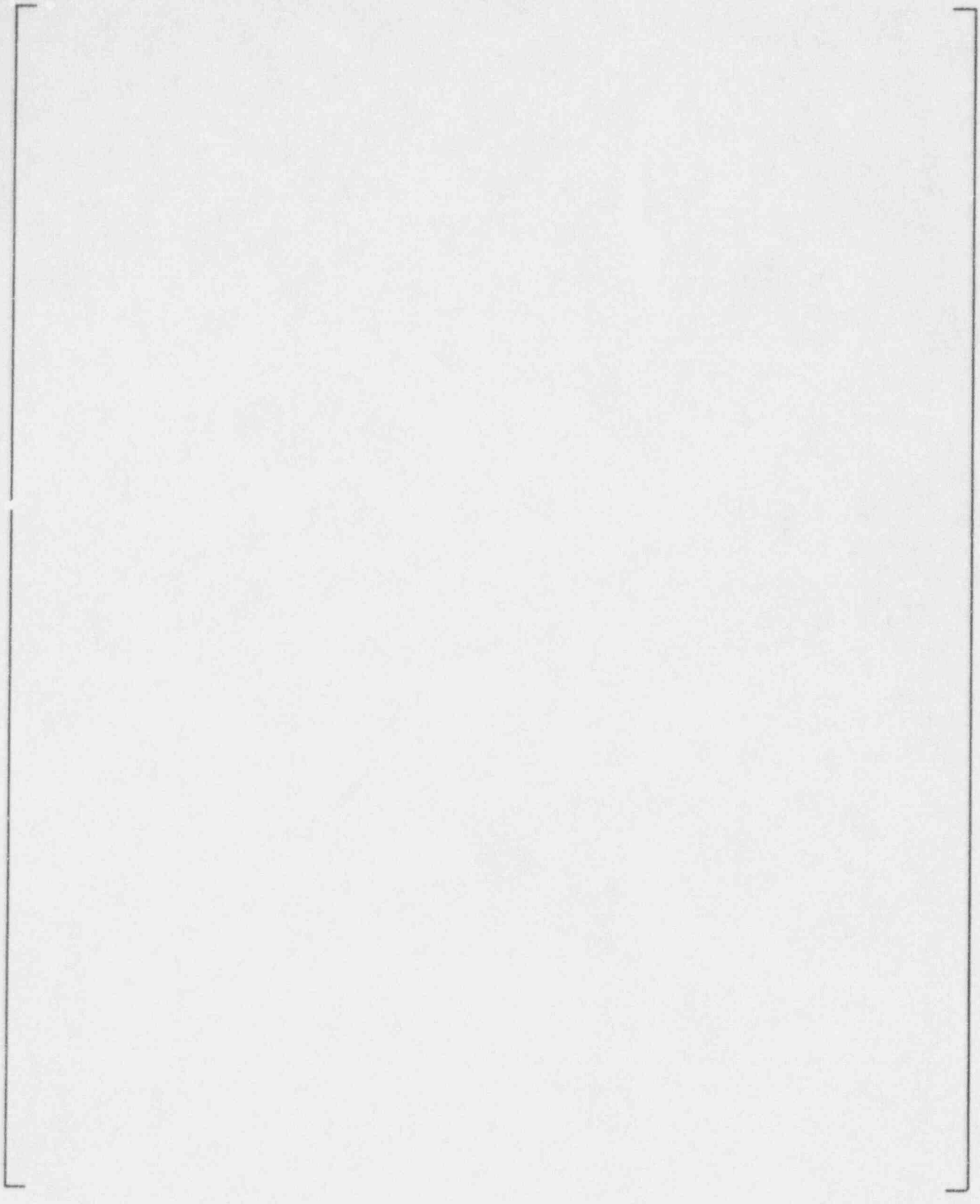

Figure 1-11 Comparison of Ideally Scaled SPES-2 Break Flows to SPES-2 Response with Power Compensation

a,b,c

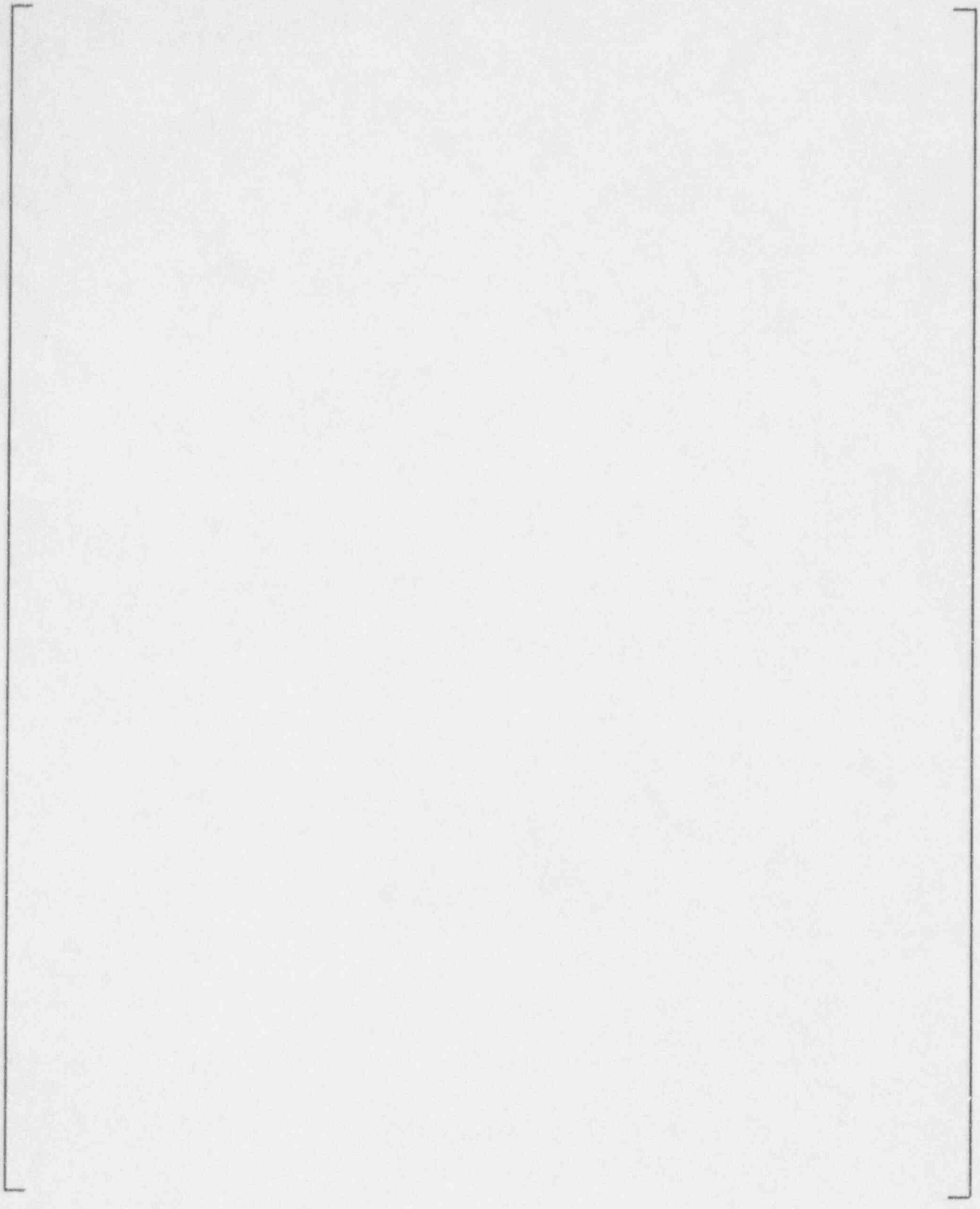

Figure 1-12 Comparison of Ideally Scaled SPES-2 Response for the CMT Level to the SPES-2 Response with Power Compensation

a,b,c

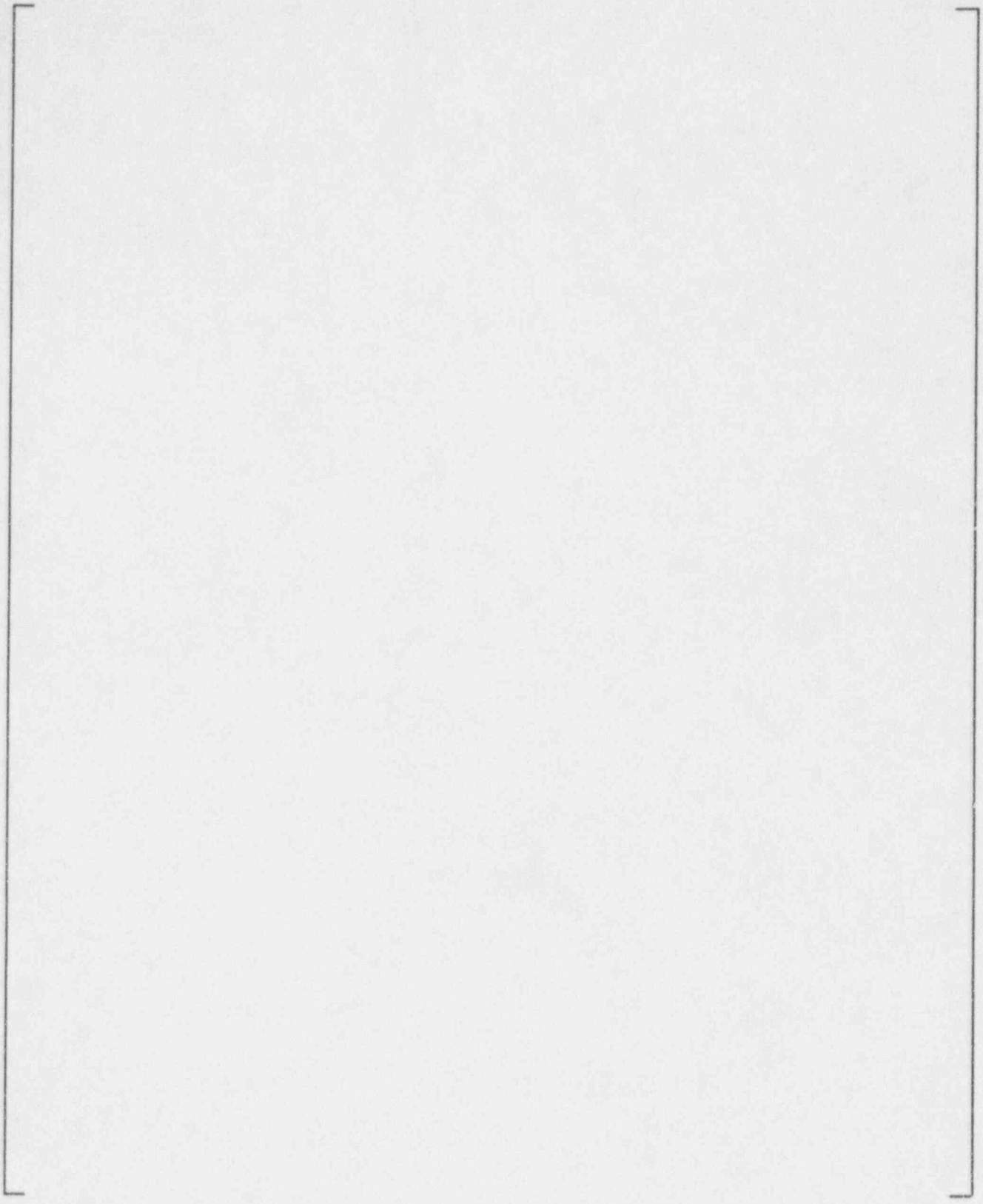

Figure 1-13 Comparison of the CMT Injection Flows Between the Ideally Scaled SPES-2 Response to the SPES-2 Response with Power Compensation

a,b,c

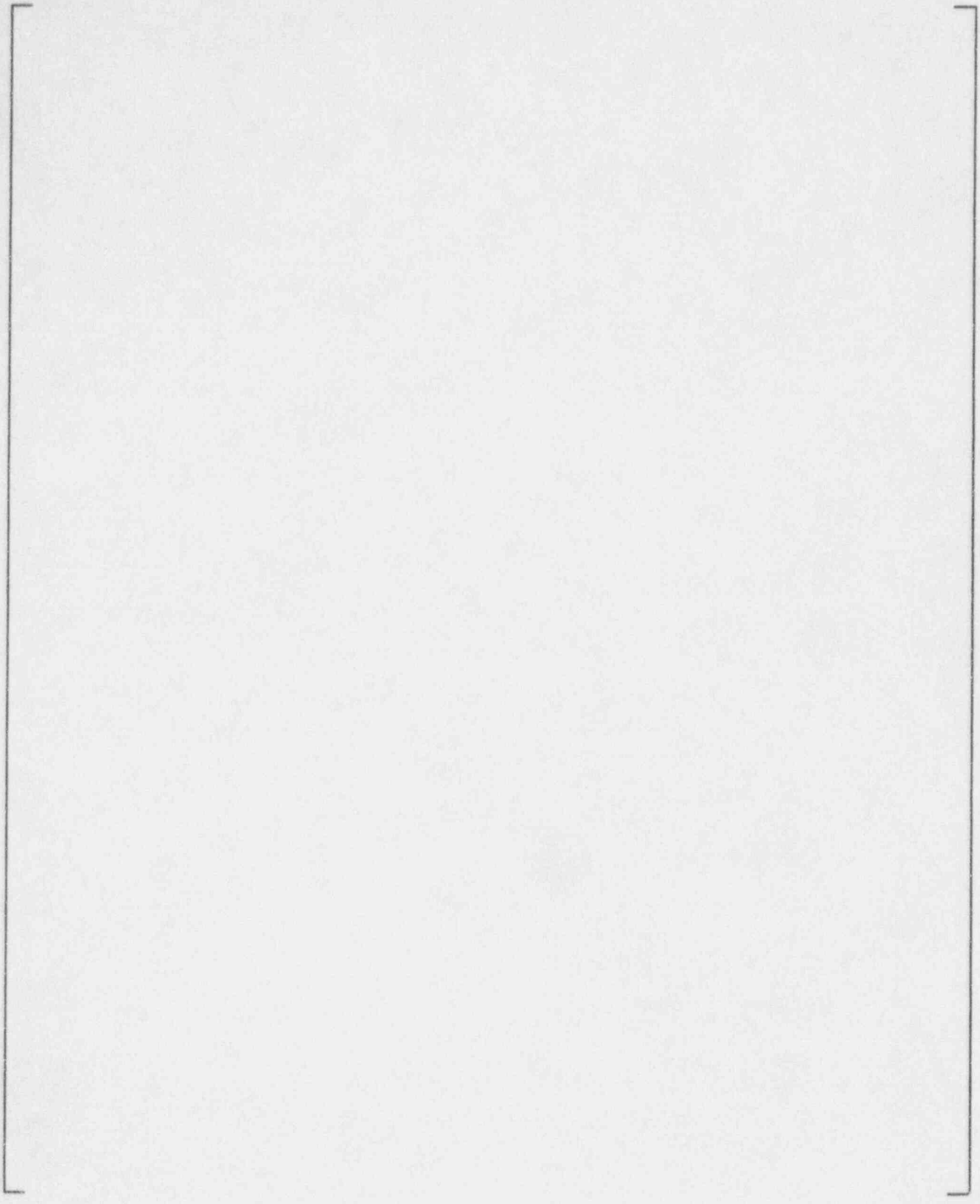

Figure 1-14 Comparison of the Pressurizer Collapsed Level with the Ideally Scaled Pressurizer and the Existing Pressurizer for a 2-Inch Cold-Leg Break

a,b,c

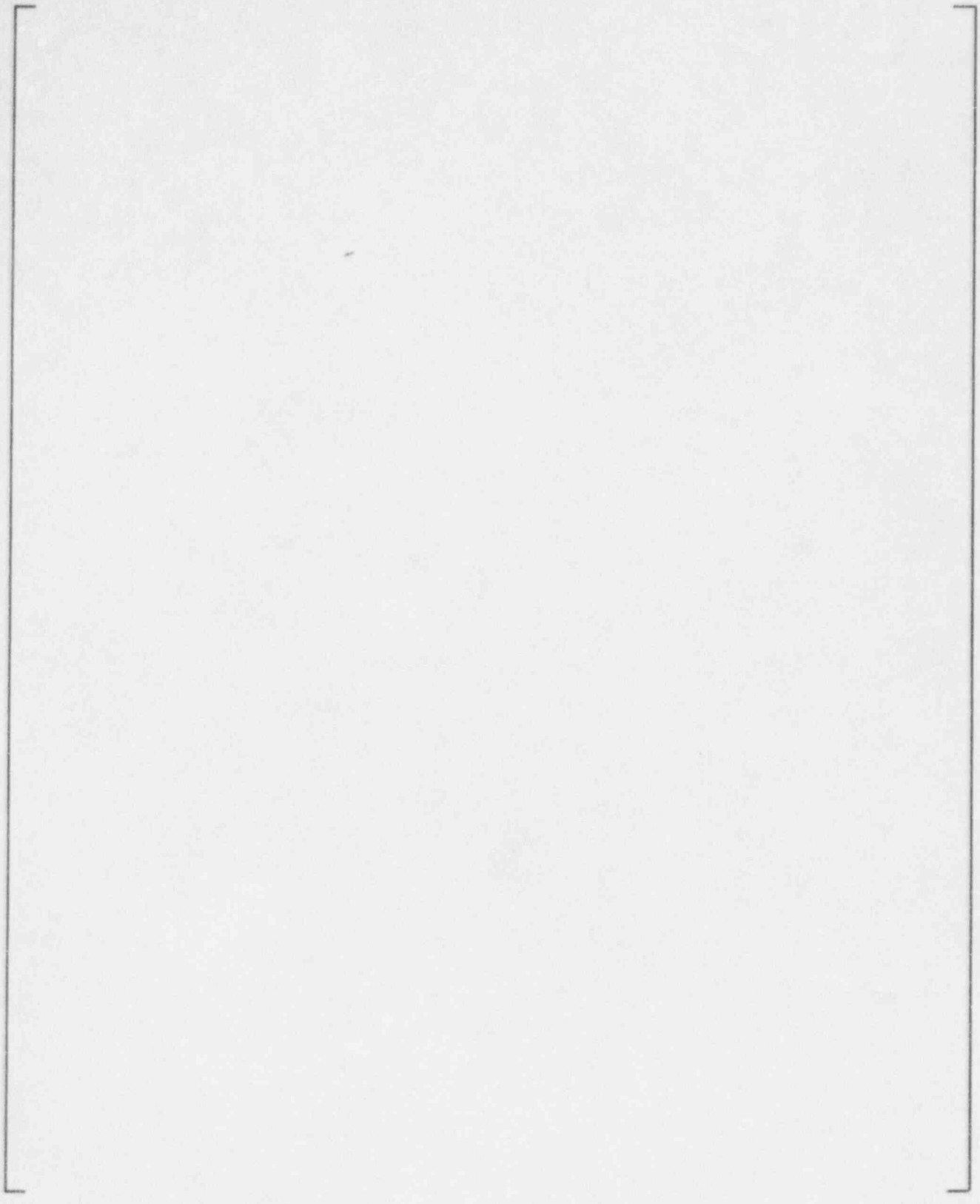

Figure 1-15 Comparison of the ADS-1 Flows for the Ideally Scaled SPES-2 Pressurizer to the Existing Pressurizer for a 2-Inch Cold-Leg Break

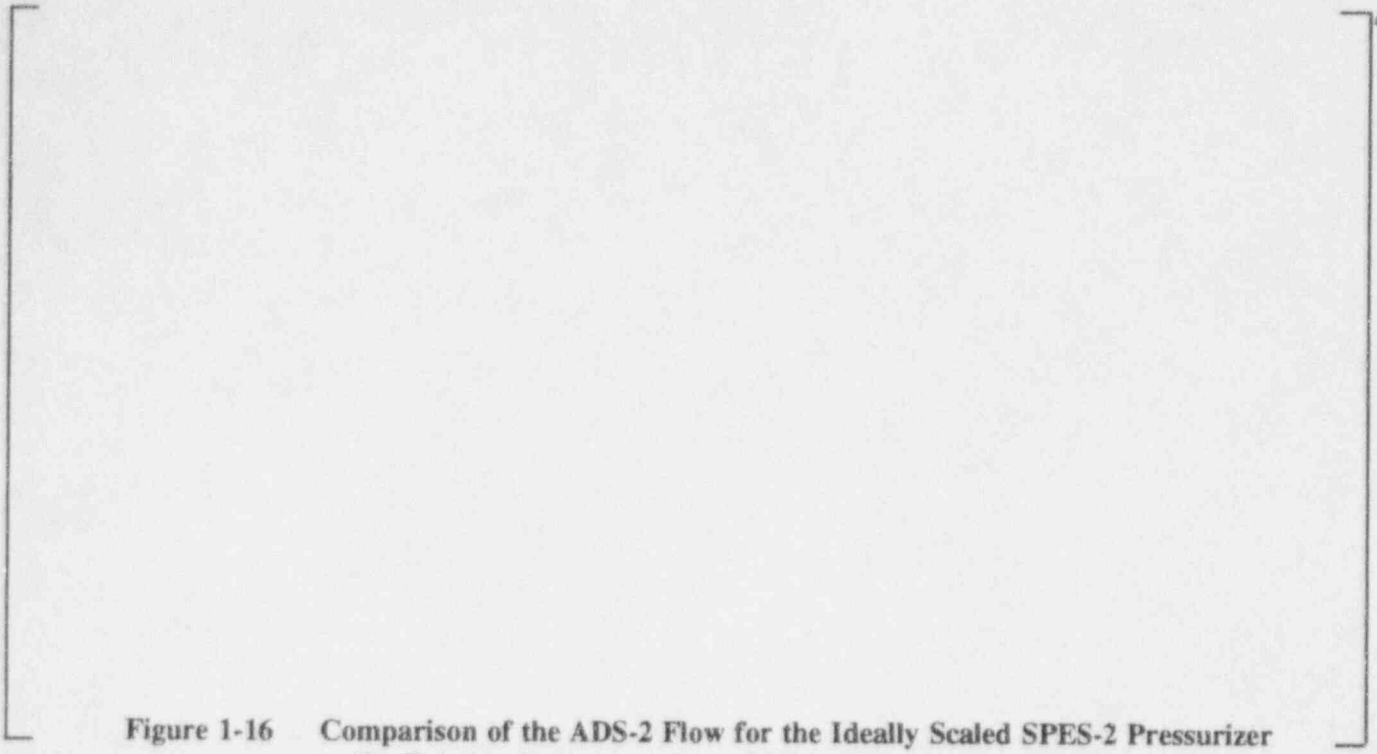
a,b,c

Figure 1-16 Comparison of the ADS-2 Flow for the Ideally Scaled SPES-2 Pressurizer to the Existing Pressurizer for a 2-Inch Cold-Leg Break


a,b,c

Figure 1-17 Comparison of the ADS-3 Flows for the Ideally Scaled Pressurizer to the Existing Pressurizer for a 2-Inch Cold-Leg Break

Figure 1-18 Comparison of the SPES-2 Primary System Mass with the Ideally Scaled Pressurizer and the Existing Pressurizer for a 2-Inch Cold-Leg Break

2.0 SPES-2 ANALYSIS METHODOLOGY - COMPONENT ANALYSIS

The SPES-2 facility is a full-pressure, full-height representation of the AP600 design, which has been used to simulate loss-of-coolant accident (LOCA) and non-LOCA accident scenarios. The primary purpose of this facility is to investigate the behavior of the passive core cooling systems over a range of faulted conditions. The SPES-2 facility represents the following components of the AP600:

- The primary circuit including the core, pressure vessel, loop pipework, and pressurizer.
- The steam generators.
- The passive safety systems (core makeup tanks [CMTs], in-containment refueling water storage tank [IRWST], passive residual heat removal [PRHR] and automatic depressurization system [ADS]) and the accumulators.
- Nonsafety systems (chemical volume and control system [CVCS], normal residual heat removal [NRHR], and startup feedwater system [SFWS]).

A computer code has been developed to perform test analysis of the SPES-2 tests.

In analyzing the results this code performs a mass and energy balance has been undertaken for all the main system components, and an overall mass and energy balance assessment has been undertaken. The models and data used in SPESAN to undertake this analysis are described in this section. All dimension data used for this analysis were taken from WCAP-14073, *SPES-2 Facility Description*.[2]

2.1 Core Makeup Tank (CMT)

The core makeup tank is a passive safety feature unique to the AP600. The CMTs consist of two tanks of cold, borated water maintained at system pressure, each connected at the top to a cold leg and connected at the bottom, through check valves and normally-closed isolation valves, to a direct vessel injection line. The CMTs are designed to passively inject water into the core in the event of a LOCA.

In the SPES-2 facility, the CMT is surrounded by a steel guard vessel.[2] The guard vessel is included in the energy balance calculations.

2.1.1 CMT Mass Balance and Liquid Level Calculations

The mass inventory in each CMT is found directly from the vertical pressure difference across the tank. The pressure difference is interpreted as an elevation head since the frictional and acceleration pressure drop terms are negligible due to the low flow rate in the CMT. The collapsed liquid level is found from this same pressure difference using measured fluid temperatures and pressure to determine fluid density distribution. The contribution of the CMT to the primary system mass balance is the fluid mass inventory. Other calculations include the injection flow from the bottom of the CMT

toward the direct vessel injection (DVI) line (which is measured directly) and the flow through the cold-leg balance line (CLBL) from a cold leg to the top the CMT (which is found by a mass balance in the CMT). These terms provide bases for comparison to computer models.

CMT Mass Inventory

The mass of fluid in each CMT is calculated as the sum of four vertical differential pressure measurements, multiplied by the effective average cross-sectional area of the tank as shown in Table 2.1.1-1. This area was found by dividing the measured total tank volume by the total height between the top and bottom differential pressure taps.

$$M_{CMT} = A_{CMT} \left(\sum_{i=1}^{4} \Delta P_{L-CMT-i} \right) \frac{g_c}{g} \qquad (2.1\text{-}1)$$

where:

M_{CMT} = mass of water and steam in the CMT (lbm)
A_{CMT} = horizontal inner cross-sectional area of the CMT; [ ]^{a,b,c}
$\Delta P_{L-CMT-i}$ = one of four adjacent vertical differential pressures measured in the CMT ($lb_f/ft.^2$)
g = gravity ($ft./sec.^2$)
g_c = gravitational constant ($lbm\text{-}ft.)/(lbf\text{-}sec.^2$)

CMT Flow Rates

The CMT drain flow rate is directly measured in the drain line and is expected to always show positive flow because of the check valve in the line.

The flow rate between the cold leg and the top of the CMT is equal to the sum of the drain flow rate and the rate of change of the CMT fluid mass.

$$\dot{m}_{in} = \dot{m}_{inj} + (M_{CMT,\,j} - M_{CMT,\,j-1}) \,/\, (t_j - t_{j-1}) \qquad (2.1\text{-}2)$$

where:

$\dot{m}_{in}$ = mass flow rate into the top of the CMT (lbm/sec.)

$\dot{m}_{inj}$ = measured drain flow rate from the CMT (lbm/sec.)

$M_{CMT,\,j}$ = CMT fluid mass at time t_j (lbm)

$M_{CMT, j-1}$ = CMT fluid mass at time t_{j-1} (lbm)

The CMT drain instrumentation are given in Table 2.1.1-2.

CMT Collapsed Liquid Level

The collapsed liquid level is calculated based on the sum of four vertical differential pressure measurements. The liquid level is that level for which the integral of fluid density times incremental height is equal to the total vertical pressure drop. The density of liquid is calculated based on the temperature at each fluid thermocouple, or saturation temperature if that is lower. The liquid density for the span between each adjacent pair of fluid thermocouples is assumed to be the average of the densities at those two thermocouple locations. Above the top thermocouple and below the bottom thermocouple, the density is assumed to be the same as that at the nearest thermocouple. Saturated steam is assumed above the collapsed liquid level. Pressure at the top of the CMT is used to find all fluid densities. The liquid level is limited to be between the bottom and top differential pressure taps.

$$\int_{z_0}^{L} \rho(z)\, dz + (z_{nTc+1} - L)\rho_g (P_{Top}) = \sum_{i=1}^{4} \Delta P_{L-CMT-i} \frac{g_c}{g} \qquad (2.1\text{-}3)$$

Except that

$$z_0 \le L \le z_{nTC+1}$$

where:

P_{Top} = pressure in the top of the CMT (psia)
L = elevation of the liquid level in the CMT (ft.)
$z_0 = 0$ = elevation of the bottom CMT differential pressure instrument tap (ft.)
z_1 = elevation of the bottom CMT fluid thermocouple (ft.)
z_2 = elevation of the second CMT fluid thermocouple (ft.)
...
z_{nTC} = elevation of the top CMT fluid thermocouple (ft.)
z_{nTC+1} = elevation of the top CMT differential pressure instrument tap (ft.)
$\rho_g(P_{Top})$ = density of saturated steam at P_{Top} (lbm/ft^3)
$\rho(z)$ = $(\rho_f(P_{Top}, T(z_j)) + \rho_f(P_{top}, T(z_{j+1})))/2$ (lbm/ft^3) for $z_j \le z < z_{j+1}$, $j = 1, 2, \ldots nTC$

and where:

$\rho_f(P,T)$ = density of liquid water at pressure P, temperature = min (T, T_{sat} (P)) (lbm/ft.^{3})

$T(z_j)$ = temperature indicated by the CMT fluid thermocouple at z_j, or by the nearest fluid thermocouple for j = 0 or j = nTC+1 (°F)

$T_{sat}(P)$ = saturation temperature at pressure P (°F)

The instrumentation used to calculate the collapsed liquid level is given in Table 2.1.1-3.

CMT Mixture Level

To determine whether significant steam is stored with the liquid region in the CMTs, an attempt is made to calculate a mixture level (that is, the lower limit of the region containing essentially no liquid).

A local liquid level is first calculated within each of the four ranges of elevation in the CMT for which elevation pressure drop is measured. Exactly the same logic is used within each range as is used to find collapsed water level using the sum of the four pressure drops.

$$\int_{Z_{bi}}^{L_i} \rho(z)\, dz + (z_{ti} - L)\rho_g\,(P_{Top}) = \Delta P_{L\text{-}CMT\text{-}i}\,\frac{g_c}{g} \qquad (2.1\text{-}4)$$

where:

L_i = local elevation of the liquid level based on $\Delta P_{L\text{-}CMT\text{-}i}$ (ft.)

Z_{bi} = elevation of bottom tap of $\Delta P_{L\text{-}CMT\text{-}i}$ (ft.)

Z_{ti} = elevation of top tap of $\Delta P_{L\text{-}CMT\text{-}i}$ (ft.)

Normally this analysis is expected to show that, in the range which contains the collapsed level, the steam/water interface level is the same as the collapsed level. Ranges below this interface are full of liquid, and ranges above this interface are full of steam only.

When significant flashing occurs in a range below the steam/water interface, a void fraction will be found in that range. Also, in the range containing the collapsed level the local liquid level will be higher by a corresponding amount. In such a case, the void fraction in the range containing a level, below the interface, is assumed equal to the void fraction in the range below it. To avoid large misinterpretations resulting from small errors in data, we exclude ranges where the calculated local level is below 2 percent of the range (that is, essentially empty range) is excluded. Thus a mixture level is defined as follows:

$$L_{mix} = \max \left[L_i / (z_{ti-1} - L_{i-1}) / (Z_{ti-1} - Z_{bi-1}) \right]_{i=2}^{i} \qquad (2.1\text{-}5)$$

$$\text{for } L_i > z_{bi} + 0.02\,(Z_{ti} - Z_{bi})$$

where:

L_{mix} = mixture level (ft.)

TABLE 2.1.1-1 INSTRUMENTS FOR CALCULATING CMT MASS		
Description	**Instrumentation Tag**	**Variable**
Elevation pressure difference, CMT-A	DP-A41E, DP-A42E, DP-A43E, DP-A44E	$\Delta P_{L\text{-}CMT\text{-}i}$
Elevation pressure difference, CMT-B	DP-B41E, DP-B42E, DP-B43E, DP-B44E	$\Delta P_{L\text{-}CMT\text{-}i}$

TABLE 2.1.1-2 INSTRUMENTS FOR CALCULATING CMT MASS INLET FLOW		
Description	**Instrumentation Tag**	**Variable**
Drain flow, CMT-A	F_A40E	m_{inj}
Drain flow, CMT-B	F_B40E	m_{inj}

TABLE 2.1.1-3 INSTRUMENTS FOR CALCULATING CMT COLLAPSED LIQUID LEVEL		
Description	**Instrumentation Tag**	**Variable**
Elevation pressure difference, CMT-A	DP-A41E, DP-A42E, DP-A42E, DP-A44E	$\Delta P_{L\text{-}CMT\text{-}i}$
Elevation pressure difference, CMT-B	DP-B41E, DP-B42E, DP-B42E, DP-B44E	$\Delta P_{L\text{-}CMT\text{-}i}$
Top pressure, CMT-A	P-A40E	P_{Top}
Top pressure, CMT-A	P-B40E	P_{Top}
Fluid temperatures, CMT-A	T-A401E, T-A402E, T-A403E, T-A404E, T-A405E, T-A406E, T-A407E, T-A408E, T-A409E, T-A410E, T-A411E, T-A412E, T-A413E, T-A414E, T-A415E, T-A416E, T-A417E, T-A418E, T-A419E, T-A420E	$T(z_j)$
Fluid temperatures, CMT-B	T-B401E, T-B403E, T-B405E, T-B407E, T-B409E, T-B411E, T-B413E, T-B415E, T-B417E, T-B420E	$T(z_j)$

2.1.2 CMT Energy Balance Calculations

Several components of energy transfer must be determined to establish an overall energy balance for the CMT. These include the energy flow into the CMT from the CLBL, the energy flow out of the CMT through the drain line, energy storage in the CMT fluid, heat storage in the CMT vessel and guard vessel, and metal and heat loss to the surroundings. Each component is calculated from the instrumentation available in the tests. The overall CMT energy balance is used to determine the relative magnitudes of each component and to provide a basis for comparison to computer models.

The total of the fluid energy storage metal energy stored and energy loss is used in the overall energy balance.

Energy Storage in the CMT Fluid

The rate of change of internal energy in the CMT fluid is determined by calculating the internal energy at each time step and differentiating with respect to time. The internal energy is found as the integral of the product of fluid density times specific enthalpy in the CMT, minus the product of pressure and volume of the CMT. The specific enthalpy and density of fluid below the calculated liquid level are assumed to be the averages of the properties of the liquid at the temperatures at the two nearest fluid thermocouples, or at the nearest thermocouple for the regions below the bottom thermocouple or above the top thermocouple, or at saturation temperature if that is lower. The fluid above the liquid level is assumed to be saturated steam. The pressure measured in the top of the CMT is used for all properties.

$$U_{tot} = A_{CMT}\left[\int_{z_o}^{L} \rho(z)\, h(z)\, dz + (z_{nTc+1} - L)\, \rho_g h_g\, (P_{Top}) - P_{Top}\, (z_{nTc-1} - z_o)J\right] \qquad (2.1\text{-}6)$$

where:

U_{tot} = total fluid internal energy in the CMT (Btu)
$h_g(P_{Top})$ = enthalpy of saturated steam at P_{top} (Btu/lbm)
$h(z)$ = $(h_f(P_{Top}, T(z_j)) + h_f(P_{Top}, T(z_{j+1})))/2$ for $z_j \le z < z_{j+1}$, $j = 1, 2, \ldots nTC$
J = Joules constant

and where:

$h_f(P,T)$ = specific enthalpy of liquid water at pressure P, temperature T (Btu/lbm)

Other terms are defined under collapsed liquid level calculation in Section 2.1.1.

Thermocouples used in the fluid energy calculations are listed in Tables 2.12-4 and 2.1.2-5.

The fluid thermocouples along with the elevation and associated volume are shown in Table 2.1.2-4 for CMT-A, and Table 2.1.2-5 for CMT-B.

The rate of energy storage in the CMT fluid is given by the following equation:

$$Q_{fluid\text{-}store} = dU_{tot}/dt = (U_{tot\text{-}i} - U_{tot\text{-}i\text{-}1}) / (t_j - t_{j\text{-}1}) \quad (2.1\text{-}7)$$

where:

$Q_{fluid\text{-}store}$ = rate of change of energy storage in CMT (Btu/sec.)
$U_{tot\text{-}i}$ = total energy of fluid at time t_j (Btu)
$U_{tot\text{-}i\text{-}1}$ = total energy of fluid at time $t_{j\text{-}i}$ (Btu)
t_j = present time (sec.)
$t_{j\text{-}1}$ = previous time (sec.)

Heat Loss to the Surroundings

The heat transfer from the CMT fluid to the surroundings consists of the heat stored in the guard vessel wall, and the heat loss from guard vessel to the ambient. The thermocouples used to determine these heat losses are summarized in Table 2.1.2-1.

Heat Storage in the CMT Wall

The heat storage rate in the CMT wall is given by the following equation:

$$Q_{CMT\text{-}store} = M_{CMT\text{-}wall}\, c_p \frac{dT}{dt} \quad (2.1\text{-}8)$$

where:

$Q_{CMT\text{-}store}$ = heat storage rate in the CMT wall (Btu/sec.)
$M_{CMT\text{-}wall}$ = mass of the CMT tank (lbm)
c_p = specific heat of the CMT tank (0.123 Btu/lbm-°F for stainless steel) (Btu/lbm-°F)
dT/dt = time rate of change of the CMT wall temperature (°F/sec.)

The CMT wall temperature is measured at several axial segments; with eight thermocouples for CMT-A, and four thermocouples for CMT-B.

Thus the total heat storage rate is

$$Q_{CMT\text{-}store} = c_p \sum M_i \left[T_i(t_j) - T_i(t_{j-1}) \right] / (t_j - t_{j-1}) \qquad (2.1\text{-}9)$$

where:

M_i = masses of the CMT wall associated with each thermocouple (lbm)
t_j = present time (sec)
t_{j-1} = previous time (sec)
T_i = measured temperatures at times t_j and t_{j-1} (°F)

The CMT wall mass associated with each thermocouple is summarized in Table 2.1.2-2.

Heat Transfer from the CMT Wall to the Guard Vessel

The heat transfer from the CMT wall to the guard vessel is given by the following equation:

$$Q_{CMT\text{-}GV} = Q_{c/c} + Q_{rad} \qquad (2.1\text{-}10)$$

where:

$Q_{CMT\text{-}GV}$ = heat transfer from the CMT wall to the guard vessel (Btu/sec.)
$Q_{c/c}$ = heat transfer due to convection and conduction through the air gap (Btu/sec.)
Q_{rad} = heat transfer via radiation (Btu/sec.)

The heat transfer through the air gap depends strongly on the fraction of the CMT wall that is heated. Free convection cells, caused by the temperature difference between the hot CMT wall and the cold guard vessel wall, can significantly enhance the heat transfer across the air gap. Holman[6] defines an equivalent thermal conductivity for the air in the gap, as enhanced by free convection:

$$k_{eq} = k\ 0.197\ (Gr\ Pr)^{1/4}\ (L/\delta)^{-1/9} \qquad (2.1\text{-}11)$$

where:

k_{eq} = the equivalent thermal conductivity across the gap (Btu/sec.-ft.-°F)
k = thermal conductivity of the air in the gap (Btu/sec.-ft.-°F)
L = heated length of the CMT wall (ft.)
δ = distance between the walls (ft.)
Pr = Prandtl number of the air in the gap
Gr = Grashof number

The Grashof number is given by the following:

$$Gr = g\ \beta\ (T_{CMT} - T_{GVid})\ \delta^3 / \nu^2 \qquad (2.1\text{-}12)$$

where:

ν = kinematic viscosity of the air ($ft.^2/sec.$)
β = coefficient of volumetric expansion, 1/T(R) ($°R^{-1}$)
T_{CMT} = average CMT wall temperature (°F)
T_{GVid} = average guard vessel temperature at the inside diameter (°F)

Thus, the heat transfer via conduction/convection through the enclosed air space is

$$Q_{c/c} = A_{CMT}\ k_{eq}\ (T_{CMT} - T_{GVid})/\delta \qquad (2.1\text{-}13)$$

where:

A_{CMT} = surface area of the CMT ($ft.^2$)

Radiation heat transfer from the CMT wall to the guard vessel is given by the following equation:

$$Q_{rad} = \sigma\ \varepsilon_{avg}\ A_{CMT}\ (T_{CMT}^4 - T_{GVid}^4) \qquad (2.1\text{-}14)$$

where:

Q_{rad} = radiation heat transfer from the CMT wall to the guard vessel (Btu/sec.)
σ = Stefan-Boltzmann constant ($Btu/sec.\text{-}ft.^2\text{-}°R^4$)
ε_{avg} = average surface emissivity

The average surface emissivity is given by the following equation:

$$\varepsilon_{avg} = 1/(\ 1/\varepsilon_{CMT} + 1/\varepsilon_{GVid} - 1) \qquad (2.1\text{-}15)$$

where:

ε_{CMT} = emissivity of the CMT wall
ε_{GVid} = emissivity of the guard vessel (assumed to be 0.5)

Heat Storage in the Guard Vessel

The heat storage rate in the guard vessel wall is given by the following equation:

$$Q_{GV\text{-}store} = M_{GV\text{-}wall}\ C_p\ \frac{dT_{GV}}{dt} \qquad (2.1\text{-}16)$$

where:

$Q_{GV\text{-}store}$ = heat storage rate in the guard vessel wall (Btu/sec.)
$M_{GV\text{-}wall}$ = mass of the guard vessel (lbm)
c_p = specific heat of the guard vessel (0.1 Btu/lbm°F for steel)
$\frac{dT_{GV}}{dt}$ = time rate of change of the guard vessel temperature, which is calculated by averaging the inside and outside wall temperatures (°F/sec.)

The guard vessel temperature is measured at two axial segments for both CMTs.

Thus, the total heat storage rate is

$$Q_{GV\text{-}store} = c_p \sum M_i\ [\ T_i(t_j) - T_i(t_{j-1})\ ]\ /(\ t_j - t_{j-1}\ ) \qquad (2.1\text{-}17)$$

where:

M_i = masses associated with each thermocouple (lbm)

The guard vessel mass associated with each thermocouple is shown in Table 2.1.2-3.

Heat Transfer from the Guard Vessel to the Surroundings

The heat transfer from the guard vessel to the surroundings is comprised of free convection and radiation from the outer surface of the guard vessel. The free convection component is given by the following equation:

$$Q_{free} = A_{GV}\ \lambda_{free}\ (\ T_{GV} - T_{amb}\ ) \qquad (2.1\text{-}18)$$

where:

Q_{free} = free convection component (Btu/sec.)
A_{GV} = guard vessel surface area (ft.^{2})
T_{GVod} = guard vessel temperature (°F)
T_{amb} = ambient temperature (°F)
λ_{free} = free convection heat transfer coefficient (Btu/sec.-ft.^{2}-°F)

The free convection heat transfer coefficient is given by the following equation:

$$\lambda_{free} = k_{air}/H \, [0.13 \, (Gr \, Pr)^{1/3} \,] \qquad (2.1\text{-}19)$$

where:

k_{air} = air thermal conductivity (Btu/sec.-ft.-°F)
H = height of the guard vessel (ft.)
Pr = Prandtl number of the air

The Grashof number is given by the following equation:

$$Gr = g \, \beta \, (T_{GVod} - T_{amb}) \, H^3 / \nu^2 \qquad (2.1\text{-}20)$$

Radiation heat transfer from the guard vessel to the ambient is given by the following equation:

$$Q_{rad\text{-}GV} = \sigma \, \varepsilon \, A_{GVod} \, (\, T_{GV}^4 - T_{amb}^4 \,) \qquad (2.1\text{-}21)$$

where:

$Q_{rad\text{-}GV}$ = radiation heat transfer from the guard vessel to the ambient (Btu/sec.)
σ = Stefan-Boltzmann constant (Btu/sec.-ft.^{2}-°R^4)
ε = guard vessel surface emissivity (assumed 0.5)

The steam equation is applied to the steam region, and the water equation is applied to the liquid region of the tank. The measured water level is used to determine which thermocouples are measuring water or steam. The elevations of the thermocouples are compared to the level and the steam equations are applied to the thermocouples above the interface, and the liquid equations are applied to the thermocouples below the interface.

Overall Energy Balance for the CMT

The overall energy balance for the CMT is given by the following equation:

$$Q_{in} = Q_{out} + Q_{fluid\text{-}store} + Q_{wall} \qquad (2.1\text{-}22)$$

where:

Q_{in} = heat carried into the CMT from the CLBL (Btu/sec.)
Q_{out} = heat carried out of the CMT through the discharge line (Btu/sec.)
Q_{wall} = heat transferred from the fluid to the CMT wall (Btu/sec.)

The heat transferred from the fluid to the CMT wall is given by the following equation:

$$Q_{wall} = Q_{CMT\text{-}store} + Q_{CV\text{-}store} + Q_{free} + Q_{rad\text{-}CV} \quad (2.1\text{-}23)$$

The heat carried out of the CMT is given by the following equation:

$$Q_{out} = h_{out}\ \dot{m}_{out} \quad (2.1\text{-}24)$$

where:

Q_{out} = heat carried out of the CMT (Btu/sec.)
h_{out} = enthalpy of the liquid in the discharge line (Btu/lbm)
$\dot{m}_{out}$ = flow rate in the discharge line (lbm/sec.)

Alternatively, the heat carried into the CMT by the fluid from the balance line is given by the following equation:

$$Q_{in\text{-}alt} = h_{in}\ \dot{m}_{in} \quad (2.1\text{-}25)$$

where:

h_{in} = enthalpy of the liquid or steam entering the CMT (Btu/lbm)
$\dot{m}_{out}$ = flow rate into the CMT from the CLBL (lbm/sec.)

The mass flow rate into the CMT is calculated from the mass flow out the discharge line and the change in mass inside the CMT.

$$\dot{m}_{in} = \dot{m}_{out} + \left\{ M_{fluid}\ (t_j) - M_{fluid}\ (t_{j-1}) \right\} / (t_j - t_{j-1}) \quad (2.1\text{-}26)$$

where:

M_{fluid} = fluid mass in the CMT at times j and j-1 (lbm)

Thus, an estimate of the validity of the energy balance can be determined by comparing the calculated value of Q_{in} from Equation (2.1-21) with $h_{in}\dot{m}_{in}$ as follows:

$$Q_{error} = Q_{in} - h_{in}\, m_{in} \qquad (2.1\text{-}27)$$

where:

Q_{error} = difference in the CMT energy balance (Btu/sec.)

The instruments used to perform the overall energy balance are summarized in Table 2.1.2-6.

An alternate estimate of error is found by comparing different methods of determining the heat transfer to the guard vessel.

$$Q_{error\text{-}ht} = Q_{CMT\text{-}GV} - (Q_{GV\text{-}store} + Q_{free\text{-}GV} + Q_{rad\text{-}GV}) \qquad (2.1\text{-}28)$$

where:

$Q_{error\text{-}ht}$ = error in heat balance resulting from heat transfer to guard vessel (Btu/sec.)
$Q_{free\text{-}GV}$ = free convection heat loss from guard vessel (Btu/sec.)
$Q_{rad\text{-}GV}$ = radiation heat loss from guard vessel (Btu/sec.)

TABLE 2.1.2-1 TEMPERATURES FOR CALCULATING CMT ENERGY BALANCE	
Description	**Instrumentation Tag**
Outer CMT wall, lower half - A	TW-A45E, TW-A46E, TW-A47E, TW-A48E
Outer CMT wall, lower half - B	TW-B46E, TW-B48E
Air space, lower half - A	T-A42A
Air space, lower half - B	T-B42A
Guard vessel inner diameter, lower half - A	TW-A42AI
Guard vessel inner diameter, lower half - B	TW-B42AI
Guard vessel outer diameter, lower half - A	TW-A42AE
Guard vessel outer diameter, lower half - B	TW-B42AE
Outer CMT wall, upper half - A	TW-A41E, TW-A42E, TW-A43E, TW-A44E
Outer CMT wall, upper half - B	TW-B41E, TW-B44E
Air space, upper half - A	T-A41A
Air space, upper half - B	T-B41A
Guard vessel inner diameter, upper half - A	TW-A41AI
Guard vessel inner diameter, upper half - B	TW-B41AI
Guard vessel outer diameter, upper half - A	TW-A41AE
Guard vessel outer diameter, upper half - B	TW-B41AE
Ambient temperature	TPLANT

TABLE 2.1.2-2 CMT WALL MASSES ASSOCIATED WITH THERMOCOUPLES			
Thermocouple - CMT-A	**CMT Wall Mass A**	**Thermocouple - CMT-B**	**CMT Wall Mass B**
TW-A41E	[ ]^{a,b,c}	TW-B41E	[ ]^{a,b,c}
TW-A42E	[ ]^{a,b,c}		
TW-A43E	[ ]^{a,b,c}		
TW-A44E	[ ]^{a,b,c}	TW-B44E	[ ]^{a,b,c}
TW-A45E	[ ]^{a,b,c}		
TW-A46E	[ ]^{a,b,c}	TW-B46E	[ ]^{a,b,c}
TW-A47E	[ ]^{a,b,c}		
TW-A48E	[ ]^{a,b,c}	TW-B48E	[ ]^{a,b,c}

TABLE 2.1.2-3 GUARD VESSEL MASSES ASSOCIATED WITH THERMOCOUPLES			
Thermocouple - CMT-A	**Guard Vessel Mass A**	**Thermocouple - CMT-B**	**Guard Vessel Mass B**
TW-A41AI	[ ]^{a,b,c}	TW-B41AI	[ ]^{a,b,c}
TW-A42AI	[ ]^{a,b,c}	TW-B42AI	[ ]^{a,b,c}

TABLE 2.1.2-4
THERMOCOUPLES USED TO
CALCULATE INTERNAL ENERGY FOR CMT-A

Number	Instrument Tag	Elevation (ft.)
1	T-A401E	[ ]a,b,c
2	T-A402E	
3	T-A403E	
4	T-A404E	
5	T-A405E	
6	T-A406E	
7	T-A407E	
8	T-A408E	
9	T-A409E	
10	T-A410E	
11	T-A411E	
12	T-A412E	
13	T-A413E	
14	T-A414E	
15	T-A415E	
16	T-A416E	
17	T-A417E	
18	T-A418E	
19	T-A419E	
20	T-A420E	

TABLE 2.1.2-5 THERMOCOUPLES USED TO CALCULATE INTERNAL ENERGY FOR CMT-B		
Number	**Instrument Tag**	**Elevation (ft.)**
1	T-B401E	a,b,c
2	T-B403E	
3	T-B405E	
4	T-B407E	
5	T-B409E	
6	T-B411E	
7	T-B413E	
8	T-B415E	
9	T-B417E	
10	T-B420E	

TABLE 2.1.2-6 THERMOCOUPLES USED TO CALCULATE OVERALL CMT ENERGY BALANCE	
Description	**Instrument Tag**
Inlet temperature, CMT-A	T-A29P
Inlet temperature, CMT-B	T-B29P
Outlet temperature, CMT-A	T-A421E
Outlet temperature, CMT-B	T-B421E
Level, CMT-A	L_A40E
Level, CMT-B	L_B40E
Discharge flow, CMT-A	F_A40E
Discharge flow, CMT-B	F_B40E
Pressure, CMT-A	P-A40E
Pressure, CMT-B	P-B40E

2.2 Passive Residual Heat Removal System

The PRHR passively removes the primary system heat via natural circulation flow from the hot leg to a heat exchanger (HX) located in the IRWST. For SPES-2, this HX consists of either single or multiple tubes that enter the IRWST near the top of the tank, traverse horizontally for a short distance ([ ]^{a,b,c}), turn 90 degrees downward to include a vertical section ([ ]^{a,b,c}), turn 90 degrees into a second horizontal section ([ ]^{a,b,c}), and then exit the IRWST near the bottom of the tank.

2.2.1 In-Containment Refueling Water Storage Tank (IRWST) Mass Inventory

The mass of water in the IRWST has been determined from the water level (differential pressure) and temperature instruments listed in Table 2.2.1-1, assuming the water is always at atmospheric pressure.

The mass inventory is calculated using the following equation:

$$M_{IRWST} = \left(L_{IRWST,0}\, \rho_{IRWST,1} + 144\, \Delta P_{L\text{-}IRWST} \frac{g_c}{g} \right) A_{IRWST} \qquad (2.2\text{-}1)$$

where:

M_{IRWST} = mass of water in the IRWST (lbm)
$\Delta P_{L\text{-}IRWST}$ = differential pressure across the IRWST ($lb_f/ft.^2$)
$L_{IRWST,0}$ = length of the IRWST below the bottom of the level measuring instruments; [ ]^{a,b,c}
A_{IRWST} = cross-sectional area of the IRWST; [ ]^{a,b,c}
$\rho_{IRWST,1}$ = density of water at the bottom of the IRWST ($lbm/ft.^3$)

The collapsed water level is calculated using the following equation:

$$L_{IRWST} = C_2\, \Delta P_{L\text{-}IRWST} \frac{g_c}{g} \qquad (2.2\text{-}2)$$

where:

L_{IRWST} = measured IRWST water level (ft.)
C_2 = $144\, \rho_{IRWST}^{-1}$ (ft./psi); a conversion from differential pressure to level allowing for the current density

The density of water has been calculated, at each time point, from water table properties as follows:

- Assuming the water in the IRWST is at atmospheric pressure (14.7 psi), the saturation temperature is calculated.

- If the measured water temperature is at or exceeds the saturation temperature, the density is determined from tables for saturated liquid using the current water temperature.

- If the measured water temperature is below the saturation temperature, the density is calculated from tables for subcooled liquid using the current temperature and an assumed pressure of 14.7 psi.

For the calculation of the water density in the entire IRWST, the volume-weighted mean temperature of the measurements listed in Table 2.2.1-1 has been used. For the mass calculation, the water density at the bottom of the IRWST has been calculated using the temperature reading of the lowest thermocouple.

IRWST Mass Balance

The IRWST discharges to the power channel through direct vessel injection (DVI) lines A and B. The flow to each of the DVIs has been monitored via two venturi differential pressure devices, as listed in Table 2.2.1-2.

The IRWST flow devices provided valid measurements in all tests except S00303 when alternatives from F_A61E and F_B61E were used.

The mass discharged through each DVI line, in each time step, is calculated by multiplying the current discharge flow rate by the time step length, provided that the flow rate exceeds 0.05 lbm/sec. which is the minimum detectible signal relative to the noise in the measurement. A running total of the integrated mass discharged through each DVI line is determined by adding the mass discharged during the time step to the integrated mass from the end of the previous time step.

The PRHR HX deposits heat into the IRWST, so it is possible for water to boil off as well as to be injected to the DVIs. However, it is expected that the boil-off will recondense within the tank, thus there is no need to make allowance for this.

The calculated mass inventory in the IRWST for two successive time points has been used to determine a rate of change of mass using the following equation:

$$\frac{dM_{IRWST}}{dt} = \left(\frac{M_{IRWST}(t_j) - M_{IRWST}(t_{j-1})}{t_j - t_{j-1}} \right) \qquad (2.2\text{-}3)$$

where:

M_{IRWST} = mass of water in the IRWST (lbm)
t_j = current time (sec.)
t_{j-1} = previous time (sec.)

The mass of water in the IRWST has previously been calculated as given in Equation 2.2-1. For the first time point processed, a zero rate of mass change is assigned.

TABLE 2.2.1-1
IRWST INSTRUMENTATION FOR
CALCULATING IRWST MASS INVENTORY

Description	Instrument	Variable
Level of water in IRWST (differential pressure)	L-060E	$\Delta P_{L\text{-}IRWST}$
Temperature of water in IRWST (lowest thermocouple)	T-061E	$T_{IRWST,1}$
Temperature of water in IRWST (second lowest thermocouple)	T-062E	$T_{IRWST,2}$
Temperature of water in IRWST (midpoint thermocouple)	T-063E	$T_{IRWST,3}$
Temperature of water in IRWST (second highest thermocouple)	T-064E	$T_{IRWST,4}$
Temperature of water in IRWST (uppermost thermocouple)	T-065E	$T_{IRWST,5}$

TABLE 2.2.1-2
FLOW MEASURING INSTRUMENTS FOR
DISCHARGE FROM IRWST TO THE DVI LINES

Description	Instrument	Variable
Flow out of IRWST to DVI-A	F_A60E	$\dot{m}_{IRWSTA}$
Flow out of IRWST to DVI-B	F_B60E	$\dot{m}_{IRWSTB}$

2.2.2 Energy Balance on the PRHR/IRWST

To determine the effectiveness of the PRHR during an accident sequence, an energy balance is performed to determine the integrated heat transfer from the PRHR tube(s) to the IRWST water. This quantity can be calculated in a variety of ways:

1. Determine the calorimetric heat balance on the primary (tube) side.

2. Determine the heat transfer via natural convection and boiling from the tubes to the IRWST water.

3. Determine the time rate of change of the IRWST internal energy.

Each method is used to calculate and compare the PRHR/IRWST heat transfer as a function of time.

The instruments used to determine these quantities are summarized in Table 2.2.2-1.

Calorimetric Heat Balance on the Primary Side

The heat balance on the primary side is given by the following equation:

$$Q_{cal} = \dot{m} (h_{in} - h_{out}) \qquad (2.2\text{-}4)$$

where:

Q_{cal} = heat transfer determined by the primary (tube side) conditions (Btu/sec.)

$\dot{m}_{out}$ = mass flow rate through the PRHR tube(s) (lbm/sec.)

h_{in} = PRHR inlet enthalpy (Btu/lbm)

h_{out} = PRHR discharge enthalpy evaluated at T_{out} (Btu/lbm)

During the tests, it is possible for the PRHR inlet flow to be two-phase. For the PRHR inlet, a U-tube is provided, and two differential pressure cells are used to estimate the inlet void fraction. The signals from the two differential pressure cells are added together to cancel the friction component of the pressure drop. The void fraction is estimated by the following equation:

$$\alpha = 1 - (\Delta P_A - \Delta P_B) / (2\Delta P_{el}) \qquad (2.2\text{-}5)$$

where:

α = PRHR inlet void fraction

ΔP_A = differential pressure measurement of the riser portion of the U-tube ($lb_f/ft.$)

ΔP_{ji} = differential pressure measurement of the downward portion of the U-tube ($lb_f/ft.$)
ΔP_{el} = elevation hydrostatic pressure due to the water in each side of the U-tube

The elevation hydrostatic pressure due to the water in each side of the U-tube is given by the following equation:

$$\Delta P_{el} = H * \rho_f \, g/g_c \tag{2.2-6}$$

where:

H = height of the U-tube (ft.)
ρ_f = liquid density ($lbm/ft.^3$)

The quality of the inlet flow is then estimated from the void fraction to determine the inlet enthalpy. Assuming a two-phase homogeneous flow (no slip), the quality can be calculated from the void fraction by the following equation:

$$x = \frac{\alpha \rho_g}{(1-\alpha)\,\rho_f + \alpha \rho_g} \tag{2.2-7}$$

The quality is then used to calculate the inlet enthalpy:

$$h_{in} = h_f + x(h_g - h_f) \tag{2.2-8}$$

where:

h_{in} = inlet enthalpy (Btu/lbm)
h_f = saturated liquid enthalpy evaluated at T_{in} (Btu/lbm)
h_g = saturate vapor enthalpy evaluated at T_{in} (Btu/lbm)

Thus the total integrated energy transfer is given by the following equation:

$$U_{cal} = \int Q_{cal} \, dt = \sum_j Q_{cal_j} \, \Delta t_j \tag{2.2-9}$$

where:

U_{cal} = integrated heat transfer (Btu)
Q_{cal_j} = heat transfer across the PRHR tube at time step, Δt_j (Btu/sec.)

Heat Transfer Between the PRHR Tubes and the IRWST

The heat transfer between the PRHR tubes and the IRWST is characterized by subcooled boiling at the PRHR inlet and free convection along the vertical and lower horizontal sections of the tubes. Boiling occurs due to the combination of high PRHR inlet temperature, and the lower saturation temperature associated with the lower hydrostatic pressure at the top of the IRWST.

The temperature of the tube wall and the bulk temperature in the tank are used to determine the heat transfer coefficient. If the wall temperature is greater than the bulk temperature in the tank, subcooled boiling occurs, greatly increasing the local heat transfer relative to free convection. Due to the lack of detailed wall temperature measurements, it is necessary to interpolate and extrapolate to provide the detail needed to perform the heat balance.

Heat Transfer from the Inlet Horizontal Tube

The inlet tube contains a two-phase mixture that readily condenses. The high heat fluxes associated with condensation on the inside of the tubes are matched on the outside, creating the potential for subcooled boiling. Subcooled boiling is assumed to occur when the external wall temperature of the tube exceeds the saturation temperature in the tank in the vicinity of the tube. The subcooled boiling correlation, from Lahey and Moody[7] is

$$\lambda = C_2 (T_w - T_{sat})^n / (T_w - T_{bulk}) \qquad (2.2\text{-}10)$$

where:

λ = the boiling heat transfer coefficient (Btu/sec.-ft.^{2}-°F)
T_w = tube wall temperature (°F)
T_{sat} = saturation temperature in the tank (°F)
T_{bulk} = bulk temperature in the tank in the vicinity of the tubes (°F)

C_2 and n are constants given by the following equations:

$$C_2 = 15.6\ P^{1.156}$$
$$n = 2.3 / P^{0.0234}$$

where P is the pressure in the tank in the vicinity of the tubes ($lb_f/ft.^2$).

For the case where the tube wall temperature is less than the saturation temperature, the heat transfer coefficient is calculated using the free convection correlation for horizontal tubes from Holman[6] as follows:

$$\lambda = k/d\ 0.53 (GrPr)^{1/4} \qquad (2.2\text{-}11)$$

where:

λ = the free convection heat transfer coefficient (Btu/sec.-ft.^{2}-°F)
k = liquid thermal conductivity in the tank (Btu/sec.-ft.-°F)
d = tube outer diameter (ft.)
Pr = liquid Prandtl number
Gr = liquid Grashof number

The liquid Grashof number is given by the following equation:

$$Gr = g\beta (T_w - T_{bulk}) d^3 / \nu^2 \qquad (2.2\text{-}12)$$

where:

g = gravitational constant (ft./sec.^{2})
ν = liquid kinematic viscosity (ft.^{2}/sec.)
β = volumetric expansion coefficient (1/°R)

The volumetric expansion coefficient is given by the following equation:

$$\beta = (\rho_{bulk} - \rho_w) / [\rho_w (T_w - T_{bulk})] \qquad (2.2\text{-}13)$$

where:

ρ_{bulk} = liquid density evaluated at the bulk tank temperature (lbm/ft.^{3})
ρ_w = liquid density evaluated at the wall temperature (lbm/ft.^{3})

The energy transfer in this section of the PRHR tubes is given by the following equation:

$$Q_{HOR-1} = N_{tubes} A_{HOR-1} \lambda (T_w - T_{bulk}) \qquad (2.2\text{-}14)$$

where:

Q_{HOR-1} = energy transferred from the tube wall to the IRWST fluid for the horizontal inlet tube section (Btu/sec.)
N_{tubes} = number of PRHR tubes in operation
A_{HOR-1} = surface area of the inlet tube (ft.^{2})
λ = either the subcooled boiling or free convection heat transfer coefficient (Btu/sec.-ft.^{2}-°F)

Heat Transfer from the Vertical Segment

The heat transfer rate in the vertical segment was evaluated in the same way except that the free convection correlation for vertical cylinders was used. The free convection heat transfer coefficient is given by Holman[6] as follows:

$$\lambda = k\ 0.13\ [\ g\beta(\ T_w - T_{bulk}\ )\ Pr\ /\ \nu^2\ ]^{1/3} \qquad (2.2\text{-}15)$$

Subcooled boiling may occur near the top of the vertical segment, but the combination of cooler fluid inside the tubes and increased saturation temperature as the tube descends makes boiling unlikely anywhere else. The energy transfer in this section is given by the following equation:

$$Q_{VERT} = N_{tubes}\ A_{VERT}\ \lambda\ (T_w - T_{bulk}) \qquad (2.2\text{-}16)$$

where:

Q_{VERT} = energy transferred from the tube wall to the IRWST fluid for the vertical section (Btu/sec.)
A_{VERT} = surface area of the vertical tubes ($ft.^2$)

Heat Transfer from the Outlet Horizontal Section

The heat transfer from the outlet horizontal section is due to free convection and is calculated as given in Equation (2.2-14) as follows:

$$Q_{HOR-2} = N_{tubes}\ A_{HOR-2}\ \lambda\ (T_w - T_{bulk}) \qquad (2.2\text{-}17)$$

Because the heat transfer coefficient is dependent on the local wall temperature, the calculations on the inlet horizontal and vertical tube segments are divided into ten sections, each using the local value of the wall temperature. The tube wall temperature is measured at the center of the horizontal inlet section, the center of the vertical section, and the center of the horizontal outlet section. It is necessary, therefore, to linearly interpolate between the measured temperature and to extrapolate between the measured temperature at the center of the horizontal inlet section and the point where the tube first enters the tank. It is proposed that the wall temperature is greater than the value measured in the center of the section by ΔT_{offset}. To determine the value of the offset, the calorimetric heat balance is evaluated at some time in the transient. The value is chosen to match the calorimetric heat transfer rate. The offset value is then held constant over the entire test. This correction was found to be necessary due to underprediction of the heat transfer rate relative to the calorimetric rate. The effects of this assumption are discussed in Section 4.0.

Thus the total energy transfer from the PRHR tube walls to the IRWST water is

$$Q_{tubes\ tot} = Q_{HOR-1} + Q_{VERT} + Q_{HOR-2} \qquad (2.2\text{-}18)$$

Change in the Internal Energy of the IRWST

A final measure of the heat transfer rate can be approximated from the change in the internal energy of the IRWST. The tank is measured at five elevations, each is assumed to represent some fraction of the tank volume. The design of the PRHR insures that the tank will remain highly stratified with warm water on top, and cold water on the bottom. The internal energy at a point in time is given by the following equation:

$$U = \sum (h - P/\rho J)_i \, V_i \rho_i \qquad (2.2\text{-}19)$$

where:

U = IRWST fluid internal energy (Btu)
h = liquid enthalpy (Btu/lbm)
P = pressure ($lb_f/ft.^2$)
ρ = density ($lbm/ft.^3$)
V = volume associated with the thermocouple ($ft.^3$)
J = Joules constant

The fluid internal energy is used in the overall energy balance.

The five thermocouples that measure the tank water temperature are located near the PRHR tubes. When the PRHR is operating, the measured temperatures are approximately 2.5°F higher than the temperature of the water volume represented by the thermocouple. Thus, the model assumes a 2.5°F reduction in the measured thermocouple temperatures when the PRHR is operational. The effects of this assumption are discussed in Section 4.0.

The total increase in the tank internal energy is calculated by subtracting the calculated internal energy from the initial value. In addition, the energy of the discharge flow is added to this difference to determine the integrated energy increase at the end of the transient. There are three methods of determining the PRHR/IRWST energy transfer: the tube-side heat balance, the external tube heat transfer, and the change in the IRWST fluid energy provide independent calculations of the IRWST/PRHR performance during PRHR operation.

TABLE 2.2.2-1 INSTRUMENTATION FOR CALCULATING THE PRHR/IRWST HEAT BALANCE	
Description	**Instrumentation Tag**
PRHR inlet temperature	T-A82E
PRHR outlet temperature	T-A83E
PRHR fluid temp - upper piping	T-A181E
PRHR fluid temp - lower piping	T-A182E
PRHR tube wall temperatures	TW-A81E, TW-A181E, TW-A182E, TW-A183E
IRWST tank temperatures	T-061E, T-062E, T-063E, T-064E, T-065E
PRHR flow	F_A80E
Differential pressure cells to determine void fraction	DP-A81AE, DP-B81BE
IRWST liquid level	L_060E
PRHR pressure	P-017P

2.3 Accumulator

The accumulators provide a source of cold, borated water to the core after the primary system pressure reaches the accumulator pressure (~700 psia). The desired pressure is maintained by pressurizing a gas space at the top of the accumulators. As the system pressure falls below the accumulator pressure, a valve in the accumulator discharge line opens, and the gas in the accumulators expands, forcing liquid into the primary system. After the accumulators have completely discharged, the gas is injected into the reactor coolant system (RCS). The presence of noncondensible gas may have an effect on the performance of the passive heat removal systems, especially the PRHR.

2.3.1 Accumulator Mass Inventory

The mass of water in the two accumulators has been determined from the predetermined water level temperature, and pressure instruments listed in Table 2.3.1-1.

While the measured water level is greater than zero, the mass inventory is calculated using the following equation:

$$M_{ACC} = (V_{ACC,0} + L_{ACC}\ A_{ACC})\ \rho_{ACC} \qquad (2.3\text{-}1)$$

where:

M_{ACC} = mass of water in the accumulator (lbm)

ρ_{ACC} = density of water in the accumulator (lbm/ft.^{3})

$V_{ACC,0}$ = volume of the accumulator below the bottom of the level measuring instruments; [ ]^{a,b,c}

A_{ACC} = cross-sectional area of the accumulator over the length of the level instruments; [ ]^{a,b,c}

L_{ACC} = measured accumulator water level (ft.)

The density of water has been calculated, at each time point, from water table properties as follows:

- Given the current measured pressure, the saturation temperature is calculated.
- If the current water temperature is at or exceeds the saturation temperature, the density is determined from tables for saturated liquid using the current water temperature.
- If the current water temperature is below the saturation temperature, the density is calculated from tables for subcooled liquid using the current temperature and pressure.

When the measured water level falls to zero (that is, to the lower pressure tap), the mass in the accumulator is calculated by subtracting the mass discharged during that time step from the mass present at the start of the time step. The mass discharged is determined from the flow measurements

listed in Table 2.3.1-2. The mass of water is not allowed to fall below zero, and only flows greater than 0.05 lbm/s (which is necessary to neglect noise in the measurement) are included.

Accumulator Mass Balance

The two accumulators discharge to the power channel through DVI lines A and B. The flow to the DVIs has been monitored via two venturi differential pressure devices as listed in Table 2.3.1-2.

The accumulator flow devices provided reliable measurements in all tests except S00706. The mass discharged by each accumulator, in each time step, is calculated by multiplying the current discharge flow rate by the time step length, provided the flow rate exceeds 0.05 $lbms^{-1}$. A running total of the integrated mass discharged by each accumulator is determined by adding the mass discharged during the time step to the integrated mass from the end of the previous time step.

Since the downcomer injection represents the only flow to or from the accumulators, the change of mass inventory over any time step should balance with the mass flow rate determined by the respective discharge line. The calculated mass inventories in each of the two accumulators for two successive time points, have been used to determine a rate of change of mass using the following equation:

$$\frac{dM_{ACC}}{dt} = \left(\frac{M_{ACC}(t_j) - M_{ACC}(t_{j-1})}{t_j - t_{j-1}} \right) \qquad (2.3\text{-}2)$$

where:

M_{ACC} = mass of fluid in the accumulator (lbm)
t_j = current time (sec.)
t_{j-1} = previous time (sec.)

The mass of fluid in each accumulator has previously been calculated as described above. For the first time point processed, a zero rate of mass change is assigned.

TABLE 2.3.1-1
INSTRUMENTATION FOR
CALCULATING ACCUMULATOR MASS INVENTORY

Description	Instrument	Variable
Level of water in accumulator-A	L_A20E	L_{ACCA}
Pressure at top of accumulator-A	P-A20E	P_{ACCA}
Temperature of water in accumulator-A	T-A22E	T_{ACCA}
Level of water in accumulator-B	L_B20E	L_{ACCB}
Pressure at top of accumulator-B	P-B20E	P_{ACCB}
Temperature of water in accumulator-B	T-B22E	T_{ACCB}

TABLE 2.3.1-2
FLOW MEASURING INSTRUMENTS FOR
DISCHARGE FROM ACCUMULATORS TO THE DVI LINES

Description	Instrument	Variable
Flow out of accumulator-A to DVI-A	F_A20E	$\dot{m}_{ACCA}$
Flow out of accumulator-B to DVI-B	F_B20E	$\dot{m}_{ACCB}$

2.3.2 Energy Balance on the Accumulators

To determine the performance of the accumulators during accident sequences, an energy balance is performed which consists of determining the internal energy in the accumulator water as a function of time. In addition, the energy leaving the accumulator, which consists of the measured flow multiplied by the liquid enthalpy, is compared to the change in the accumulator internal energy with respect to time.

A second calculation is performed to determine the expansion characteristics of the gas in the accumulators during the injection phase and the total mass of gas injected into the RCS.

The instruments used to determine these quantities are summarized in Table 2.3.2-1.

Internal Energy of the Accumulator Fluid

The internal energy of the water in the tank is given by the following equation:

$$U = (h - P/\rho J) V\rho \qquad (2.3\text{-}3)$$

where:

h = liquid enthalpy (Btu/lbm)
P = pressure ($lb_f/ft.^2$)
ρ = density ($lbm/ft.^3$)
V = volume ($ft.^3$)
J = Joule's constant

The liquid enthalpy and density are evaluated at the liquid temperature.

The fluid internal energy relative to the start of the test is used to determine an overall energy balance.

Behavior of the Noncondensible Gas in the Accumulators

The noncondensible gas expands as the pressure decreases and the tank empties. The relationship governing the expansion of an ideal gas is given by the following equation:

$$P V^{\kappa} = \text{const.} \qquad (2.3\text{-}4)$$

where:

P = gas pressure ($lb_f/ft.^2$)
V = gas volume ($ft.^3$)
κ = gas expansion exponent

For adiabatic expansion, which occurs rapidly,

$$\kappa = 1.4$$

For isothermal expansion, which occurs slowly,

$$\kappa = 1.0$$

The expansion exponent is determined from the test data by using the measured pressure and the volume at the start of accumulator discharge, and at the end of accumulator discharge. The exponent is derived from the Ideal Gas Law which is applied at the gas temperature.

$$\kappa = (P_2 - P_1)(V_2 + V_1)/\{ (P_2 + P_1)(V_2 - V_1) \} \quad (2.3\text{-}5)$$

Finally, the mass of gas discharged from the accumulators into the RCS is given by the following equation:

$$M_{exit} = M_{gas}(t_o) - M_{gas}(t) \quad (2.3\text{-}6)$$

where:

M_{exit} = mass of gas discharged (lbm)
$M_{gas}(t_o)$ = mass of the gas at time zero (lbm)
$M_{gas}(t)$ = mass of the gas at some point in time (lbm)

The mass of the gas is calculated using the Ideal Gas Law:

$$M_{gas} = PV/RT \quad (2.3\text{-}7)$$

where:

M_{gas} = mass of gas in the accumulator (lbm)
P = gas pressure ($lb_f/ft.^2$)
R = ideal gas constant
T = absolute temperature of the gas (°R)

The mass of the gas is constant until the accumulators are completely drained.

Change in the Energy of the Accumulator Tank Metal

The change of metal temperature over the course of the test must be accounted to provide an accurate estimate of the overall energy balance. The energy in the metal as a function of time is given by the following equation:

$$U_{metal}(t) = M\ c_p\ T(t) \qquad (2.3\text{-}8)$$

where:

$U_{metal}(t)$ = quantity of heat contained in the metal (Btu)
M = mass of metal in the accumulator (lbm)
c_p = specific heat of the metal (Btu/lbm-°F)
T(t) = absolute temperature of the metal as a function of time (°F)

The change in the energy contained in the metal is given by the following equation:

$$\Delta U_{metal} = \{U_{metal}(t) - U_{metal}(t_o)\} \qquad (2.3\text{-}9)$$

where:

ΔU_{metal} = change in the metal energy relative to time zero
$U_{metal}(t)$ = energy content of the metal at time t
$U_{metal}(t_o)$ = energy content of the metal at time t_o

The mass metal in the accumulator is [ ]^{a,b,c} per loop, and the specific heat is 0.108 Btu/lbm-°F.

TABLE 2.3.2-1 INSTRUMENTATION FOR CALCULATING ACCUMULATOR ENERGY BALANCE	
Description	**Instrumentation Tag**
Pressure - accumulator-A	P-A20E
Pressure - accumulator-B	P-B20E
Gas temperature - A	T-A21E
Gas temperature - B	T-B21E
Liquid temperature - A	T-A22E
Liquid temperature - B	T-B22E
Discharge flow - A	F_A20E
Discharge flow - B	F_B20E
Liquid level - A	As calculated for mass balance
Liquid level - B	As calculated for mass balance

2.4 Steam Generator

The SPES-2 facility represents two steam generators with both primary and secondary sides. The primary side is composed of the U-tubes and an inlet and an outlet plenum. The secondary side consists of a riser region, a separator, and a steam dome with an outlet to the main steam lines. Water is supplied to the secondary side by feedwater and start-up feedwater pipe work.

During normal operation and the initial stages of a fault, the steam generators remove heat from the primary circuit via the steam generator U-tubes. During all but the steam line break simulations, the secondary-side steam lines are isolated and heat transfer from the primary ceases rapidly. Subsequently, there may be a small reverse flow of heat (secondary to primary); however, this is very difficult to measure.

2.4.1 Steam Generator Mass Inventory

Both primary and secondary sides of the steam generator have been considered for both loops of the SPES-2 system. The hot and cold halves of the primary side have been treated separately. Only the riser region of the secondary has been considered; that is, up to the top of the level measuring differential pressure tap (DP-A10S and DP-B10S).

Steam Generator Primary-Side Mass Inventory

The steam generator primary side consists of an inlet and an outlet volume plus the U-tubes. The U-tubes themselves can be considered as a region within the tube plate, a straight active length and a bent length. This defines the following volumes:

[ ]a,b,c

The mass of water in the steam generator primary side has been determined from the differential pressure, temperature, and pressure instruments listed in Table 2.4.1-1.

The level of water in the hot and cold halves of the two steam generator primary sides have been determined from the relevant summed differential pressure measurements using the following equation:

$$L_{SGP} = C_2 \, \Delta P_{SGP} \, \frac{g_c}{g} \qquad (2.4\text{-}1)$$

where:

L_{SGP} = calculated water level (ft.). The maximum allowed level is the span of the differential pressure measurements, which is [ ]^{a,b,c}

ΔP_{SGP} = differential pressure across the hot or cold side of the steam generator primary (psi)

C_2 = 144 ρ_{SGP}^{-1} (ft./psi) conversion from differential pressure to level allowing for the current density

The calculated water level is used to determine the volume of the steam generator primary side filled by the collapsed liquid using linear interpolation in a tabulation of volume versus level defined by the dimensions listed above. Since the above dimensions are for the entire primary side and each calculation considers the separate halves, half the indicated volume is used. The mass inventory is then calculated using the following equation:

$$M_{SGP} = V_{SGP}\ \rho_{SGP} \qquad (2.4\text{-}2)$$

where:

M_{SGP} = mass of water in the segment of the primary side (lbm)

ρ_{SGP} = density of water in the segment of the primary side (lbm/ft.^{3})

V_{SGP} = volume of the primary side filled with water (ft.^{3}) as determined from the collapsed liquid level

The density of water has been calculated, at each time point, from water table properties as follows:

- Given the current measured pressure, the saturation temperature is calculated.
- If the current water temperature is at or exceeds the saturation temperature, the density is determined from tables for saturated liquid using the current water temperature.
- If the current water temperature is below the saturation temperature, the density is calculated from tables for subcooled liquid using the current temperature and pressure.

The current temperature for the hot side is the steam generator inlet temperature, while the steam generator outlet temperature is used for the cold side.

Steam Generator Primary-Side Mass Balance

The calculated mass inventory, for each half of the steam generator primary side, for two successive time points, has been used to determine a rate of change of mass using the following equation:

$$\frac{dM_{SGP}}{dt} = \left(\frac{M_{SGP}(t_j) - M_{SGP}(t_{j-1})}{t_j - t_{j-1}} \right) \qquad (2.4\text{-}3)$$

where:

M_{SGP} = mass of fluid in the steam generator primary side (lbm)
t_j = current time (sec.)
t_{j-1} = previous time (sec.)

The mass of fluid has previously been calculated as described above. For the first time point processed, a zero rate of mass change is assigned.

Steam Generator Secondary-Side Mass Inventory

The steam generator secondary consists of a riser, downcomers, a separator, and a steam dome. To calculate the secondary-side mass inventory, the region covered by the level measurement (up to an elevation of 17.807 m) has been considered. All other regions, including the tubular downcomer, have been neglected since no DP-cells are available. The region modeled includes the following volumes:

Riser Volume: [ ]^{a,b,c}
Lower Separator Volume:

The mass of water in the secondary side has been determined from the differential pressure, temperature, and pressure instruments listed in Table 2.4.1-2.

Two values for the level of water in each of the steam generator secondary sides have been determined by using both the single level measurement and the summed individual differential pressure measurements in the following:

$$L_{SGS} = C_2 \, \Delta P_{SGS} \, \frac{g_c}{g} \qquad (2.4\text{-}4)$$

where:

L_{SGS} = calculated water level (ft.); the maximum allowed level is the span of the differential pressure measurements, which is [ ]^{a,b,c}
ΔP_{SGS} = differential pressure across the steam generator secondary side (psi)
C_2 = 144 ρ_{SGS}^{-1} (ft./psi); conversion from differential pressure to level allowing for the current density

The calculated water level is used to determine the volume of the steam generator secondary side filled by the collapsed liquid using linear interpolation in a tabulation of volume versus level defined by the dimensions listed above. The mass inventory is then calculated using:

$$M_{SGS} = V_{SGS} \, \rho_{SGS} \qquad (2.4\text{-}5)$$

where:

M_{SGS} = mass of water in the secondary side (lbm)
ρ_{SGS} = density of water in the secondary side (lbm/ft.^{3})
V_{SGS} = volume of the secondary side filled with water (ft.^{3}) as determined from the collapsed liquid level

The density of water has been calculated, at each time point, from water table properties as follows:

- Given the current measured pressure, the saturation temperature is calculated.
- If the current water temperature is at or exceeds the saturation temperature, the density is determined from tables for saturated liquid using the current water temperature.
- If the current water temperature is below the saturation temperature, the density is calculated from tables for subcooled liquid using the current temperature and pressure.

The current temperature for the steam generator secondary side is calculated as the arithmetic mean of the temperature measurements listed in Table 2.4.1-2, for the relevant steam generator.

Steam Generator Secondary-Side Mass Balance

The calculated mass inventory, for each steam generator secondary side, for two successive time points, has been used to determine a rate of change of mass using the following equation:

$$\frac{dM_{SGS}}{dt} = \left(\frac{M_{SGS}(t_j) - M_{SGS}(t_{j-1})}{t_j - t_{j-1}} \right) \qquad (2.4\text{-}6)$$

where:

M_{SGS} = mass of fluid in the lower plenum (lbm)
t_j = current time (sec.)
t_{j-1} = previous time (sec.)

The mass of fluid has previously been calculated as described above. For the first time point processed, a zero rate of mass change is assigned.

TABLE 2.4.1-1
INSTRUMENTATION FOR CALCULATING
STEAM GENERATOR PRIMARY-SIDE MASS INVENTORIES

Description	Instrument	Variable
Differential pressure lower hot side - steam generator-A	DP-A05P	$\Delta P_{SGPA,1}$
Differential pressure upper hot side - steam generator-A	DP-A06P	$\Delta P_{SGPA,2}$
Differential pressure upper cold side - steam generator-A	DP-A07P	$\Delta P_{SGPA,3}$
Differential pressure lower cold side - steam generator-A	DP-A08P	$\Delta P_{SGPA,4}$
Pressure at steam generator-A inlet	P-A04P	P_{SGPA}
Temperature at steam generator-A inlet	T-A04P	$T_{SGPA,1}$
Temperature at steam generator-A outlet	T-A10P	$T_{SGPA,2}$
Differential pressure lower hot side - steam generator-B	DP-B05P	$\Delta P_{SGPB,1}$
Differential pressure upper hot side - steam generator-B	DP-B06P	$\Delta P_{SGPB,2}$
Differential pressure upper cold side - steam generator-B	DP-B07P	$\Delta P_{SGPB,3}$
Differential pressure lower cold side - steam generator-B	DP-B08P	$\Delta P_{SGPB,4}$
Pressure at steam generator-B inlet	P-B04P	P_{SGPB}
Temperature at steam generator-A inlet	T-B04P	$T_{SGPB,1}$
Temperature at steam generator-A outlet	T-B10P	$T_{SGPB,2}$

TABLE 2.4.1-2
INSTRUMENTATION FOR CALCULATING
STEAM GENERATOR SECONDARY-SIDE MASS INVENTORIES

Description	Instrument	Variable
Level (differential pressure) measurement - steam generator-A	L-A10S	L_{SGSA}
Differential pressure lower riser region - steam generator-A	DP-A01S	$\Delta P_{SGSA,1}$
Differential pressure upper riser region - steam generator-A	DP-A02S	$\Delta P_{SGSA,2}$
Differential pressure lower separator - steam generator-A	DP-A03S	$\Delta P_{SGSA,3}$
Pressure at steam generator-A outlet (steam dome)	P-A04S	P_{SGSA}
Temperature in riser region - steam generator-A (4.357 m hot)	T-A05S	$T_{SGSA,1}$
Temperature in riser region - steam generator-A (8.357 m hot)	T-A06S	$T_{SGSA,2}$
Temperature in riser region - steam generator-A (12.357 m hot)	T-A07S	$T_{SGSA,3}$
Temperature in riser region - steam generator-A (8.357 m hot)	T-A08S	$T_{SGSA,4}$
Temperature in riser region - steam generator-A (4.357 m hot)	T-A09S	$T_{SGSA,5}$
Level (differential pressure) measurement - steam generator-B	L-B10S	L_{SGSB}
Differential pressure lower riser region - steam generator-B	DP-B01S	$\Delta P_{SGSB,1}$
Differential pressure upper riser region - steam generator-B	DP-B02S	$\Delta P_{SGSB,2}$
Differential pressure lower separator - steam generator-B	DP-B03S	$\Delta P_{SGSB,3}$
Pressure at steam generator-B outlet (steam dome)	P-B04S	P_{SGSB}
Temperature in riser region - steam generator-B (4.357 m hot)	T-B05S	$T_{SGSB,1}$
Temperature in riser region - steam generator-B (8.357 m hot)	T-B06S	$T_{SGSB,2}$
Temperature in riser region - steam generator-B (12.357 m hot)	T-B07S	$T_{SGSB,3}$
Temperature in riser region - steam generator-B (8.357 m hot)	T-B08S	$T_{SGSB,4}$
Temperature in riser region - steam generator-B (4.357 m hot)	T-B09S	$T_{SGSB,5}$

2.4.2 Energy Balance on the Steam Generators

At the initiation of an accident, the steam generators are isolated from the secondary side by actuating the main steam isolation valves (MSIVs). The exception to this is the affected steam generator during a steam line break event. Thus, for nearly all the events, heat transfer between the primary and secondary sides quickly drops as the flow through the tubes stops. This causes the entire steam generator to reach equilibrium temperature, which slowly decays as heat is lost to the environment.

For LOCA events, the primary pressure decreases rapidly, while the secondary pressure drops very slowly. The temperature on the primary side drops until the primary side pressure reaches a value slightly larger than the secondary-side pressure. At this time, both sides are at saturated conditions at their representative pressures, and the generators are heat sinks. As the primary pressure continues to fall, the vapor in the tubes superheats due to reverse heat transfer from the secondary side, which vapor-locks the steam generator, effectively preventing flow of colder fluid into the primary side from the hot leg.

The energy balance on the steam generators consists of determining the heat transfer rate between the primary and secondary sides. For most accident scenarios, thermal equilibrium occurs at the point where the primary and secondary pressures are nearly equal and the energy transfer from the primary to secondary is small after this time. For LOCA events, thermal equilibrium occurs relatively quickly; whereas for the steam line break, heat transfer in the affected steam generator continues until later in the event.

In the region of the tubes, three temperature measurements are available; the primary fluid temperature inside the tubes, the external tube wall temperature, and the fluid temperature on the secondary side. For the LOCA events, the fluid conditions on the primary side are expected to vary from single-phase liquid at the start of the event, to two-phase liquid as the primary pressure falls and the flow stops, to superheated steam when the primary pressure falls to below the secondary pressure. By contrast, single-phase liquid at or near the saturation temperature is expected on the secondary side for the duration of the transient. Thus, it is easier to determine the heat transfer from the external tube walls to the secondary fluid.

A second measure of the heat transfer can be determined by calculating the change in the internal energy for the secondary side.

The instruments used to determine these quantities are summarized in Table 2.4.2-1.

Heat Transfer Between the Tube Walls and the Secondary Fluid

The primary-to-secondary energy transfer rate at operating conditions is determined from the steady-state hot-preoperational tests[8] and the difference between the measured input power and the heat loss to the surroundings.

$$Q_{SG} = Q_{rods} - Q_{surr} \tag{2.4-7}$$

where:

Q_{SG} = heat transfer from the primary system to the secondary system in the steam generators (Btu/sec.)

Q_{rods} = power output from the core (Btu/sec.)

Q_{surr} = heat loss to the surroundings (Btu/sec.)

For full-power operation, the total energy transfer for both steam generators is approximately

$$Q_{SG} = 5000 \text{ kW} \tag{2.4-8}$$

The overall heat transfer coefficient, $\lambda_{overall}$, between the primary and secondary sides is defined as

$$\lambda_{overall} = \frac{Q_{SG}}{2\ A_{tot}\ (\overline{T}_p - \overline{T}_s)} \tag{2.4-9}$$

where:

A_{tot} = total heat transfer area of the U tube ($ft.^2$)

$\overline{T}_p$ = average tube-side-temperature during normal operation (°F)

$\overline{T}_s$ = average shell-side-temperature during normal operation (°F)

For normal operating conditions,

$$\lambda_{overall} = 1324 \text{ Btu/sec.-ft.}^2\text{-°F} \tag{2.4-10}$$

This value is used to evaluate the primary-to-secondary heat transfer until the primary pressure falls below the secondary pressure. At this point, the small amount of reverse heat transfer is governed by free convection on the secondary side to the primary side.

The heat transfer between the tube walls and the secondary fluid is determined by calculating the free convection heat transfer coefficient:

$$\lambda_{free} = 0.13\ k\ [g\ \beta\ abs\ (T_w - T_s)\ Pr/v^2] \tag{2.4-11}$$

where:

k = fluid thermal conductivity (Btu/sec.-ft.-°F)
T_w = wall temperature, defined as the average between the primary and secondary temperatures (°F)
T_s = secondary fluid temperature near the wall (°F)
Pr = fluid Prandtl number
β = volumetric expansion coefficient (1/°R)

The volumetric expansion coefficient is given by the following equation:

$$\beta = (\rho_s - \rho_w) / [\rho_w (T_w - T_s)] \quad (2.4\text{-}12)$$

where:

ρ_s = liquid density evaluated at the bulk tank temperature (lbm/ft.^{3})
ρ_w = liquid density evaluated at the wall temperature (lbm/ft.^{3})

Internal Energy of the Primary Side

The internal energy of the water in the primary side is given by the following equation:

$$U = (h - P/\rho J) M \quad (2.4\text{-}13)$$

where:

h = liquid enthalpy (Btu/lbm)
P = pressure (lb$_f$/ft.^{2})
ρ = density (lbm/ft.^{3})
M = primary fluid mass (lbm)
J = Joule's constant

The liquid enthalpy and density are evaluated at the liquid temperature.

Change in the Energy of the Steam Generator Tube Metal

Since the overall heat balance is to be performed over the primary system, only the metal mass of the steam generator tubes is considered. The change of metal temperature over the course of the test must be accounted to provide an accurate estimate of the overall energy balance. The energy in the metal as a function of time is given by the following equation:

$$U_{metal} (t) = M c_p T (t) \quad (2.4\text{-}14)$$

where:

U_{metal} (t) = quantity of heat contained in the metal (Btu)
M = mass of metal in the steam generator tubes (lbm)
c_p = specific heat of the metal (Btu/lbm-°F)
T(t) = absolute temperature of the metal as a function of time (°F)

The change in the energy contained in the metal is given by the following:

$$\Delta U_{metal} = [U_{metal}(t) - U_{metal}(t_o)] \quad (2.4\text{-}15)$$

where:

ΔU_{metal} = change in the metal energy relative to time zero
$U_{metal}(t)$ = energy content of the metal at time t
$U_{metal}(t_o)$ = energy content of the metal at time t_o

The metal mass of the steam generator tubes is [ ]^{a,b,c} per loop, and the specific heat is 0.123 Btu/lbm-°F.

TABLE 2.4.2-1 INSTRUMENTATION FOR CALCULATING STEAM GENERATOR ENERGY BALANCE	
Description	**Instrumentation Tag**
Pressure - primary - A	P-A04P
Pressure - primary - B	P-B04P
Pressure - secondary - A	P-A04S
Pressure - secondary - B	P-B04S
Differential pressure cells - secondary -A	DP-A01S, DP-A02S, DP-A03S, DP-A04S, DP-A05S, DP-A06S
Differential pressure cells - secondary - B	DP-B01S, DP-B02S, DP-B03S, DP-B04S, DP-B05S, DP-B06S
Primary fluid temperatures - A	T-A05P, TA06P, T-A07P, T-A08P, TA09P
Primary fluid temperatures - B	T-B05P, T-B06P, T-B07P, T-B08P, T-B09P
Secondary fluid temperatures - A	T-A05S, T-A06S, T-A07S, T-A08S, T-A09S
Secondary fluid temperatures - B	T-B05S, T-B06S, T-B07S, T-B08S, T-B09S
Secondary level	As calculated for mass balance

2.5 Pressurizer

The pressurizer provides control over the primary system pressure and temperature. During normal operation, the pressurizer is partly full of water and partly full of steam. During an accident sequence, the pressurizer is part of the depressurization system as the first-, second-, and third-stage automatic depressurization system (ADS) lines are located at the top of the pressurizer.

2.5.1 Pressurizer and Surge Line Mass Inventory

Pressurizer Mass Inventory

The mass of water in the pressurizer has been determined from the individual differential pressure measurements. The level of water in the pressurizer is also determined from the single differential pressure reading included for this purpose. During some transients the water level may exceed the upper tap of this measurement. The level, differential pressure, pressure, and temperature instruments used are listed in Table 2.5.1-1.

Using the measured differential pressures, the water level is determined in two ways. First, it is calculated using the following equation:

$$L_{PZR} = C_2 \, \Delta P_{PZR} \frac{g_c}{g} \qquad (2.5\text{-}1)$$

where:

L_{PZR} = calculate pressurizer water level (ft.)

ΔP_{PZR} = total pressure change across the pressurizer (psi), as determined from the sum of the individual pressure drop readings listed in Table 2.5.1-1

That is, the sum of the individual pressure drop readings is

$$\Delta P_{PZR} = \sum_{i=1}^{7} \Delta P_{PZR,i} \qquad (2.5\text{-}2)$$

C_2 = $144 \, \rho_{PZR}^{-1}$ (ft./psi); conversion from differential pressure to level allowing for the current density

The mass of water in the pressurizer is then calculated using the following equation:

$$M_{PZR} = L_{PZR}\ A_{PZR}\ \rho_{PZR} \qquad (2.5\text{-}3)$$

where:

M_{PZR} = mass of water in the pressurizer (lbm)
ρ_{PZR} = density of water in the pressurizer (lbm/ft.^{3})
A_{PZR} = cross-sectional area of the pressurizer; [ ]^{a,b,c}
L_{PZR} = calculated collapsed water level (ft.)

The density of water has been calculated, at each time point, from water table properties as follows:

- The saturation temperature is calculated from the pressure at the bottom of the pressurizer. The pressure at the bottom of the pressurizer is determined using the following equation:

$$P_{PZR-BOT} = P_{PZR} + \sum_{i=1}^{7} \Delta P_{PZR,i} \qquad (2.5\text{-}4)$$

- If the current average water temperature in the pressurizer is at or exceeds the saturation temperature, the density is determined from tables for saturated liquid using the current average water temperature.

- If the current average water temperature in the pressurizer is below the saturation temperature, the density is calculated from tables for subcooled liquid using the current average temperature and the pressure at the bottom of the pressurizer.

The second method of calculating the collapsed water level from the individual differential pressure readings determines the level of water indicated for each individual differential pressure measurement cell. The total water level is calculated using the following equation:

$$L_{PZR} = \sum_{i=1}^{7} C_{2,i}\ \Delta P_{PZR,i}\ \frac{g_c}{g} \qquad (2.5\text{-}5)$$

where:

$\Delta P_{PZR,i}$ = differential pressure across the cell (psi)
$C_{2,i}$ = local conversion factor allowing for the density in the cell (ft./psi)

In this case, the total mass of water in the pressurizer is calculated from the following equation:

$$M_{PZR} = 144\ A_{PZR} \sum_{i=1}^{7} \Delta P_{PZR,i} \frac{g_c}{g} \qquad (2.5\text{-}6)$$

The density in the cell is calculated using the pressure at the bottom of the cell and the temperature at the cell midpoint. The temperature at the cell midpoint is calculated by linear interpolation in the measured temperature data.

An alternative collapsed water level can be calculated from the level measuring differential pressure reading using the following equation:

$$L_{PZR} = C_2\ \Delta P_{L\text{-}PZR} \frac{g_c}{g} \qquad (2.5\text{-}7)$$

where C_2 is the same conversion factor used for calculating the water level from the summed individual differential pressure measurements. While the level remains below the upper tap of the single differential pressure cell, this level should be very similar to that determined from the summed readings.

Pressurizer Mass Balance

The pressurizer is connected to hot leg-A via the surge line. The pressurizer can also discharge via the first three stages of the ADS. Flow through the surge line and the ADS trains should have been monitored by turbine flow meters (F-015P and F-030P, respectively). Unfortunately, these meters did not operate properly throughout the experiments. The calculated mass inventory in the pressurizer for two successive time points have been used to determine a rate of change of mass using:

$$\frac{dM_{PZR}}{dt} = \left(\frac{M_{PZR}(t_j) - M_{PZR}(t_{j-1})}{t_j - t_{j-1}} \right) \qquad (2.5\text{-}8)$$

where:

M_{PZR} = mass of water in the pressurizer (lbm)
t_j = current time (sec.)
t_{j-1} = previous time (sec.)

The mass of water in the pressurizer has previously been calculated as described above. The rate of change of mass has been calculated for both methods of determining the mass. The automatic depressurization system (ADS) flow is estimated by differentiating the mass of water in the ADS catch tanks over successive time steps. In all cases, for the first time point processed, a zero rate of change of mass is assigned.

Surge Line Mass Inventory

The mass of water in the pressurizer surge line has been determined from the differential pressure, temperature, and pressure instruments listed in Table 2.5.1-2.

The fraction of the surge line that is filled with water is calculated for each differential pressure cell using the following equation:

$$F_{SL,i} = \frac{C_{2,i}\ \Delta P_{SL,i}}{L_{SL,i}}\ \frac{g_c}{g} \qquad (2.5\text{-}9)$$

where:

$F_{SL,i}$ = fractional length of water in the portion of the surge line covered by the differential pressure cell

$\Delta P_{SL,i}$ = differential pressure across the portion of the surge line (psi)

$C_{2,i}$ = $144\ \rho_{SL,i}^{-1}$ (ft./psi) is a conversion factor from differential pressure to collapsed liquid level allowing for the current local water density

$L_{SL,i}$ = span of surge line differential pressure measurements (which are [ ]^{a,b,c} for DP-020P, [.]^{a,b,c} for DP-019P, and [ ]^{a,b,c} for DP-018P)

The total surge line mass inventory is calculated using the following equation:

$$M_{SL} = \sum_{i=1}^{3} F_{SL,i}\ \rho_{SL,i}\ V_{SL,i} \qquad (2.5\text{-}10)$$

where:

M_{SL} = mass in the surge line (lbm)

$\rho_{SL,i}$ = local density in the surge line (lbm/ft.^{3})

$V_{SL,i}$ = volume of the portion of the surge line covered by the differential pressure measurement (which are [ ]^{a,b,c} for DP-020P, [ ]^{a,b,c} for DP-019P, and [ ]^{a,b,c} for DP-018P)

The density of water has been calculated, at each time point, from water table properties as follows:

- Given the current measured pressure, the saturation temperature is calculated. The measured pressure is calculated at the bottom of each differential pressure measurement cell using the pressure at the bottom of the pressurizer and the pressure change down the surge line to that point.

- If the current water temperature is at, or exceeds the saturation temperature, the density is determined from tables for saturated liquid using the current water temperature.

- If the current water temperature is below the saturation temperature, the density is calculated from tables for subcooled liquid using the current temperature and pressure.

The current water temperature in each of the surge line differential pressure cells is that given by the appropriate local thermocouple listed in Table 2.5.1-2.

Surge Line Mass Balance

The SPES-2 facility included a turbine flow measuring device in the pressurizer surge line (F-015P). This meter did not operate properly in any of the tests. The calculated mass inventories in the surge line, for two successive time points, have been used to determine a rate of change of mass using:

$$\frac{dM_{SL}}{dt} = \left(\frac{M_{SL}(t_j) - M_{SL}(t_{j-1})}{t_j - t_{j-1}} \right) \qquad (2.5\text{-}11)$$

where:

M_{SL} = mass of fluid in the surge line (lbm)
t_j = current time (sec.)
t_{j-1} = previous time (sec.)

The mass of fluid in the surge line has previously been calculated as described above. For the first time point processed, a zero rate of change of mass is assigned.

TABLE 2.5.1-1 INSTRUMENTATION FOR CALCULATING PRESSURIZER MASS INVENTORY		
Description	**Instrument**	**Variable**
Level of water in pressurizer (differential pressure)	L-010P	$\Delta P_{L\text{-}PZR}$
Pressure at top of pressurizer	P-027P	P_{PZR}
Differential pressure (5.871 m to 7.314 m)	DP-021P	$\Delta P_{PZR,1}$
Differential pressure (7.314 m to 8.758 m)	DP-022P	$\Delta P_{PZR,2}$
Differential pressure (8.758 m to 10.202 m)	DP-023P	$\Delta P_{PZR,3}$
Differential pressure (10.202 m to 11.164 m)	DP-024P	$\Delta P_{PZR,4}$
Differential pressure (11.164 m to 12.076 m)	DP-025P	$\Delta P_{PZR,5}$
Differential pressure (12.076 m to 12.396 m)	DP-026P	$\Delta P_{PZR,6}$
Differential pressure (12.396 m to 12.631 m)	DP-027P	$\Delta P_{PZR,7}$
Temperature of water in pressurizer (6.106 m)	T-021P	$T_{PZR,1}$
Temperature of water in pressurizer (7.364 m)	T-022P	$T_{PZR,2}$
Temperature of water in pressurizer (8.622 m)	T-023P	$T_{PZR,3}$
Temperature of water in pressurizer (9.880 m)	T-024P	$T_{PZR,4}$
Temperature of water in pressurizer (11.138 m)	T-025P	$T_{PZR,5}$
Temperature of water in pressurizer (12.369 m)	T-026P	$T_{PZR,6}$

TABLE 2.5.1-2 INSTRUMENTATION FOR CALCULATING SURGE LINE MASS INVENTORY		
Description	**Instrument**	**Variable**
Differential pressure upper length of surge line	DP-020P	$\Delta P_{SL,1}$
Differential pressure middle length of surge line	DP-019P	$\Delta P_{SL,2}$
Differential pressure lower length of surge line	DP-018P	$\Delta P_{SL,3}$
Temperature of surge line upper thermocouple (5.371 m)	T-020P	$T_{SL,1}$
Temperature of surge line middle thermocouple (2.255 m)	T-019PL	$T_{SL,2}$
Temperature of surge line lower thermocouple (1.002 m)	T-018P	$T_{SL,3}$

2.5.2 Energy Balance on the Pressurizer

To determine the performance of the pressurizer during accident sequences, an energy balance is performed which consists of determining the internal energy in the accumulator water as a function of time. The energy leaving the pressurizer via ADS-1, ADS-2, ADS-3 is discussed in Section 2.7.4.

Internal Energy of the Pressurizer Fluid

The internal energy of the water in the tank is calculated for six volumes where temperature measurements are available. The total internal energy is given by the following equation:

$$U = \sum_{i=1}^{6} (h_{f-i} - P_i / \rho_{f-i} J)\ V_{f-i}\ \rho_{f-i} + (h_{g-i} - \rho_i / \rho_{g-i} J) V_{g-i}\ \rho_{g-i} \qquad (2.5\text{-}12)$$

where:

U = total pressurizer fluid energy (Btu)
h_{f-i} = liquid enthalpy in volume i (Btu/lbm)
P_i = pressure in volume i ($lb_f/ft.^2$)
ρ_{f-i} = liquid density in volume i ($lbm/ft.^3$)
V_{f-i} = liquid volume in volume i ($ft.^3$)
h_{g-i} = vapor enthalpy in volume i (Btu/lbm)
ρ_{g-i} = vapor density in volume i ($lbm/ft.^3$)
V_{g-i} = vapor volume in volume i ($ft.^3$)
J = Joule's constant

The fluid internal energy relative to the start of the test is used to determine an overall energy balance.

Change in the Energy of the Pressurizer Metal

The change of metal temperature over the course of the test must be accounted to provide an accurate estimate of the overall energy balance. The energy in the metal as a function of time is given by the following equation:

$$U_{metal}(t) = M\ c_p\ T(t) \qquad (2.5\text{-}13)$$

where:

U_{metal} (t) = quantity of heat contained in the metal as a function of time (Btu)
M = mass of metal in the pressurizer (lbm)
c_p = specific heat of the metal (Btu/lbm-°F)
T(t) = absolute temperature of the metal as a function of time (°R)

The change in the energy contained in the metal is given by the following equation:

$$\Delta U_{metal} = [U_{metal}(t) - U_{metal}(t_o)] \quad (2.5\text{-}14)$$

where:

ΔU_{metal} = change in the metal energy relative to time t_o
$U_{metal}(t_o)$ = energy content of the metal at time t_o

The metal mass of the pressurizer is [ ]^{a,b,c}, and the specific heat is 0.123 Btu/lbm-°F.

2.6 Power Channel and Downcomer

For the SPES-2 tests, the AP600 core is represented by the power channel. The power channel consists of a core region; a downcomer, which collects flow from the cold legs and delivers it to the lower plenum; and an upper plenum-head assembly, which distributes flow to the hot legs. The active fuel region of the core contains [ ]^{a,b,c} full length, electrically heated, simulated fuel rods.

2.6.1 Power Channel Mass Inventory

The SPES-2 power channel is divided into the following regions in order to determine the total mass inventory:

- The annular downcomer
- The tubular downcomer
- The lower plenum - the region below the tubular downcomer outlet
- The core (the heated rod bundle)
- The upper plenum consisting of three parts: the fuel exit cell, a region below the hot-leg elevation, and one above the hot-leg elevation
- The upper head

The total mass inventory (M_{PCHAN}) at any time is given by the some of the inventories for the aforementioned regions. The calculated mass inventory for two successive time points has been used to determine a rate of change of mass using the following equation:

$$\frac{dM_{PCHAN}}{dt} = \left(\frac{M_{PCHAN}(t_j) - M_{PCHAN}(t_{j-1})}{t_j - t_{j-1}} \right) \qquad (2.6\text{-}1)$$

where:

M_{PCHAN} = total mass of fluid in the power channel (lbm)
t_j = current time (sec.)
t_{j-1} = previous time (sec.)

Except for the annular and tubular downcomers, the power channel divisions given above do not entirely correspond to those given in the *SPES-2 Facility Description*[2] (Table 5 and Figure B1). They have instead been defined relative to the spans of the differential pressure cells (see Figure 3 of the *SPES-2 Facility Description*[2]) that have been used to determine the collapsed liquid levels and, hence, the mass inventories as follows:

Lower Plenum	DP-004P
Core	DP-000P (DP-005P, DP-011P, DP012P and DP-013P)
Upper Plenum	DP-014P (the fuel exit cell) DP-015 and DP-016
Upper Head	DP-017P

Further details on the assumptions regarding the extent of each region are given below. The upper head bypass and the core bypass have been neglected in calculating the total power channel mass inventory.

Annular Downcomer Mass Inventory

The annular downcomer is considered as extending from the outlet of the upper-head bypass to the top of the tubular downcomer. The total volume of this region is [ ]^{a,b,c} ([ ]^{a,b,c}; Table 5 of the *SPES-2 Facility Description*[2]). The four cold legs and the two DVI lines deliver their mass inventory to the core via this annular downcomer.

The mass of water in the annular downcomer has been determined from the differential pressure, temperature, and pressure instruments listed in Table 2.6.1-1.

The fraction of the annular downcomer filled with water is calculated using the following equation:

$$F_{ADC} = \frac{C_2 \, \Delta P_{ADC}}{L_{\Delta P}} \frac{g_c}{g} \qquad (2.6\text{-}2)$$

where:

F_{ADC} = fractional water level in the annular downcomer. If this is greater than unity, then unity is assumed. Such a situation may arise during forced flow when there is a dynamic contribution to the measured differential pressure. However, during such periods the annular downcomer will be water solid.

ΔP_{ADC} = arithmetic mean differential pressure from the cold legs to the tubular downcomer ($lbf/ft.^3$)

C_2 = $144 \, \rho_{ADC}^{-1}$ (ft./psi); conversion factor from differential pressure to collapsed liquid level allowing for the current water density in the hot leg

L_{ADC} = span of annular downcomer differential pressure measurements (which is [ ]^{a,b,c})

The mass inventory is calculated using the following equation:

$$M_{ADC} = F_{ADC} \, \rho_{ADC} \, V_{ADC} \qquad (2.6\text{-}3)$$

where:

M_{ADC} = mass in the annular downcomer (lbm)

ρ_{ADC} = density in the annular downcomer ($lbm/ft.^3$)

V_{ADC} = total volume of the annular downcomer ([ ]^{a,b,c}). That is, the fractional level is taken to include the volume above the top of the differential pressure cells.

The density of water has been calculated, at each time point, from water table properties as follows:

- Given the current measured pressure, the saturation temperature is calculated.
- If the current water temperature is at or exceeds the saturation temperature, the density is determined from tables for saturated liquid using the current water temperature.
- If the current water temperature is below the saturation temperature the density is calculated from tables for subcooled liquid using the current temperature and pressure.

The current temperature for the annular downcomer is taken as the average temperature between the cold legs and the tubular downcomer as calculated from the arithmetic mean of the instruments listed in Table 2.6.1-1.

Annular Downcomer Mass Balance

The calculated mass inventory for the annular downcomer for two successive time points has been used to determine a rate of change of mass using the following equation:

$$\frac{dM_{ADC}}{dt} = \left(\frac{M_{ADC}(t_j) - M_{ADC}(t_{j-1})}{t_j - t_{j-1}} \right) \qquad (2.6\text{-}4)$$

where:

M_{ADC} = mass of fluid in the annular downcomer (lbm)
t_j = current time (sec.)
t_{j-1} = previous time (sec.)

The mass of fluid has been calculated previously as described above. For the first time point processed, a zero rate of mass change is assigned.

Tubular Downcomer Mass Inventory

The tubular downcomer extends from the annular downcomer to the bottom of the core region. The total volume of the tubular downcomer is [ ]^{a,b,c} ([ ]^{a,b,c}; see Table 5 of the *SPES-2 Facility Description*[2]).

The mass of water in the tubular downcomer has been determined from the differential pressure, temperature, and pressure instruments listed in Table 2.6.1-2.

The fraction of the tubular downcomer filled with water is calculated using the following equation:

$$F_{TDC} = \frac{C_2 \, \Delta P_{TDC}}{L_{\Delta P}} \frac{g_c}{g} \qquad (2.6\text{-}5)$$

where:

F_{TDC} = fractional water level in the tubular downcomer. If this is greater than unity, then unity is assumed. Such a situation may arise during forced flow when there is a

dynamic contribution to the measured differential pressure. However, during such periods the tubular downcomer will be water solid. To ensure this, a value of unity is assumed when the measured flow in the tubular downcomer ($\dot{m}_{TDC}$) is greater than [ ]^{a,b,c} The initial flow is of order [ ]^{a,b,c}

ΔP_{TDC} = total differential pressure from the annular downcomer to the bottom of the tubular downcomer (lbf/ft.^{3})

C_2 = 144 ρ_{ADC}^{-1} (ft./psi); conversion factor from differential pressure to collapsed liquid level allowing for the current water density in the hot leg

$L_{\Delta P}$ = span of tubular downcomer differential pressure measurements; [ ]^{a,b,c}

The mass inventory is calculated using the following equation:

$$M_{TDC} = F_{TDC}\, \rho_{TDC}\, V_{TDC} \qquad (2.6\text{-}6)$$

where:

M_{TDC} = mass in the tubular downcomer (lbm)

ρ_{TDC} = density in the tubular downcomer (lbm/ft.^{3})

V_{TDC} = total volume of the tubular downcomer ([ ]^{a,b,c})

The density of water has been calculated, at each time point, from water table properties as follows:

- Given the current measured pressure, the saturation temperature is calculated.
- If the current water temperature is at or exceeds the saturation temperature, the density is determined from tables for saturated liquid using the current water temperature.
- If the current water temperature is below the saturation temperature the density is calculated from tables for subcooled liquid using the current temperature and pressure.

The current temperature for the tubular downcomer is taken as the average temperature between the inlet and outlet as calculated from the arithmetic mean of the instruments listed in Table 2.6.1-2.

Tubular Downcomer Mass Balance

The calculated mass inventory for the tubular downcomer for two successive time points, has been used to determine a rate of change of mass using the following equation:

$$\frac{dM_{TDC}}{dt} = \left(\frac{M_{TDC}(t_j) - M_{TDC}(t_{j-1})}{t_j - t_{j-1}} \right) \qquad (2.6\text{-}7)$$

where:

M_{TDC} = mass of fluid in the tubular downcomer (lbm)
t_j = current time (sec.)
t_{j-1} = previous time (sec.)

The mass of fluid has previously been calculated as described above. For the first time point processed, a zero rate of mass change is assigned.

Lower-Plenum Mass Inventory

The lower plenum is below the outlet of the tubular downcomer. For the purpose of mass inventory calculations, the lower plenum has been defined as the region encompassed by the differential pressure cell DP-004 plus the volume below the bottom tap of this cell. This covers three separate volumes as listed below (with respect to a zero elevation at the lower differential pressure tap):

a,b,c

[ ]

The mass of water in the lower plenum has been determined from the differential pressure, temperature, and pressure instruments listed in Table 2.6.1-3.

The level of water in the lower plenum is calculated using the following equation:

$$L_{LOWP} = C_2 \, \Delta P_{LOWP} \, \frac{g_c}{g} \qquad (2.6\text{-}8)$$

where:

L_{LOWP} = calculated water level (ft.). The maximum allowed level is [ ]^{a,b,c}
ΔP_{LOWP} = differential pressure across the lower plenum (lbf/ft.^{2})
C_2 = 144 ρ_{LOWP}^{-1} (ft./psi); conversion from differential pressure to level allowing for the current density

The calculated water level is used to determine the volume of the lower plenum filled by the collapsed liquid using linear interpolation in a tabulation of volume versus level defined by the dimensions listed above. The zero level volume is set to allow for the region of the lower plenum below the differential pressure lower tap. The mass inventory is then calculated using the following equation:

$$M_{LOWP} = V_{LOWP}\,\rho_{LOWP} \tag{2.6-9}$$

where:

M_{LOWP} = mass of water in the lower plenum (lbm)
ρ_{LOWP} = density of water in the lower plenum (lbm/ft.^{3})
V_{LOWP} = volume of the lower plenum filled with water (ft.^{3}), as determined from the collapsed liquid level

The density of water has been calculated, at each time point, from water table properties as follows:

- Given the current measured pressure, the saturation temperature is calculated.
- If the current water temperature is at or exceeds the saturation temperature, the density is determined from tables for saturated liquid using the current water temperature.
- If the current water temperature is below the saturation temperature the density is calculated from tables for subcooled liquid using the current temperature and pressure.

The current temperature for the lower plenum is calculated as the arithmetic mean of the measurements listed in Table 2.6.1-3.

Lower-Plenum Mass Balance

The calculated mass inventory for the lower plenum for two successive time points has been used to determine a rate of change of mass using the following equation:

$$\frac{dM_{LOWP}}{dt} = \left(\frac{M_{LOWP}(t_j) - M_{LOWP}(t_{j-1})}{t_j - t_{j-1}} \right) \tag{2.6-10}$$

where:

M_{LOWP} = mass of fluid in the lower plenum (lbm)
t_j = current time (sec.)
t_{j-1} = previous time (sec.)

The mass of fluid has previously been calculated as described above. For the first time point processed, a zero rate of mass change is assigned.

Core Mass Inventory

The core region encompasses the volume at the level of the tubular downcomer outlet and the fuel to near the top of the heated lengths, as defined by the differential pressure cell DP-000P. This includes five separate volumes as listed below (with zero elevation at the lower tap of DP-000P):

a,b,c

[

]

The mass of water in the core has been determined from the differential pressure, temperature, and pressure instruments listed in Table 2.6.1-4.

The collapsed level of water in the core is calculated in two ways: using either the measured total differential pressure or the sum of the individual differential pressure measurements.

$$L_{CORE} = C_2 \, \Delta P_{CORE} \, \frac{g_c}{g} \qquad (2.6\text{-}11)$$

where:

L_{CORE} = calculated water level (ft.). The maximum allowed level is [ ]^{a,b,c}
ΔP_{CORE} = differential pressure across the core (lbf/ft.^{2})
C_2 = 144 ρ_{CORE}^{-1} (ft./psi); conversion from differential pressure to level allowing for the current water density

The calculated water level is used to determine the volume of the core filled by the collapsed liquid using linear interpolation in a tabulation of volume versus level defined by the dimensions listed above. The mass inventory is then calculated (for both liquid levels calculated from the single measured and summed core differential pressures) using the following equation:

$$M_{CORE} = V_{CORE}\,\rho_{CORE} \qquad (2.6\text{-}12)$$

where:

M_{CORE} = mass of water in the core (lbm)
ρ_{CORE} = density of water in the core (lbm/ft.^{3})
V_{CORE} = volume of the core filled with water (ft.^{3}) as determined from the collapsed liquid level

The density of water has been calculated, at each time point, from water table properties as follows:

- Given the current measured pressure, the saturation temperature is calculated.
- If the current water temperature is at or exceeds the saturation temperature, the density is determined from tables for saturated liquid using the current water temperature.
- If the current water temperature is below the saturation temperature the density is calculated from tables for subcooled liquid using the current temperature and pressure.

The current temperature for the core has been calculated as the arithmetic mean of the core inlet and outlet temperatures as listed in Table 2.6.1-4.

Core Mass Balance

The calculated mass inventory for the core region, for two successive time points, has been used to determine a rate of change of mass using the following equation:

$$\frac{dM_{CORE}}{dt} = \left(\frac{M_{CORE}(t_j) - M_{CORE}(t_{j-1})}{t_j - t_{j-1}} \right) \qquad (2.6\text{-}13)$$

where:

M_{CORE} = mass of fluid in the core region (lbm)
t_j = current time (sec.)
t_{j-1} = previous time (sec.)

The mass of fluid has previously been calculated as described above. For the first time point processed, a zero rate of mass change is assigned. This calculation has been undertaken for the mass inventories calculated both from the single differential pressure cell and the four individual cells.

Upper-Plenum Mass Inventory

The upper plenum has been considered to extend from the top of the core (as defined above) to the bottom of the upper head (see below). As such it consists of three regions: a fuel exit cell (the span of DP-014P), a region from the fuel exit cell to the hot-leg elevation, and a region from the hot-leg elevation to the upper head. The dimensions of these regions are listed below:

Fuel exit cell: This contains the top of the fuel rods and therefore includes an area change. There are two volume regions as follows:

a,b,c

[ ]

Region below hot legs:

a,b,c

[ ]

Region above hot legs:

a,b,c

[ ]

The mass of water in each of the three upper plenum regions has been determined from the differential pressure, temperature, and pressure instruments listed in Table 2.6.1-5.

The level of water in each of the three upper plenum regions is calculated using the following equation:

$$L_{UPP} = C_2 \, \Delta P_{UPP} \, \frac{g_c}{g} \qquad (2.6\text{-}14)$$

where:

L_{UPP} = calculated water level (ft.). The maximum allowed level within each region of the upper plenum corresponds to the total length listed above.

ΔP_{UPP} = differential pressure across the upper plenum region being considered ($lbf/ft.^2$)

C_2 = $144 \, \rho_{UPP}^{-1}$ (ft./psi); conversion from differential pressure to level allowing for the current density

For the heated rod bundle exit cell the calculated water level is used to determine the collapsed liquid level. The fluid volume is determined by linear interpolation in a tabulation of water volume versus

level as defined by the dimensions listed above. The mass inventory is then calculated using the following equation:

$$M_{FOUT} = V_{FOUT}\ \rho_{FOUT} \qquad (2.6\text{-}15)$$

where:

M_{FOUT} = mass of water in the heated rod bundle exit cell (lbm)
ρ_{FOUT} = density of water in the heated rod bundle exit cell (lbm/ft.^{3})
V_{FOUT} = volume of the heated rod bundle exit cell filled with water (in cubic feet) as determined from the collapsed liquid level

Within the other two regions of the upper plenum, there is no flow area change and the mass within each region is calculated using the following equation:

$$M_{UPP} = L_{UPP}\ A_{UPP}\ \rho_{UPP} \qquad (2.6\text{-}16)$$

where:

M_{UPP} = mass of water in the upper-plenum region (lbm)
ρ_{UPP} = density of water in the upper-plenum region (lbm/ft.^{3})
L_{UPP} = calculated collapsed liquid level within the upper-plenum region being considered (ft.)
A_{UPP} = flow area for the upper-plenum region (ft.^{2})

The density of water has been calculated, at each time point, for each upper-plenum region, from water table properties as follows:

- Given the current measured pressure, the saturation temperature is calculated.
- If the current water temperature is at or exceeds the saturation temperature, the density is determined from tables for saturated liquid using the current water temperature.
- If the current water temperature is below the saturation temperature the density is calculated from tables for subcooled liquid using the current temperature and pressure.

The current temperature for the fuel exit cell is taken as the fuel exit temperature. For the other two upper plenum volumes the arithmetic mean of the measured hot-leg temperatures listed in Table 2.6.1-5 is used.

Upper-Plenum Mass Balance

The calculated mass inventory for each of the upper-plenum volumes, for two successive time points, has been used to determine a rate of change of mass using the following equation:

$$\frac{dM_{UPP}}{dt} = \left(\frac{M_{UPP}(t_j) - M_{UPP}(t_{j-1})}{t_j - t_{j-1}} \right) \qquad (2.6\text{-}17)$$

where:

M_{UPP} = mass of fluid in the upper-plenum volume (lbm)
t_j = current time (sec.)
t_{j-1} = previous time (sec.)

The mass of fluid has previously been calculated as described above. For the first time point processed, a zero rate of mass change is assigned.

Upper-Head Mass Inventory

The upper head lies above the upper plenum. For the purpose of mass inventory calculations the head has been defined as the region encompassed by the differential pressure cell DP-017 plus the volume above the upper tap of this cell. This includes three separate volumes as listed below (with elevations relative to the bottom of the differential pressure cell):

[ ]a,b,c

The mass of water in the lower plenum has been determined from the differential pressure, temperature, and pressure instruments listed in Table 2.6.1-6.

The level of water in the upper head is calculated using:

$$L_{HEAD} = C_2 \, \Delta P_{HEAD} \, \frac{g_c}{g} \qquad (2.6\text{-}18)$$

where:

L_{HEAD} = calculated water level (ft.)

ΔP_{HEAD} = differential pressure across the upper head (lbf/ft.^{2})
C_2 = 144 ρ_{HEAD}^{-1} (ft./psi); conversion from differential pressure to level allowing for the current density

If the indicated level is greater than or equal to the span of the differential pressure cell (that is [ ]^{a,b,c}) then the entire upper head volume is assumed to be filled. Otherwise, the calculated water level is used to determine the volume of the upper head filled by the collapsed liquid using linear interpolation in a tabulation of volume versus level defined by the dimensions listed above. The mass inventory is then calculated using:

$$M_{HEAD} = V_{HEAD}\ \rho_{HEAD} \qquad (2.6\text{-}19)$$

where:

M_{HEAD} = mass of water in the upper head (lbm)
ρ_{HEAD} = density of water in the upper head (lbm/ft.^{3})
V_{HEAD} = volume of the upper head filled with water (ft.^{3}) as determined from the collapsed liquid level

The density of water has been calculated, at each time point, from water table properties as follows:

- Given the current measured pressure, the saturation temperature is calculated.
- If the current water temperature is at or exceeds the saturation temperature, the density is determined from tables for saturated liquid using the current water temperature.
- If the current water temperature is below the saturation temperature, the density is calculated from tables for subcooled liquid using the current temperature and pressure.

Upper-Head Mass Balance

The calculated mass inventory for the upper head for two successive time points has been used to determine a rate of change of mass using the following equation:

$$\frac{dM_{HEAD}}{dt} = \left(\frac{M_{HEAD}(t_j) - M_{HEAD}(t_{j-1})}{t_j - t_{j-1}} \right) \qquad (2.6\text{-}20)$$

where:

M_{HEAD} = mass of fluid in the upper head (lbm)
t_j = current time (sec.)
t_{j-1} = previous time (sec.)

The mass of fluid has previously been calculated as described above. For the first time point processed, a zero rate of mass change is assigned.

Calculation of Power Channel Two-Phase Level

Once forced flow is lost, there will be a variation in water phase throughout the power channel, from liquid, through two phase to steam. At any point in the transient, calculated collapsed liquid levels can be used to calculate the mass distribution in the power channel and to estimate the void fraction. This has been done using the following algorithm:

- Starting from DP-013P in the riser region to the upper head, the first differential pressure cell in which the collapsed liquid level is less than four inches, for two consecutive time steps, is located. The two-phase level and mixture is assumed to exist in the cell below this one. The first empty cell is denoted the ith cell, so the two-phase level exists in the i-1 cell.

- The average static void fraction, for the differential pressure cell below the one in which the two-phase level exists, is calculated assuming the frictional and acceleration pressure drops are negligible as:

$$\alpha_{i-2} = 1.0 - \frac{L_{i-2}}{L_{\Delta P,i-2}} \qquad (2.6\text{-}21)$$

where:

α_{i-2} = void fraction for the cell below that containing the two-phase level (as calculated above)
L_{i-2} = collapsed liquid level in the cell below that in which the two-phase level exists (ft.)
$L_{\Delta P,i-2}$ = span of the differential pressure taps in the cell below that in which the two-phase level exists (ft.)

- The level of the two-phase interface is calculated by assuming that the two-phase fluid within that cell has the same void fraction as the fluid in the cell below, so that:

$$L_{2\phi} = \sum_{j=1}^{i-2} L_{\Delta P,j} + MIN\left[L_{\Delta P,i-1} , \frac{L_{i-1}}{1.0-\alpha_{i-2}} \right] - L_{TOF} \qquad (2.6\text{-}22)$$

where:

$L_{2\phi}$ = calculated level of the two-phase to steam interface relative to the top of the heated rod bundle (ft.)

$L_{\Delta P,j}$ = span of the ith differential pressure cell (ft.). All cells below that containing the two-phase level are included.

$L_{\Delta P,i-1}$ = span of the differential pressure cell containing the two-phase level (ft.). This is used to ensure that the expanded level for this cell does not exceed the span of the differential pressure measurement.

L_{i-1} = collapsed liquid level in the cell containing the two-phase level (ft.)

α_{i-2} = void fraction for the cell below that containing the two-phase level (as calculated above)

L_{TOF} = level of the top of the fuel relative to the lower tap of DP-013P (ft.). This adjusts the two-phase level to be relative to the top of the heated rod bundle.

If all differential pressure cells have a level in excess of four inches, then either a water solid power channel is assumed for cases when the head level exceeds the span of the upper-head differential pressure cell, or the above two phase level is applied to the upper head collapsed liquid level.

If the two-phase level is indicated to be within the DP-013P differential pressure cell, then the two-phase level is set to the collapsed liquid level for that cell less the top of fuel elevation. If the collapsed level for DP-013P cell is less than four inches, then the two phase level is set to minus the elevation of the top of the heated rod bundle. Analysis undertaken for the *SPES-2 Final Data Report*[1] indicate that neither situation will arise. However, noise in the data may lead to spurious indications of levels within the core. Using two consecutive time steps to check for a low level will remove some of this noise, but not necessarily all. Messages are therefore issued by the data analysis code, SPESAN, on the main output along with the setting of a negative level.

TABLE 2.6.1-1 INSTRUMENTATION FOR CALCULATING ANNULAR DOWNCOMER MASS INVENTORY		
Description	**Instrument**	**Variable**
Pressure at bottom of tubular downcomer	P-001P	P_{TDC}
Temperature at nozzle from cold leg-A1	T-A021PL0	T_{CLA1}
Temperature at nozzle from cold leg-B1	T-B021PL0	T_{CLB1}
Temperature at nozzle from cold leg-A2	T-A022PL0	T_{CLA2}
Temperature at nozzle from cold leg-B2	T-B022PL0	T_{CLB2}
Temperature at inlet to tubular downcomer	T-001P	$T_{TDC,1}$
Differential pressure - cold leg-A1 to tubular downcomer	DP-A021P	$\Delta P_{ADC,1}$
Differential pressure - cold leg-B1 to tubular downcomer	DP-B021P	$\Delta P_{ADC,2}$
Differential pressure - cold leg-A2 to tubular downcomer	DP-A022P	$\Delta P_{ADC,3}$
Differential pressure - cold leg-B2 to tubular downcomer	DP-B022P	$\Delta P_{ADC,4}$

TABLE 2.6.1-2 INSTRUMENTATION FOR CALCULATING TUBULAR DOWNCOMER MASS INVENTORY		
Description	**Instrument**	**Variable**
Pressure at bottom of tubular downcomer	P-001P	P_{TDC}
Temperature at inlet to tubular downcomer	T-001P	$T_{TDC,1}$
Temperature at midpoint of tubular downcomer	T-002P	$T_{TDC,2}$
Temperature at outlet of tubular downcomer	T-003P	$T_{TDC,3}$
Differential pressure - upper tubular downcomer	DP-001P	$\Delta P_{TDC,1}$
Differential pressure - lower tubular downcomer	DP-002P	$\Delta P_{TDC,2}$
Flow through tubular downcomer	F_003P	$\dot{m}_{TDC}$

TABLE 2.6.1-3 INSTRUMENTATION FOR CALCULATING LOWER PLENUM MASS INVENTORY		
Description	**Instrument**	**Variable**
Differential pressure across lower plenum	DP-004P	ΔP_{LOWP}
Pressure at bottom of tubular downcomer	P-001P	P_{TDC}
Temperature of water at bottom of tubular downcomer	T-003P	T_{TDC}
Temperature of water at bottom of lower plenum	T-004P	T_{LOWP}

TABLE 2.6.1-4 INSTRUMENTATION FOR CALCULATING CORE MASS INVENTORY		
Description	**Instrument**	**Variable**
Total differential pressure across core	DP-000P	ΔP_{CORE}
Differential pressure ([ ]^{a,b,c})	DP-005P	$\Delta P_{CORE,1}$
Differential pressure ([ ]^{a,b,c})	DP-011P	$\Delta P_{CORE,2}$
Differential pressure ([ ]^{a,b,c})	DP-012P	$\Delta P_{CORE,3}$
Differential pressure ([ ]^{a,b,c})	DP-013P	$\Delta P_{CORE,4}$
Pressure at bottom of tubular downcomer	P-001P	P_{TDC}
Temperature of water at core inlet (tubular downcomer outlet)	T-003P	T_{TDC}
Temperature of water at core outlet	T-015P	T_{FOUT}

TABLE 2.6.1-5 INSTRUMENTATION FOR CALCULATING UPPER-PLENUM MASS INVENTORY		
Description	**Instrument**	**Variable**
Pressure at bottom of tubular downcomer	P-001P	P_{TDC}
Pressure at top of head (for regions below 2 above hot legs)	P-017P	P_{HEAD}
Differential pressure across fuel exit cell	DP-014P	ΔP_{FOUT}
Differential pressure across upper plenum region below hot legs from hot leg- to fuel exit cell	DP-A15P	$\Delta P_{UPP,1A}$
Differential pressure across upper plenum region below hot legs from hot leg-B to fuel exit cell	DP-B15P	$\Delta P_{UPP,1B}$
Differential pressure across upper plenum region above hot legs from hot leg-A to upper head	DP-A16P	$\Delta P_{UPP,2A}$
Differential pressure across upper plenum region above hot legs from hot leg-B to upper head	DP-B16P	$\Delta P_{UPP,2B}$
Temperature of water at core outlet	T-015P	T_{FOUT}
Temperature of water in hot leg-A	T-A03PO	T_{HLA}
Temperature of water in hot leg-B	T-B03PO	T_{HLB}

TABLE 2.6.1-6 INSTRUMENTATION FOR CALCULATING UPPER-HEAD MASS INVENTORY		
Description	**Instrument**	**Variable**
Differential pressure across upper head	DP-017P	ΔP_{HEAD}
Pressure at top of upper head	P-017P	P_{HEAD}
Temperature of water at top of upper head	T-016P	T_{HEAD}

2.6.2 Energy Balance on the Power Channel

The energy balance on the power channel is used to determine the following:

- Core average void fraction during accident conditions
- Quality of the flow exiting the core
- Steam generation rate

The instruments used to determine these quantities are summarized in Table 2.6.2-1.

Core Heat Balance

The heat balance on the fluid passing through the core is given by the following equation:

$$Q_{core} = \dot{m}_{core} (h_{in} - h_{out}) \qquad (2.6\text{-}23)$$

where:

$\dot{m}_{core}$ = mass flow rate through the core (lbm/sec.)
h_{in} = core inlet enthalpy (Btu/lbm)
h_{out} = core outlet enthalpy (Btu/lbm)

During these tests, it is possible for the core flow to exit as a two-phase mixture. Thus, the core outlet enthalpy can be written in terms of the quality x:

$$h_{out} = h_f + x (h_g - h_f) \qquad (2.6\text{-}24)$$

where:

h_f = saturated liquid enthalpy (Btu/lbm)
h_g = saturated vapor enthalpy (Btu/lbm)

The void fraction from the core outlet is used to determine the quality. The void fraction is determined from the collapsed liquid level at the core outlet:

$$\alpha_{exit} = 1 - (\Delta P_{exit} C_2 / L_{taps}) \qquad (2.6\text{-}25)$$

where:

α_{exit} = core outlet void fraction
ΔP_{exit} = differential pressure cell measurement at the core exit ($lbf/ft.^2$)
C_2 = $144\ \rho_{HEAD}^{-1}$ (ft./psi) conversion to feet for the fluid density

L_{taps} = elevation difference between the taps of the differential pressure cell (ft.)

The exit quality is estimated from the void fraction, assuming homogeneous flow, (no slip) which is calculated from the pressure drop measurements as:

$$x_{exit} = \frac{\alpha_{exit}\rho_g}{(1-\alpha_{exit})\rho_f + \alpha_{exit}\rho_g} \quad (2.6\text{-}26)$$

where:

x_{exit} = core outlet quality
ρ_f = liquid density (lbm/ft.^{3})
ρ_g = vapor density (lbm/ft.^{3})

Finally, the steam generation rate is given by the following equation:

$$\dot{m}_{steam} = \dot{m}\ x_{exit} \quad (2.6\text{-}27)$$

The core average void fraction is estimated from the collapsed liquid level in the core.

$$\alpha_{core\text{-}avg} = 1 - (\Delta P_{core}\ C_2 / \frac{g_c}{g}) \quad (2.6\text{-}28)$$

where:

$\alpha_{core\text{-}avg}$ = core average void fraction
ΔP_{core} = differential pressure cell measurement over the core region (lbf/ft.^{2})
L_{taps} = elevation difference between the taps of the differential pressure cell (ft.)

Internal Energy of the Power Channel Fluid

The internal energy of the fluid in each of the power channel regions is given by the following equation:

$$U = (h - P/\rho\ J)\ M \quad (2.6\text{-}29)$$

where:

h = fluid enthalpy (Btu/lbm)
P = fluid pressure (lbm/ft.^{2})
ρ = fluid density (lbm/ft.^{3})

M = mass of the fluid in a region (lbm)
J = Joule's constant

The fluid internal energy is determined for the tabular downcomer, annular downcomer, lower plenum, core region, fuel outlet region, upper plenum, and head regions. These values are summed and used to determine the overall energy balance.

Change in the Energy of the Power Channel Metal

The change of metal temperature over the course of the test must be accounted to provide an accurate estimate of the overall energy balance. The energy in the metal as a function of time is given by the following equation:

$$U_{metal}(t) = M\ c_p\ T(t) \qquad (2.6\text{-}30)$$

where

$U_{metal}(t)$ = quantity of heat contained in the metal as a function of time (Btu)
M = mass of metal in the power channel (lbm)
c_p = specific heat of the metal (Btu/lbm-°F)
T(t) = absolute temperature of the metal as a function of time (°F)

The change in the energy contained in the metal is given by the following equation:

$$\Delta U_{metal} = \{\ U_{metal}(t) - U_{metal}(t_o)\ \} \qquad (2.6\text{-}31)$$

where:

ΔU_{metal} = change in the metal energy relative to time to (Btu)
$U_{metal}(t_o)$ = energy content of the metal at time to (Btu)

The metal mass of the power channel is [ ]^{a,b,c}, and the specific heat is 0.123 Btu/lbm-°F.

The quantities needed to perform these calculations are presented in Table 2.6.2-2.

TABLE 2.6.2-1 INSTRUMENTATION FOR CALCULATING THE POWER CHANNEL HEAT BALANCE	
Description	**Instrumentation Tag**
Core axial temperatures	TW-011011, TW-012P50, TW-014P49, TW-015P23, TW-016P14, TW-018P20, TW-019P82, TW-020P61
Core power	W_00P
Core exit differential pressure measurement	DP-014P
Overall core differential pressure measurement	DP-000P
Fluid temperature at fuel inlet	T-003P
Fluid temperature at fuel outlet	T-015P

TABLE 2.6.2-2 QUANTITIES NEEDED TO CALCULATE THE POWER CHANNEL HEAT BALANCE	
Description	**Value**
Tap elevation difference for DP-014P	[ ] a,b,c
Tap elevation difference for DP-000P	
Number of rods in the core	
Rod outer diameter	0.374 in.
Rod length	12 ft.

2.7 Hot- and Cold-Leg Piping

The mass and energy balance for the SPES-2 piping has been limited to the hot legs, cold legs and surge line. The error introduced by neglecting the remaining piping is discussed in Section 4.0.

2.7.1 Hot-Leg Mass Inventory

The mass of water in the two hot legs has been determined from the differential pressure, temperature and pressure instruments listed in Table 2.7.1-1.

The fraction of the hot leg that is filled with water is calculated using the following equation:

$$F_{HL} = \frac{C_2 \, \Delta P_{HL}}{L_{HL}} \frac{g_c}{g} \qquad (2.7\text{-}1)$$

where:

F_{HL} = fractional level of water in the hot leg. If the calculated fraction is greater than unity, which is possible while water is still flowing through the hot leg, then the hot leg is assumed to be filled with water (that is, $F_{HL} = 1$)

ΔP_{HL} = differential pressure across the hot leg ($lbf/ft.^2$)

C_2 = $144 \, \rho_{HL}^{-1}$ (ft./psi); conversion factor from differential pressure to collapsed liquid level allowing for the current water density in the hot leg

L_{HL} = span of hot leg differential pressure measurement ([ ]^{a,b,c})

The mass inventory is calculated assuming that the same homogeneous two-phase mixture is present in all segments of the hot leg. Thus,

$$M_{HL} = F_{HL} \, \rho_{HL} \, V_{HL} \qquad (2.7\text{-}2)$$

where:

M_{HL} = mass in the hot leg (lbm)

ρ_{HL} = density in the hot leg ($lbm/ft.^3$)

V_{HL} = total volume of the hot leg ([ ]^{a,b,c})

The density of water has been calculated, at each time point, from water table properties as follows:

- Given the current measured pressure, the saturation temperature is calculated.
- If the current water temperature is at or exceeds the saturation temperature, the density is determined from tables for saturated liquid using the current water temperature.

- If the current water temperature is below the saturation temperature the density is calculated from tables for subcooled liquid using the current temperature and pressure.

Hot-Leg Mass Balance

The SPES-2 facility included turbine/meters for measuring hot leg-A, pressurizer surge line, and ADS-4 volumetric flow rates. Unfortunately, these meters did not operate properly for the majority of the tests. No flow measurement was performed for hot leg-B. It is therefore not possible to perform a direct mass balance for the hot legs. The calculated mass inventories in each of the two hot legs, for two successive time points have been used to determine a rate of change of mass using the following equation:

$$\frac{dM_{HL}}{dt} = \left(\frac{M_{HL}(t_j) - M_{HL}(t_{j-1})}{t_j - t_{j-1}} \right) \qquad (2.7\text{-}3)$$

where:

M_{HL} = mass of fluid in the hot leg (lbm)
t_j = current time (sec.)
t_{j-1} = previous time (sec.)

The mass of fluid in each hot leg has previously been calculated as described above.

TABLE 2.7.1-1
INSTRUMENTATION FOR CALCULATING HOT-LEG MASS INVENTORY

Description	Instrument	Variable
Differential pressure across hot leg-A	DP-A04P	ΔP_{HLA}
Pressure of hot leg-A at inlet to steam generator-A	P-A04P	P_{HLA}
Temperature of hot leg-A at core outlet from vertical thermocouple	T-A03PL	T_{HLA}
Differential pressure across hot leg-B	DP-B04P	ΔP_{HLB}
Pressure of hot leg-B at inlet to steam generator-B	P-B04P	P_{HLB}
Temperature of hot leg-B at core outlet from vertical thermocouple	T-B03PL	T_{HLB}

2.7.2 Cold-Leg/Pump Suction Mass Inventory

The complete pipe run from the steam generator outlet to the power channel inlet has been considered. This includes the pump suction, the pumps, and the cold legs themselves. The variation in volume with height (relative to the bottom of the relevant differential pressure lower tap) in these pipe lengths is given below:

Cold leg-1 and cold leg-2 on each loop:

[ ]^{a,b,c}

It has been assumed that the whole cold leg has drained when the fluid level falls below 0.246 ft.

Pump suction on each loop:

[ ]^{a,b,c}

In addition, each pump has a volume of [ ]^{a,b,c}, which is included in the pump suction volume when the calculated pump suction level is greater than six inches. When the pump suction is full, the volume of the final bend into the steam generator ([ ]^{a,b,c}) is also included.

The mass of water in the cold legs has been determined from the differential pressure, temperature, and pressure instruments listed in Table 2.7.1-2 and Table 2.7.1-3.

Both the cold leg and pump suction pipe lengths have been treated in similar ways. The level of water in each pipe length has been determined from the following:

$$L_{PIPE} = C_2 \, \Delta P_{PIPE} \, \frac{g_c}{g} \qquad (2.7\text{-}4)$$

where:

L_{PIPE} = calculated water level (ft.). The maximum allowed level is the span of the differential pressure measurements, which is [ ]^{a,b,c} for the cold legs and [ ]^{a,b,c} for each pump suction. If the measured flow in the relevant cold leg exceeds 5 lbm/sec., then that cold leg is assumed to be water solid. If the flow exceeds this value for any cold leg on the same loop then the pump suction is also assumed to be water solid.

ΔP_{PIPE} = differential pressure across the relevant pipe (lbf/ft.^{2})

C_2 = 144 ρ_{PIPE}^{-1} (ft./psi); conversion from differential pressure to level allowing for the current density

The calculated water level is used to determine the volume of the relevant pipe filled by the collapsed liquid using linear interpolation in a tabulation of volume versus level defined by the dimensions listed above. The mass inventory is then calculated using the following equation:

$$M_{PIPE} = V_{PIPE}\ \rho_{PIPE} \qquad (2.7\text{-}5)$$

where:

M_{PIPE} = mass of water in the pipe (lbm)

ρ_{PIPE} = density of water in the pipe (lbm/ft.^{3})

V_{PIPE} = volume of the pipe filled with water (ft.^{3}) as determined from the collapsed liquid level

For the pump suction, if the calculated level is greater than six inches, then the pump is assumed to be water solid and the mass of water within it is added to that for the pump suction using the same water density as the pump suction. Furthermore, if the level calculated from the differential pressure is equal to the span of the measurement taps, then the volume of the final bend into the steam generator is included.

The density of water has been calculated, at each time point, from water table properties as follows:

- Given the current measured pressure, the saturation temperature is calculated.
- If the current water temperature is at or exceeds the saturation temperature, the density is determined from tables for saturated liquid using the current water temperature.
- If the current water temperature is below the saturation temperature the density is calculated from tables for subcooled liquid using the current temperature and pressure.

The current temperature for the pipe is calculated as the arithmetic mean of the temperature measurements listed in Table 2.7.2-1 for the relevant pipe.

A total mass of water in the complete pipe run from the steam generator outlet to the power channel inlet is calculated by summing the inventories for the three components to each loop, that is the two cold legs and the pump suction (including the pump).

Cold-Leg/Pump Suction Mass Balance

The calculated mass inventory, for each cold leg and pump suction pipe length, for two successive time points, has been used to determine a rate of change of mass using the following equation:

$$\frac{dM_{PIPE}}{dt} = \left(\frac{M_{PIPE}(t_j) - M_{PIPE}(t_{j-1})}{t_j - t_{j-1}} \right) \qquad (2.7\text{-}6)$$

where:

M_{PIPE} = mass of fluid in the lower plenum (lbm)
t_j = current time (sec.)
t_{j-1} = previous time (sec.)

The mass of fluid has previously been calculated as described above. For the first time point processed, a zero rate of mass change is assigned.

TABLE 2.7.2-1
INSTRUMENTATION FOR CALCULATING COLD-LEG MASS INVENTORIES

Description	Instrument	Variable
Differential pressure cold leg-A1	DP-A001P	ΔP_{CLA1}
Differential pressure cold leg-A2	DP-A002P	ΔP_{CLA2}
Pressure in hot leg-A at steam generator-A inlet	P-A04P	P_{HLA}
Temperature in common length of cold leg-A	T-A01P	T_{CLA}
Temperature in cold leg-A1 pipe	T-A011P	T_{CLA1}
Temperature in cold leg-A2 pipe	T-A012P	T_{CLA2}
Differential pressure cold leg-B1	DP-B001P	ΔP_{CLB1}
Differential pressure cold leg-B2	DP-B002P	ΔP_{CLB21}
Pressure in hot leg-B at steam generator-B inlet	P-B04P	P_{HLB}
Temperature in common length of cold leg-B	T-B01P	T_{CLB}
Temperature in cold leg-B1 pipe	T-B011P	T_{CLB1}
Temperature in cold leg-B2 pipe	T-B012P	T_{CLB2}
Differential pressure pump suction A	DP-A09P	ΔP_{PSA}
Pressure in hot leg-A at steam generator-A inlet	P-A04P	P_{HLA}
Flow in cold leg-A1 pipe	F_A01P	$\dot{m}_{CLA1}$
Flow in cold leg-A2 pipe	F_A02P	$\dot{m}_{CLA2}$
Temperature at top of pump suction A	T-A10P	T_{PSA}
Temperature at bottom of pump suction A	T-A11P	T_{PSA}
Differential pressure pump suction B	DP-B09P	ΔP_{PSB}
Pressure in hot leg-B at steam generator-B inlet	P-B04P	P_{HLB}
Flow in cold leg-B1 pipe	F_B01P	$\dot{m}_{CLB1}$
Flow in cold leg-B2 pipe	F_B02P	$\dot{m}_{CLB2}$
Temperature at top of pump suction B	T-B10P	T_{PSB}
Temperature at bottom of pump suction B	T-B/011P	T_{PSB}

2.7.3 Energy Balance on the Primary System Piping

An energy balance on the primary system piping is provided to account for the energy in the fluid and pipe walls to accurately predict an overall system energy balance. The primary system piping consists of the cold legs, hot legs, and the surge line. The remainder of the piping runs; the DVI lines, cold leg-to-CMT balance lines, etc., have not been included due to the lack of instrumentation.

The instruments used to determine these quantities are summarized in Table 2.7.3-1.

Change in the Internal Energy of the Fluid in the Piping

The internal energy of the fluid in the piping is given by the following equation:

$$U = (h - P/\rho\ J)\ V\rho \qquad (2.7\text{-}7)$$

where:

h = fluid enthalpy (Btu/lbm)
P = fluid pressure (lbf/ft.^{2})
ρ = fluid density (lbm/ft.^{3})
V = volume inside the pipe (ft.^{3})
J = Joules constant

The fluid enthalpy and density are evaluated at the fluid temperature.

The net change in the fluid internal energy is given by the following equation:

$$\Delta U = U(t) - U_o \qquad (2.7\text{-}8)$$

where:

U(t) = fluid internal energy as a function of time (Btu)
U_o = fluid internal energy at the start of the test (Btu)

Change in the Energy of the Piping Metal

The change of metal temperature over the course of the test must be accounted to provide an accurate estimate of the overall energy balance. The energy in the metal as a function of time is given by the following equation:

$$U_{metal}(t) = M\ c_p\ T(t) \qquad (2.7\text{-}9)$$

where:

$U_{metal}(t)$ = quantity of heat contained in the metal as a function of time (Btu)
M = mass of a section of piping (lbm)
c_p = specific heat of the metal (Btu/lbm-°F)
T(t) = absolute temperature of the metal as a function of time (°R)

The change in the energy contained in the metal is given by the following equation:

$$\Delta U_{metal} = \{ U_{metal}(t) - U_{metal}(t_o) \} \quad (2.7\text{-}10)$$

where:

ΔU_{metal} = change in the metal energy relative to time to (Btu)
$U_{metal}(t_o)$ = energy content of the metal at time to (Btu)

The metal masses for the primary system piping is summarized in Table 2.7.3-2.

As with the other components, the heat losses to the surroundings are accounted for in the overall energy balance.

TABLE 2.7.3-1 INSTRUMENTATION FOR CALCULATING THE PIPING ENERGY BALANCE	
Description	**Instrumentation Tag**
Hot-leg temperature (A & B)	P-A20E
Hot-leg pressure (A & B)	P-B20E
Cold-leg temperature (A & B)	T-A21E
Cold-leg pressure (A & B)	T-B21E
Surge line temperature (A & B)	T-A22E
Surge line pressure (A & B)	T-B22E

TABLE 2.7.3-2 METAL MASS AND SPECIFIC HEAT FOR DETERMINING PIPING METAL ENERGY		
Description	**Mass (lbm)**	**c_p (Btu/lbm-°F)**
Hot legs (per loop)	[ ] a,b,c	0.123
Cold legs (per loop)	[ ]	0.123
Surge line	[ ]	0.123

2.8 Fluid Exiting Through ADS and Breaks

The mass of the fluid exiting the primary system via the ADS and breaks is measured in catch tanks. No measurement of the flow quality is available, but approximations are made to estimate the energy loss.

2.8.1 Rate of Mass Loss to ADS and Break Catch Tanks

The imposed break in LOCA simulations, ADS lines 1 to 3 and ADS line 4 all feed to catch tanks, which give integrated measures of the total mass lost from the system to date through these routes. These masses are measured using the devices as listed in Table 2.8.2-1.

The rate flow to each catch tank is then calculated using the integrated mass measurements from two consecutive times. That is,

$$\frac{dM_{TANK}}{dt} = \left(\frac{M_{TANK}(t_j) - M_{TANK}(t_{j-1})}{t_j - t_{j-1}} \right) \qquad (2.8\text{-}1)$$

where:

M_{TANK} = measured mass of fluid in the tank (lbm)
t_j = current time (sec.)
t_{j-1} = previous time (sec.)

The ADS lines also included turbine flow meters. Unfortunately, these meters failed to operate properly in all the experiments.

2.8.2 Energy Released Through the ADS and Break

The total energy of the fluid exiting the primary system is determined by the following equation:

$$U_{catch} = U_{ADS123} + U_{ADS4} + U_{break} \qquad (2.8\text{-}2)$$

where:

U_{catch} = total energy of the fluid exiting the primary system (Btu)
U_{ADS123} = energy of the fluid exiting ADS-1, ADS-2, and ADS-3 (Btu)
U_{ADS4} = energy of the fluid exiting ADS-4 (Btu)
U_{break} = energy of the fluid exiting the break (for LOCA) (Btu)

Energy Lost Through ADS-1, ADS-2, and ADS-3

The quantity of energy loss from the pressurizer during ADS-1, ADS-2, and ADS-3 operation is given by the following equation:

$$U_{ADS123} = M_{ADS123}\, h_{ADS123} \qquad (2.8\text{-}3)$$

where:

U_{ADS123} = energy exiting through ADS-1, ADS-2, and ADS-3 (Btu)
M_{ADS123} = mass accumulated in the catch tank (lbm)
h_{ADS123} = enthalpy of the flow leaving the pressurizer (Btu/lbm)

To determine the exit enthalpy, the differential pressure cell at the top of the pressurizer is used to estimate the void fraction.

$$\alpha_{exit} = 1 - (\Delta P_{exit}\, C_2 / L_{taps}\frac{g_c}{g}) \qquad (2.8\text{-}4)$$

where:

ΔP_{exit} = differential pressure cell measurement at the top of the pressurizer (lbf/ft.^{2})
C_2 = conversion to feet for the actual fluid density
L_{taps} = elevation difference between the taps of the differential pressure cell (ft.)

The exit quality can be calculated from the void fraction for homogeneous flow (no slip) by the following equation:

$$x_{exit} = \alpha_{exit}\rho_g / \{ (1-\alpha_{exit})\rho_f - \alpha_{exit}\rho_g \} \qquad (2.8\text{-}5)$$

where:

x_{exit} = exit quality
ρ_f = liquid density (lbm/ft.^{3})
ρ_g = vapor density (lbm/ft.^{3})

Finally, the enthalpy of the fluid leaving the pressurizer via the ADS is

$$h_{ADS123} = h_f + x_{exit} (h_g - h_f) \qquad (2.8\text{-}6)$$

where:

h_f = saturated liquid enthalpy (Btu/lbm)
h_g = saturated vapor enthalpy (Btu/lbm)

Energy Lost Through ADS-4

The quantity of energy loss from the primary system during ADS-4 operation is given by the following equation:

$$U_{ADS4} = M_{ADS4}\, h_{ADS4} \qquad (2.8\text{-}7)$$

where:

U_{ADS4} = energy exiting through ADS-4 (Btu)
M_{ADS4} = mass accumulated in the ADS-4 catch tank (lbm)
h_{ADS4} = enthalpy of the flow leaving hot leg (Btu/lbm)

The enthalpy of the flow through ADS-4 is approximated by using assuming that only saturated liquid is discharged out ADS-4. The effects of this assumption will be evaluated in Section 4.0.

Energy Lost Through the Break

The quantity of energy loss from the primary system through the break is given by the following equation:

$$U_{break} = M_{break}\, h_{break} \qquad (2.8\text{-}8)$$

where:

U_{break} = energy exiting through break (Btu)
M_{break} = mass accumulated in the break catch tank (lbm)
h_{break} = enthalpy of the flow leaving the break (Btu/lbm)

The enthalpy of the flow out the break is approximated by using the enthalpy of saturated liquid at the break location temperature. The effects of this assumption will be evaluated in Section 4.0.

For the double-ended guillotine (DEG) break tests, and for the steam generator tube rupture (SGTR) tests, the ADS-4 catch tank doubles as either a second break catch tank, or a receptacle for steam generator secondary side overflow. The energy associated with the mass is calculated by assuming saturated liquid at break location temperatures.

The instruments used to evaluate the energy loss through the ADS and break are summarized in Table 2.8.2-1.

TABLE 2.8.2-1 INSTRUMENTATION FOR CALCULATING THE ADS AND BREAK ENERGY BALANCE	
Description	**Instrumentation Tag**
Hot-leg temperature (A & B)	T-A03PL, T-B03PL
Hot-leg pressure (A & B)	P-A04P, P-B04P
Pressurizer pressure	P-027P
Differential pressure at top of pressurizer	DP-026P
Break catch tank mass	IF-005P
ADS-1,-2,-3 catch tank mass	IF-030P
ADS-4 catch tank mass	IF-040P

2.9 System Analysis

To determine the validity of the individual component mass and energy inventories, an overall system mass and energy balance is calculated.

2.9.1 Total System Mass Inventory

For each transient time, the total system mass inventory is determined by summing the contributions from all the components considered except the steam generator secondary side. That is,

- Two accumulators
- ADS-1 to -3, ADS-4 and break catch tanks
- Two core makeup tanks
- Four cold legs, two pumps, and two pump suction pipes
- Two hot legs
- IRWST tank
- Power channel
- Pressurizer and surge line
- Steam generator tubes

For the three catch tanks, the initial measured mass may be nonzero. This is allowed for in calculating the total system mass. The percentage system mass relative to time zero, and the rate of change over each time step are also calculated at each time point.

In addition, the mass within the power channel, hot legs, cold legs, pump, pump suction, and steam generator primary side is determined for each time step. The percentage of the initial value for this mass is also determined. An alternative system mass, which excludes the contribution from the IRWST tank is also included.

Total System Mass Balance

The primary system has been grouped under the following categories:

- The loops containing the power channel, two hot legs, two pumps with their associated pump suction and cold leg lines, two sets of steam generator U-tubes, the surge line, and the pressurizer.

- The sources, which are the two accumulators, the two CMTs, and the IRWST. For two of the tests (S00504 and S01309), this includes the nonsafety systems (that is, the CVCS and the NRHR).

- The sinks, which are the break and ADS catch tanks, and the CMTs, which received water from the loops via the CLBLs.

The mass in each of these three parts of the system has been determined for each time point, together with the integrated mass discharged from the loops to each of the sinks and the integrated mass injected from each source. The latter has been determined from the following:

- The available flow measuring devices. For test S00504, the flow measurements for the CVCS and NRHR have been included. For test S01309, a constant CVCS flow of [ ]^{a,b,c} has been assumed for the CVCS, for the entire transient, in line with the data supplied in the *Final Data Report.*[1]

- From the change in calculated component water mass since the start of the test. For the CMTs, this includes an allowance for the flow of water into the CMTs via the cold leg balance lines; that is,

$$M_{CMT,OUT}(t) = M_{CMT}(0) + M_{CMT,IN}(t) - M_{CMT}(t) \qquad (2.9\text{-}1)$$

The system mass balance error is computed at each transient time using the following equation:

$$M_{ERROR}(t) = \int_0^t \frac{dM_{LOOP}}{dt}\, dt - \int_0^t \dot{m}_{source}\, dt + \int_0^t \dot{m}_{sink}\, dt \qquad (2.9\text{-}2)$$

which is integrated to give the following:

$$M_{ERROR}(t) = M_{LOOP}(t) - (M_{LOOP}(0) + M_{SOURCE}(t) - M_{SINK}(t)) \qquad (2.9\text{-}3)$$

where:

$\dot{m}_{SOURCE}$ = mass flow from sources
$\dot{m}_{SINK}$ = mass flow out sinks
$M_{ERROR}(t)$ = current mass balance error (lbm)
$M_{LOOP}(t)$ = current total mass in all the loop components (lbm)
$M_{LOOP}(0)$ = initial total mass in all the loop components (lbm)
$M_{SOURCE}(t)$ = current integrated mass injected to the loops from all sources (lbm)
$M_{SINK}(t)$ = current integrated mass discharged from the loops to all the sinks (lbm)

2.9.2 Overall System Energy Balance

An overall energy balance on the test facility is achieved by considering the primary system, including the IRWST tank water as a control volume. Energy is added to the volume through the heated rods in the power channel. Energy is extracted from the following: the volume through the heat losses to the environment; the fluid loss through the break; ADS-1, ADS-2, ADS-3, and ADS-4; and the energy loss through the steam generators. Finally, the change in the internal energy of the fluid and metal inside the control volume is determined to complete the energy balance. The overall system energy balance primary for SPES-2 is written as follows:

$$U_{error} = U_{rods} - U_{fl\text{-}out} - U_{surr} - U_{sg} - (U - U_o)_{fluid} - (U - U_o)_{metal} + U_{NS} \qquad (2.9\text{-}4)$$

where:

U_{error} = error in the overall energy balance (Btu)
U_{rods} = integrated power in the heated rods (Btu)
$U_{fl\text{-}out}$ = energy of the fluid leaving the control volume (Btu)
U_{sg} = integrated heat transfer in the steam generators (Btu)
ΔU_{fl} = change in the energy of the fluid in the control volume (Btu)
ΔU_{mt} = change in the energy of the metal in the control volume (Btu)
U_{surr} = integrated heat loss to the surroundings (Btu)
U_{NS} = energy of the fluid injected via nonsafety systems (Btu)

The heat loss to the surroundings is given in the *SPES-2 Hot Pre-Operational Tests Results*[8] as

$$Q_{surr} = 0.0015\ T_{cl}^{2} + 0.0175\ T_{cl} - 0.72 \qquad (2.9\text{-}5)$$

where:

Q_{surr} = heat loss to the surroundings (Btu/sec.)
T_{cl} = cold-leg temperature in °C

The integrated heat loss to the surroundings is given by the following equation:

$$U_{surr} = \int Q_{surr}\, dt = \sum Q_{surr\text{-}j}\, \Delta t_j \qquad (2.9\text{-}6)$$

where:

$Q_{surr\text{-}j}$ = heat loss over a given time step, Δt_j (Btu/sec.)

The change in the fluid energy relative to time zero is calculated by summing the fluid energy for each component at each time step, then subtracting the value at time zero.

$$\Delta U_{fl} = \sum U_{fl\text{-}i\text{-}j} - \sum U_{fl\text{-}i\text{-}o} \qquad (2.9\text{-}7)$$

where:

$U_{fl\text{-}i\text{-}j}$ = energy content of the fluid in component i at time t_j (Btu)
$U_{fl\text{-}i\text{-}o}$ = energy content of the fluid in component i at time t_o (Btu)

The integrated rod power is defined by the following equation:

$$U_{rods} = \int Q_{rods}\, dt = \sum Q_{rods\text{-}i}\, \Delta t_j \qquad (2.9\text{-}8)$$

where:

$Q_{rods\text{-}j}$ = measured power over time step, Δt_j (Btu/sec.)

Finally, the integrated steam generator power is defined by the following equation:

$$U_{sg} = \int Q_{sg}\, dt = \sum Q_{sg\text{-}j}\, \Delta t_j \qquad (2.9\text{-}9)$$

where:

$Q_{sg\text{-}j}$ = heat transferred from the primary side to the secondary side at time step, Δt_j (Btu/sec.)

The error in the energy balance, U_{error}, gives an indication of the applicability of the various assumptions which were used to calculate the energy balance.

2.9.3 System Event Timings

The timing of key events in each transient have been determined using the instruments listed in Table 2.9.3-1.

For each of the limit switches, the event actuation is determined by any one of the two switches changing state. The only exception to this is CMT-B, as only one of the limit switches was good in all tests, this has been used to determine the actuation time. For the other events, the following logic is used:

- The initiating event is always assumed to occur at time zero.

- Reactor trip is determined when the core power falls to 90 percent of the value at time zero for three consecutive time points.

- Reactor coolant pump trip is determined to occur when the measured differential pressure falls to 90 percent of the value at time zero for three consecutive time points.

- Accumulator injection is determined to occur when the measured injection flow, associated with each accumulator, first exceeds 0.05 lbm/sec. for three consecutive time steps. The time the accumulators are fully drained is determined when the accumulator mass falls to zero.

- IRWST injection is determined to occur when the measured injection flow, to either DVI line, first exceeds 0.05 lbm/sec.

The system pressure, that is the pressure at the top of the pressurizer, is stored at the time when each of the events is detected. At the end of the main calculation loop a list of any events occurring after the initiating event, is given in the order they occur along with the associated system pressure.

TABLE 2.9.3-1 INSTRUMENTATION FOR DETERMINING THE TIMING OF TRANSIENT EVENTS	
Description	**Instrument**
CMT-A injection line limit switches	Z_A40EC, Z_A40EO
CMT-B injection line limit switches	Z_B40EO
CMT-A to cold-leg balance line limit switches	Z_A45PC, Z_A45PO
CMT-B to cold leg balance line limit switches	A_B45PC, Z_B45PO
ADS-1 limit switches	Z_001PC, Z_001PO
ADS-2 limit switches	Z_002PC, Z_002PO
ADS-3 limit switches	Z_003PC, Z_A03PO
ADS-4A limit switches	Z_A04PC, Z_A04PO
ADS-4B limit switches	Z_B04PC, Z_B04PO
PRHR supply line limit switches	Z_A81EC, Z_A81EO
Main feedwater isolation limit switches - loop A	Z_A02SC, Z_A02SO
Main feedwater isolation limit switches - loop B	Z_B02SC, Z_B02SO
Main steam line isolation limit switches - loop A	Z_A04SC, Z_A04SO
Main steam line isolation limit switches - loop B	Z_B04SC, Z_B04SO
Steam generator PORV operation limit switches - loop A	Z_A06SC, Z_A06SO
Steam generator PORV operation limit switches - loop B	Z_B06SC, Z_B06SO
Core power generation	W-00P
Reactor coolant pump-A differential pressure	DP-A00P
Reactor coolant pump-B differential pressure	DP-B00P
Accumulator-A injection flow	F_A20E
Accumulator-B injection flow	F_B20E
IRWST injection flows to DVI line A and DVI line B	F_A60E, F_B60E

2.10 Nomenclature

A	=	area ($ft.^2$)
C_2	=	conversion from differential pressure to level (144/ρ ft./psia)
c_p	=	specific heat (Btu/lbm-°F)
d	=	tube diameter (ft.)
F	=	fractional level
g	=	gravity ($ft./sec^2$)
g_c	=	gravitational constant ($lbm-ft/lbf-sec.^2$)
Gr	=	Grashof number
h	=	specific enthalpy (Btu/lbm)
H	=	height (ft.)
J	=	Joules constant (778 Btu/ft-lbf)
K	=	thermal conductivity (Btu/sec.-ft.-°F)
L	=	level (ft.)
M	=	mass of fluid (lbm)
n	=	exponent on subcooled boiling correlation
N	=	number
P	=	pressure (lbf/ft^2)
Pr	=	Prandtl number
Q	=	energy transfer rate (Btu/sec)
R	=	ideal gas constant
t	=	time (sec.)
T	=	temperature (°F)
u	=	internal energy of fluid (Btu)
V	=	volume ($ft.^3$)
x	=	quality
z	=	elevation (ft.)
ṁ	=	mass flow rate (lbm/sec.)
α	=	void fraction
β	=	coefficient of volumetric expansion (1/°R)
δ	=	gap between walls for free convection (ft.)
ΔP	=	differential pressure (psid)
ΔU	=	change in internal energy (Btu)
ε	=	emissivity
κ	=	gas expansion exponent
λ	=	convective heat transfer coefficient ($Btu/sec.-ft.^2-°F$)
ν	=	Kinematic viscosity ($ft.^2/sec.$)
ρ	=	density ($lbm/ft.^3$)
σ	=	Stefan-Boltzmann constant ($Btu/sec.-ft.^2-°R^4$)

Subscripts

A	=	component A
ACC	=	pertains to accumulators
ADC	=	pertains to annular downcomer
ADS123	=	pertains to ADS-1, ADS-2, and ADS-3
ADS4	=	pertains to ADS-4
air	=	pertains to air
alt	=	alternative calculation
amb	=	ambient
avg	=	average
B	=	component B
Bot, b	=	bottom
break	=	pertains to the break
bulk	=	pertains to bulk fluid conditions
c/c	=	pertains to combined convective and conductive heat transfer
cal	=	calorimetric heat balance
CL	=	pertains to cold leg
CMT	=	core makeup tank
CMT-GV	=	guard vessel to CMT
CMT-Store	=	stored in CMT wall
CORE	=	pertains to core
eq	=	equivalent
error	=	difference in mass or energy balance
error-ht	=	difference in heat transfer calculation
exit	=	pertains to discharge or exit conditions
f	=	pertains to saturated liquid
fl-out	=	fluid out
fluid, fl	=	pertains to fluid
fluid-store	=	pertains to fluid storage
Fout	=	pertains to fuel outlet region
free	=	pertains to free convection
g	=	pertains to saturated vapor
gas	=	pertains to accumulator charging gas
GV-Store	=	stored in CMT guard vessel wall
GVid	=	CMT guard vessel inside diameter
GVod	=	CMT guard vessel outside diameter
HEAD	=	pertains to upper head
HL	=	pertains to hot leg
HOR-1	=	pertains to IRWST inlet tube
HOR-2	=	pertains to IRWST outlet tube
in	=	pertains to flow into a component

IRWST	=	pertains to the IRWST
j	=	pertains to time t_j
j-1	=	pertains to time t_{j-1}
LOOP	=	pertains to primary system
LOWP	=	pertains to lower plenum
metal	=	pertains to component metal
mix	=	pertains to mixture
NS	=	pertains to non-safety systems
out	=	pertains to flow out of a component
p	=	primary
PCHAN	=	pertains to power channel
PIPE	=	pertains to pipes
PZR	=	pertains to pressurizer
rad	=	pertains to radiative heat transfer
rods	=	pertains to heater rods in core
s	=	secondary
sat	=	pertains to saturated conditions
SG	=	steam generator
SINK	=	pertains to sinks
SL	=	pertains to surge line
SOURCE	=	pertains to safety injection sources
surr	=	surroundings
TANK	=	pertains to catch tanks
taps	=	between differential pressure-cell taps
TC	=	thermo-couple
TDC	=	pertains to tabular downcomer
ToF	=	top of fuel
Top, t	=	top of CMT
tot	=	total
tubes	=	pertains to IRWST tubes
UPP	=	pertains to upper plenum
vert	=	pertains to IRWST vertical tube section
z0	=	two-phase

3.0 ANALYSIS OF SPES-2 TEST DATA

The phenomena identification ranking table (PIRT) for AP600 small-break loss-of-coolant accident (SBLOCA) provided a guide for the SPES-2 testing (Table 1-2). The table helped identify the instrumentation needed to record specific phenomena and also the manner in which the tests were performed. An initial acceptance evaluation of the tests against meeting the needs documented in the PIRT was performed in WCAP-14309, *Final Data Report*.[1] This evaluation included the functioning of critical instruments and the acceptability of the initial test conditions.

The analysis of the test data documented in this report is divided into two sections. This section evaluates each event in general terms and presents the general results of the analysis represented by the standard package of analysis data. Loss-of-coolant accident (LOCA) events in the SPES-2 test were marked by different phases as identified in the phenomenon identification ranking table (PIRT) in Section 1.0. These phases were characterized by the primary system pressure and the thermal-hydraulic phenomena occurring within the primary and safety systems. The different event phases selected for the purpose of detailed evaluation of the LOCA events are as follows:

- Blowdown phase
- Natural circulation phase
- Automatic depressurization system (ADS) phase
- In-containment refueling water storage tank (IRWST) injection phase

Section 4.0 evaluates some of the most important specific phenomena identified in the PIRT for the SPES-2 testing and how these phenomena affected critical parameters during the test.

3.1 Introduction

The analysis of the SPES-2 test data was performed by the SPESAN computer code. This code was developed specifically to perform a continuous mass and energy balance for the primary side in each test, including the accumulators, the core makeup tanks (CMTs), the IRWST, and the passive residual heat removal (PRHR). Also part of these calculations were the collapsed levels in the various components, including the power channel. The actual two-phase level was calculated in the power channel to establish the actual coverage of the heater bundle during the test.

The SPES-2 facility was not required to be instrumented to allow a rigorous energy balance performed for the tests,[9] since measurements of the quality of the fluid leaving the system through the break and the ADS was not performed. However, by applying some reasonable assumptions about the quality of the break flow and the ADS-4 flow and by determining the void fraction (and accordingly the quality) of the fluid leaving the system through ADS-1, ADS-2, and ADS-3 from differential pressure measurements in the pressurizer, a coarse overall energy balance can be derived for the system for the LOCA tests.

The overall system considered in the mass and energy balances consists of the primary system (power channel, primary loops, and pressurizer), the CMTs, the accumulators, and the IRWST. The internal energy of the fluid for each part of the system was calculated throughout the event. The heat loss to the surroundings was calculated based on the data from the SPES-2 *Hot Pre-operational Test Results,*[8] and the thermal inertia of the system hardware was based on the system overall metal mass. Included in this section is a discussion of the analysis results for each test along with a set of 82 standard plots. Additional plots are included to aid in characterizing the phenomena observed for each test.

The SPESAN code was used to analyze each test. Most of the quantities were calculated on a time step by time step basis; however, time derivatives and other calculations susceptible to noise were calculated using time averaging of the data to provide a better representation of the results.

3.2 Analysis of the Two-Inch Cold-Leg Break without Nonsafety Systems (S00303)

This matrix test simulated a 2-in. break in the bottom of cold leg-B2. The test began with the initiation of the break in cold leg-B2, which was the cold leg with the CMT-B pressure balance line connection. The break location was on the power channel side of the cold leg from the core makeup tank (CMT) balance line connection. This test was performed without any nonsafety systems' pumps operating. That is, it was performed without the chemical and volume control system (CVCS) makeup pumps, steam generator startup feedwater (SFW) pumps, and normal residual heat removal system (NRHR) pumps.

3.2.1 Summary of Test Observations

Blowdown Phase

Figure 3.2-83 shows plant primary system pressure during matrix test S00303 (as measured at the top of the pressurizer) during the S00303 test, with selected component actuations and plant responses shown in relation to primary system pressure.

The blowdown phase began with the initiation of the break, which caused the pressurizer to drain. This resulted in a rapid reduction in pressure. The reactor trip (R) signal initiated at [ ]^{a,b,c} psia, and the safety systems actuation (S) signal initiated at [ ]^{a,b,c} psia. The R and the S signals initiated the following actions:

- Decay heat simulation (with heat loss compensation) initiated.
- The main steam line isolation valves (MSLIVs) closed.
- The main feedwater isolation valves (MFWIVs) shut off.
- The CMT injection valves opened.
- The passive residual heat removal (PRHR) return flow valve opened.
- The reactor coolant pumps (RCPs) shut down.

The recirculation flow through the CMTs and the flow through the PRHR began immediately after the isolation valve opened. Boiling in the heated rod bundle was initiated by the reduction of the system pressure to saturation level. The upper plenum flashed while the fluid level dropped to hot-leg elevation based on the level measurements. The flashing on the hot-leg side of the heated rod bundle stopped the rapid drop in primary system pressure. When the RCPs shut down (at [ ]^{a,b,c}), the flow through the rod bundle began to oscillate (approximately [ ]^{a,b,c} period). This resulted in oscillations in the rod bundle and the upper-plenum void fraction, upper-plenum temperature, and system pressure.

Natural Circulation Phase

After the primary system pressure reached a near steady-state condition, the system transitioned into the natural circulation phase. During the initial stages of the natural circulation phase, the rod bundle

void fraction increased. This resulted in two-phase fluid and a void in the upper plenum and also two-phase fluid in the hot legs. The hot leg-B fluid had a void fraction very close to that observed in the upper plenum. The void fraction in hot leg-A was much lower due to the selective removal of vapor from the hot leg by the PRHR inlet line.

As the system continued to drain, the two-phase flow in the hot legs resulted in a break in the single-phase and two-phase natural circulation in the steam generator U-tubes. Steam from the two-phase mixture collected in the top of the U-tubes, thereby draining the steam generator U-tubes. This stopped the flow through the primary system, and the power channel flow was predominantly composed of the flow through the PRHR and the CMT injection. Some reflux condensing of the steam may have continued to occur in the U-tubes since the steam generators were still a heat sink at this time. The oscillations of the collapsed level observed through the rod bundle and in the upper plenum terminated when the natural circulation ended in the steam generators. Approximately [ ]^{a,b,c} into the event, the natural circulation was broken in steam generator-B due to the higher void fraction in hot leg-B. Approximately [ ]^{a,b,c} later, the natural circulation was broken in steam generator-A.

A two-phase flow through the PRHR, consisting of alternating slugs of steam and saturated water, had an average integrated void fraction significantly greater than that seen in the upper plenum. Due to boiling in the rod bundle, two-phase flow entered the hot leg from the upper plenum and flowed through the PRHR heat exchanger (HX), which is located in the in-containment refueling water storage tank (IRWST). The average void fraction in the PRHR inlet was as high as [ ]^{a,b,c}, which enhanced the PRHR flow and heat transfer from the primary system when compared with single-phase saturated or subcooled water. When the flow stabilized after the initial flow oscillations, a heat removal rate of [ ]^{a,b,c} was calculated. This calculation was based on the void fraction of the flow in the PRHR supply line, the flow rate, the temperature, and the pressure. This calculation assumes a slip coefficient of 1 between steam and water.

When the natural circulation was broken in the B-side cold legs (that is, when the cold legs had partially emptied), the CMTs converted from the recirculation mode to the draindown mode of injection. This increased the cold injection flow and the rate of system pressure decay. This occurred at approximately [ ]^{a,b,c} for CMT-B and [ ]^{a,b,c} for CMT-A. When system pressure dropped to the saturation pressure for the upper head, the upper head began to drain (at 400 seconds).

During the first [ ]^{a,b,c} of this event, [ ]^{a,b,c} of water were expelled through the break while draining the pressurizer, the steam generator U-tubes, the power channel upper head, the power channel upper plenum above the hot leg, most of the cold legs, and approximately [ ]^{a,b,c} of the CMTs. The heated rods in the power channel that simulated the core decay heat reduced the power level to approximately [ ]^{a,b,c} at [ ]^{a,b,c}. This value consisted of [ ]^{a,b,c} decay heat and [ ]^{a,b,c} heat loss compensation. The break flow was steady, indicating that cold leg-B2 was not totally empty.

Automatic Depressurization System Phase

The ADS phase of the transient began with the actuation of ADS-1 (at approximately 900 seconds into the event). ADS-2 and ADS-3 occurred within the next [ ]^{a,b,c}. The heat loss compensation was terminated from the decay heat simulation when ADS-1 occurred, and the rod bundle power level was reduced to approximately [ ]^{a,b,c}.

The ADS actuation increased the rate of primary system depressurization and resulted in a high level of injection flow from the accumulators. The rapid injection of cold fluid from the accumulators (at [ ]^{a,b,c} into the event) subcooled the whole primary system, temporarily refilling the power channel/upper plenum and the pressurizer. When the accumulator discharge ended, the flow through the heater bundle was reduced to the injection rate of the CMTs and the PRHR HX flow, and boiling occurred again in the heater bundle. Two-phase flow occurred again in hot leg-A, the PRHR HX, and the ADS via the pressurizer.

The liquid discharge through the break was replaced by saturated steam at approximately [ ]^{a,b,c} (Figure 3.2-68). During the ADS period, approximately [ ]^{a,b,c} of subcooled water were discharged from ADS-1, ADS-2, and ADS-3. This water was primarily supplied by the accumulator discharge and was followed by an increase in the heater bundle void fraction after the accumulators drained and only the CMTs provided power channel injection. ADS-4 occurred at [ ]^{a,b,c}, and the pressurizer water level fell. The fluid discharge through ADS-1, ADS-2, and ADS-3 ended, and fluid was discharged through ADS-4. The pressurizer drained again, and a small amount of CMT flow still entered the direct vessel injection (DVI) line.

IRWST Injection Phase

When system pressure had been reduced below the pressure corresponding to the water elevation head of the IRWST, flow from the IRWST entered the DVI line and the IRWST injection phase began. Shortly thereafter, the CMT flow ended. The flow from the IRWST subcooled the primary system, the core boiling slowly ended, and the upper plenum partially refilled above the hot-leg elevation. The PRHR drained approximately [ ]^{a,b,c} into the event and was no longer effective. A steady flow of subcooled water was then flowing from the IRWST into the DVI line, through the power channel, and left the primary system through ADS-4.

The heater bundle (active core) remained fully covered by a two-phase mixture at all times during this event. There was no indication of an increase in heater rod temperatures due to lack of cooling.

3.2.2 Analysis of the S00303 Test Data

The analysis of the SPES-2 test was performed using the SPESAN computer code. The code performs a detailed accounting of the coolant inventory in all parts of the system from the start to the end of the test. Also, the internal energy of all components and parts of the facility, including the energy losses from the break and ADS flows, are calculated throughout the event. It is noted that the mass balance

and the energy transfer calculations are performed in much greater detail than was performed in WCAP-14309, *Final Data Report.*[1] The results of the test data analysis are presented in Figures 3.2-1 through 3.2-82. Mass balance snapshots for all the major primary system components, at various points of interest throughout the transient, are presented in Table 3.2-1.

Mass Balance

Overall Mass Balance

The uncertainty in the overall mass balance is an indication of the overall quality of the test. The total water inventory is tracked from the start until the end of the test. Figures 3.2-74, 3.2-75, and 3.2-76 show the overall mass balance and the error (uncertainty) in mass balance for S00303.

The overall mass balance for S00303 (Figure 3.2-74) shows a small variation of water inventory during the event, resulting from the overall uncertainty in the instrumentation and the assumptions of the mass balance model used to determine the total water inventory. The average total inventory during the test was indicated to be approximately 30 lbm higher than the initial system mass, and a final mass was indicated to be approximately 50 lbm above the initial mass. Figure 3.2-75 shows the difference between the total mass during the event and the initial mass (mass balance error) when the inventory was calculated by integrating the flows. Figure 3.2-76 shows the mass balance error when inventory was calculated based on the catch tank weight and component level measurements. The mass balance error based on flow measurements varied from +50 lbm to -50 lbm, while the weight and level measurements resulted in an average error of approximately +40 lbm during the event, and a final error of +50 lbm at the end of the event.

Water Inventory for the Power Channel and the Loop

Maintenance of coolant coverage of the heater bundle is the most critical issue for the power channel. The heater bundle coverage during a loss-of-coolant accident (LOCA) event often consists of two-phase fluid, which can have a very high void fraction. Figure 3.2-40 shows the level of two-phase fluid in the power channel as calculated from the measured pressure drop data, which was then used to infer a void fraction and two-phase level. Since this represents the true two-phase level, it will be different than the collapsed liquid level in the heater bundle.

For S00303, the calculated two-phase fluid level in the upper plenum decreased to the hot-leg elevation (Figure 3.2-40), and it remains at this elevation for most of the event. The accumulator injection ([ ]^{a,b,c}) partially condensed the steam bubble in the upper plenum causing the level to rise. Following the end of the accumulator injection, the two-phase level again decreased this time to approximately [ ]^{a,b,c} below the hot-leg elevation. This occurred at the time of minimum power channel water inventory (Figure 3.2-39), before the IRWST injection started to refill the power channel (at [ ]^{a,b,c}). The IRWST injection also partially condensed the steam bubble in the upper plenum causing the level to rise above the hot-leg elevation again.

The collapsed level in the annular downcomer and tubular downcomer are shown in Figures 3.2-42 (annular downcomer) and 3.2-44 (tubular downcomer). The annular downcomer was full until approximately [ ]^{a,b,c} into the event. At that time, the level starts to decrease, but it is maintained above the elevation of the hot leg until after the end of the accumulator injection (approximately [ ]^{a,b,c}). The level then deceased and drained the annular downcomer by [ ]^{a,b,c}, and reached a minimum level in the tubular downcomer at approximately [ ]^{a,b,c}. This corresponded to the time of minimum water inventory in the power channel shown in Figure 3.2-39. Figure 3.2-62 shows the maximum cladding temperature during the event and compares this temperature with the saturation temperature. There were no indications of loss of cooling for the heater rods during this event, which confirms that the estimated two-phase level in the power channel remains above the top of the heated rod bundle.

Collapsed fluid level in the rod bundle (Figure 3.2-48), and the rod bundle exit void fraction (Figure 3.2-61) show that the rod bundle was water solid before the break was initiated. The rod bundle exit void fraction was determined from DP-014P which covers the span from rod bundle near the top of the active fuel (TAF) elevation to the lower part of the upper plenum. Two-phase flow with approximately [ ]^{a,b,c} average void fraction existed in the rod bundle prior to the accumulator injection. During the accumulator injection, the rod bundle became essentially water solid. However, when the accumulator injection ended, the collapsed level again started to decrease. The rod bundle exit void fraction reached approximately [ ]^{a,b,c} prior to the start of the IRWST injection phase, starting at approximately [ ]^{a,b,c}.

The collapsed level in the upper plenum (Figures 3.2-52 and 3.2-54) decreased to approximately [ ]^{a,b,c} below the hot leg before the accumulator injection, followed by a period when the level in the upper plenum increased above the hot leg during the accumulator injection. This period was followed by a drop in the collapsed level to approximately [ ]^{a,b,c} below the hot leg at the time of minimum water inventory before the IRWST injection started.

The water inventory in the power channel (Figure 3.2-39) had two minima: before the accumulator injection, and before the IRWST injection. The second minimum was more severe, showing a total power channel inventory of approximately [ ]^{a,b,c} of starting inventory) at that time. The total primary system inventory (power channel, pressurizer, and loops), shown in Figure 3.2-77, reaches approximately [ ]^{a,b,c} of starting inventory) for this minimum.

Water Injection/Ejection

The injected fluid mass from all injection sources is shown in Figure 3.2-78. Figure 3.2-79 shows the total source inventory and the injected and ejected masses during the event. Starting with a total of approximately [ ]^{a,b,c} source inventory, only [ ]^{a,b,c} ([ ]^{a,b,c} of available source water) was used by the end of the event.

Energy Balance

PRHR Heat Transfer

The heat transfer from the PRHR to the IRWST gives a unique possibility of comparing heat transfer on the primary and the secondary side. A method of calculating the heat rejection by the PRHR HX into the IRWST is described in Section 2.2-2, and a comparison of three heat transfer calculations is given in Section 4.0. The PRHR primary-side heat transfer was calculated based on the measured exit flow rate and the difference in enthalpy of the inlet and exit flows. Since the S00303 test had two-phase flow conditions in the hot legs and PRHR, the inlet flow void fraction was determined (Figure 3.2-21) and used to establish the effective enthalpy of the two-phase inlet flow. The outlet flow from the PRHR HX was always subcooled water. The primary side two-phase heat transfer for S00303 (shown in Figure 3.2-19) was considerably greater than the heat transfer measured for single-phase flow through the PRHR during the hot preoperational testing (see WCAP-14309, *Final Data Report*).[1] Figure 3.2-18 shows the calculated heat transfer from the PRHR external tube surface to the water in the IRWST by the three-tube sections of the HX. On the inside, the top part of the PRHR HX acted as a condenser, where the steam of the two-phase fluid extracted from hot leg-A was condensed. The top horizontal tube transfers the greatest amount of heat. The condensation process on the inside effectively heated this tube wall temperature above the boiling point for the water in the IRWST, resulting in very effective nucleate boiling heat transfer from the outside surface. The vertical and the bottom horizontal sections of the HX, for the most part, subcooled with a less effective free convection heat transfer to the IRWST water, and they contributed less to the overall heat transfer of the PRHR.

Figure 3.2-17 shows the internal energy of the IRWST water, the integrated power from the primary side of the PRHR HX, and the heat transfer from the PRHR HX external surfaces. The internal energy in the IRWST water was calculated based on thermocouples located at various elevations in the IWRST tank, which were allocated different control volumes to arrive at an effective average temperature. Due to the severe temperature stratification in the IRWST tank, this technique only produces good results until the IRWST starts to drain.

For S00303, there was a good correlation between the three heat transfer calculations. Up to [ ]^{a,b,c}, the PRHR primary-side calculation and the IRWST internal energy calculation were very close. After [ ]^{a,b,c}, the IRWST internal energy appeared to increase significantly due to the effect of draindown on the thermocouple readings. However, since there is very little energy being provided by the PRHR after [ ]^{a,b,c}, this apparent increase does not reflect an actual increase in the average water temperature and IRWST internal energy. The comparison shown in Figure 3.2-17 indicates that the PRHR primary-side heat transfer calculation is valid for this test.

Steam Generator Heat Transfer

Figure 3.2-32 shows the heat transfer in the steam generators for S00303. Heat transfer from the primary to secondary side is significantly reduced after the pumps trip. This is due to reduced flow,

and decreased heat transfer coefficients in the tubes. Figure 3.2-33 shows the pressures on the primary side and the secondary side of the steam generators. The pressures show that the steam generators were available as heat sinks until approximately [ ]^{a,b,c} into the event, at which time the primary-side pressure dropped below the secondary, and heat transfer ceases. Also shown in Figure 3.2-32 is the PRHR heat transfer, which removed heat from the system after the steam generators heat transfer had ended. Figure 3.2-28 shows the water inventory in the steam generators primary side, which includes inlet and outlet plena and U-tubes. When full, the steam generator inlet and outlet plena contain approximately [ ]^{a,b,c} of water. When the primary-side pressure dropped below the secondary-side pressure (approximately [ ]^{a,b,c}), the steam generator's U-tubes are essentially drained of water and contain trapped steam which becomes more and more superheated as the primary-side pressure decays.

Overall Energy Balance

Figure 3.2-80 shows the integrated energy of the fluid streams leaving the system. The energy content of the break flow was greatly reduced when ADS-1 occurred since, although the break flow converted to steam, the mass flowrate became very low. For ADS-1, ADS-2 and ADS-3 the same happened when ADS-4 occurred.

Figure 3.2-81 shows all the energy components in the heat balance for the system. Throughout the event, heated rod bundle power was the dominant heat input to the system, and during the initial part of the event the steam generators provided the dominant heat extraction. When the primary and secondary system pressures equalized, and the steam generator U-tubes drained (about [ ]^{a,b,c}), the steam generator became thermally isolated from the primary system and did not affect the rest of the event. Figure 3.2-80 shows the energy loss from the break and the ADS flows as calculated based on assumptions described in Section 2.0. The average energy loss from the fluids ejected from the system during the first [ ]^{a,b,c} of the event was approximately [ ]^{a,b,c}, which was reduced to approximately [ ]^{a,b,c} from about [ ]^{a,b,c} to the end of the test.

From approximately [ ]^{a,b,c}, more energy left the system through the break and ADS flows than was generated by the heater bundle, and the overall energy stored within the system (fluid and metal mass) decreased to compensate. The average loss of the metal thermal energy for the first [ ]^{a,b,c} was approximately [ ]^{a,b,c}, which was greater than the heated rod power for most of this period. After approximately [ ]^{a,b,c} the metal and fluid energy stabilized in the system, and the rate of the fluid energy leaving the system (primarily via ADS-4) matched the core input power well. This steady-state condition existed for the rest of the event.

Figure 3.2-82 shows that the accumulated error in the energy balance increased rapidly from [ ]^{a,b,c} (during the accumulator discharge into the primary system). This error was a consequence of the rapid drop in the metal energy seen in Figure 3.2-81, which was calculated based on fluid temperatures. In reality, the calculated decrease of metal energy occurs at a

slower rate than indicated by the fluid thermocouples due to the large thermal inertia of the heavy walled components. The increasing error and the error peak shown in Figure 3.2-82 at [ ]^{a,b,c} are therefore a consequence of taking credit for metal heat too fast during the event, and this error largely disappeared within the following [ ]^{a,b,c} when the metal temperatures catches up with the fluid temperatures. In evaluating the overall error in the accuracy of the energy balance this peak was disregarded. On this basis the maximum error band for Figure 3.2-82 is approximately -50000/+100000 Btu, which corresponds a maximum error of 10 percent of the total fluid energy ejected from the system. The error at the end of the event is approximately 8 percent of the total ejected fluid energy.

Other Observations

Pressure Decay

Figure 3.2-3 shows the primary system pressure during the S00303 test. Throughout this event, the pressure was controlled by the saturation pressure of the hottest fluid volume in the primary system. At the initiation of the break, the controlling fluid volume was in the pressurizer and surge line; however, within the first [ ]^{a,b,c} (after the initial blowdown phase) this shifted to the power channel upper plenum. Figure 3.2-2 shows that the temperature of the upper plenum was equal to the saturation temperature corresponding to the primary system pressure measured in the upper head during the natural circulation phase and into the ADS phase. The pressure stabilized at the saturation pressure for the upper plenum and then continued a slow pressure decay responding to the cooling caused by the CMTs injection. Figure 3.2-3 shows an increase in the pressure decay rate occurred at approximately [ ]^{a,b,c}, when the CMTs transitioned from natural circulation injection to draindown injection, which essentially doubled the injection rate of cold water into the DVI. The higher injection rate resulted in a more rapid temperature drop in the upper plenum (fuel exit in Figure 3.2-2), which was reflected in a more rapid pressure decay. With the actuation of ADS-1 at approximately [ ]^{a,b,c}, the pressure dropped rapidly due to the increase rate of mass ejected from the system (Figure 3.2-68), and the increased flow of cold water being injected into the annular downcomer and flowing through the core. This continued to reduce the power channel inlet plenum temperature, and subcool the heated rod bundle due to the higher flow. Since the power channel outlet plenum became subcooled at approximately [ ]^{a,b,c}, the hottest fluid in the system was in the pressurizer, the cold legs, and the CMTs, and the pressure was partially supported by the flashing of the fluid in one or several of these locations. When the accumulator discharge ended (approximately [ ]^{a,b,c}), the lower-plenum temperature increased due to the metal heat, and the upper-plenum temperature increased to the saturation temperature and again took control of the system pressure for the rest of the event. It is noted here that, at the end of the accumulator injection, a large amount of nitrogen from the accumulators was injected into the primary system. This injection had very little immediate effect on the primary system, but as will be discussed in Section 4.0, affected the upper plenum the PRHR HX, and the CMT at later stages of the event.

The actuation of ADS-4 (at approximately [ ]^{a,b,c}) lowered the system pressure sufficiently to allow gravity injection flow from the IRWST into the DVI nozzles. This flow was sufficiently high

to subcool the primary system, ending core boiling and partially collapsing the steam bubble in the upper plenum and bringing the system to a near atmospheric internal pressure.

Ejection Flows

Figure 3.2-68 shows the individual mass flows leaving the system via the break and the ADS. The individual flow rates are given in Figures 3.2-69, 3.2-70, and 3.2-71. The break and ADS-4 flows are assumed to consist of saturated water. For ADS-1, ADS-2, and ADS-3, it was assumed that the flow consisted of saturated water if the void fraction measured in the top of the pressurizer (Figure 3.2-73) was less than [ ]^{a,b,c}; and it was assumed that the flow consisted of saturated steam if it was greater than [ ]^{a,b,c}.

The total mass flow rate leaving the system was reasonably steady for S00303 (as seen in Figure 3.2-79). Figure 3.2-80 shows that the energy of the fluid ejection was steady, at an average rate of [ ]^{a,b,c} for the first [ ]^{a,b,c}, and then decreased to 125 Btu/sec. for the rest of the event. The change in energy ejection rate was related to actuation of ADS-4, which caused the pressurizer to drain, converted the ADS-1, ADS-2, and ADS-3 flow to steam with a low mass flow rate, and simultaneously started fluid ejection through ADS-4.

ADS-1 opened at approximately [ ]^{a,b,c}, followed by ADS-2 and ADS-3 within the next [ ]^{a,b,c}. The break flow changed from saturated water to steam; however, due to the low mass flow rate (Figure 3.2-68), the energy removal by the break flow (Figure 3.2-80) became very low. The energy leaving the system through ADS-1, ADS-2, and ADS-3 was greater than that through the break and ADS-4, and it provided an effective means of removing the stored metal energy from the system (as seen in Figure 3.2-81).

The mass leaving the system via ADS-1, ADS-2, and ADS-3 during the next 1000 seconds was greater than the break flow, and also the energy loss through the ADS 1-3 exceeded the energy loss by the break flow (Figure 3.2-80).

ADS-4 opened at approximately [ ]^{a,b,c}, and the ADS-1, ADS-2, and ADS-3 flows converted to steam with a very low mass flow rate and energy loss rate. The ADS-4 flow stabilized at a rate that matched the injection rate from the IRWST (Figure 3.2-79), and the energy removal via ADS-4 was comparable to the heated rod power (Figure 3.2-81).

Comparison to the Small Break LOCA PIRT Phenomena

Table 1-1 shows the identified and ranked small-break LOCA (SBLOCA) phenomena that are of importance for the AP600 SB LOCA. SPES-2 test S00303 provides data that will address the phenomena marked high and medium such that computer code validation using this data will cover the phenomena of importance for the AP600.

Examining the blowdown period, the break and ADS flows were measured as well as the decay power and mixture level in the different components. The effects of flashing were inferred from the levels and the flows in the system as SPES depressurized. The stored energy in the vessel and other components was calculated as part of the test energy balance. The natural circulation behavior in the system and CMTs was measured. The pressurizer flow regime was not directly measured, but the mixture level in this line was measured. The steam generator heat transfer was calculated from the measurements, as well as the PRHR heat transfer.

During the natural circulation period, the phenomena ranked high and medium were also addressed in the SPES facility, with the exception of the hot-leg pattern. The particular phenomena is indirectly addressed in the SPES facility, with the exception of the hot-leg flow pattern. This particular phenomena is indirectly addressed by the mixture level, which is measured in the hot leg, as well as the mixture levels, which are measured in the steam generator tubes and plena. As these components drain, the hot leg remains full. Once these components have drained, the core steaming rate and the mixture levels measured in the hot leg can be used to infer the flow regime. The break flow, decay power, vessel, and component mixture levels are all measured. The CMT flow and temperature behavior and the PRHR heat transfer are also measured. The mixture levels and energy storage in the components, both metal and fluid, are also measured, as well as the injection flows and pressure drops.

For the ADS period, the ADS flows are measured for all flow paths. The CMT and accumulator flows and draining behavior are measured, as well as the mixture levels in all components. Again, the hot-leg flow pattern is not directly measured; but it can be inferred by the mixture level, the core steaming rates, and the ADS-4 behavior.

The IRWST period is the conclusion of the SBLOCA transient. Once stable IRWST injection has occurred, the transient transitions into long-term cooling. The key phenomena for this period (as identified in Table 1-1) include the IRWST injection flow, the hot-leg behavior, the ADS-4 flow rate (which is now the main vent path for the system) and the mixture levels in the simulated reactor vessel. These phenomena are all captured in the SPES test facility.

The PIRT table indicates the key thermal-hydraulic phenomena that are of importance for understanding the AP600 SBLOCA. The phenomena identified in this table have been captured in the SPES-2 experiments such that the data and analysis can be used to assess the performance of the safety analysis computer codes used to model the AP600 passive safety systems.

TABLE 3.2-1
COMPONENT MASS VARIATIONS IN TEST S00303

	Start Fault	End Blowdown	CMT to Draindown	ADS-1 Starts	First Acc. Empty	ADS-4 Starts	IRWST Starts	End of Transient
Event time								
Power channel								
PC: core								
PC: downcomers								
PC: upper plenum								
Hot leg-A								
Hot leg-B								
Cold leg-A								
Cold leg-B								
SG primary-A								
SG primary-B								
Pressurizer + SL								
CMT-A								
CMT-B								
Accumulator-A								
Accumulator-B								
IRWST								

a,b,c

TEST ANALYSIS STANDARD PLOT PACKAGE Figures 3.2-1 Through 3.2-83				
Fig. No.	**Component**	**Variables**	**Units**	**Description**
3.2-1	Power channel	CORE-POW	kW	Core power
3.2-2	Power channel	TSAT, TAVTDC, TFOUT	°F	Core inlet/outlet temperature, saturation temperature
3.2-3	Pressurizer	PPZRTOP	psia	System pressure
3.2-4	Steam generator	PSGAS, PSGBS	psia	Primary and secondary pressure in steam generators
3.2-5	Steam generator	TAVGSGA, TAVGSGB	°F	Average fluid temperature in steam generators
3.2-6	CMT	MCMTA, MCMTB	lbm	Fluid mass in CMTs
3.2-7	CMT	CLEVELA, CLEVELB	ft.	Collapsed liquid level in CMTs
3.2-8	CMT	MOUTCMTA, MOUTCMTB, MINCMTA, MINCMTB	lbm	Integrated mass in/out of CMTs
3.2-9	CMT	FLOWOUTA, FLOWOUTB	lbm/sec.	Measured flow out of CMTs
3.2-10	CMT	FLOWINA, FLOWINB	lbm/sec.	Calculated flow into CMTs
3.2-11	CMT	BLFRACA, BLFRACB	Fraction	Fractional differential pressure in cold leg-CMT balance lines
3.2-12	CMT	UTOT-A, UTOT-B	Btu	Fluid energy in CMTs
3.2-13	IRWST/PRHR	MIRWST	lbm	Mass of fluid in IRWST

TEST ANALYSIS STANDARD PLOT PACKAGE Figures 3.2-1 Through 3.2-83 (Cont.)				
Fig. No.	**Component**	**Variables**	**Units**	**Description**
3.2-14	IRWST/PRHR	LIRWST	ft.	Collapsed liquid level in IRWST
3.2-15	IRWST/PRHR	FIRWST	lbm/sec.	Measured discharge flow from IRWST
3.2-16	IRWST/PRHR	MOUTDVIA, MOUTDVIB	lbm	Integrated mass out DVI lines
3.2-17	IRWST/PRHR	INT-QCAL, INT-QTUB, U-UO	Btu	Comparison of energy transfer from PRHR tubes to IRWST
3.2-18	IRWST/PRHR	Q-HOR-1, Q-VERT, Q-HOR-2, QTUBEXT	Btu/sec.	Breakdown of heat transfer from different sections of PRHR tube
3.2-19	IRWST/PRHR	Q-CALIM	Btu/sec.	PRHR/IRWST heat transfer calculated on tube side
3.2-20	IRWST/PRHR	FLOWTUBE	lbm/sec.	Measured outlet flow from PRHR tube
3.2-21	IRWST/PRHR	VOID-FRC		Calculated PRHR inlet void fraction
3.2-22	Accumulator	MACCA, MACCB	lbm	Mass of fluid in accumulators
3.2-23	Accumulator	LACCA, LACCB	ft.	Collapsed liquid level in accumulators
3.2-24	Accumulator	MEASFLWA, MEASFLWB	lbm/sec.	Measured flow from accumulators
3.2-25	Accumulator	MOUTACCA, MOUTACCB	lbm	Integrated mass out of accumulators
3.2-26	Accumulator	U-TOT-A, U-TOT-B	Btu	Energy of fluid in accumulators

TEST ANALYSIS STANDARD PLOT PACKAGE Figures 3.2-1 Through 3.2-83 (Cont.)				
Fig. No.	**Component**	**Variables**	**Units**	**Description**
3.2-27	Accumulator	AIRMASSA, AIRMASSB	lbm	Mass of air exiting accumulators
3.2-28	Steam generator	MSGAP, MSGBP	lbm	Mass of fluid in steam generators - primary side
3.2-29	Steam generator	LSGAH, LSGAC, LSGBH, LSGBC	ft.	Collapsed liquid levels in steam generators - primary side - hot and cold sides of U-tubes
3.2-30	Steam generator	MSGAH, MSGAC, MSGBH, MSBGC	lbm	Mass of fluid in steam generators - primary side - hot and cold sides of U-tubes
3.2-31	Steam generator	LSGSA, LSGSB	ft.	Collapsed liquid levels in steam generators - secondary side
3.2-32	Steam generator	Q-TRNF-A, Q-TRNF-B, Q-CALIM	Btu/sec.	Heat transfer in steam generators heat transfer in PRHR
3.2-33	Steam generator	PRESS-PA, PRESS-PB, PREF-A, PREF-B	psia	Primary and secondary pressure in steam generators
3.2-34	Pressurizer	MPZR	lbm	Fluid mass in pressurizer
3.2-35	Pressurizer	LPZR	ft.	Collapsed liquid level in pressurizer
3.2-36	Pressurizer	MSL	lbm	Fluid mass in surge line
3.2-37	Pressurizer	LSL	ft.	Collapsed liquid level in surge line
3.2-38	Pressurizer	UPZR	Btu	Fluid energy in pressurizer
3.2-39	Power channel	MPCHN	lbm	Total fluid mass in power channel

TEST ANALYSIS STANDARD PLOT PACKAGE Figures 3.2-1 Through 3.2-83 (Cont.)				
Fig. No.	**Component**	**Variables**	**Units**	**Description**
3.2-40	Power channel	L2PHASE, LDVI, LHL, LCL	ft.	Two-phase liquid level in power channel vs. DVI, hot-leg, and cold-leg elevations
3.2-41	Power channel	MANDC	lbm	Fluid mass in annular downcomer
3.2-42	Power channel	LANDC, LDVI, LHL, LCL	ft.	Collapsed liquid level in annular downcomer vs. DVI, hot-leg, and cold-leg elevations
3.2-43	Power channel	MTDC	lbm	Fluid mass in tubular downcomer
3.2-44	Power channel	LTDC, LBOF, LTOF	ft.	Collapsed liquid level in tubular downcomer vs. top of active fuel and bottom of active fuel levels
3.2-45	Power channel	MLOWP	lbm	Fluid mass in lower plenum
3.2-46	Power channel	LLOWP	ft.	Collapsed liquid level in lower plenum
3.2-47	Power channel	MCORE	lbm	Fluid mass in core region
3.2-48	Power channel	LCORE	ft.	Collapsed liquid level in core
3.2-49	Power channel	MFOUT	lbm	Fluid mass in core outlet region
3.2-50	Power channel	LFOUT	ft.	Collapsed liquid level in core outlet region
3.2-51	Power channel	MUPPL	lbm	Fluid mass in the lower portion of the upper plenum
3.2-52	Power channel	LUPPL	ft.	Collapsed liquid level in the lower portion of the upper plenum

TEST ANALYSIS STANDARD PLOT PACKAGE Figures 3.2-1 Through 3.2-83 (Cont.)				
Fig. No.	**Component**	**Variables**	**Units**	**Description**
3.2-53	Power channel	MUPPU	lbm	Fluid mass in the upper portion of the upper plenum
3.2-54	Power channel	LUPPU	ft.	Collapsed liquid level in the upper portion of the upper plenum
3.2-55	Power channel	MHEAD	lbm	Fluid mass in the upper head
3.2-56	Power channel	LHEAD	ft.	Collapsed liquid level in the upper head
3.2-57	Power channel	UPC	Btu	Total fluid energy in power channel
3.2-58	Power channel	Q-FLUX	Btu/sec.-ft.^{2}	Average heat flux on the heated rods
3.2-59	Power channel	STM-RATE	lbm/sec.	Core steam generation rate
3.2-60	Power channel	FLOWCOR	lbm/sec.	Calculated core flow
3.2-61	Power channel	VOIDOUT		Void fraction at core exit
3.2-62	Power channel	TMAX, TSAT, TMAX-TSAT	°F	Maximum clad temperature, saturation temperature and delta
3.2-63	Hot leg	MHLA, MHLB	lbm	Fluid mass in hot legs
3.2-64	Hot leg	FLA, FLB	Fraction	Fractional collapsed liquid level in hot legs
3.2-65	Cold leg	MCLA, MCLB	lbm	Fluid mass in cold legs
3.2-66	Cold leg	LCLA1, LCLA2, LPSA	ft.	Collapsed liquid levels in cold leg-A
3.2-67	Cold leg	LCLB1, LCLB2, LPSB	ft.	Collapsed liquid levels in cold leg-B

TEST ANALYSIS STANDARD PLOT PACKAGE Figures 3.2-1 Through 3.2-83 (Cont.)				
Fig. No.	**Component**	**Variables**	**Units**	**Description**
3.2-68	Total system mass	MADS1-3, MADS4, BRKMASS	lbm	Catch tank mass for ADS-1, ADS-2, ADS-3, ADS-4, and break
3.2-69	Total system mass	DMADS1-3	lbm/sec.	Calculated flow out ADS-1, ADS-2, ADS-3
3.2-70	Total system mass	DMADS4	lbm/sec.	Calculated flow out ADS-4
3.2-71	Total system mass	BRKFLOW	lbm/sec.	Calculated flow out break
3.2-72	Total system energy	UADS123, UADS4, UBREAK	Btu	Integrated fluid energy for ADS-1, ADS-2, ADS-3, ADS-4, and the break
3.2-73	Total system energy	VOID		Calculated void fraction for ADS-1, ADS-2, and ADS-3
3.2-74	Total system mass	MTOTAL, MTOT0	lbm	Total system fluid mass vs. initial fluid mass
3.2-75	Total system mass	ERRLOP	lbm	Error in the mass balance (using measured and calculated flows)
3.2-76	Total system mass	ERRLOP1	lbm	Error in the mass balance (using fluid inventory)
3.2-77	Total system mass	MPCLTOT, MPCLO	lbm	Total fluid mass in power channel and loops vs. initial fluid mass
3.2-78	Total system mass	MACOUT, MCMOUT, MIROUT	lbm	Total integrated mass discharged from accumulators, CMTs, and IRWST
3.2-79	Total system mass	MSOURCE, MSINK, MSOURIN	lbm	Total source inventory, total mass ejected from primary system, and total mass injected to primary system
3.2-80	Total system energy	UADS123, UBREAK, UADS4, UCATCH	Btu	Integrated fluid energy exiting via ADS-1, ADS-2, ADS-3, ADS-4, and the break, and the sum

TEST ANALYSIS STANDARD PLOT PACKAGE Figures 3.2-1 Through 3.2-83 (Cont.)				
Fig. No.	**Component**	**Variables**	**Units**	**Description**
3.2-81	Total system energy	USURR, UCATCH, UQIN, UFLD-UO, UMTL-UO, USG	Btu	Overall energy balance including integrated rod power, steam generator power, and heat loss to the surroundings, energy exiting via ADS and break, energy input via nonsafety systems, and change in primary system fluid and metal energy relative to start of test
3.2-82	Total system energy	UERROR, ERROR-%	Btu, %	Error in overall energy balance relative to initial fluid and metal energy
3.2-83	System pressure	- -	psia	Test event phases and system pressure

The figures listed are proprietary and, therefore,
are not available in the Class 3 version of this report.

These figures are available in the Class 2 version of this report.

3.3 Analysis of the Two-Inch Cold-Leg Break without Nonsafety Systems (S01703)—Repeat of S00303

Matrix test S01703 was performed to determine the repeatability of the SPES-2 system responses for identical events in the SPES-2 facility by performing a repeat of test S00303. Test S00303 was the first matrix test to be performed, and test S01703 was the last in the series of tests.

Matrix test S01703 simulated a 2-in. break in the bottom of cold leg-B2. The event began with the initiation of the break in cold leg-B2, which was the cold leg with the CMT-B pressure balance line connection. The break location was on the power channel side of the cold leg from the core makeup tank (CMT) balance line connection. This test was performed without any nonsafety systems' pumps operating. That is, it was performed without the chemical and volume control system (CVCS) makeup pumps, steam generator startup feedwater (SFW) pumps, and normal residual heat removal system (NRHR) pumps.

3.3.1 Summary of Test Observations

Since this was a repeat of a test which was described in Section 3.2, only notable differences in the system response and behavior are discussed for S01703.

When comparing the test data from test S01703 with test S00303, there are few notable differences. Most of those which are apparent can be explained as minor differences in initial conditions for the test and as a difference in the amount of mass discharged from the break.

Figure 3.3-83 shows the plant primary system pressure during S01703 test (as measured at the top of the pressurizer), with selected component actuations and plant responses shown in relation to the primary system pressure. Comparison of Figure 3.3-83 with Figure 3.2-83 shows that the primary system pressure for the two tests are essentially identical.

The two tests are near identical in terms of absolute pressure and timing of the system responses. A slightly earlier reactor coolant pump (RCP) trip for S01703 caused a slight shift in the pressure recovery that followed the pump trip. For the start of the pressure decay phase (PDP), the pressure and the pressure oscillations were essentially identical for the two events.

During the first part of the ADS phase, the S01703 test maintained a slightly higher temperature for the upper plenum than S00303, which caused the system pressure for S01703 to be slightly higher. The temperature in the lower plenum was approximately [ ]^{a,b,c} cooler for test S01703 than for S00303 during and after the accumulator injection. This was apparently due to a [ ]^{a,b,c} lower water temperature for the accumulators in test S01703. The accumulator injection ended at nearly identical times for both tests. ADS-4 occurred approximately [ ]^{a,b,c} later for S01703, and the subcooling effect of the IRWST injection flow on the upper-plenum temperature occurred [ ]^{a,b,c} later than for test S00303.

The annular downcomer drained approximately [ ]^{a,b,c} later for test S01703 than S00303, and the refill was started at identical times. The minimum level in the tubular downcomer during the IRWST injection phase reached [ ]^{a,b,c} for S01703, and [ ]^{a,b,c} for S00303. The minimum collapsed levels in the heater bundle after the accumulator injection were essentially identical (core void fraction calculated to be [ ]^{a,b,c} for test S00303 and [ ]^{a,b,c} for test S01703). For each test, the minimum level in the tubular downcomer and the maximum void fraction in the heater bundle occurred at the same time. For S01703, the minimum level occurred approximately [ ]^{a,b,c} later than for S00303.

3.3.2 Analysis of the S01703 Test Data

The analysis of the SPES-2 test was performed using the SPESAN computer code. The code performs a detailed accounting of the coolant inventory in all parts of the system from the start to the end of the test. Also, the internal energy of all components and parts of the facility, including the energy losses from the break and ADS flows, are calculated throughout the test. It is noted that the mass balance and the energy transfer calculations are performed in much greater detail than was performed in WCAP-14304, *Final Data Report.*[1] The results of the test data analysis are presented in Figures 3.3-1 through 3.3-82. Since this test is a repeat of S00303, and the test results are very similar, the discussion of the test data analysis presented in the figures will point out differences between S01703 and S00303 analysis results. Mass balance snapshots for all the major primary system components, at various points of interest throughout the transient, are presented in Table 3.3-1.

Mass Balance

Overall Mass Balance

The uncertainty in the overall mass balance is an indication of the overall quality of the test. The total water inventory is tracked from the start until the end of the test. Figures 3.3-74, 3.3-75, and 3.3-76 show the overall mass balance and the error (uncertainty) in mass balance for S01703.

The overall mass balance for S01703 in Figure 3.3-74 shows a small variation of water inventory during the test, resulting from the overall uncertainty in the instrumentation and the assumptions of the mass balance model used to determine the total water inventory. The average total inventory during the test was indicated to be approximately the same as the initial system mass, and a final mass was indicated to be approximately 15 lbm above the initial mass. Figure 3.3-75 shows the difference between the total mass during the test and the initial mass (mass balance error) when the inventory was calculated by integrating the flows. The mass balance error based on flow measurements (Figure 3.3-75) varied from +50 lbm to -100 lbm, while the final error was -40 lbm. The mass balance error based on the weight and level measurements (Figure 3.3-76) resulted in an uncertainty band of +40 lbm to -60 lbm, and a final error of +10 lbm.

Water Inventory for the Power Channel and the Loop

Maintenance of the coolant coverage of the heater bundle is the most critical issue for the power channel. The heater bundle coverage during a loss-of-coolant accident (LOCA) event often consists of two-phase fluid, which can have a very high void fraction. Figure 3.3-40 shows the true level of two-phase fluid in the power channel as measured from the elevation of the top of the core (TAF). Since this represents the true two-phase level, it will be different than the collapsed liquid level in the heater bundle.

For S01703, the two-phase level in the upper plenum responded essentially identical to S00303. The minimum level decreased to approximately [ ]^{a,b,c} below the hot-leg elevation at [ ]^{a,b,c}. This occurred at the time of minimum power channel water inventory, before the IRWST injection started (at [ ]^{a,b,c}) to refill the power channel.

The level on the cold side of the power channel is shown in Figures 3.3-42 (annular downcomer) and 3.3-44 (tubular downcomer). The annular downcomer was full until approximately [ ]^{a,b,c} into the test. At that time, the level starts to decrease, but it is maintained above the elevation of the hot leg until after the end of the accumulator injection (approximately [ ]^{a,b,c}).

The water inventory in the power channel (Figure 3.3-39) had two minima; before the accumulator injection, and before the IRWST injection. The second minimum was more severe showing a total power channel inventory of approximately [ ]^{a,b,c} of starting inventory) at that time. The total primary system inventory (power channel, pressurizer and loops), shown in Figure 3.3-77, reaches approximately [ ]^{a,b,c} of starting inventory) for this minimum.

Water Injection/Ejection

The injected fluid mass from all injection sources is shown in Figure 3.3-78. Figure 3.3-79 shows the total source inventory and the injected and ejected masses during the test. Starting with a total of approximately [ ]^{a,b,c} source inventory, only approximately [ ]^{a,b,c} of available source water) was used by the end of the test.

Energy Balance

PRHR Heat Transfer

Figure 3.3-18 shows the calculated heat transfer from the PRHR external tube surface to the water in the IRWST by the three tube section of the heat exchanger. The top part of the PRHR heat exchanger performed as a condenser, where the steam of the two-phase fluid extracted from hot leg-A was condensed. The top horizontal tube transfers the greatest amount of heat. The condensation process on the inside effectively heated this tube wall temperature above the boiling point for the water in the IRWST, resulting in very effective nucleate boiling heat transfer from the outside surface. The vertical and the bottom horizontal sections of the heat exchanger for the most part subcooled the fluid with a

less effective free convection heat transfer to the IRWST water, and contributed less to the overall heat transfer of the PRHR.

Comparing the results of the heat transfer calculated for the tube outside surface between S00303 and S01703, shows an approximately [ ]^{a,b,c} higher value for S01703. There are two differences in the test data for the two tests. The measured tube temperature for S01703 is significantly higher than for S00303, and the starting temperature for the IRWST water was significantly lower. This apparent increased thermal gradient may be part of the reason for the higher calculated heat transfer. However, since the PRHR calculated heat transfer compared closely with the internal energy increase in the IRWST, these values are believed correct. The heat transfer calculated for the outside tube surface is in error, probably due to a problem with the thermocouple reading for the tube external surfaces.

Steam Generator Heat Transfer

Figure 3.3-32 shows the heat transfer in the steam generators for S01703, and Figure 3.3-33 shows the pressures on the primary side and the secondary side of the steam generators. Also shown in Figure 3.3-32 is the PRHR heat transfer which removed heat from the system after the steam generators heat transfer had ended.

Overall Energy Balance

Figure 3.3-81 shows all the components in the energy balance for the system. These are essentially identical to those calculated for S00303.

Figure 3.3-82 shows the accumulated energy balance error during the S01703 event, which is essentially identical to that calculated for S00303.

Other Observations

Pressure Decay

Figure 3.3-3 shows the primary system pressure during the S01703 test, which was essentially identical to the pressure during S00303.

Ejection Flows

Figure 3.3-68 shows the individual mass flows leaving the system via the break and the ADS. The most significant difference between S01703 and S00303 was the mass loss through the break. For S01703, the mass loss was approximately [ ]^{a,b,c} (at [ ]^{a,b,c}), as compared with 800 lbm for S00303. The ADS fluid losses were similar for the two tests.

TABLE 3.3-1
COMPONENT MASS VARIATIONS FOR TEST S01703

	Start Fault	End Blowdown	CMT to Draindown	ADS-1 Starts	First Acc. Empty	ADS-4 Starts	IRWST Starts	End of Transient
Event time								
Power channel								
PC: core								
PC: downcomers								
PC: upper plenum								
Hot leg-A								
Hot leg-B								
Cold leg-A								
Cold leg-B								
SG primary-A								
SG primary-B								
Pressurizer + SL								
CMT-A								
CMT-B								
Accumulator-A								
Accumulator-B								
IRWST								

TEST ANALYSIS STANDARD PLOT PACKAGE Figures 3.3-1 Through 3.3-83				
Fig. No.	**Component**	**Variables**	**Units**	**Description**
3.3-1	Power channel	CORE-POW	kW	Core power
3.3-2	Power channel	TSAT, TAVTDC, TFOUT	°F	Core inlet/outlet temperature, saturation temperature
3.3-3	Pressurizer	PPZRTOP	psia	System pressure
3.3-4	Steam generator	PSGAS, PSGBS	psia	Primary and secondary pressure in steam generators
3.3-5	Steam generator	TAVGSGA, TAVGSGB	°F	Average fluid temperature in steam generators
3.3-6	CMT	MCMTA, MCMTB	lbm	Fluid mass in CMTs
3.3-7	CMT	CLEVELA, CLEVELB	ft.	Collapsed liquid level in CMTs
3.3-8	CMT	MOUTCMTA, MOUTCMTB, MINCMTA, MINCMTB	lbm	Integrated mass in/out of CMTs
3.3-9	CMT	FLOWOUTA, FLOWOUTB	lbm/sec.	Measured flow out of CMTs
3.3-10	CMT	FLOWINA, FLOWINB	lbm/sec.	Calculated flow into CMTs
3.3-11	CMT	BLFRACA, BLFRACB	Fraction	Fractional differential pressure in cold leg-CMT balance lines
3.3-12	CMT	UTOT-A, UTOT-B	Btu	Fluid energy in CMTs
3.3-13	IRWST/PRHR	MIRWST	lbm	Mass of fluid in IRWST
3.3-14	IRWST/PRHR	LIRWST	ft.	Collapsed liquid level in IRWST
3.3-15	IRWST/PRHR	FIRWST	lbm/sec.	Measured discharge flow from IRWST

TEST ANALYSIS STANDARD PLOT PACKAGE Figures 3.3-1 Through 3.3-83 (Cont.)				
Fig. No.	**Component**	**Variables**	**Units**	**Description**
3.3-16	IRWST/PRHR	MOUTDVIA, MOUTDVIB	lbm	Integrated mass out of DVI lines
3.3-17	IRWST/PRHR	INT-QCAL, INT-QTUB, U-UO	Btu	Comparison of energy transfer from PRHR tubes to IRWST
3.3-18	IRWST/PRHR	Q-HOR-1, Q-VERT, Q-HOR-2, QTUBEXT	Btu/sec.	Breakdown of heat transfer from different sections of PRHR tube
3.3-19	IRWST/PRHR	Q-CALIM	Btu/sec.	PRHR/IRWST heat transfer calculated on tube side
3.3-20	IRWST/PRHR	FLOWTUBE	lbm/sec.	Measured outlet flow from PRHR tube
3.3-21	IRWST/PRHR	VOID-FRC		Calculated PRHR inlet void fraction
3.3-22	Accumulator	MACCA, MACCB	lbm	Mass of fluid in accumulators
3.3-23	Accumulator	LACCA, LACCB	ft.	Collapsed liquid level in accumulators
3.3-24	Accumulator	MEASFLWA, MEASFLWB	lbm/sec.	Measured flow from accumulators
3.3-25	Accumulator	MOUTACCA, MOUTACCB	lbm	Integrated mass out of accumulators
3.3-26	Accumulator	U-TOT-A, U-TOT-B	Btu	Energy of fluid in accumulators
3.3-27	Accumulator	AIRMASSA, AIRMASSB	lbm	Mass of air exiting accumulators
3.3-28	Steam generator	MSGAP, SGBP	lbm	Mass of fluid in steam generators - primary side
3.3-29	Steam generator	LSGAH, LSGAC, LSGBH, LSGBC	ft.	Collapsed liquid levels in steam generators - primary side - hot and cold sides of U-tubes

TEST ANALYSIS STANDARD PLOT PACKAGE
Figures 3.3-1 Through 3.3-83 (Cont.)

Fig. No.	Component	Variables	Units	Description
3.3-30	Steam generator	MSGAH, MSGAC, MSGBH, MSBGC	lbm	Mass of fluid in steam generators - primary side - hot and cold sides of U-tubes
3.3-31	Steam generator	LSGSA, LSGSB	ft.	Collapsed liquid levels in steam generators - secondary side
3.3-32	Steam generator	Q-TRNF-A, Q-TRNF-B, Q-CALIM	Btu/sec.	Heat transfer in steam generators heat transfer in PRHR
3.3-33	Steam generator	PRESS-PA, PRESS-PB, PREF-A, PREF-B	psia	Primary and secondary pressure in steam generators
3.3-34	Pressurizer	MPZR	lbm	Fluid mass in pressurizer
3.3-35	Pressurizer	LPZR	ft.	Collapsed liquid level in pressurizer
3.3-36	Pressurizer	MSL	lbm	Fluid mass in surge line
3.3-37	Pressurizer	LSL	ft.	Collapsed liquid level in surge line
3.3-38	Pressurizer	UPZR	Btu	Fluid energy in pressurizer
3.3-39	Power channel	MPCHN	lbm	Total fluid mass in power channel
3.3-40	Power channel	L2PHASE, LDVI, LHL, LCL	ft.	Two-phase liquid level in power channel vs. DVI, hot-leg, and cold-leg elevations
3.3-41	Power channel	MANDC	lbm	Fluid mass in annular downcomer
3.3-42	Power channel	LANDC, LDVI, LHL, LCL	ft.	Collapsed liquid level in annular downcomer vs. DVI, hot-leg, and cold-leg elevations

TEST ANALYSIS STANDARD PLOT PACKAGE Figures 3.3-1 Through 3.3-83 (Cont.)				
Fig. No.	**Component**	**Variables**	**Units**	**Description**
3.3-43	Power channel	MTDC	lbm	Fluid mass in tubular downcomer
3.3-44	Power channel	LTDC, LBOF, LTOF	ft.	Collapsed liquid level in tubular downcomer vs. top of active fuel and bottom of active fuel levels
3.3-45	Power channel	MLOWP	lbm	Fluid mass in lower plenum
3.3-46	Power channel	LLOWP	ft.	Collapsed liquid level in lower plenum
3.3-47	Power channel	MCORE	lbm	Fluid mass in core region
3.3-48	Power channel	LCORE	ft.	Collapsed liquid level in core
3.3-49	Power channel	MFOUT	lbm	Fluid mass in core outlet region
3.3-50	Power channel	LFOUT	ft.	Collapsed liquid level in core outlet region
3.3-51	Power channel	MUPPL	lbm	Fluid mass in the lower portion of the upper plenum
3.3-52	Power channel	LUPPL	ft.	Collapsed liquid level in the lower portion of the upper plenum
3.3-53	Power channel	MUPPU	lbm	Fluid mass in the upper portion of the upper plenum
3.3-54	Power channel	LUPPU	ft.	Collapsed liquid level in the upper portion of the upper plenum
3.3-55	Power channel	MHEAD	lbm	Fluid mass in the upper head
3.3-56	Power channel	LHEAD	ft.	Collapsed liquid level in the upper head

TEST ANALYSIS STANDARD PLOT PACKAGE
Figures 3.3-1 Through 3.3-83 (Cont.)

Fig. No.	Component	Variables	Units	Description
3.3-57	Power channel	UPC	Btu	Total fluid energy in power channel
3.3-58	Power channel	Q-FLUX	Btu/sec.-ft.^{2}	Average heat flux on the heated rods
3.3-59	Power channel	STM-RATE	lbm/sec.	Core steam generation rate
3.3-60	Power channel	FLOWCOR	lbm/sec.	Calculated core flow
3.3-61	Power channel	VOIDOUT		Void fraction at core exit
3.3-62	Power channel	TMAX, TSAT, TMAX-TSAT	°F	Maximum clad temperature, saturation temperature and delta
3.3-63	Hot leg	MHLA, MHLB	lbm	Fluid mass in hot legs
3.3-64	Hot leg	FLA, FLB	Fraction	Fractional collapsed liquid level in hot legs
3.3-65	Cold leg	MCLA, MCLB	lbm	Fluid mass in cold legs
3.3-66	Cold leg	LCLA1, LCLA2, LPSA	ft.	Collapsed liquid levels in cold leg-A
3.3-67	Cold leg	LCLB1, LCLB2, LPSB	ft.	Collapsed liquid levels in cold leg-B
3.3-68	Total system mass	MADS1-3, MADS4, BRKMASS	lbm	Catch tank mass for ADS-1, ADS-2, ADS-3, ADS-4, and break
3.3-69	Total system mass	DMADS1-3	lbm/sec.	Calculated flow out ADS-1, ADS-2, and ADS-3
3.3-70	Total system mass	DMADS4	lbm/sec.	Calculated flow out ADS-4
3.3-71	Total system mass	BRKFLOW	lbm/sec.	Calculated flow out break
3.3-72	Total system energy	UADS123, UADS4, UBREAK	Btu	Integrated fluid energy for ADS-1, ADS-2, ADS-3, ADS-4, and the break

TEST ANALYSIS STANDARD PLOT PACKAGE
Figures 3.3-1 Through 3.3-83 (Cont.)

Fig. No.	Component	Variables	Units	Description
3.3-73	Total system energy	VOID		Calculated void fraction for ADS-1, ADS-2, and ADS-3
3.3-74	Total system mass	MTOTAL, MTOT0	lbm	Total system fluid mass vs. initial fluid mass
3.3-75	Total system mass	ERRLOP	lbm	Error in the mass balance (using measured and calculated flows)
3.3-76	Total system mass	ERRLOP1	lbm	Error in the mass balance (using fluid inventory)
3.3-77	Total system mass	MPCLTOT, MPCLO	lbm	Total fluid mass in power channel and loops vs. initial fluid mass
3.3-78	Total system mass	MACOUT, MCMOUT, MIROUT	lbm	Total integrated mass discharged from accumulators, CMTs, and IRWST
3.3-79	Total system mass	MSOURCE, MSINK, MSOURIN	lbm	Total source inventory, total mass ejected from primary system, and total mass injected to primary system
3.3-80	Total system energy	UADS123, UBREAK, UADS4, UCATCH	Btu	Integrated fluid energy exiting via ADS-1, ADS-2, ADS-3, ADS-4, and the break, and the sum
3.3-81	Total system energy	USURR, UCATCH, UQIN, UFLD-UO, UMTL-UO, USG	Btu	Overall energy balance including integrated rod power, steam generator power, and heat loss to the surroundings, energy exiting via ads and break, energy input via nonsafety systems, and change in primary system fluid and metal energy relative to start of test
3.3-82	Total system energy	UERROR, ERROR-%	Btu, %	Error in overall energy balance, relative to initial fluid and metal energy
3.3-83	System pressure	---	psia	Test event phases and system pressure

The figures listed are proprietary and, therefore,
are not available in the Class 3 version of this report.

These figures are available in the Class 2 version of this report.

3.4 Analysis of the Two-Inch Cold-Leg Break with Nonsafety Systems (S00504)

This matrix test simulated a 2-in. break in the bottom of cold leg-B2. The event began with the initiation of the break in cold leg-B2, which is the cold leg with the CMT-B pressure balance line connection. The break location was on the power-channel side of the cold leg from the core makeup tank (CMT) balance line connection. This test was performed with nonsafety systems' pumps operating. That is, it was performed without the chemical and volume control system (CVCS) makeup pumps, steam generator startup feedwater (SFW) pumps, and normal residual heat removal system (NRHR) pumps.

3.4.1 Summary of Test Observations

Figure 3.4-83 shows plant primary system pressure as measured at the top of the pressurizer during the S00504 test, with selected component actuations and plant responses shown in relation to primary system pressure. Comparison of system pressure versus time for S00504 (Figure 3.4-83) with S00303 (Figure 3.2-83) shows a high degree of similarity. The main differences in the system response are the following:

- ADS-1 occurred [ ]^{a,b,c} later
- ADS-4 never occurred for S00504

The IDP began with the initiation of the break, which caused the pressurizer to drain. This resulted in a rapid reduction in pressure. The reactor trip (R) signal initiated at [ ]^{a,b,c}, and the safety systems actuation (S) signal initiated at [ ]^{a,b,c}. The R and the S signals initiated the following actions:

- Decay heat simulation (with heat loss compensation) initiated.
- The main steam line isolation valves (MSLIVs) closed.
- The main feedwater isolation valve (MFWIV) shut off.
- The CMT injection valves opened.
- The passive residual heat removal (PRHR) return flow valve opened.
- The reactor coolant pumps (RCPs) shut down.

The recirculation flow through the CMTs and PRHR flow began immediately after the isolation valve opened. Boiling in the heated rod bundle was initiated by the reduction of the system pressure to the saturation point. The upper plenum flashed while the fluid level dropped down to the hot-leg elevation. The flashing on the hot-leg side of the heater bundle stopped the rapid drop in primary system pressure. When the RCPs shut down (at 85 seconds), the flow through the rod bundle began to oscillate (approximately [ ]^{a,b,c} oscillation period). This resulted in oscillations in the rod bundle and upper-plenum void fraction, upper-plenum temperature, and system pressure.

During the initial stages of the pressure decay phase (PDP), the heater bundle void fraction increased. This resulted in an increasing void fraction in the upper plenum and the hot legs. Hot leg-B fluid had

a void fraction very close to that observed at the outlet of the rod bundle. The void fraction in hot leg-A was much lower due to the selective removal of vapor from the hot leg by the PRHR inlet line.

As a result of the two-phase flow in the hot legs, steam from the two-phase mixture collected in the top of the U-tubes, thereby initiating draining of the steam generator U-tubes. This stopped the natural circulation flow through the primary system. The void fraction oscillations observed through the heater bundle and in the upper plenum terminated when the flow through the steam generator U-tubes ended. The natural circulation flow through the steam generators stopped approximately [ ]^{a,b,c} into the event.

Two-phase flow through the PRHR, consisting of alternating slugs of steam and saturated water, had an average integrated void fraction significantly greater than seen in the upper plenum. Due to boiling in the rod bundle, two-phase flow entered the hot leg from the upper plenum and flowed through the PRHR heat exchanger (HX) located in the in-containment residual water storage tank (IRWST). The average void fraction in the PRHR inlet was as high as [ ]^{a,b,c}, which enhanced the PRHR heat rejection from the primary system when compared with the single-phase saturated or subcooled water due to the level of condensation. When the flow stabilized after the initial flow oscillations, a heat removal rate of [ ]^{a,b,c} was calculated. This calculation was based on the void fraction of the flow in the PRHR supply line, the flow rate, the PRHR inlet and outlet temperatures, and the pressure. This calculation assumes a slip coefficient of 1 between water and steam and may give slightly lower values than the actual heat transfer. It should, therefore, be used for test-to-test comparison only.

When the B-side cold legs drained to the cold-leg nozzle elevation, the CMTs converted from the recirculation mode to the draindown mode of injection. This increased the cold injection flow and the rate of system pressure decay. This occurred at approximately [ ]^{a,b,c} for CMT-B and [ ]^{a,b,c} for CMT-A. When system pressure dropped to saturation pressure for the upper head, the upper head began to drain (at [ ]^{a,b,c}).

During the first [ ]^{a,b,c} of this test (until ADS-1), [ ]^{a,b,c} of water were expelled through the break, while draining the following: the pressurizer, the steam generator U-tubes, the power channel upper head, the power channel upper plenum above the hot leg, most of the cold legs, and approximately [ ]^{a,b,c} of the CMTs. The heated rods in the power channel that simulate the core decay heat reduced the power level to approximately [ ]^{a,b,c}. This value consisted of [ ]^{a,b,c} decay heat and [ ]^{a,b,c} heat loss compensation. The break flow was steady, indicating that cold leg-B2 was not totally empty.

The automatic depressurization system (ADS) phase began with the actuation of ADS-1 (at [ ]^{a,b,c}). ADS-2 and ADS-3 occurred within the next [ ]^{a,b,c}. The heat loss compensation was terminated from the decay heat simulation when ADS-1 occurred and the rod bundle power level was reduced to approximately [ ]^{a,b,c}.

The ADS actuation increased the rate of primary system depressurization and resulted in a high level of injection flow from the accumulators. The rapid injection of cold fluid from the accumulators ([ ]^{a,b,c}) subcooled the whole primary system, temporarily refilling the power channel upper plenum and filling the pressurizer for the rest of the event. Significant boiling was not detected in the heater bundle for the rest of the event. The upper plenum reached saturation temperature, and the level dropped to the hot-leg elevation until the NRHR flow subcooled the heater bundle and the upper plenum (thereby refilling the upper plenum) for the rest of the event.

The liquid discharge through the break was replaced temporarily by saturated steam at approximately [ ]^{a,b,c}. However, a steady liquid break flow supplied by the NRHR restarted at [ ]^{a,b,c}. The PRHR flow stopped approximately [ ]^{a,b,c} into the event. During the ADS phase, approximately [ ]^{a,b,c} of subcooled water were discharged from ADS-1, ADS-2, and ADS-3. This water was supplied primarily by the accumulator discharge and the continuing NRHR flow.

Subcooled water was then flowing steadily from the NRHR into the direct vessel injection (DVI) line and left the primary system through ADS-1, ADS-2, and ADS-3 and the break.

Since the CMTs never drained to the level needed for ADS-4 actuation, ADS-4 never occurred in S00504.

3.4.2 Analysis of the S00504 Test Data

The analysis of the SPES-2 test was performed using the SPESAN computer code. The code performs a detailed accounting of the coolant inventory in all parts of the system from the start to the end of the test. Also, the internal energy of all components and parts of the facility, including the energy losses from the break and ADS flows, are calculated throughout the event. It is noted that the mass balance and the energy transfer calculations are performed in much greater detail than was performed in WCAP-14309, *Final Data Report.*[1] The results of the test data analysis are presented in Figures 3.4-1 through 3.4-82. Mass balance snapshots for all the major primary system components, at various points of interest throughout the transient, are presented in Table 3.4-1.

Mass Balance

Overall Mass Balance

The uncertainty in the overall mass balance is an indication of the overall quality of the test. The total water inventory is tracked from the start until the end of the test. Figures 3.4-74, 3.4-75, and 3.4-76 show the overall mass balance and the error (uncertainty) in mass balance for S00504.

The overall mass balance for S00504 (Figure 3.4-74) shows a small variation of water inventory during the event, resulting from the overall uncertainty in the instrumentation and the assumptions of the mass balance model used to determine the total water inventory. The average total inventory

during the test (Figure 3.4-74) increased by [ ]^{a,b,c} by the end of test due to CVCS and NRHR injection. The total mass injected by CVCS and NRHR was [ ]^{a,b,c} (*Final Data Report*[1]) and, thereafter, the final mass was indicated to be [ ]^{a,b,c} below the initial mass. Figure 3.4-75 shows the difference between the total mass during the event and the initial mass (mass balance error) when the inventory was calculated by integrating the flows. Figure 3.4-76 shows the mass balance error when inventory was calculated based on the catch tank weight and component level measurements. The mass balance error based on flow measurements varied from 0 to -120 lbm, while the weight and level measurements resulted in an average error varying approximately from 10 to -100 lbm during the event, and a final error of -70 lbm at the end of the event.

Water Inventory for the Power Channel and the Loop

Maintenance of coolant coverage of the heater bundle was the most critical issue for the power channel. The heater bundle coverage during a loss-of-coolant accident (LOCA) event often consists of two-phase fluid, which can have a very high void fraction. Figure 3.4-40 shows the true level of two-phase fluid in the power channel as measured from the elevation of the top of the core (TAF). Since this represents the true two-phase level, it will be different than the collapsed liquid level in the heater bundle.

For S00504, the two-phase level in the upper plenum decreased to the hot-leg elevation, and remained at this elevation for most of the event. The accumulator injection [ ]^{a,b,c} partially condensed the steam bubble in the upper plenum causing the level to rise. Following the end of the accumulator injection, the two-phase level again decreased to the hot-leg elevation. This occurred at the time of minimum power channel-water inventory (approximately [ ]^{a,b,c}), before the NRHR injection started to refill the power channel. The NRHR injection also partially condensed the steam bubble in the upper plenum causing the two-phase level to rise above the hot-leg elevation.

The level on the cold side of the power channel is shown in Figures 3.4-42 (annular downcomer) and 3.4-44 (tubular downcomer). The annular downcomer was full until approximately [ ]^{a,b,c} into the event. At that time, the level started to decrease and reached a minimum level in the annular downcomer at approximately [ ]^{a,b,c}. This corresponded to the time of the second minimum for water inventory in the power channel shown in Figure 3.4-39. Figure 3.4-62 shows the maximum cladding temperature during the event and compares this temperature with the saturation temperature. There was no indication of loss of cooling for the heater rods during this event.

The collapsed fluid level in the rod bundle (Figure 3.4-48) and the rod bundle exit void fraction (Figure 3.4-61) show that the rod bundle was water solid before the break was initiated. The rod bundle exit void fraction was determined from DP-014P, which covers the span from rod bundle near the top of the active fuel (TAF) elevation to the lower part of the upper plenum. Two-phase flow with approximately [ ]^{a,b,c} average void fraction existed in the rod bundle prior to the accumulator injection. During the accumulator injection and later until the end of the test, the rod bundle became essentially water solid.

The collapsed level in the upper plenum (Figures 3.4-52 and 3.4-54) decreased to approximately [ ]^{a,b,c} below the hot leg before the accumulator injection, followed by a period when the level in the upper plenum increased above the hot leg during the accumulator injection. This period was followed by a drop in the collapsed level to approximately the hot-leg elevation at the time of minimum water inventory before the NRHR injection flow filled the upper plenum.

The water inventory in the power channel (Figure 3.4-39) had two minima; before the accumulator injection, and after accumulator injection before the increasing IRWST injection started to fill the power channel. The first minimum was more severe showing a total power channel inventory of approximately [ ]^{a,b,c} ([ ]^{a,b,c} of starting inventory) at that time. The total primary system inventory (power channel, pressurizer, and loops), shown in Figure 3.4-77, reached approximately [ ]^{a,b,c} ([ ]^{a,b,c} of starting inventory) for this minimum.

Water Injection/Ejection

The injected fluid mass from all injection sources is shown in Figure 3.4-78. Figure 3.4-79 shows the total source inventory and the injected and ejected masses during the event. Starting with a total of approximately [ ]^{a,b,c} source inventory, only [ ]^{a,b,c} ([ ]^{a,b,c} of available source water, CVCS and NRHR not included) was used by the end of the event.

Energy Balance

PRHR Heat Transfer

The heat transfer from the PRHR to the IRWST gave a unique possibility of comparing heat transfer on the primary and the secondary side. A method of calculating the heat rejection by the PRHR HX into the IRWST is described in Section 2.2-2, and a comparison of three heat transfer calculations are given in Section 4.0. The PRHR primary-side heat transfer was calculated based on the measured exit flow rate, and the difference in enthalpy of the inlet and exit flows. Since the S00504 test had two-phase flow conditions in the hot legs and PRHR, the inlet flow void fraction was determined (Figure 3.4-21) and used to establish the effective enthalpy of the two-phase inlet flow. The outlet flow from the PRHR HX was always subcooled water. The primary-side two-phase heat transfer for S00504 (shown in Figure 3.4-19) was considerably greater than the heat transfer measured for single-phase flow through the PRHR during the hot pre-operational testing (see WCAP-14309, *Final Data Report*)[1]. Figure 3.4-18 shows the calculated heat transfer from the PRHR external tube surface to the water in the IRWST by the three-tube section of the HX. The top part of the PRHR HX acted as a condenser, where the steam of the two-phase fluid extracted from hot leg-A was condensed. The top horizontal tube transfers the greatest amount of heat. The condensation process on the inside effectively heated this tube wall temperature above the boiling point for the water in the IRWST, resulting in very effective nucleate boiling heat transfer from the outside surface. The vertical and the bottom horizontal sections of the HX, for the most part, remained subcooled with a less effective free convection heat transfer to the IRWST water and contributed, therefore, far less to the overall heat transfer of the PRHR.

Figure 3.4-17 shows the internal energy of the IRWST water, the integrated power from the primary side of the PRHR HX, and the heat transfer from the PRHR HX external surfaces. The internal energy in the IRWST water was calculated based on thermocouples located at various elevations in the IRWST tank, which were allocated different control volumes to arrive at an effective average temperature.

For S00504 there was good correlation between the three heat transfer calculations. Up to [ ]^{a,b,c} the PRHR primary-side calculation and the IRWST internal energy calculation are very close. After [ ]^{a,b,c}, the IRWST internal energy appeared to decrease slightly due to the effect of temperature decrease at the top of the IRWST tank after the PRHR flow stopped at [ ]^{a,b,c} (temperature stratification decreased). The small increase in the PRHR primary-side calculation after PRHR flow stops ([ ]^{a,b,c}) was related to the nonzero average PRHR flow rate signal due to its restriction below zero. The comparison shown in Figure 3.4-17 indicates that the three energy calculations are consistent and must be valid.

Steam Generator Heat Transfer

Figure 3.4-32 shows the heat transfer in the steam generators for S00504, and Figure 3.4-33 shows the pressures on the primary side and the secondary side of the steam generators. Heat transfer was sharply reduced after the pumps were tripped due to the reduction of flow in the tubes. The pressures show that the steam generators were available as heat sinks until approximately [ ]^{a,b,c} into the event, at which time the primary side pressure dropped below the secondary making the steam generators a potential heat source for the primary system. Figure 3.4-28 shows the water inventory in the steam generators primary side, which includes inlet and outlet plena and U-tubes. When full, the steam generator inlet and outlet plena contain approximately [ ]^{a,b,c} of water. When the primary-side pressure dropped below the secondary-side pressure (approximately [ ]^{a,b,c}), the steam generators U-tubes were essentially drained of water and contained trapped steam, which became more and more superheated as the primary-side pressure decayed.

The heat transfer calculated for the steam generators decreased rapidly after the rod bundle power was reduced to decay heat plus heat loss compensation, and it disappeared after approximately [ ]^{a,b,c}. Also shown in Figure 3.4-32 is the PRHR heat transfer, which removed heat from the system after the steam generators heat transfer had ended.

Overall Energy Balance

Figure 3.4-80 shows the integrated energy of the fluid streams leaving the system. The energy content of the break flow is greatly reduced when ADS-1 occurred. The energy flow through ADS-1, ADS-2, and ADS-3 decreased after [ ]^{a,b,c} with decreasing system pressure and temperature and stabilized after [ ]^{a,b,c}.

Figure 3.4-81 shows all the energy components in the heat balance for the system. Throughout the event, rod bundle power was the dominant heat input to the system, and during the initial part of the

event the steam generators provided the dominant heat extraction. After the pumps trip, flow through the primary steam generator tubes was sharply reduced, and the heat transfer from the primary to secondary side was reduced dramatically. When the primary- and secondary-system pressures equalized and the steam generator U-tubes drained (about [ ]^{a,b,c}), the steam generator became thermally isolated from the primary system, and it did not affect the rest of the event. Figure 3.4-80 shows the energy loss from the break and the ADS flows as calculated based on assumptions described in Section 2.0. The average energy loss from the fluids ejected from the system during the first [ ]^{a,b,c} of the event was approximately [ ]^{a,b,c} ([ ]^{a,b,c}). The average energy loss then was reduced to approximately [ ]^{a,b,c} ([ ]^{a,b,c}) from about [ ]^{a,b,c} to the end of the test.

From approximately [ ]^{a,b,c} to the end of the test more energy left the system through the break and ADS flows than was generated by the rod bundle. From [ ]^{a,b,c} overall system energy stored within the system (fluid and metal) decreased to compensate. After [ ]^{a,b,c}, the energy loss through the break and ADS flows decreased and the system fluid energy stayed approximately constant, but metal mass thermal energy decreased. The average loss of the metal thermal energy after [ ]^{a,b,c} was approximately [ ]^{a,b,c}.

Figure 3.4-82 shows the accumulated energy balance error during the event. During the initial part of the transient, an increasing error was generated by a greater-than-actual heat transfer being calculated for the steam generator. This was a consequence of an assumed overall heat transfer coefficient (HTC) for the steam generator, which was calculated from full-power/full-flow conditions (before time "0"), which were higher than the actual HTC at the lower flow conditions existing after the pumps have shut down. Figure 3.4-82 also shows that the error in the energy balance increased rapidly from [ ]^{a,b,c} (during the accumulator discharge into the primary system). This error was a consequence of the rapid change in the metal energy seen in Figure 3.4-81, which was calculated based on fluid temperatures. In reality, the calculated change of metal energy occurred at a slower rate than indicated by the fluid thermocouples due to the large thermal inertia of the heavy-walled components. The error peak shown in Figure 3.4-82 at [ ]^{a,b,c} was, therefore, a consequence of taking credit for metal heat too fast during the event, and this error disappeared after [ ]^{a,b,c} when the metal temperatures catch up with the fluid temperatures. In evaluating the overall error in the accuracy of the energy balance this peak is disregarded. On this basis, the maximum error band for Figure 3.4-82 is approximately -60000 to +140000 Btu, which corresponds to within [ ]^{a,b,c} of the total fluid energy ejected from the system. The error at the end of the event was approximately [ ]^{a,b,c} of the total ejected fluid energy.

Other Observations

Pressure Decay

Figure 3.4-3 shows the primary system pressure during the S00504 test. Throughout this event, the pressure was controlled by the saturation pressure of the hottest fluid volume in the primary system. At the initiation of the break, the controlling fluid volume was in the pressurizer and surge line; however, this shifted within the first [ ]^{a,b,c} (after the initial blowdown phase) to the power channel upper plenum.

Figure 3.4-2 shows that the temperature of the upper plenum was equal to the saturation temperature corresponding to the primary system pressure measured in the upper head during the natural circulation phase and into the ADS phase. The pressure stabilized at the saturation pressure for the upper plenum, and then continued a slow pressure decay responding to the CMTs injection. Figure 3.4-3 shows the increase in the pressure decay rate that occurred at approximately [ ]^{a,b,c}, when the CMTs transitioned from natural circulation injection to draindown injection, which essentially doubled the injection rate of cold water into the DVI. The higher injection rate resulted in a more rapid temperature drop in the upper plenum (fuel exit in Figure 3.4-2), which was reflected in a more rapid pressure decay. With the actuation of ADS-1 at approximately [ ]^{a,b,c}, the pressure dropped rapidly due to the increased rate of mass ejected from the system (Figure 3.4-68), and the increased flow of cold water being injected into the annular downcomer and flowing through the rod bundle. This continued to reduce the power channel inlet plenum temperature, and subcooled the heated rod bundle due to the higher flow. Since the power channel outlet plenum became subcooled at approximately [ ]^{a,b,c}, the hottest fluid in the system was in the pressurizer, the cold legs, and the CMTs, and the pressure was partially supported by the flashing of the fluid in one or several of these locations. When the accumulator discharge ended (approximately [ ]^{a,b,c}), the lower- plenum temperature increased due to the metal heat, and the upper-plenum temperature increased to the saturation temperature and again took over control of the system pressure. It is noted here that at the end of the accumulator injection, a large amount of nitrogen from the accumulators was injected into the primary system. This injection had very little immediate effect on the primary system, but as will be discussed in Section 4.0, affects the upper plenum, the PRHR HX, and the CMT at later stages of the event.

Injection flow from the NRHR into the DVI nozzles increased after accumulator injection. This flow was sufficiently high to subcool the primary system, ending rod bundle boiling and partially collapsing the steam bubble in the upper plenum, and bringing the system to a near atmospheric internal pressure.

Ejection Flows

Figure 3.4-68 shows the individual mass flows leaving the system via the break and the ADS. The individual flow rates are given in Figures 3.4-69, 3.4-70, and 3.4-71. The break flow consisted of saturated water. For ADS-1, ADS-2, and ADS-3 it was assumed that the flow consisted of saturated

water if the void fraction measured in the top of the pressurizer (Figure 3.4-73) was less than [ ]^{a,b,c}.

The total mass flow rate leaving the system was reasonably steady for S00504 (as seen in Figure 3-4.79). Figure 3.4-80 shows that the energy of the fluid ejection was steady at an average rate of [ ]^{a,b,c} for the first [ ]^{a,b,c} and then decreased to [ ]^{a,b,c} for the rest of the event. The decrease in energy ejection rate was related to the primary system pressure, which stayed approximately steady after [ ]^{a,b,c} little above the atmospheric pressure.

ADS-1 opened at approximately [ ]^{a,b,c}, followed by ADS-2 and ADS-3 within the next [ ]^{a,b,c}. The break flow changed from saturated water to steam, and the energy removal by the break flow (Figure 3.4-80) reduced. After accumulator injection the break flow changed back from saturated steam to water. When the NRHR flow increased the break mass flowrate again increased (after [ ]^{a,b,c}) but energy flow rate stayed low because of low fluid temperature in the cold legs. The energy was leaving the system also through ADS-1, ADS-2, and ADS-3. Mass flow rate through the ADS-1, ADS-2, and ADS-3 stayed high throughout the event (Figure 3.4-68). When the pressurizer was refilled at approximately [ ]^{a,b,c} the flow through ADS changed from steam to water, and the energy loss via ADS-1, ADS-2, and ADS-3 decreased due to low fluid temperature in the primary system.

TABLE 3.4-1
COMPONENT MASS VARIATIONS IN TEST S00504

	Start Fault	End Blowdown	CMT to Draindown	ADS-1 Starts	First Acc. Empty	ADS-4 Starts	IRWST Starts	End of Transient
Event time								
Power channel								
PC: core								
PC: downcomers								
PC: upper plenum								
Hot leg-A								
Hot leg-B								
Cold leg-A								
Cold leg-B								
SG primary-A								
SG primary-B								
Pressurizer+SL								
CMT-A								
CMT-B								
Accumulator-A								
Accumulator-B								
IRWST								

a,b,c

TEST ANALYSIS STANDARD PLOT PACKAGE Figures 3.4-1 Through 3.4-83				
Fig. No.	**Component**	**Variables**	**Units**	**Description**
3.4-1	Power channel	CORE-POW	kW	Core power
3.4-2	Power channel	TSAT, TAVTDC, TFOUT	°F	Core inlet/outlet temperature, saturation temperature
3.4-3	Pressurizer	PPZRTOP	psia	System pressure
3.4-4	Steam generator	PSGAS, PSGBS	psia	Primary and secondary pressure in steam generators
3.4-5	Steam generator	TAVGSGA, TAVGSGB	°F	Average fluid temperature in steam generators
3.4-6	CMT	MCMTA, MCMTB	lbm	Fluid mass in CMTs
3.4-7	CMT	CLEVELA, CLEVELB	ft.	Collapsed liquid level in CMTs
3.4-8	CMT	MOUTCMTA, MOUTCMTB, MINCMTA, MINCMTB	lbm	Integrated mass in/out of CMTs
3.4-9	CMT	FLOWOUTA, FLOWOUTB	lbm/sec.	Measured flow out of CMTs
3.4-10	CMT	FLOWINA, FLOWINB	lbm/sec.	Calculated flow into CMTs
3.4-11	CMT	BLFRACA, BLFRACB	Fraction	Fractional differential pressure in cold leg-CMT balance lines
3.4-12	CMT	UTOT-A, UTOT-B	Btu	Fluid energy in CMTs
3.4-13	IRWST/PRHR	MIRWST	lbm	Mass of fluid in IRWST
3.4-14	IRWST/PRHR	LIRWST	ft.	Collapsed liquid level in IRWST
3.4-15	IRWST/PRHR	FIRWST	lbm/sec.	Measured discharge flow from IRWST

TEST ANALYSIS STANDARD PLOT PACKAGE Figures 3.4-1 Through 3.4-83 (Cont.)				
Fig. No.	**Component**	**Variables**	**Units**	**Description**
3.4-16	IRWST/PRHR	MOUTDVIA, MOUTDVIB	lbm	Integrated mass out of DVI lines
3.4-17	IRWST/PRHR	INT-QCAL, INT-QTUB, U-UO	Btu	Comparison of energy transfer from PRHR tubes to IRWST
3.4-18	IRWST/PRHR	Q-HOR-1, Q-VERT, Q-HOR-2 QTUBEXT	Btu/sec.	Breakdown of heat transfer from different sections of PRHR tube
3.4-19	IRWST/PRHR	Q-CALIM	Btu/sec.	PRHR/IRWST heat transfer calculated on tube side
3.4-20	IRWST/PRHR	FLOWTUBE	lbm/sec.	Measured outlet flow from PRHR tube
3.4-21	IRWST/PRHR	VOID-FRC		Calculated PRHR Inlet void fraction
3.4-22	Accumulator	MACCA, MACCB	lbm	Mass of fluid in accumulators
3.4-23	Accumulator	LACCA, LACCB	ft.	Collapsed liquid level in accumulators
3.4-24	Accumulator	MEASFLWA, MEASFLWB	lbm/sec.	Measured flow from accumulators
3.4-25	Accumulator	MOUTACCA, MOUTACCB	lbm	Integrated mass out of accumulators
3.4-26	Accumulator	U-TOT-A, U-TOT-B	Btu	Energy of fluid in accumulators
3.4-27	Accumulator	AIRMASSA, AIRMASSB	lbm	Mass of air exiting accumulators
3.4-28	Steam generator	MSGAP, MSGBP	lbm	Mass of fluid in steam generators - primary side
3.4-29	Steam generator	LSGAH, LSGAC, LSGBH, LSGBC	ft.	Collapsed liquid levels in steam generators - primary side - hot and cold sides of U-tubes

TEST ANALYSIS STANDARD PLOT PACKAGE
Figures 3.4-1 Through 3.4-83 (Cont.)

Fig. No.	Component	Variables	Units	Description
3.4-30	Steam generator	MSGAH, MSGAC, MSGBH, MSBGC	lbm	Mass of fluid in steam generators - primary side - hot and cold sides of U-tubes
3.4-31	Steam generator	LSGSA, LSGSB	ft.	Collapsed liquid levels in steam generators - secondary side
3.4-32	Steam generator	Q-TRNF-A, Q-TRNF-B, Q-CALIM	Btu/sec.	Heat transfer in steam generators heat transfer in PRHR
3.4-33	Steam generator	PRESS-PA, PRESS-PB, PREF-A, PREF-B	psia	Primary and secondary pressure in steam generators
3.4-34	Pressurizer	MPZR	lbm	Fluid mass in pressurizer
3.4-35	Pressurizer	LPZR	ft.	Collapsed liquid level in pressurizer
3.4-36	Pressurizer	MSL	lbm	Fluid mass in surge line
3.4-37	Pressurizer	LSL	ft.	Collapsed liquid level in surge line
3.4-38	Pressurizer	UPZR	Btu	Fluid energy in pressurizer
3.4-39	Power channel	MPCHN	lbm	Total fluid mass in power channel
3.4-40	Power channel	L2PHASE, LDVI, LHL, LCL	ft.	Two-phase liquid level in power channel vs. DVI, hot-leg, and cold-leg elevations
3.4-41	Power channel	MANDC	lbm	Fluid mass in annular downcomer
3.4-42	Power channel	LANDC, LDVI, LHL, LCL	ft.	Collapsed liquid level in annular downcomer vs. DVI, hot-leg, and cold-leg elevations

TEST ANALYSIS STANDARD PLOT PACKAGE Figures 3.4-1 Through 3.4-83 (Cont.)				
Fig. No.	**Component**	**Variables**	**Units**	**Description**
3.4-43	Power channel	MTDC	lbm	Fluid mass in tubular downcomer
3.4-44	Power channel	LTDC, LBOF, LTOF	ft.	Collapsed liquid level in tubular downcomer vs. top of active fuel and bottom of active fuel levels
3.4-45	Power channel	MLOWP	lbm	Fluid mass in lower plenum
3.4-46	Power channel	LLOWP	ft.	Collapsed liquid level in lower plenum
3.4-47	Power channel	MCORE	lbm	Fluid mass in core region
3.4-48	Power channel	LCORE	ft.	Collapsed liquid level in core
3.4-49	Power channel	MFOUT	lbm	Fluid mass in core outlet region
3.4-50	Power channel	LFOUT	ft.	Collapsed liquid level in core outlet region
3.4-51	Power channel	MUPPL	lbm	Fluid mass in the lower portion of the upper plenum
3.4-52	Power channel	LUPPL	ft.	Collapsed liquid level in the lower portion of the upper plenum
3.4-53	Power channel	MUPPU	lbm	Fluid mass in the upper portion of the upper plenum
3.4-54	Power channel	LUPPU	ft.	Collapsed liquid level in the upper portion of the upper plenum
3.4-55	Power channel	MHEAD	lbm	Fluid mass in the upper head
3.4-56	Power channel	LHEAD	ft.	Collapsed liquid level in the upper head

TEST ANALYSIS STANDARD PLOT PACKAGE Figures 3.4-1 Through 3.4-83 (Cont.)				
Fig. No.	**Component**	**Variables**	**Units**	**Description**
3.4-57	Power channel	UPC	Btu	Total fluid energy in power channel
3.4-58	Power channel	Q-FLUX	Btu/sec.-ft.^{2}	Average heat flux on the heated rods
3.4-59	Power channel	STM-RATE	lbm/sec.	Core steam generation rate
3.4-60	Power channel	FLOWCOR	lbm/sec.	Calculated core flow
3.4-61	Power channel	VOIDOUT		Void fraction at core exit
3.4-62	Power channel	TMAX, TSAT, TMAX-TSAT	°F	Maximum clad temperature, saturation temperature and delta
3.4-63	Hot leg	MHLA, MHLB	lbm	Fluid mass in hot legs
3.4-64	Hot leg	FLA, FLB	Fraction	Fractional collapsed liquid level in hot legs
3.4-65	Cold leg	MCLA, MCLB	lbm	Fluid mass in cold legs
3.4-66	Cold leg	LCLA1, LCLA2, LPSA	ft.	Collapsed liquid levels in cold leg-A
3.4-67	Cold leg	LCLB1, LCLB2, LPSB	ft.	Collapsed liquid levels in cold leg-N
3.4-68	Total system mass	MADS1-3, MADS4, BRKMASS	lbm	Catch tank mass for ADS-1, ADS-2, ADS-3, ADS-4, and break
3.4-69	Total system mass	DMADS1-3	lbm/sec.	Calculated flow out ADS 1-3
3.4-70	Total system mass	DMADS4	lbm/sec.	Calculated flow out ADS 4
3.4-71	Total system mass	BRKFLOW	lbm/sec.	Calculated flow out break
3.4-72	Total system energy	UADS123, UADS4, UBREAK	Btu	Integrated fluid energy for ADS-1, ADS-2, ADS-3, ADS4, and the break

TEST ANALYSIS STANDARD PLOT PACKAGE Figures 3.4-1 Through 3.4-83 (Cont.)				
Fig. No.	**Component**	**Variables**	**Units**	**Description**
3.4-73	Total system energy	VOID		Calculated void fraction for ADS-1, ADS-2, and ADS-3
3.4-74	Total system mass	MTOTAL, MTOTO	lbm	Total system fluid mass vs. Initial fluid mass
3.4-75	Total system mass	ERRLOP	lbm	Error in the mass balance (using measured and calculated flows)
3.4-76	Total system mass	ERRLOP1	lbm	Error in the mass balance (using fluid inventory)
3.4-77	Total system mass	MPCLTOT, MPCLO	lbm	Total fluid mass in power channel and loops vs. Initial fluid mass
3.4-78	Total system mass	MACOUT, MCMOUT, MIROUT	lbm	Total integrated mass discharged from accumulators, CMTs, and IRWST
3.4-79	Total system mass	MSOURCE, MSINK, MSOURIN	lbm	Total source inventory, total mass ejected from primary system, and total mass injected to primary system
3.4-80	Total system energy	UADS123, UBREAK, UADS4, UCATCH	Btu	Integrated fluid energy exiting via ADS-1, ADS-2, ADS-3, ADS-4, and the break, and the sum
3.4-81	Total system energy	USURR, UCATCH, UQIN, UFLD-UO, UMTL-UO, USG	Btu	Overall energy balance including integrated rod power, steam generator power, and heat loss to the surroundings, energy exiting via ads and break, energy input via nonsafety systems, and change in primary system fluid and metal energy relative to start of test
3.4-82	Total system energy	UERROR, ERROR-%	Btu, %	Error in overall energy balance, relative to initial fluid and metal energy
3.4-83	System pressure	– –	psia	Test event phases and system pressure

The figures listed are proprietary and, therefore,
are not available in the Class 3 version of this report.

These figures are available in the Class 2 version of this report.

3.5 Analysis of the One-Inch Cold-Leg Break without Nonsafety Systems (S00401)

This matrix test simulated a 1-in. break in the bottom of cold leg-B2. The event began with the initiation of the break in cold leg-B2, which was the cold leg with the CMT-B pressure balance line connection. The break location was on the reactor-vessel side of the cold leg from the core makeup tank (CMT) balance line connection. This test was performed without any nonsafety systems' pumps operating. That is, it was performed without the chemical and volume control system (CVCS) makeup pumps, steam generator startup feedwater (SFW) pumps, and normal residual heat removal system (NRHR) pumps.

3.5.1 Summary of Test Observations

Figure 3.5-83 shows the plant primary system pressure during matrix test S00401 (as measured at the top of the pressurizer) during the S00401 event, with selected component actuations and plant responses shown in relation to primary system pressure.

The IDP began with the initiation of the break, which caused the pressurizer to drain. This resulted in a rapid reduction in pressure. The reactor trip (R) signal initiated at [ ]^{a,b,c}. The safety systems actuation (S) signal initiated at [ ]^{a,b,c}. The R and the S signals initiated the following actions:

- Decay heat simulation (with heat loss compensation) initiated.
- The main steam line isolation valves (MSLIVs) closed.
- The main feedwater isolation valves (MFWIVs) shutoff.
- The CMT injection valves opened.
- The passive residual heat removal (PRHR) return flow valve opened.
- The reactor coolant pumps (RCPs) shut down.

The recirculation flow through the CMTs and flow through the PRHR began immediately after the isolation valve opened. Boiling in the heated rod bundle was initiated by the reduction of the system pressure to saturation level. The upper plenum flashed while the fluid level in the upper plenum dropped to the hot-leg elevation. The flashing on the hot-leg side of the heater rod bundle stopped the rapid drop in primary system pressure. When the RCPs shut down (at [ ]^{a,b,c}), the flow through the rod bundle began to oscillate (period [ ]^{a,b,c}). This resulted in oscillations in the rod bundle and upper-plenum void fraction, upper-plenum temperature, and system pressure.

During the initial stages of the PDP, the heater bundle void fraction increased. This caused an increasing void fraction in the upper plenum and the hot legs. The hot leg-B fluid had a void fraction close to that observed in the upper plenum. The void fraction in hot leg-A was lower due to the selective removal of vapor from the hot leg by the PRHR inlet line.

Two-phase flow in the hot legs initiated the draining of the steam generator U-tubes. Steam from the two-phase mixture collected in the top of the U-tubes, thereby draining the steam generator U-tubes.

This stopped the flow through the primary system. The void fraction oscillations observed through the rod bundle and in the upper plenum ended when the flow stopped through the steam generators. Approximately [ ]^{a,b,c} into the event, the flow stopped in steam generator-B due to the higher void fraction in hot leg-B. Approximately [ ]^{a,b,c} later, the flow stopped in steam generator-A.

Two-phase flow into the PRHR valve consisted of intermittent periods of saturated water and steam. It had a void fraction significantly greater than that seen in the upper plenum. Due to boiling in the rod bundle, two-phase flow entered the hot leg from the upper plenum and flowed through the PRHR heat exchanger (HX) in the in-containment refueling water storage tank (IRWST). The average integrated void fraction in the PRHR inlet was as high as [ ]^{a,b,c}, which enhanced the PRHR heat transfer from the primary system to the IRWST when compared with single-phase saturated or subcooled water. When the flow stabilized after the initial flow oscillations, a heat removal rate of [ ]^{a,b,c} was calculated. This calculation was based on the average void fraction of the flow in the PRHR supply line, the measured return flow, the temperatures, and the pressure. This calculation assumes a slip coefficient of 1 between water and steam and may give slightly lower values than the actual heat transfer. It should, therefore, be used for test-to-test comparison only.

When system pressure dropped to saturation pressure for the upper head, it began to drain (at [ ]^{a,b,c}).

When the CMT balance lines drained (when the cold legs B had partially emptied), the CMTs converted from the pure recirculation mode to a recirculation with intermittent draindown mode of injection. This occurred at approximately [ ]^{a,b,c} for CMT-B and [ ]^{a,b,c} for CMT-A.

During the first [ ]^{a,b,c} before the ADS-1 actuation of this event, [ ]^{a,b,c} of water were expelled through the break while draining the pressurizer, the steam generator U-tubes, the power channel upper head, the power channel upper plenum above the hot leg, most of the cold legs, and approximately [ ]^{a,b,c} of the CMTs. The heated rods in the power channel, which simulate the core decay heat, reduced the power level to approximately [ ]^{a,b,c} at [ ]^{a,b,c} seconds. This value consisted of [ ]^{a,b,c} decay heat and [ ]^{a,b,c} heat loss compensation. The break flow was steady, indicating that cold leg-B2 was not totally empty.

The ADS phase began with the actuation of ADS-1 (at approximately [ ]^{a,b,c}). ADS-2 and ADS-3 occurred within the next [ ]^{a,b,c}. The heat loss compensation was terminated from the decay heat simulation when ADS-1 occurred, and the rod bundle power level was reduced to approximately [ ]^{a,b,c}.

The ADS actuation increased the rate of primary system depressurization and resulted in a high level of injection flow from the accumulators. The rapid injection of cold fluid from the accumulators (at [ ]^{a,b,c}) and the CMTs subcooled the whole primary system, temporarily refilling the power channel/upper plenum and the pressurizer. When the accumulator discharge ended,

the flow through the heater bundle was reduced to the injection rate of the CMTs and the PRHR HX flow, and boiling occurred again in the heater bundle. Two-phase flow occurred again in hot leg-A, the PRHR HX, and the ADS via the pressurizer.

The liquid discharge through the break was replaced by saturated steam at approximately [ ]^{a,b,c}. During the ADS phase, approximately 910 lbm of subcooled water were discharged from ADS-1, ADS-2, and ADS-3. This water was supplied primarily by the accumulator discharge and was followed by an increase in rod bundle void fraction after the accumulators drained and only the CMTs provided injection.

The post-ADS phase began when ADS-4 actuated. ADS-4 occurred at [ ]^{a,b,c}, and the pressurizer water level fell. The fluid discharge through ADS-1, ADS-2, and ADS-3 ended, and fluid was discharged through ADS-4. The pressurizer drained again, and a small amount of CMT flow still entered the direct vessel injection (DVI) line. When system pressure had been reduced below the pressure corresponding to the water elevation head of the IRWST, flow from the IRWST entered the DVI line. Shortly thereafter, the CMT flow ended. The flow from the IRWST subcooled the primary system, the rod bundle boiling slowly ended, and the upper plenum partially refilled. The PRHR drained approximately [ ]^{a,b,c} into the event and was no longer effective. A steady flow of subcooled water then flowed from the IRWST into the DVI line, through the power channel, and left the primary system through ADS-4.

3.5.2 Analysis of the S00401 Test Data

The analysis of the SPES-2 test was performed using the SPESAN computer code. The code performs a detailed accounting of the coolant inventory in all parts of the system from the start to the end of the test. Also, the internal energy of all components and parts of the facility, including the energy losses from the break and ADS flows, are calculated throughout the event. It is noted that the mass balance and the energy transfer calculations are performed in much greater detail than was performed in WCAP-14309, *Final Data Report*.[1] The results of the test data analysis are presented in Figures 3.5-1 through 3.5-82. Mass balance snapshots for all the major primary system components, at various points of interest throughout the transient, are presented in Table 3-5-1.

Mass Balance

Overall Mass Balance

The uncertainty in the overall mass balance is an indication of the overall quality of the test. The total water inventory is tracked from the start until the end of the test. Figures 3.5-74, 3.5-75, and 3.5-76 show the overall mass balance and the error (uncertainty) in mass balance for S00401.

The overall mass balance for S00401 (Figure 3.5-74) shows a small variation of water inventory during the event, resulting from the overall uncertainty in the instrumentation and the assumptions of the mass balance model used to determine the total water inventory. The average total inventory

during the test was indicated to be approximately [ ]^{a,b,c} higher than the initial system mass, and a final mass was indicated to be approximately [ ]^{a,b,c} above the initial mass. Figure 3.5-75 shows the difference between the total mass during the event and the initial mass (mass balance error) when the inventory was calculated by integrating the flows. Figure 3.5-76 shows the mass balance error when inventory was calculated based on the catch tank weight and component level measurements. The mass balance error, based on flow measurements, varied from 0 to 120 lbm; the weight and level measurements resulted in an average error varying approximately from -20 to +70 lbm during the event, and a final error of +70 lbm at the end of the event.

Water Inventory for the Power Channel and the Loop

Maintenance of coolant coverage of the heater bundle is the most critical issue for the power channel. The heater bundle coverage during a loss-of-coolant accident (LOCA) event often consists of two-phase fluid, which can have a very high void fraction. Figure 3.5-40 shows the true level of two-phase fluid in the power channel as measured from the elevation of the top of the core (TAF). Since this represents the true two-phase level, it will be different than the collapsed liquid level in the heater bundle.

For S00401, the two-phase level in the upper plenum decreased to the hot-leg elevation, and remained at this elevation for most of the event. The accumulator injection ([ ]^{a,b,c}) partially condensed the steam bubble in the upper plenum causing the level to rise. Following the end of the accumulator injection, the two-phase level again decreased this time to approximately [ ]^{a,b,c} below the hot-leg elevation. This occurred at the time of minimum power channel water inventory, before the IRWST injection started (at [ ]^{a,b,c}) to refill the power channel. The IRWST injection also partially condensed the steam bubble in the upper plenum causing the level to rise above the hot-leg elevation.

The level on the cold side of the power channel is shown in Figures 3.5-42 (annular downcomer) and 44 (tubular downcomer). The annular downcomer was full until approximately [ ]^{a,b,c} into the event. At that time, the level started to decrease, but it was maintained above the elevation of the hot leg until after the end of the accumulator injection (approximately [ ]^{a,b,c}). The level then decreased and drained the annular downcomer by [ ]^{a,b,c}, and reached a minimum level in the tubular downcomer at approximately [ ]^{a,b,c}. This corresponded to the time of minimum water inventory in the power channel shown in Figure 3.5-39. Figure 3.5-62 shows the maximum cladding temperature during the event and compares this temperature with the saturation temperature. There was no indication of loss of cooling for the heater rods during this event.

The collapsed fluid level in the rod bundle (Figure 3.5-48), and the rod bundle exit void fraction (Figure 3.5-61) show that the rod bundle was water solid before the break was initiated. The rod bundle exit void fraction was determined from DP-014P, which covers the span from the rod bundle near the TAF elevation to the lower part of the upper plenum. Two-phase flow with approximately [ ]^{a,b,c} average void fraction exists in the rod bundle prior to the accumulator injection. During the accumulator injection, the rod bundle became essentially water solid. However, when the

accumulator injection ended, the collapsed level again started to decrease. The rod bundle exit void fraction reached approximately [ ] prior to the start of the IRWST injection phase, starting at approximately [ ]^{a,b,c}.

The collapsed level in the upper plenum (Figures 3.5-52 and 3.5-54) decreased to approximately [ ]^{a,b,c} below the hot leg before the accumulator injection, followed by a period when the level in the upper plenum increased above the hot leg during the accumulator injection. This period was followed by a drop in the collapsed level to approximately [ ]^{a,b,c} below the hot leg at the time of minimum water inventory before the IRWST injection started.

The water inventory in the power channel (Figure 3.5-39) had three minima; when the CMT draindown started, before the accumulator injection, and before the IRWST injection. The third minimum was more severe showing a total power channel inventory of approximately [ ]^{a,b,c} ([ ]^{a,b,c} of starting inventory) at that time. The total primary system inventory (power channel, pressurizer and loops), shown in Figure 3.5-77, reached approximately [ ]^{a,b,c} ([ ]^{a,b,c} of starting inventory) for this minimum.

Water Injection/Ejection

The injected fluid mass from all injection sources is shown in Figure 3.5-78. Figure 3.5-79 shows the total source inventory and the injected and ejected masses during the event. Starting with a total of approximately [ ]^{a,b,c} source inventory, only [ ]^{a,b,c} ([ ]^{a,b,c} of available source water) was used by the end of the event.

Energy Balance

PRHR Heat Transfer

The heat transfer from the PRHR to the IRWST gave a unique possibility of comparing heat transfer on the primary and the secondary side. A method of calculating the heat rejection by the PRHR HX into the IRWST is described in Section 2.2-2, and a comparison of three heat transfer calculations is given in Section 4.0. The PRHR primary-side heat transfer was calculated based on the measured exit flow rate, and the difference in enthalpy of the inlet and exit flows. Since the S00401 test had two-phase flow conditions in the hot legs and PRHR, the inlet flow void fraction was determined (Figure 3.5-21) and used to establish the effective enthalpy of the two-phase inlet flow. The outlet flow from the PRHR heat exchanger was always subcooled water. The primary-side two-phase heat transfer for S00401, shown in Figure 3.5-19, was considerably greater than the heat transfer measured for single-phase flow through the PRHR during the hot preoperational testing (see WCAP-14309, *Final Data Report*).[1] Figure 3.5-18 shows the calculated heat transfer from the PRHR external tube surface to the water in the IRWST by the three-tube section of the HX. The top part of the PRHR heat exchanger acted as a condenser, where the steam of the two-phase fluid extracted from hot leg-A was condensed. The top horizontal tube transfers the greatest amount of heat. The condensation process on the inside effectively heated this tube wall temperature above the boiling point for the water in the

IRWST, resulting in very effective nucleate boiling heat transfer from the outside surface. The vertical and the bottom horizontal sections of the heat exchanger remains for the most part subcooled with a less effective free convection heat transfer to the IRWST water and contributed, therefore, far less to the overall heat transfer of the PRHR.

Figure 3.5-17 shows the internal energy of the IRWST water, the integrated power from the primary side of the PRHR heat exchanger, and the heat transfer from the PRHR heat exchanger external surfaces. The internal energy in the IRWST water was calculated based on thermocouples located at various elevations in the IRWST tank, which were allocated different control volumes to arrive at an effective average temperature. Due to the severe temperature stratification in the IRWST tank, this technique only produced good results until the IRWST started to drain.

For S00401 there was good correlation between the three heat transfer calculations. Up to [ ]^{a,b,c} the PRHR primary-side calculation and the IRWST internal energy calculation are very close. After [ ]^{a,b,c}, the IRWST internal energy appeared to increase significantly due to the effect of draindown on the thermocouple readings. However, since there was very little energy being provided by the PRHR after [ ]^{a,b,c}, this apparent increase does not reflect an actual increase in the average water temperature and IRWST internal energy. The comparison shown in Figure 3.5-17 indicates that the three energy calculations are consistent.

Steam Generator Heat Transfer

Figure 3.5-32 shows the heat transfer in the steam generators for S00401, and Figure 3.5-33 shows the pressures on the primary side and the secondary side of the steam generators. Heat transfer is sharply reduced after the pumps are triped due to the reduction of flow in the tubes. The pressures show that the steam generators were available as heat sinks until approximately [ ]^{a,b,c} into the event, at which time the primary-side pressure dropped below the secondary making the steam generators a potential heat source for the primary system. Figure 3.5-28 shows the water inventory in the steam generators primary side, which includes inlet and outlet plena and U-tubes. When full, the steam generator inlet and outlet plena contains approximately [ ]^{a,b,c} of water. When the primary-side pressure dropped below the secondary-side pressure (approximately [ ]^{a,b,c}), the steam generators' U-tubes are essentially drained of water and contain trapped steam, which becomes more and more superheated as the primary-side pressure decays.

The heat transfer calculated for the steam generators decreased rapidly after the pumps were tripped and disappeared after approximately [ ]^{a,b,c}. Also shown in Figure 3.5-32 is the PRHR heat transfer, which removed heat from the system after the steam generators heat transfer had ended.

Overall Energy Balance

Figure 3.5-80 shows the integrated energy of the fluid streams leaving the system. The energy content of the break flow was greatly reduced when ADS-1 occurred, since although the break flow converted

to steam, the mass flow rate became very low. For ADS-1, ADS-2 and ADS-3 the same happened when ADS-4 occurred.

Figure 3.5-81 shows all the energy components in the heat balance for the system. Throughout the event, rod bundle power was the dominant heat input to the system, and during the initial part of the event the steam generators provide the dominant heat extraction. After the pumps trip, flow through the steam generator tubes is sharply reduced, and the heat transfer from the primary to secondary side is dramatically reduced. When the primary and secondary system pressures equalize, and the steam generator U-tubes drain (about [ ]^{a,b,c}), the steam generator becomes thermally isolated from the primary system, and does not affect the rest of the event. Figure 3.5-80 shows the energy loss from the break and the ADS flows as calculated based on assumptions described in Section 2.0. The average energy loss from the fluids ejected from the system during the first [ ]^{a,b,c} of the event was approximately [ ]^{a,b,c}. The average energy loss increased to [ ]^{a,b,c} after 4600 seconds and then was reduced to approximately [ ]^{a,b,c} from about [ ]^{a,b,c} to the end of the test.

From approximately [ ]^{a,b,c}, more energy was generated by the heated rod bundle than left the system through the break and the overall energy stored within the system increased (metal mass energy decreased and fluid energy increased).

From [ ]^{a,b,c}, more energy left the system through the ADS flows than was generated by the rod bundle, and overall system energy stored within the system (fluid and metal) decreased to compensate. The average loss of the metal thermal energy after 4600 seconds was approximately [ ]^{a,b,c}, which was greater than the rod bundle power at this time [ ]^{a,b,c}.

After approximately [ ]^{a,b,c} the fluid energy stabilize in the system, and the rate of the fluid energy leaving the system (primarily via ADS-4) still exceeded the core input power while metal thermal energy decreased. This condition existed for the rest of the event.

Figure 3.5-82 shows the accumulated energy balance error during the event. During the initial part of the transient, an increasing error was generated by a greater-than-actual heat transfer being calculated for the steam generator. This is a consequence of an assumed overall heat transfer coefficient (HTC) for the steam generator, which was calculated from full-power/full-flow conditions (before time 0), which was higher than the actual HTC at the lower flow conditions existing after the pumps have shut down. Figure 3.5-82 also shows that the error in the energy balance varied rapidly from [ ]^{a,b,c} (during the accumulator discharge into the primary system, ADS-4 and IRWST actuation). This error was a consequence of the rapid change in the metal energy seen in Figure 3.5-81, which was calculated based on fluid temperatures. In reality, the calculated change of metal energy occurred at a slower rate than indicated by the fluid thermocouples due to the large thermal inertia of the heavy walled components. The varying error and the error peak shown in Figure 3.5-82 at [ ]^{a,b,c} were, therefore, a consequence of taking credit for metal heat too fast during the event, and this error disappearred after [ ]^{a,b,c} when the metal temperatures

catches up with the fluid temperatures. The maximum error band for Figure 3.5-82 is approximately -150000 to -0 Btu, which corresponds to within 8 to 14 percent of the total fluid energy ejected from the system. The error at the end of the event is approximately 0 percent of the total ejected fluid energy.

Other Observations

Pressure Decay

Figure 3.5-3 shows the primary system pressure during the S00401 test. Throughout this event the pressure was controlled by the saturation pressure of the hottest fluid volume in the primary system. At the initiation of the break, the controlling fluid volume was in the pressurizer and surge line; however, this shifted within the first [ ]^{a,b,c} (after the initial blowdown phase) to the power channel upper plenum.

Figure 3.5-2 shows that the temperature of the upper plenum was equal to the saturation temperature corresponding to the primary system pressure measured in the upper head during the natural circulation phase and into the ADS phase. The pressure stabilized at the saturation pressure for the upper plenum, and then continued a slow pressure decay responding to the CMTs injection. Figure 3.5-3 shows an increase in the pressure decay rate that occurred at approximately [ ]^{a,b,c}, when the CMTs transitioned from natural circulation injection to draindown injection, which essentially doubled the injection rate of cold water into the DVI. The higher injection rate resulted in a more rapid temperature drop in the upper plenum (fuel exit in Figure 3.5-2), which was reflected in a more rapid pressure decay. With the actuation of ADS-1 at approximately [ ]^{a,b,c}, the pressure dropped rapidly due to the increased rate of mass ejected from the system (Figure 3.5-68), and the increased flow of cold water being injected into the annular downcomer and flowing through the rod bundle. This continued to reduce the power channel inlet plenum temperature, and subcooled the heated rod bundle due to the higher flow. Since the power channel outlet plenum became subcooled at approximately [ ]^{a,b,c}, the hottest fluid in the system was in the pressurizer, the cold legs, and the CMTs, and the pressure was partially supported by the flashing of the fluid in one or several of these locations. When the accumulator discharge ended (approximately [ ]^{a,b,c}), the lower-plenum temperature increased due to the metal heat, and the upper-plenum temperature increased to the saturation temperature and again took over control of the system pressure for the rest of the event. It is noted here that at the end of the accumulator injection, a large amount of nitrogen from the accumulators was injected into the primary system. This injection had very little immediate effect on the primary system but, as will be discussed in Section 4.0, affected the upper plenum, the PRHR HX, and the CMT at later stages of the event.

The actuation of ADS-4 (at approximately [ ]^{a,b,c}) lowered the system pressure sufficiently to allow gravity injection flow from the IRWST into the DVI nozzles. This flow was sufficiently high to subcool the primary system, ending rod bundle boiling and partially collapsing the steam bubble in the upper plenum, and bringing the system to a near-atmospheric internal pressure.

Ejection Flows

Figure 3.5-68 shows the individual mass flows leaving the system via the break and the ADS. The individual flow rates are given in Figures 3.5-69, 3.5-70, and 3.5-71. The break and ADS-4 flows consisted of saturated water. For ADS 1, ADS-2, and ADS-3 it was assumed that the flow consisted of saturated water if the void fraction measured in the top of the pressurizer (Figure 3.5-73) was less than [ ]^{a,b,c} percent. The total mass flow rate leaving the system was reasonably steady for S00401, as seen in Figure 3.5-79. Figure 3.5-80 shows that the energy of the fluid ejection was steady at an average rate of [ ]^{a,b,c} for the first [ ]^{a,b,c}, increased to [ ]^{a,b,c} after [ ]^{a,b,c}, and then decreased to [ ]^{a,b,c} for the rest of the event. The increase in energy ejection rate was caused by ADS-1, ADS-2, and ADS-3 actuation. The decrease in energy ejection rate was related to actuation of ADS-4, which caused the pressurizer to drain, converted the ADS-1, ADS-2, and ADS-3 flow to steam with a low mass flow rate and, simultaneously, started fluid ejection through ADS-4.

ADS-1 opened at approximately [ ]^{a,b,c}, followed by ADS-2 and ADS-3 within the next [ ]^{a,b,c}. The break flow changes from saturated water to steam, but due to the low-mass flow rate (Figure 3.5-68), the energy removal by the break flow (Figure 3.5-80) becomes very low. The energy was leaving the system through ADS 1-3 at a greater rate than through the break and ADS-4, and provided an effective means of removing the stored metal energy from the system, as seen in Figure 3.5-81. The mass flow rate leaving the system via ADS 1, ADS-2, and ADS-3 during the next [ ]^{a,b,c} was greater than the break flow, and also the energy loss through the ADS-1, ADS-2, and ADS-3 exceeded the energy loss by the break flow (Figure 3.5-80).

ADS-4 opened at approximately 5700 seconds, and the ADS-1, ADS-2, and ADS-3 flows converted to steam with a very low-mass flow rate and energy loss rate. The ADS-4 flow stabilized at a rate that matched the injection rate from the IRWST (Figure 3.5-79), and the energy removal via ADS-4 was comparable to the heated rod power (Figure 3.5-81).

TABLE 3.5-1
COMPONENT MASS VARIATIONS IN TESTS S00401

	Start Fault	End Blowdown	CMT to Draindown	ADS-1 Starts	First Acc. Empty	ADS-4 Starts	IRWST Starts	End of Transient
Event time								
Power channel (PC)								
PC: core								
PC: downcomers								
PC: upper plenum								
Hot leg-A								
Hot leg-B								
Cold leg-A								
Cold leg-B								
SG primary-A								
SG primary-B								
Pressurizer + SL								
CMT-A								
CMT-B								
Accumulator-A								
Accumulator-B								
IRWST								

a,b,c

TEST ANALYSIS STANDARD PLOT PACKAGE Figures 3.5-1 Through 3.5-83				
Fig. No.	**Component**	**Variables**	**Units**	**Description**
3.5-1	Power channel	CORE-POW	kW	Core power
3.5-2	Power channel	TSAT, TAVTDC, TFOUT	°F	Core inlet/outlet temperature, saturation temperature
3.5-3	Pressurizer	PPZRTOP	psia	System pressure
3.5-4	Steam generator	PSGAS,PSGBS	psia	Primary and secondary pressure in steam generators
3.5-5	Steam generator	TAVGSGA,TAVGSGB	°F	Average fluid temperature in steam generators
3.5-6	CMT	MCMTA,MCMTB	lbm	Fluid mass in CMTs
3.5-7	CMT	CLEVELA,CLEVELB	ft.	Collapsed liquid level in CMTs
3.5-8	CMT	MOUTCMTA, MOUTCMTB, MINCMTA, MINCMTB	lbm	Integrated mass in/out of CMTs
3.5-9	CMT	FLOWOUTA, FLOWOUTB	lbm/sec.	Measured flow out of CMTs
3.5-10	CMT	FLOWINA, FLOWINB	lbm/sec.	Calculated flow into CMTs
3.5-11	CMT	BLFRACA, BLFRACB	Fraction	Fractional differential pressure in cold leg-CMT balance lines
3.5-12	CMT	UTOT-A, UTOT-B	Btu	Fluid energy in CMTs
3.5-13	IRWST/PRHR	MIRWST	lbm	Mass of fluid in IRWST
3.5-14	IRWST/PRHR	LIRWST	ft.	Collapsed liquid level in IRWST
3.5-15	IRWST/PRHR	FIRWST	lbm/sec.	Measured discharge flow from IRWST

TEST ANALYSIS STANDARD PLOT PACKAGE Figures 3.5-1 Through 3.5-83 (Cont.)				
Fig. No.	**Component**	**Variables**	**Units**	**Description**
3.5-16	IRWST/PRHR	MOUTDVIA, MOUTDVIB	lbm	Integrated mass out of DVI lines
3.5-17	IRWST/PRHR	INT-QCAL, INT-QTUB, U-UO	Btu	Comparison of energy transfer from PRHR tubes to IRWST
3.5-18	IRWST/PRHR	Q-HOR-1, Q-VERT, Q-HOR-2, QTUBEXT	Btu/sec.	Breakdown of heat transfer from different sections of PRHR tube
3.5-19	IRWST/PRHR	Q-CALIM	Btu/sec.	PRHR/IRWST heat transfer calculated on tube side
3.5-20	IRWST/PRHR	FLOWTUBE	lbm/sec.	Measured outlet flow from PRHR tube
3.5-21	IRWST/PRHR	VOID-FRC		Calculated PRHR Inlet void fraction
3.5-22	Accumulator	MACCA, MACCB	lbm	Mass of fluid in accumulators
3.5-23	Accumulator	LACCA, LACCB	ft.	Collapsed liquid level in accumulators
3.5-24	Accumulator	MEASFLWA, MEASFLWB	lbm/sec.	Measured flow from accumulators
3.5-25	Accumulator	MOUTACCA, MOUTACCB	lbm	Integrated mass out of accumulators
3.5-26	Accumulator	U-TOT-A, U-TOT-B	Btu	Energy of fluid in accumulators
3.5-27	Accumulator	AIRMASSA, AIRMASSB	lbm	Mass of air exiting accumulators
3.5-28	Steam generator	MSGAP,MSGBP	lbm	Mass of fluid in steam generators - primary side
3.5-29	Steam generator	LSGAH, LSGAC, LSGBH, LSGBC	ft.	Collapsed liquid levels in steam generators - primary side - hot and cold sides of U-tubes

TEST ANALYSIS STANDARD PLOT PACKAGE
Figures 3.5-1 Through 3.5-83 (Cont.)

Fig. No.	Component	Variables	Units	Description
3.5-30	Steam generator	MSGAH, MSGAC, MSGBH, MSBGC	lbm	Mass of fluid in steam generators - primary side - hot and cold sides of U-tubes
3.5-31	Steam generator	LSGSA, LSGSB	ft.	Collapsed liquid levels in steam generators - secondary side
3.5-32	Steam generator	Q-TRNF-A, Q-TRNF-B, Q-CALIM	Btu/sec.	Heat transfer in steam generators heat transfer in PRHR
3.5-33	Steam generator	PRESS-PA, PRESS-PB, PREF-A, PREF-B	psia	Primary and secondary pressure in steam generators
3.5-34	Pressurizer	MPZR	lbm	Fluid mass in pressurizer
3.5-35	Pressurizer	LPZR	ft.	Collapsed liquid level in pressurizer
3.5-36	Pressurizer	MSL	lbm	Fluid mass in surge line
3.5-37	Pressurizer	LSL	ft.	Collapsed liquid level in surge line
3.5-38	Pressurizer	UPZR	Btu	Fluid energy in pressurizer
3.5-39	Power channel	MPCHN	lbm	Total fluid mass in power channel
3.5-40	Power channel	L2PHASE, LDVI, LHL, LCL	ft.	Two-phase liquid level in power channel vs. DVI, hot-leg, and cold-leg elevations
3.5-41	Power channel	MANDC	lbm	Fluid mass in annular downcomer
3.5-42	Power channel	LANDC, LDVI, LHL, LCL	ft.	Collapsed liquid level in annular downcomer vs. DVI, hot-leg, and cold-leg elevations

TEST ANALYSIS STANDARD PLOT PACKAGE Figures 3.5-1 Through 3.5-83 (Cont.)				
Fig. No.	**Component**	**Variables**	**Units**	**Description**
3.5-43	Power channel	MTDC	lbm	Fluid mass in tubular downcomer
3.5-44	Power channel	LTDC, LBOF, LTOF	ft.	Collapsed liquid level in tubular downcomer vs. top of active fuel and bottom of active fuel levels
3.5-45	Power channel	MLOWP	lbm	Fluid mass in lower plenum
3.5-46	Power channel	LLOWP	ft.	Collapsed liquid level in lower plenum
3.5-47	Power channel	MCORE	lbm	Fluid mass in core region
3.5-48	Power channel	LCORE	ft.	Collapsed liquid level in core
3.5-49	Power channel	MFOUT	lbm	Fluid mass in core outlet region
3.5-50	Power channel	LFOUT	ft.	Collapsed liquid level in core outlet region
3.5-51	Power channel	MUPPL	lbm	Fluid mass in the lower portion of the upper plenum
3.5-52	Power channel	LUPPL	ft.	Collapsed liquid level in the lower portion of the upper plenum
3.5-53	Power channel	MUPPU	lbm	Fluid mass in the upper portion of the upper plenum
3.5-54	Power channel	LUPPU	ft.	Collapsed liquid level in the upper portion of the upper plenum
3.5-55	Power channel	MHEAD	lbm	Fluid mass in the upper head
3.5-56	Power channel	LHEAD	ft.	Collapsed liquid level in the upper head

TEST ANALYSIS STANDARD PLOT PACKAGE Figures 3.5-1 Through 3.5-83 (Cont.)				
Fig. No.	**Component**	**Variables**	**Units**	**Description**
3.5-57	Power channel	UPC	Btu	Total fluid energy in power channel
3.5-58	Power channel	Q-FLUX	Btu/sec.-ft.^{2}	Average heat flux on the heated rods
3.5-59	Power channel	STM-RATE	lbm/sec.	Core steam generation rate
3.5-60	Power channel	FLOWCOR	lbm/sec.	Calculated core flow
3.5-61	Power channel	VOIDOUT		Void fraction at core exit
3.5-62	Power channel	TMAX, TSAT, TMAX-TSAT	°F	Maximum clad temperature, saturation temperature and delta
3.5-63	Hot leg	MHLA, MHLB	lbm	Fluid mass in hot legs
3.5-64	Hot leg	FLA, FLB	Fraction	Fractional collapsed liquid level in hot legs
3.5-65	Cold leg	MCLA, MCLB	lbm	Fluid mass in cold legs
3.5-66	Cold leg	LCLA1, LCLA2, LPSA	ft.	Collapsed liquid levels in cold leg-A
3.5-67	Cold leg	LCLB1, LCLB2, LPSB	ft.	Collapsed liquid levels in cold leg-B
3.5-68	Total system mass	MADS1-3, MADS4, BRKMASS	lbm	Catch tank mass for ADS-1, ADS-2, ADS-3, ADS-4, and break
3.5-69	Total system mass	DMADS1-3	lbm/sec.	Calculated flow out of ADS 1-3
3.5-70	Total system mass	DMADS4	lbm/sec.	Calculated flow out ADS 4
3.5-71	Total system mass	BRKFLOW	lbm/sec.	Calculated flow out break
3.5-72	Total system energy	UADS123, UADS4, UBREAK	Btu	Integrated fluid energy for ADS-1, ADS-2, ADS-3, ADS4, and the break

TEST ANALYSIS STANDARD PLOT PACKAGE Figures 3.5-1 Through 3.5-83 (Cont.)				
Fig. No.	**Component**	**Variables**	**Units**	**Description**
3.5-73	Total system energy	VOID		Calculated foid fraction for ADS-1, ADS-2, and ADS-3
3.5-74	Total system mass	MTOTAL, MTOT0	lbm	Total system fluid mass vs. Initial fluid mass
3.5-75	Total system mass	ERRLOP	lbm	Error in the mass balance (using measured and calculated flows)
3.5-76	Total system mass	ERRLOP1	lbm	Error in the mass balance (using fluid inventory)
3.5-77	Total system mass	MPCLTOT, MPCLO	lbm	Total fluid mass in power channel and loops vs. Initial fluid mass
3.5-78	Total system mass	MACOUT, MCMOUT, MIROUT	lbm	Total integrated mass discharged from accumulators, CMTs, and IRWST
3.5-79	Total system mass	MSOURCE, MSINK, MSOURIN	lbm	Total source inventory, total mass ejected from primary system, and total mass injected to primary system
3.5-80	Total system energy	UADS123, UBREAK, UADS4, UCATCH	Btu	Integrated fluid energy exiting via ADS-1, ADS-2, ADS-3, ADS-4, and the break, and the sum
3.5-81	Total system energy	USURR, UCATCH, UQIN, UFLD-UO, UMTL-UO, USG	Btu	Overall energy balance including integrated rod power, steam generator power, and heat loss to the surroundings, energy exiting via ads and break, energy input via nonsafety systems, and change in primary system fluid and metal energy relative to start of test
3.5-82	Total system energy	UERROR, ERROR-%	Btu, %	Error in overall energy balance, relative to initial fluid and metal energy
3.5-83	System pressure	---	psia	Test event phases and system pressure

The figures listed are proprietary and, therefore,
are not available in the Class 3 version of this report.

These figures are available in the Class 2 version of this report.

3.6 Analysis of the One-Inch Cold-Leg Break without Nonsafety Systems (S01613)

This matrix test simulated a 1-in. break in the bottom of cold leg-B2. The event began with the initiation of the break in cold leg-B2, which was the cold leg with the CMT-B pressure balance line connection. The break location was on the reactor-vessel side of the cold leg from the core makeup tank (CMT) balance line connection. This test was performed without any nonsafety systems' pumps operating. That is, it was performed without the chemical and volume control system (CVCS) makeup pumps, steam generator startup feedwater (SFW) pumps, and normal residual heat removal system (NRHR) pumps. This test is identical to test S00401, with the exception that three passive residual heat removal heat exchanger (PRHR HX) tubes were used in S01613 versus just one PRHR HX tube in test S00401.

3.6.1 Summary of Test Observations

Figure 3.6-83 shows plant primary system pressure during matrix test S01613 (as measured at the top of the pressurizer) during the S01613 event, with selected component actuations and plant responses shown in relation to primary system pressure.

The IDP began with the initiation of the break, which caused the pressurizer to drain. This resulted in a rapid reduction in pressure. The reactor trip (R) signal initiated at [ ]^{a,b,c}, and the safety systems actuation (S) signal initiated at [ ]^{a,b,c}. The R and the S signals initiated the following actions:

- Decay heat simulation (with heat loss compensation) initiated.
- The main steam line isolation valves (MSLIVs) closed.
- The main feedwater isolation valves (MFWIVs) shut off.
- The CMT injection valves opened.
- The passive residual heat removal (PRHR) return flow valve opened.
- The reactor coolant pumps (RCPs) shut down.

The recirculation flow through the CMTs and flow through the PRHR valve started immediately after the isolation valve opened. Boiling in the heated rod bundle was initiated by the reduction of the core and upper-plenum pressure to saturation level. The upper plenum flashed while the fluid level in the upper plenum dropped to the hot-leg elevation. The flashing on the hot-leg side of the core stopped the rapid drop in primary system pressure. When the RCPs shut down (at [ ]^{a,b,c}), the flow through the heater bundle began to oscillate (approximately [ ]^{a,b,c} period). This resulted in oscillations in the rod bundle and upper-plenum void fraction, upper-plenum temperature, and system pressure.

During the initial stages of the pressure decay phase (PDP), the rod bundle void fraction increased. This resulted in an increasing void fraction in the upper plenum and the hot legs. The hot leg-B fluid had a void fraction very close to that observed in the upper plenum. The void fraction in hot leg-A was much lower due to the selective removal of vapor from the hot leg by the PRHR inlet line.

Two-phase flow in the hot legs initiated the draindown of the steam generator U-tubes. Steam from the two-phase mixture collected in the top of the U-tubes, thereby draining the steam generator U-tubes. This stopped the flow through the primary system. The void fraction oscillations observed through the rod bundle and in the upper plenum terminated when the flow through the steam generators stopped.

Approximately [ ]^{a,b,c} into the event the flow through steam generator-B stopped due to the higher void fraction in hot leg-B. Approximately [ ]^{a,b,c} later, the flow through steam generator-A stopped.

Two-phase flow through the PRHR valve had a void fraction significantly greater than seen in the upper plenum. Due to boiling in the rod bundle, two-phase flow entered the hot leg from the upper plenum and flowed through the PRHR HX in the in-containment refueling water storage tank (IRWST). The average integrated void fraction in the PRHR inlet was as high as [ ]^{a,b,c}, which enhanced the PRHR from the primary system when compared with single-phase saturated or subcooled water. When the flow stabilized after the initial flow oscillations, a heat removal rate of [ ]^{a,b,c} was calculated. This calculation was based on the average void fraction of the flow in the PRHR supply line, the flow, the temperature, and the pressure. This calculation assumes a slip coefficient of 1 between steam and water and may give a slightly lower values than the actual heat transfer. It should, therefore, be used for test-to-test comparison only.

When system pressure dropped to saturation pressure for the upper head, the upper head began to drain (at [ ]^{a,b,c}).

When the B-side cold legs had partially emptied, the CMTs converted from the recirculation mode to the draindown mode of injection. This increased the cold injection flow and the rate of system pressure decay. This occurred at approximately [ ]^{a,b,c} for both CMTs.

During the first [ ]^{a,b,c} of this event, [ ]^{a,b,c} of water was expelled through the break while draining the pressurizer, the steam generator U-tubes, the power channel/upper head, the power channel/upper plenum above the hot leg, most of the cold legs, and approximately [ ]^{a,b,c} of the CMTs. The heated rods in the power channel that simulated the core decay heat reduced the power level to approximately [ ]^{a,b,c}. This value consisted of [ ]^{a,b,c} decay heat and [ ]^{a,b,c} heat loss compensation. The break flow was steady, indicating that cold leg-B2 was not totally empty.

The ADS phase began with the actuation of ADS-1 (at approximately [ ]^{a,b,c}). ADS-2 and ADS-3 occurred within the next [ ]^{a,b,c}. The heat loss compensation was terminated from the decay heat simulation when ADS-1 occurred, and the rod bundle power level was reduced to approximately [ ]^{a,b,c}.

The ADS actuation increased the rate of primary system depressurization and resulted in a high level of injection flow from the accumulators. The rapid injection of cold fluid from the accumulators (at

[ ]^{a,b,c}) and CMTs subcooled the whole primary system, temporarily refilling the power channel/upper plenum and the pressurizer. When the accumulator discharge ended, boiling occurred again in the heater bundle, and two-phase flow again occurred in hot leg-A, the PRHR HX, and the ADS via the pressurizer.

The liquid discharge through the break was replaced by saturated steam at approximately [ ]^{a,b,c}. During the ADS phase, approximately 750 lbm of subcooled water were discharged from ADS-1, ADS-2, and ADS-3. This water was primarily supplied by the accumulator discharge and was followed by an increase in rod bundle void fraction after the accumulators drained and only the CMTs provided core injection.

The post-ADS phase began when ADS-4 actuated. ADS-4 occurred at [ ]^{a,b,c} seconds, and the pressurizer water level fell. The fluid discharge through ADS-1, ADS-2, and ADS-3 ended, and fluid was discharged through ADS-4. The pressurizer drained again, and a small amount of CMT flow still entered the direct vessel injection (DVI) line. When system pressure had been reduced below the pressure corresponding to the water elevation head of the IRWST, flow from the IRWST entered the DVI line. Shortly thereafter, the CMT flow ended. The flow from the IRWST subcooled the primary system, the rod bundle boiling slowly ended, and the upper plenum partially refilled. The PRHR drained approximately [ ]^{a,b,c} into the event and was no longer effective. A steady flow of subcooled water was then flowing from the IRWST into the DVI line, through the power channel, and left the primary system through ADS-4.

3.6.2 Analysis of the S01603 Test Data

The analysis of the SPES-2 test was performed using the SPESAN computer code. The code performs a detailed accounting of the coolant inventory in all parts of the system from the start to the end of the test. Also, the internal energy of all components and parts of the facility, including the energy losses from the break and ADS flows, were calculated throughout the event. It is noted that the mass balance and the energy transfer calculations were performed in much greater detail than was performed in WCAP-14309, *Final Data Report.*[1] The results of the test data analysis are presented in Figures 3.6-1 through 3.6-82. Mass balance snapshots for all the major primary system components, at various points of interest throughout the transient, are presented in Table 3.6-1

Mass Balance

Overall Mass Balance

The uncertainty in the overall mass balance is an indication of the overall quality of the test. The total water inventory was tracked from the start until the end of the test. Figures 3.6-74, 3.6-75, and 3.6-76 show the overall mass balance and the error (uncertainty) in mass balance for S01613.

The overall mass balance for S01613 (Figure 3.6.74) shows a small variation of water inventory during the event, resulting from the overall uncertainty in the instrumentation and the assumptions of

the mass balance model used to determine the total water inventory. The average total inventory during the test was indicated to be approximately [ ]^{a,b,c} higher than the initial system mass, and a final mass was indicated to be approximately [ ]^{a,b,c} above the initial mass. Figure 3.6-75 shows the difference between the total mass during the event and the initial mass (mass balance error) when the inventory was calculated by integrating the flows. Figure 3.6-76 shows the mass balance error when inventory was calculated based on the catch tank weight and component level measurements. The mass balance error, based on flow measurements, varied from [ ]^{a,b,c}, while the weight and level measurements resulted in an average error varying approximately from [ ]^{a,b,c} during the event, and a final error of [ ]^{a,b,c} lbm at the end of the event.

Water Inventory for the Power Channel and the Loop

Maintenance of the coolant coverage of the heater bundle was the most critical issue for the power channel. The heater bundle coverage during a loss-of-coolant accident (LOCA) event often consists of two-phase fluid, which can have a very high void fraction. Figure 3.6-40 shows the true level of two-phase fluid in the power channel as measured from the elevation of the top of the core (TAF). Since this represents the true two-phase level, it will be different than the collapsed liquid level in the heater bundle.

For S01613, the two-phase level in the upper plenum decreased to the hot-leg elevation and remained at this elevation for most of the event. The accumulator injection ([ ]^{a,b,c}) partially condensed the steam bubble in the upper plenum causing the level to rise. Following the end of the accumulator injection, the two-phase level again decreased approximately [ ]^{a,b,c} below the hot-leg elevation. This occurred at the time of minimum power channel water inventory, before the IRWST injection started (at [ ]^{a,b,c}) to refill the power channel. The IRWST injection also partially condensed the steam bubble in the upper plenum causing the level to rise above the hot-leg elevation.

The level on the cold side of the power channel is shown in Figures 3.6-42 (annular downcomer) and 3.6-44 (tubular downcomer). The annular downcomer was full until approximately [ ]^{a,b,c} seconds into the event (the end of the accumulator injection). The level then decreased and drained the annular downcomer by [ ]^{a,b,c}, and reached a minimum level in the tubular downcomer at approximately [ ]^{a,b,c}. This corresponded to the time of minimum water inventory in the power channel shown in Figure 3.6-39. Figure 3.6-62 shows the maximum cladding temperature during the event and compares this temperature with the saturation temperature. There was no indication of loss of cooling for the heater rods during this event.

The collapsed fluid level in the rod bundle (Figure 3.6-48), and the rod bundle exit void fraction (Figure 3.6-61) show that the rod bundle was water solid before the break was initiated. The rod bundle exit void fraction was determined from DP-014P which covers the span from the rod bundle near the TAF elevation to the lower part of the upper plenum. Two-phase flow with approximately [ ]^{a,b,c} average void fraction exists in the rod bundle prior to the accumulator injection. During the accumulator injection, the rod bundle became essentially water solid. However, when the accumulator injection ended, the collapsed level again started to decrease. The rod bundle exit void

fraction reached approximately [ ]^{a,b,c} prior to the start of the IRWST injection phase, starting at approximately [ ]^{a,b,c}.

The collapsed level in the upper plenum (Figures 3.6-52 and 3.6-54) decreased to approximately [ ]^{a,b,c} below the hot leg before the accumulator injection, followed by a period when the level in the upper plenum increased above the hot leg during the accumulator injection. This period was followed by a drop in the collapsed level to approximately [ ]^{a,b,c} below the hot leg at the time of minimum water inventory before the IRWST injection started.

The water inventory in the power channel (Figure 3.6-39) had [ ]^{a,b,c} minima: [when the CMT draindown started, before the accumulator injection, and before the IRWST injection.] The third minimum was more severe showing a total power channel inventory of approximately [ ]^{a,b,c} ([ ]^{a,b,c} of starting inventory) at that time. The total primary system inventory (power channel, pressurizer, and loops), shown in Figure 3.6-77, reached approximately [ ]^{a,b,c} of starting inventory) for this minimum.

Water Injection/Ejection

The injected fluid mass from all injection sources is shown in Figure 3.6-78. Figure 3.6-79 shows the total source inventory and the injected and ejected masses during the event. Starting with a total of approximately [ ]^{a,b,c} source inventory, only [ ]^{a,b,c} of available source water) was used by the end of the event.

Energy Balance

PRHR Heat Transfer

The heat transfer from the PRHR to the IRWST gives a unique possibility of comparing heat transfer on the primary and the secondary side. A method of calculating the heat rejection by the PRHR HX into the IRWST is described in Section 2.2-2, and a comparison of three heat transfer calculations is given in Section 4.0. The PRHR primary-side heat transfer was calculated based on the measured exit flow rate, and the difference in enthalpy of the inlet and exit flows. Since the S01613 test had two-phase flow conditions in the hot legs and PRHR, the inlet flow void fraction was determined (Figure 3.6-21) and used to establish the effective enthalpy of the two-phase inlet flow. The outlet flow from the PRHR HX was always subcooled water. The primary side two-phase heat transfer for S01613 (Figure 3.6-19), was considerably greater than the heat transfer measured for single-phase flow through the PRHR during the hot preoperational testing (see WCAP-14309, *Final Data Report*).[1] Figure 3.6-18 shows the calculated heat transfer from the PRHR external tube surface to the water in the IRWST by the three tube section of the HX. The top part of the PRHR HX acted as a condenser, where the steam of the two-phase fluid extracted from hot leg-A was condensed. The top horizontal tube transfers the greatest amount of heat. The condensation process on the inside effectively heated this tube wall temperature above the boiling point for the water in the IRWST, resulting in very effective nucleate boiling heat transfer from the outside surface. The vertical and the bottom

horizontal sections of the heat exchanger remain, for the most part, subcooled the fluid with a less effective free convection heat transfer to the IRWST water and contributed, therefore, far less to the overall heat transfer of the PRHR.

Figure 3.6-17 shows the internal energy of the IRWST water, the integrated power from the primary side of the PRHR HX, and the heat transfer from the PRHR HX external surfaces. The internal energy in the IRWST water was calculated based on thermocouples located at various elevations in the IRWST tank, which were allocated different control volumes to arrive at an effective average temperature. Due to the severe temperature stratification in the IRWST tank, this technique only produced good results until the IRWST started to drain.

For S01613, up to [ ]^{a,b,c} the PRHR primary-side calculation and the IRWST internal energy calculation were very close. After [ ]^{a,b,c}, the calculated IRWST internal energy appeared to increase significantly due to rapid increase of thermocouple reading, measuring temperature below the PRHR horizontal inlet tubes (T-064E). The comparison shown in Figure 3.6-17 indicates that the PRHR primary-side heat transfer from PRHR tube surface calculation gives lower energies until approximately [ ]^{a,b,c} and higher after this time compared to the other two calculations.

Steam Generator Heat Transfer

Figure 3.6-32 shows the heat transfer in the steam generators for S01613, and Figure 3.6-33 shows the pressures on the primary side and the secondary side of the steam generators. Heat transfer was sharply reduced after the pumps were tripped due to the reduction of flow in the tubes. The pressures show that the steam generators were available as heat sinks until approximately [ ]^{a,b,c} into the event, at which time the primary-side pressure dropped below the secondary, making the steam generators a potential heat source for the primary system. Figure 3.6-28 shows the water inventory in the steam generators primary side, which includes inlet and outlet plena and U-tubes. When full, the steam generator inlet and outlet plena contains approximately [ ]^{a,b,c} of water. When the primary-side pressure dropped below the secondary-side pressure (approximately [ ]^{a,b,c}), the steam generators U-tubes were essentially drained of water and contained trapped steam, which became more and more superheated as the primary-side pressure decayed.

The heat transfer calculated for the steam generators decreased rapidly after the pumps were tripped and disappeared after approximately [ ]^{a,b,c}. Also shown in Figure 3.6-32 is the PRHR heat transfer, which removed heat from the system after the steam generators heat transfer had ended.

Overall Energy Balance

Figure 3.6-80 shows the integrated energy of the fluid streams leaving the system. The energy content of the break flow was greatly reduced when ADS-1 occurred, since although the break flow converted to steam, the mass flow rate became very low. For ADS-1, ADS-2 and ADS-3, the same happened when ADS-4 occurred.

Figure 3.6-81 shows all the energy components in the heat balance for the system. Throughout the event, rod bundle power was the dominant heat input to the system, and during the initial part of the event the steam generators provide the dominant heat extraction. When the primary and secondary system pressures equalized, and the steam generator U-tubes drain (about 1800 seconds), the steam generator became thermally isolated from the primary system and did not affect the rest of the event. Figure 3.6-80 shows the energy loss from the break and the ADS flows as calculated based on assumptions described in Section 2.0. The average energy loss from the fluids ejected from the system during the first [ ]^{a,b,c} of the event was approximately [ ]^{a,b,c}. The average energy loss increased to [ ]^{a,b,c} within time period from 4800 to 5700 seconds and was reduced to approximately [ ] from about [ ]^{a,b,c} to the end of the test. From approximately [ ]^{a,b,c}, slightly more energy was generated by the heated rod bundle than left the system through the break, and the overall energy stored within the system slowly increased (metal mass energy decreased and fluid energy increased).

From [ ]^{a,b,c} to the end of the test, more energy left the system through the ADS flows than was generated by the rod bundle, and overall system energy stored within the system (fluid and metal) decreased to compensate.

Figure 3.6-82 shows the accumulated energy balance error during the event. During the initial part of the transient, an increasing error was generated by a greater-than-actual heat transfer being calculated for the steam generator. This was a consequence of an assumed overall heat transfer coefficient (HTC) for the steam generator, which is calculated from full-power/full-flow conditions (before time "0"), which was higher than the actual HTC at the lower flow conditions existing after the pumps have shut down. Figure 3.6-82 also shows that the error in the energy balance peaked at [ ]^{a,b,c} and varied rapidly from [ ]^{a,b,c} (during the accumulator discharge into the primary system, ADS-4, and IRWST actuation). This error was a consequence of the rapid change in the metal energy seen in Figure 3.6-81, which was calculated based on fluid temperatures. In reality, the calculated change of metal energy occurred at a slower rate than indicated by the fluid thermocouples, due to the large thermal inertia of the heavy-walled components. The varying error and the error peak shown in Figure 3.6-82 at [ ]^{a,b,c} are, therefore, a consequence of taking credit for metal heat too fast during the event, and this error disappears after [ ]^{a,b,c} seconds when the metal temperatures catch up with the fluid temperatures. In evaluating the overall error in the accuracy of the energy balance, these peaks were disregarded. The maximum error band for Figure 3.6-82 is approximately -80000 to +20000 Btu, which corresponds [ ]^{a,b,c} of the total fluid energy ejected from the system. The error at the end of the event was approximately [ ]^{a,b,c} of the total ejected fluid energy.

Other Observations

Pressure Decay

Figure 3.6-3 shows the primary system pressure during the S01613 test. Throughout this event, the pressure was controlled by the saturation pressure of the hottest fluid volume in the primary system.

At the initiation of the break, the controlling fluid volume was in the pressurizer and surge line; however, this shifted within the first 400 seconds (after the initial blowdown phase) to the power channel upper plenum.

Figure 3.6-2 shows that the temperature of the upper plenum was equal to the saturation temperature corresponding to the primary system pressure measured in the upper head during the natural circulation phase and into the ADS phase. The pressure stabilized at the saturation pressure for the upper plenum and then continued a slow pressure decay responding to the CMTs injection. Figure 3.6-3 shows the increase in the pressure decay rate that occurred at approximately [ ]^{a,b,c}, when the CMTs transitioned from natural circulation injection to draindown injection which essentially doubled the injection rate of cold water into the DVI. The higher injection rate resulted in a more rapid temperature drop in the upper plenum (fuel exit in Figure 3.6-2), which was reflected in a more rapid pressure decay. With the actuation of ADS-1 at approximately [ ]^{a,b,c}, the pressure dropped rapidly due to the increased rate of mass ejected from the system (Figure 3.6-68), and the increased flow of cold water being injected into the annular downcomer and flowing through the rod bundle. This continued to reduce the power channel inlet plenum temperature, and subcooled the heated rod bundle due to the higher flow. Since the power channel outlet plenum became subcooled at approximately [ ]^{a,b,c}, the hottest fluid in the system was in the pressurizer, the cold legs, and the CMTs, and the pressure was partially supported by the flashing of the fluid in one or several of these locations. When the accumulator discharge ended (approximately [ ]^{a,b,c}), the lower-plenum temperature increased due to the metal heat, and the upper-plenum temperature increased to the saturation temperature and again took over control of the system pressure for the rest of the event. It is noted here that at the end of the accumulator injection, a large amount of nitrogen from the accumulators was injected into the primary system. This injection had very little immediate effect on the primary system, but as will be discussed in Section 4.0, affects the upper plenum, the PRHR HX, and the CMT at later stages of the event.

The actuation of ADS-4 (at approximately [ ]^{a,b,c} seconds) lowered the system pressure sufficiently to allow gravity injection flow from the IRWST into the DVI nozzles. This flow was sufficiently high to subcool the primary system, ending rod bundle boiling and partially collapsing the steam bubble in the upper plenum and bringing the system to a near-atmospheric internal pressure.

Ejection Flows

Figure 3.6-68 shows the individual mass flows leaving the system via the break and the ADS. The individual flow rates are given in Figures 3.6-69, 3.6-70, and 3.6-71. The break and ADS-4 flows consisted of saturated water. For ADS-1, ADS-2, and ADS-3 it was assumed that the flow consisted of saturated water if the void fraction measured in the top of the pressurizer (Figure 3.6-73) was less than 90 percent.

The total mass flow rate leaving the system was reasonably steady for S01613, as seen in Figure 3.6-79. Figure 3.6-80 shows that the energy of the fluid ejection was steady at an average rate of [ ]^{a,b,c} for the first [ ]^{a,b,c} seconds, increased to [ ]^{a,b,c}

and then decreased to [ ]^{a,b,c} for the rest of the event. The increase in energy ejection rate was caused by ADS-1, ADS-2, and ADS-3 actuation. The decrease in energy ejection rate was related to actuation of ADS-4, which caused the pressurizer to drain, converted the ADS-1, ADS-2, and ADS-3 flow to steam with a low mass flow rate, and simultaneously started fluid ejection through ADS-4.

ADS-1 opened at approximately [ ]^{a,b,c} seconds, followed by ADS-2 and ADS-3 within the next [ ]^{a,b,c}. The break flow changes from saturated water to steam, but due to the low mass flow rate (Figure 3.6-68), the energy removal by the break flow (Figure 3.6-80) becomes very low. The energy was leaving the system through ADS-1, ADS-2, and ADS-3 at greater rate than through the break and ADS-4, and provided an effective means of removing the stored metal energy from the system, as seen in Figure 3.6-81. The mass flow rate leaving the system via ADS-1, ADS-2, and ADS-3 during the next [ ]^{a,b,c} was greater than the break flow, and also the energy loss through the ADS-1, ADS-2, and ADS-3 exceeded the energy loss by the break flow (Figure 3.6-80).

ADS-4 opened at approximately [ ]^{a,b,c}, and the ADS-1, ADS-2, and ADS-3 flows converted to steam with a very low mass flow rate and energy loss rate. The ADS-4 flow stabilized at a rate that matched the injection rate from the IRWST (Figure 3.6-79), and the energy removal via ADS-4 was comparable to the heated rod power (Figure 3.6-81).

TABLE 3.6-1
COMPONENT MASS VARIATIONS IN TEST S01613

	Start Fault	End Blowdown	CMT to Draindown	ADS-1 Starts	First Acc. Empty	ADS-4 Starts	IRWST Starts	End of Transient
Event time								
Power channel								
PC: core								
PC: downcomers								
PC: upper plenum								
Hot leg-A								
Hot leg-B								
Cold leg-A								
Cold leg-B								
SG primary-A								
SG primary-B								
Pressurizer+SL								
CMT-A								
CMT-B								
Accumulator-A								
Accumulator-B								
IRWST								

(a,b,c)

TEST ANALYSIS STANDARD PLOT PACKAGE Figures 3.6-1 Through 3.6-83				
Fig. No.	**Component**	**Variables**	**Units**	**Description**
3.6-1	Power channel	CORE-POW	kW	Core power
3.6-2	Power channel	TSAT, TAVTDC, TFOUT	°F	Core inlet/outlet temperature, saturation temperature
3.6-3	Pressurizer	PPZRTOP	psia	System pressure
3.6-4	Steam generator	PSGAS, PSGBS	psia	Primary and secondary pressure in steam generators
3.6-5	Steam generator	TAVCSGA, TAVGSGB	°F	Average fluid temperature in steam generators
3.6-6	CMT	MCMTA, MCMTB	lbm	Fluid mass in CMTs
3.6-7	CMT	CLEVELA, CLEVELB	ft.	Collapsed liquid level in CMTs
3.6-8	CMT	MOUTCMTA, MOUTCMTB, MINCMTA, MINCMTB	lbm	Integrated mass in/out of CMTs
3.6-9	CMT	FLOWOUTA, FLOWOUTB	lbm/sec.	Measured flow out of CMTs
3.6-10	CMT	FLOWINA, FLOWINB	lbm/sec.	Calculated flow into CMTs
3.6-11	CMT	BLFRACA, BLFRACB	Fraction	Fractional differential pressure in cold leg-CMT balance lines
3.6-12	CMT	UTOT-A, UTOT-B	Btu	Fluid energy in CMTs
3.6-13	IRWST/PRHR	MIRWST	lbm	Mass of fluid in IRWST
3.6-14	IRWST/PRHR	LIRWST	ft.	Collapsed liquid level in IRWST
3.6-15	IRWST/PRHR	FIRWST	lbm/sec.	Measured discharge flow from IRWST

TEST ANALYSIS STANDARD PLOT PACKAGE
Figures 3.6-1 Through 3.6-83 (Cont.)

Fig. No.	Component	Variables	Units	Description
3.6-16	IRWST/PRHR	MOUTDVIA, MOUTDVIB	lbm	Integrated mass out of DVI lines
3.6-17	IRWST/PRHR	INT-QCAL, INT-QTUB, U-UO	Btu	Comparison of energy transfer from PRHR tubes to IRWST
3.6-18	IRWST/PRHR	Q-HOR-1, Q-VERT, Q-HOR-2, QTUBEXT	Btu/sec.	Breakdown of heat transfer from different sections of PRHR tube
3.6-19	IRWST/PRHR	Q-CALIM	Btu/sec.	PRHR/IRWST heat transfer calculated on tube side
3.6-20	IRWST/PRHR	FLOWTUBE	lbm/sec.	Measured outlet flow from PRHR tube
3.6-21	IRWST/PRHR	VOID-FRC		Calculated PRHR inlet void fraction
3.6-22	Accumulator	MACCA, MACCB	lbm	Mass of fluid in accumulators
3.6-23	Accumulator	LACCA, LACCB	ft.	Collapsed liquid level in accumulators
3.6-24	Accumulator	MEASFLWA, MEASFLWB	lbm/sec.	Measured flow from accumulators
3.6-25	Accumulator	MOUTACCA, MOUTACCB	lbm	Integrated mass out of accumulators
3.6-26	Accumulator	U-TOT-A, U-TOT-B	Btu	Energy of fluid in accumulators
3.6-27	Accumulator	AIRMASSA, AIRMASSB	lbm	Mass of air exiting accumulators
3.6-28	Steam generator	MSGAP, MSGBP	lbm	Mass of fluid in steam generators - primary side
3.6-29	Steam generator	LSGAH, LSGAC, LSGBH, LSGBC	ft.	Collapsed liquid levels in steam generators - primary side - hot and cold sides of U-tubes

TEST ANALYSIS STANDARD PLOT PACKAGE
Figures 3.6-1 Through 3.6-83 (Cont.)

Fig. No.	Component	Variables	Units	Description
3.6-30	Steam generator	MSGAH, MSGAC, MSGBH, MSBGC	lbm	Mass of fluid in steam generators - primary side - hot and cold sides of U-tubes
3.6-31	Steam generator	LSGSA, LSGSB	ft.	Collapsed liquid levels in steam generators - secondary side
3.6-32	Steam generator	Q-TRNF-A, Q-TRNF-B, Q-CALIM	Btu/sec.	Heat transfer in steam generators heat transfer in PRHR
3.6-33	Steam generator	PRESS-PA, PRESS-PB, PREF-A, PREF-B	psia	Primary and secondary pressure in steam generators
3.6-34	Pressurizer	MPZR	lbm	Fluid mass in pressurizer
3.6-35	Pressurizer	LPZR	ft.	Collapsed liquid level in pressurizer
3.6-36	Pressurizer	MSL	lbm	Fluid mass in surge line
3.6-37	Pressurizer	LSL	ft.	Collapsed liquid level in surge line
3.6-38	Pressurizer	UPZR	Btu	Fluid energy in pressurizer
3.6-39	Power channel	MPCHN	lbm	Total fluid mass in power channel
3.6-40	Power channel	L2PHASE, LDVI, LHL, LCL	ft.	Two-phase liquid level in power channel vs. DVI, hot-leg, and cold-leg elevations
3.6-41	Power channel	MANDC	lbm	Fluid mass in annular downcomer
3.6-42	Power channel	LANDC, LDVI, LHL, LCL	ft.	Collapsed liquid level in annular downcomer vs. DVI, hot-leg, and cold-leg elevations

TEST ANALYSIS STANDARD PLOT PACKAGE Figures 3.6-1 Through 3.6-83 (Cont.)				
Fig. No.	**Component**	**Variables**	**Units**	**Description**
3.6-43	Power channel	MTDC	lbm	Fluid mass in tubular downcomer
3.6-44	Power channel	LTDC, LBOF, LTOF	ft.	Collapsed liquid level in tubular downcomer vs. top of active fuel and bottom of active fuel levels
3.6-45	Power channel	MLOWP	lbm	Fluid mass in lower plenum
3.6-46	Power channel	LLOWP	ft.	Collapsed liquid level in lower plenum
3.6-47	Power channel	MCORE	lbm	Fluid mass in core region
3.6-48	Power channel	LCORE	ft.	Collapsed liquid level in core
3.6-49	Power channel	MFOUT	lbm	Fluid mass in core outlet region
3.6-50	Power channel	LFOUT	ft.	Collapsed liquid level in core outlet region
3.6-51	Power channel	MUPPL	lbm	Fluid mass in the lower portion of the upper plenum
3.6-52	Power channel	LUPPL	ft.	Collapsed liquid level in the lower portion of the upper plenum
3.6-53	Power channel	MUPPU	lbm	Fluid mass in the upper portion of the upper plenum
3.6-54	Power channel	LUPPU	ft.	Collapsed liquid level in the upper portion of the upper plenum
3.6-55	Power channel	MHEAD	lbm	Fluid mass in the upper head
3.6-56	Power channel	LHEAD	ft.	Collapsed liquid level in the upper head

TEST ANALYSIS STANDARD PLOT PACKAGE Figures 3.6-1 Through 3.6-83 (Cont.)				
Fig. No.	**Component**	**Variables**	**Units**	**Description**
3.6-57	Power channel	UPC	Btu	Total fluid energy in power channel
3.6-58	Power channel	Q-FLUX	Btu/sec.-ft.^{2}	Average heat flux on the heated rods
3.6-59	Power channel	STM-RATE	lbm/sec.	Core steam generation rate
3.6-60	Power channel	FLOWCOR	lbm/sec.	Calculated core flow
3.6-61	Power channel	VOIDOUT		Void fraction at core exit
3.6-62	Power channel	TMAX, TSAT, TMAX-TSAT	°F	Maximum clad temperature, saturation temperature and delta
3.6-63	Hot leg	MHLA, MHLB	lbm	Fluid mass in hot legs
3.6-64	Hot leg	FLA, FLB	Fraction	Fractional collapsed liquid level in hot legs
3.6-65	Cold leg	MCLA, MCLB	lbm	Fluid mass in cold legs
3.6-66	Cold leg	LCLA1, LCLA2, LPSA	ft.	Collapsed liquid levels in cold leg-A
3.6-67	Cold leg	LCLB1, LCLB2, LPSB	ft.	Collapsed liquid levels in cold leg-B
3.6-68	Total system mass	MADS1-3, MADS4, BRKMASS	lbm	Catch tank mass for ADS-1, ADS-2, ADS-3, ADS-4, and break
3.6-69	Total system mass	DMADS1-3	lbm/sec.	Calculated flow out ADS 1-3
3.6-70	Total system mass	DMADS4	lbm/sec.	Calculated flow out ADS 4
3.6-71	Total system mass	BRKFLOW	lbm/sec.	Calculated flow out break
3.6-72	Total system energy	UADS123, UADS4, UBREAK	Btu	Integrated fluid energy for ADS-1, ADS-2, ADS-3, ADS4, and the break

TEST ANALYSIS STANDARD PLOT PACKAGE Figures 3.6-1 Through 3.6-83 (Cont.)				
Fig. No.	**Component**	**Variables**	**Units**	**Description**
3.6-73	Total system energy	VOID		Calculated void fraction for ADS-1, ADS-2, and ADS-3
3.6-74	Total system mass	MTOTAL, MOTTO	lbm	Total system fluid mass vs. initial fluid mass
3.6-75	Total system mass	ERRLOP	lbm	Error in the mass balance (using measured and calculated flows)
3.6-76	Total system mass	ERRLOP1	lbm	Error in the mass balance (using fluid inventory)
3.6-77	Total system mass	MPCLTOT, MPCLO	lbm	Total fluid mass in power channel and loops vs. initial fluid mass
3.6-78	Total system mass	MACOUT, MCMOUT, MIROUT	lbm	Total integrated mass discharged from accumulators, CMTs, and IRWST
3.6-79	Total system mass	MSOURCE, MSINK, MSOURIN	lbm	Total source inventory, total mass ejected from primary system, and total mass injected to primary system
3.6-80	Total system energy	UADS123, UBREAK, UADS4, UCATCH	Btu	Integrated fluid energy exiting via ADS-1, ADS-2, ADS-3, ADS-4, and the break, and the sum
3.6-81	Total system energy	USURR, UCATCH, UQIN, UFLD-UO, UMTL-UO, USG	Btu	Overall energy balance including integrated rod power, steam generator power, and heat loss to the surroundings, energy exiting via ads and break, energy input via nonsafety systems, and change in primary system fluid and metal energy relative to start of test
3.6-82	Total system energy	UERROR, ERROR-%	Btu, %	Error in overall energy balance, relative to initial fluid and metal energy
3.6-83	System pressure	—	psia	Test event phases and system pressure

The figures listed are proprietary and, therefore,
are not available in the Class 3 version of this report.

These figures are available in the Class 2 version of this report.

3.7 Analysis of the Two-Inch Direct Vessel Injection Line Break (S00605)

This matrix test simulated a 2-in. direct vessel injection (DVI) line break without any nonsafety systems operating. The event started with the initiation of the break, specifically located on the bottom of the DVI line B between emergency core cooling system (ECCS) injection and the vessel. This test was performed without any nonsafety systems' pumps operating. That is, it was performed without the (CVCS) makeup pumps, steam generator startup feedwater (SFW) pumps and normal residual heat removal (NRHR) pumps.

3.7.1 Summary of Test Observations

Figure 3.7-83 shows the plant primary system pressure during matrix test S00605 (as measured at the top of the pressurizer), with selected component actuations and plant responses shown in relation to the primary system pressure.

The IDP started with the initiation of the break, which caused the pressurizer to drain. This resulted in a rapid reduction in pressure. The reactor trip (R) signal initiated at [ ]^{a,b,c} psia and the safety systems actuation (S) initiated at [ ]^{a,b,c} psia. The R and the S signals initiated the following actions:

- Decay heat simulation (with heat loss compensation) initiated.
- The main steam line isolation valves (MSLIVs) closed.
- The main feedwater isolation valves (MFWIVs) shut off.
- The core makeup tank (CMT) injection valves opened.
- The passive residual heat removal (PRHR) return flow valve opened.
- The reactor coolant pumps (RCPs) shut down.

The recirculation flow through the CMTs and flow through the PRHR started immediately after the CMT injection valves and the PRHR return flow valve were opened. Due to the rapid loss of pressure down to saturation pressure for the rod bundle and upper plenum, boiling was initiated and the upper plenum flashed while the fluid level decreased to the hot-leg elevation. The flashing stopped the rapid drop in primary system pressure. When the RCPs were turned off (at [ ]^{a,b,c} seconds), the flow through the power channel started to oscillate (period approximately [ ]^{a,b,c} seconds), resulting in oscillations in the heated bundle and upper-plenum void fraction, the upper-plenum temperature, and system pressure.

During the pressure decay phase (PDP), the heated bundle void fraction increased. This resulted in an increasing void fraction in the upper plenum and the hot legs. The hot leg-B fluid had a void fraction very close to that of the upper plenum. The void fraction in hot leg-A was much lower due to the removal of vapor from the hot leg by the PRHR inlet line.

The two-phase flow in the hot legs initiated the draindown of the steam generator U-tubes, since steam from the two-phase mixture collected in the top of the U-tubes. This stopped the flow through the

primary system. The void fraction oscillations observed through the heated bundle ended when the flow through the steam generators stopped. The flow through steam generator-B stopped first, approximately [ ]^{a,b,c} seconds into the event, due to the higher void fraction in hot leg-B. Approximately [ ]^{a,b,c} seconds later, flow through steam generator-A stopped.

The two-phase flow through the PRHR had an average integrated void fraction significantly greater than seen in the upper plenum. Due to boiling in the heated bundle, two-phase flow entered the hot leg from the upper plenum and flowed through the PRHR heat exchanger (HX) located in the in-containment refueling water storage tank (IRWST). The average void fraction in the PRHR inlet was as high as [ ]^{a,b,c} percent, which enhanced the PRHR heat removal from the primary system when compared with single-phase saturated or subcooled water. When the flow stabilized after the initial flow oscillations, a heat removal rate of [ ]^{a,b,c} kW was calculated. This calculation was based on the void fraction of the flow in the PRHR supply line, the flow, the temperature, and the pressure. This calculation assumes a slip coefficient of 1 between steam and water and may give a slightly lower value than the actual heat transfer. It should, therefore, be used for test-to-test comparison only.

When the CMT balance lines drained (that is, when cold legs-B had partially emptied), the CMTs converted from the recirculation mode to the draindown mode of injection. This increased the cold injection flow and the rate of system pressure decay. This happened at approximately [ ]^{a,b,c} seconds for both CMTs. When the system pressure dropped to the saturation pressure for the upper head, the upper head started to drain (at 400 seconds).

During the first 805 seconds (until ADS-1 actuation), 740 lbm of subcooled water were discharged through the break while draining the pressurizer, the steam generator U-tubes, the power channel upper head, the power channel upper plenum above the hot leg, and most of the cold legs. The CMTs were partially drained, which initiated the automatic depressurization system (ADS) actuation. The core decay heat simulation had reduced the power level to approximately [ ]^{a,b,c} seconds, which consisted of [ ]^{a,b,c} kW decay heat and [ ]^{a,b,c} kW heat loss compensation. The break flow was steady, indicating that the direct vessel injection (DVI) line was full of water during this period.

The ADS actuation increased the rate of primary system depressurization and resulted in a high injection flow from the accumulators. The rapid injection of cold fluid from the accumulators (at [ ]^{a,b,c} to [ ]^{a,b,c} seconds into the event) temporarily reduced the boiling in the heated bundle and the void fractions of the flow through the heated bundle and the upper plenum. The pressurizer was temporarily refilled.

When the accumulator discharge ended, the boiling intensity increased, and the void fraction of the two-phase flow increased.

The fluid discharge through the break slowed when ADS-1 occurred at [ ]^{a,b,c} seconds (due to the additional fluid discharge through ADS-1, ADS-2, and ADS-3) and was further reduced when the accumulator discharge ended at approximately [ ]^{a,b,c} seconds. Prior to ADS-1, approximately

[ ]^{a,b,c} lbm of fluid were discharged through the break. During the ADS phase, approximately [ ]^{a,b,c} lbm of water were discharged from the ADS-1, ADS-2, and ADS-3. An additional [ ]^{a,b,c} lbm were discharged through the break. This water was supplied primarily by the accumulator discharge and was followed by an increase in heated bundle void fraction after the accumulators drained and only the CMTs provided core injection.

The post-ADS phase began when ADS-4 was actuated. ADS-4 was actuated manually (due to a facility control problem) at [ ]^{a,b,c} seconds. The fluid discharge through ADS-1, ADS-2, and ADS-3 was replaced by steam as the pressurizer drains, and fluid was now discharged through ADS-4. A small amount of CMT flow still entered the direct vessel injection (DVI) line. When the system pressure had been reduced below the pressure corresponding to the water elevation head of the (IRWST), flow from the IRWST entered the DVI line and shortly thereafter, the CMT flow ended. The flow from the IRWST slowly cooled the primary system. The core boiling slowly ended, and the upper plenum partially refilled due to condensation of the steam bubble starting at [ ]^{a,b,c} seconds. The level in the upper plenum above the hot legs again dropped to the hot-leg elevation temporarily at [ ]^{a,b,c} seconds, but was again partially refilled for the rest of the event starting at [ ]^{a,b,c} seconds.

The PRHR drained at approximately [ ]^{a,b,c} seconds into the event. A steady flow of subcooled water was then flowing from the IRWST into the DVI line, through the power channel, and left the primary system through ADS-4 and the DVI line break.

3.7.2 Analysis of the S00605 Test Data

The analysis of the SPES-2 test was performed using the SPESAN computer code. The code performs a detailed accounting of the coolant inventory in all parts of the system from the start to the end of the test. Also, the internal energy of all components and parts of the facility, including the energy losses from the break and ADS flows, are calculated throughout the event. The mass balance and the energy transfer calculations are performed in much greater detail than was performed in WCAP-14309, *Final Data Report*.[1] Mass balance snapshots for all the major primary system components, at various points of interest throughout the transition, are presented in Table 3.7-1.

Mass Balance

Overall Mass Balance

The uncertainty in the overall mass balance was an indication of the overall quality of the test. The total water inventory was tracked from the start until the end of the test. Figures 3.7-74, 3.7-75, and 3.7-76 show the overall mass balance and the error (uncertainty) in mass balance for S00605.

The overall mass balance for S00605 (Figure 3.7-74) shows a small variation of water inventory during the event, resulting from the overall uncertainty in the instrumentation and the assumptions of the mass balance model used to determine the total water inventory. The average total inventory

during the test was indicated to be approximately [ ]^{a,b,c} lbm higher than the initial system mass, and a final mass was indicated to be approximately [ ]^{a,b,c} lbm above the initial mass. Figure 3.7-75 shows the difference between the total mass during the event and the initial mass (mass balance error) when the inventory was calculated by integrating the flows. Figure 3.7-76 shows the mass balance error when inventory was calculated based on the catch tank weight and component level measurements. The mass balance error, based on flow measurements, varied from -15 to +65 lbm; the weight and level measurements resulted in an average error varying approximately from +10 to +80 lbm during the event and a final error of +80 lbm at the end of the event.

Water Inventory for the Power Channel and the Loop

Maintenance of the coolant coverage of the heated bundle was the most critical issue for the power channel. The heated bundle coverage during a loss-of-coolant accident (LOCA) event often consists of two-phase fluid, which can have a very high void fraction. Figure 3.7-40 shows the true level of two-phase fluid in the power channel as measured from the elevation of the top of the core (TAF). Since this represents the true two-phase level, it will be different than the collapsed liquid level in the heated bundle.

For S00605, the two-phase level in the upper plenum decreased to the hot-leg elevation and remained at this elevation until the ADS-1 was actuated. After the ADS-1 actuation the level decreased to approximately [ ]^{a,b,c} ft. below the hot-leg elevation. The accumulator injection ([ ]^{a,b,c} seconds) partially condensed the steam bubble in the upper plenum, causing the level to rise to the hot-leg elevation. Following the end of the accumulator injection, the two-phase level again decreased, this time to approximately [ ]^{a,b,c} ft. below the hot-leg elevation. This occurred at the time of minimum power channel water inventory, before the IRWST injection started to refill the power channel (at [ ]^{a,b,c} seconds). The IRWST injection also partially condensed the steam bubble in the upper plenum, causing the level to rise above the hot-leg elevation.

The level on the cold side of the power channel is shown in Figures 3.7-42 (annular downcomer) and 3.7-44 (tubular downcomer). The annular downcomer was full until approximately [ ]^{a,b,c} seconds into the event. At that time, the level started to decrease, but it was maintained approximately [ ]^{a,b,c} ft. below the elevation of the hot leg until after the end of the accumulator injection (approximately [ ]^{a,b,c} seconds). The level then decreased and drained the annular downcomer and reached a minimum level in the tubular downcomer at approximately [ ]^{a,b,c} seconds. This corresponded to the time of minimum water inventory in the power channel shown in Figure 3.7-39. Figure 3.7-62 shows the maximum cladding temperature during the event and compares this temperature with the saturation temperature. There was no indication of loss of cooling for the heater rods during this event.

The collapsed fluid level in the rod bundle (Figure 3.7-48), and the rod bundle exit void fraction (Figure 3.7-61) show that the rod bundle was water solid before the break was initiated. The rod bundle exit void fraction was determined from DP-014P, which covers the span from the rod bundle near the TAF elevation to the lower part of the upper plenum. Two-phase flow, with approximately

[ ]^{a,b,c} percent average void fraction, exists in the rod bundle prior to the accumulator injection. The accumulator injection did not change the rod bundle exit void fraction significantly. When the accumulator injection ended, the collapsed level again started to decrease. The rod bundle exit void fraction reached approximately [ ]^{a,b,c} percent prior to the start of the IRWST injection phase, starting at approximately [ ]^{a,b,c} seconds.

The collapsed level in the upper plenum (Figures 3.7-52 and 3.7-54) decreased to approximately [ ]^{a,b,c} ft. below the hot leg before the accumulator injection, followed by a period when the level in the upper plenum increased, then decreased to [ ]^{a,b,c} ft. below the hot-leg elevation during the accumulator injection (at approximately [ ]^{a,b,c} seconds) and temporarily increased to [ ]^{a,b,c} ft. below the hot-leg elevation. This period was followed by a drop in the collapsed level to approximately [ ]^{a,b,c} ft. below the hot leg at the time of minimum water inventory before the IRWST injection started.

The water inventory in the power channel (Figure 3.7-39) had three minima; when the CMT draindown started, during the accumulator injection, and before the IRWST injection. The third minimum was more severe, showing a total power channel inventory of approximately [ ]^{a,b,c} lbm ([ ]^{a,b,c} percent of starting inventory) at that time. The total primary system inventory (power channel, pressurizer and loops), shown in Figure 3.7-77, reaches approximately [ ]^{a,b,c} lbm ([ ]^{a,b,c} percent of starting inventory) for this minimum.

Water Injection/Ejection

The injected fluid mass from all injection sources is shown in Figure 3.7-78. Figure 3.7-79 shows the total source inventory and the injected and ejected masses during the event. Starting with a total of approximately [ ]^{a,b,c} lbm source inventory, only [ ]^{a,b,c} lbm ([ ]^{a,b,c} percent of available source water) was used by the end of the event.

Energy Balance

PRHR Heat Transfer

The heat transfer from the PRHR to the IRWST gave a unique possibility of comparing heat transfer on the primary and the secondary side. A method of calculating the heat rejection by the PRHR HX into the IRWST is described in Section 2.0, and a comparison of three heat transfer calculations are given in Section 4.0. The PRHR primary-side heat transfer was calculated based on the measured exit flow rate, and the difference in enthalpy of the inlet and exit flows. Since the S00605 test had two-phase flow conditions in the hot legs and PRHR, the inlet flow void fraction was determined (Figure 3.7-21) and used to establish the effective enthalpy of the two-phase inlet flow. The outlet flow from the PRHR HX was always subcooled water. The primary-side two-phase heat transfer for S00605, shown in Figure 3.7-19, was greater than the heat transfer measured for single phase flow through the PRHR during the hot pre-operational testing (see WCAP-14309, *Final Data Report*).[1] Figure 3.7-18 shows the calculated heat transfer from the PRHR external tube surface to the water in

the IRWST by the three-tube section of the HX. The top part of the PRHR HX acted as a condenser, where the steam of the two-phase fluid extracted from hot leg-A was condensed. The top horizontal tube transfers the greatest amount of heat. The condensation process on the inside effectively heated this tube wall temperature above the boiling point for the water in the IRWST, resulting in very effective nucleate boiling heat transfer from the outside surface. The vertical and the bottom horizontal sections of the heat exchanger remain for the most part, subcooled with a less effective free convection heat transfer to the IRWST water and contributed, therefore, far less to the overall heat transfer of the PRHR.

Figure 3.7-17 shows the internal energy of the IRWST water, the integrated power from the primary side of the PRHR HX, and the heat transfer from the PRHR heat exchanger external surfaces. The internal energy in the IRWST water was calculated based on thermocouples located at various elevations in the IRWST tank, which were allocated different control volumes to arrive at an effective average temperature. Due to the severe temperature stratification in the IRWST tank, this technique only produces good results until the IRWST started to drain.

For S00605 there was good correlation between the two heat transfer calculations. Up to [ ]^{a,b,c} seconds, the heat transfer from the PRHR external tube surface calculation and the IRWST internal energy calculation are very close. After [ ]^{a,b,c} seconds, the IRWST internal energy appeared to increase significantly due to the effect of draindown on the thermocouple readings. However, since there is very little energy being provided by the PRHR after [ ]^{a,b,c} seconds, this apparent increase does not reflect an actual increase in the average water temperature and IRWST internal energy. The comparison shown in Figure 3.7-17 indicates that the PRHR primary-side heat transfer calculation gives significantly lower energies than the other two because, for S00605, the channels DP-A81AE and DP-81BE failed, and for this calculation, incorrect void fraction 0 was used.

Steam Generator Heat Transfer

Figure 3.7-32 shows the heat transfer in the steam generators for S00605, and Figure 3.7-33 shows the pressures on the primary side and the secondary side of the steam generators. Figure 3.7-32 shows a dramatic decrease in heat transfer corresponding to the pump trip. The pressures show that the steam generators were available as heat sinks until approximately [ ]^{a,b,c} seconds into the event, at which time the primary-side pressure dropped below the secondary making the steam generators a potential heat source for the primary system. Figure 3.7-28 shows the water inventory in the steam generators primary side, which includes inlet and outlet plena and U-tubes. When full, the steam generator inlet and outlet plena contains approximately [ ]^{a,b,c} lbm of water. When the primary-side pressure dropped below the secondary-side pressure (approximately [ ]^{a,b,c} seconds), the steam generators U-tubes are essentially drained for water and contain trapped steam, which became more and more superheated as the primary side pressure decayed.

The heat transfer calculated for the steam generators decreased rapidly after the pumps are tripped, and disappears after approximately [ ]^{a,b,c} seconds. Also shown in Figure 3.7-32 is the PRHR heat transfer, which removed heat from the system after the steam generators heat transfer had ended.

Overall Energy Balance

Figure 3.7-80 shows the integrated energy of the fluid streams leaving the system. The energy content of the break flow was greatly reduced when ADS-1 occurred, since although the break flow converted to steam, the mass flow rate became very low. For ADS-1, ADS-2 and ADS-3, the same happened when ADS-4 occurred.

Figure 3.7-81 shows all the energy components in the heat balance for the system. Throughout the event, rod bundle power was the dominant heat input to the system, and during the initial part of the event, the steam generators provide the dominant heat extraction. When the primary and secondary system pressures equalized, and the steam generator U-tubes drained (about [ ]^{a,b,c} seconds), the steam generator became thermally isolated from the primary system and did not affect the rest of the event. Figure 3.7-80 shows the energy loss from the break and the ADS flows as calculated based on assumptions described in 2.0. The average energy loss from the fluids ejected from the system during the first [ ]^{a,b,c} seconds of the event was approximately [ ]^{a,b,c} kW) and then was reduced to approximately [ ]^{a,b,c} from about 1800 seconds to the end of the test. From approximately [ ]^{a,b,c} seconds more energy left the system through the ADS flows than was generated by the rod bundle, and overall system energy stored within the system (fluid and metal) decreased to compensate.

After approximately [ ]^{a,b,c} seconds, the metal and fluid energy stabilize in the system, and the rate of the fluid energy leaving the system (primarily via ADS-4) matched the core input power well. This steady-state condition existed for the rest of the event.

Figure 3.7-82 shows the accumulated energy balance error during the event. During the initial part of the transient, an increasing error was generated by a greater than actual heat transfer being calculated for the steam generator. This was a consequence of an assumed overall heat transfer coefficient (HTC) for the steam generator, which was calculated from full-power/full-flow conditions (before time 0), which was higher than the actual HTC at the lower flow conditions existing after the pumps have shut down. Figure 3.7-82 also shows that the error in the energy balance varied rapidly from [ ]^{a,b,c} seconds (during the accumulator discharge into the primary system, ADS-4 and IRWST actuation). This error was a consequence of the rapid change in the metal energy seen in Figure 3.7-81, which was calculated based on fluid temperatures. In reality, the calculated change of metal energy occurred at a slower rate than indicated by the fluid thermocouples due to the large thermal inertia of the heavy walled components. The varying error and the error peak shown in Figure 3.7-82 at [ ]^{a,b,c} seconds were, therefore, a consequence of taking credit for metal heat too fast during the event. After [ ]^{a,b,c} seconds the metal temperatures caught up with the fluid temperatures. The maximum error band for Figure 3.7-82 is approximately -120000 to +20000 Btu, which corresponded to within [ ]^{a,b,c} percent of the total fluid energy ejected from the system. The error at the end of the event is approximately 1 percent of the total ejected fluid energy.

Other Observations

Pressure Decay

Figure 3.7-3 shows the primary system pressure during the S00605 test. Throughout this event, the pressure was controlled by the saturation pressure of the hottest fluid volume in the primary system. At the initiation of the break, the controlling fluid volume was in the pressurizer and surge line; however, this shifted within the first [ ]^{a,b,c} seconds (after the initial blowdown phase) to the power channel upper plenum.

Figure 3.7-2 shows that the temperature of the upper plenum was equal to the saturation temperature corresponding to the primary system pressure measured in the upper head during the natural circulation phase and into the ADS phase. The pressure stabilized at the saturation pressure for the upper plenum, and then continued a slow pressure decay responding to the CMTs injection. Figure 3.7-3 shows an increase in the pressure decay rate that occurred at approximately [ ]^{a,b,c} seconds, after the CMTs transitioned from natural circulation injection to draindown injection, which essentially doubled the injection rate of cold water into the DVI. The higher injection rate resulted in a more rapid temperature drop in the upper plenum (fuel exit in Figure 3.7-2), which was reflected in a more rapid pressure decay. With the actuation of ADS-1 at approximately [ ]^{a,b,c} seconds, the pressure dropped rapidly due to the increased rate of mass ejected from the system (Figure 3.7-68), and the increased flow of cold water being injected into the annular downcomer and flowing through the rod bundle. This continued to reduce the PC inlet plenum temperature, and subcooled the heated rod bundle due to the higher flow. At the end of the accumulator injection, some nitrogen from accumulator-A was injected into the primary system. This injection had very little immediate effect on the primary system, but as will be discussed in Section 4.0, affects the upper plenum, the PRHR heat exchanger, and the CMT at later stages of the event.

The actuation of ADS-4 (at approximately [ ]^{a,b,c} seconds) lowered the system pressure sufficiently to allow gravity injection flow from the IRWST into the DVI nozzles. This flow was sufficiently high to subcool the primary system, ending rod bundle boiling and partially collapsing the steam bubble in the upper plenum, and bringing the system to a near atmospheric internal pressure.

Ejection Flows

Figure 3.7-68 shows the individual mass flows leaving the system via the break and the ADS. The individual flow rates are given in Figures 3.7-69, 3.7-70, and 3.7-71. The break and ADS-4 flows consisted of saturated water. For ADS-1, ADS-2, and ADS-3 it was assumed that the flow consisted of saturated water if the void fraction measured in the top of the pressurizer (Figure 3.7-73) was less than [ ]^{a,b,c} percent.

The total mass flow rate leaving the system was reasonably steady for S00605, as seen in Figure 3.7-79. Figure 3.7-80 shows that the energy of the fluid ejection was nearly steady at an average rate of [ ]^{a,b,c} Btu/sec. for the first [ ]^{a,b,c} seconds, and then decreased to [ ]^{a,b,c} Btu/sec. for the rest of

the event. The decrease in energy ejection rate was related to actuation of ADS-4, which caused the pressurizer to drain, converted the ADS-1, ADS-2, and ADS-3 flow to steam with a low-mass flow rate, and simultaneously started fluid ejection through ADS-4.

ADS-1 opened at approximately [ ]^{a,b,c} seconds, followed by ADS-2 and ADS-3 within the next [ ]^{a,b,c} seconds. Due to the low mass flow rate (Figure 3.7-68) and a relatively low temperature in the DVI line, the energy removal by the break flow (Figure 3.7-80) becomes very low. The energy was leaving the system through ADS-1, ADS-2, and ADS-3 at greater rate than through the break and ADS-4, and provided an effective means of removing the stored metal energy from the system, as seen in Figure 3.7-81. The mass flow rate leaving the system via ADS-1, ADS-2, and ADS-3 during the next [ ]^{a,b,c} seconds was greater than the break flow, and also the energy loss through the ADS-1, ADS-2, and ADS-3, exceeded the energy loss by the break flow (Figure 3.7-80) in this time period.

ADS-4 opened at approximately [ ]^{a,b,c} seconds, and the ADS-1, ADS-2, and ADS-3 flows converted to steam with a very low mass flow rate and energy loss rate. The ADS-4 flow stabilized at a rate which matched the injection rate from the IRWST (Figure 3.7-79), and the energy removal via ADS-4 was comparable to the heated rod power (Figure 3.7-81).

TABLE 3.7-1
COMPONENT MASS VARIATIONS IN TEST S00605

	Start Fault	End Blowdown	CMT to Draindown	ADS-1 Starts	First Acc. Empty	ADS-4 Starts	IRWST Starts	End of Transient
Event time								
Power channel								
PC: core								
PC: downcomers								
PC: upper plenum								
Hot leg-A								
Hot leg-B								
Cold leg-A								
Cold leg-B								
SG primary-A								
SG primary-B								
Pressurizer+SL								
CMT-A								
CMT-B								
Accumulator-A								
Accumulator-B								
IRWST								

a,b,c

TEST ANALYSIS STANDARD PLOT PACKAGE Figures 3.7-1 Through 3.7-83				
Fig. No.	**Component**	**Variables**	**Units**	**Description**
3.7-1	Power channel	CORE-POW	kW	Core power
3.7-2	Power channel	TSAT, TAVTDC, TFOUT	°F	Core inlet/outlet temperature, saturation temperature
3.7-3	Pressurizer	PPZRTOP	psia	System pressure
3.7-4	Steam generator	PSGAS, PSGBS	psia	Primary and secondary pressure in steam generators
3.7-5	Steam generator	TAVGSGA,TAVGSGB	°F	Average fluid temperature in steam generators
3.7-6	CMT	MCMTA, MCMTB	lbm	Fluid mass in CMTs
3.7-7	CMT	CLEVELA, CLEVELB	ft.	Collapsed liquid level in CMTs
3.7-8	CMT	MOUTCMTA, MOUTCMTB, MINCMTA, MINCMTB	lbm	Integrated mass in/out of CMTs
3.7-9	CMT	FLOWOUTA, FLOWOUTB	lbm/sec.	Measured flow out of CMTs
3.7-10	CMT	FLOWINA, FLOWINB	lbm/sec.	Calculated flow into CMTs
3.7-11	CMT	BLFRACA, BLFRACB	Fraction	Fractional differential pressure in cold leg-CMT balance lines
3.7-12	CMT	UTOT-A, UTOT-B	Btu	Fluid energy in CMTs
3.7-13	IRWST/PRHR	MIRWST	lbm	Mass of fluid in IRWST
3.7-14	IRWST/PRHR	LIRWST	ft.	Collapsed liquid level in IRWST
3.7-15	IRWST/PRHR	FIRWST	lbm/sec.	Measured discharge flow from IRWST

TEST ANALYSIS STANDARD PLOT PACKAGE Figures 3.7-1 Through 3.7-83 (Cont.)				
Fig. No.	**Component**	**Variables**	**Units**	**Description**
3.7-16	IRWST/PRHR	MOUTDVIA, MOUTDVIB	lbm	Integrated mass out of DVI lines
3.7-17	IRWST/PRHR	INT-QCAL, INT-QTUB, U-UO	Btu	Comparison of energy transfer from PRHR tubes to IRWST
3.7-18	IRWST/PRHR	Q-HOR-1, Q-VERT, Q-HOR-2, QTUBEXT	Btu/sec.	Breakdown of heat transfer from different sections of PRHR tube
3.7-19	IRWST/PRHR	Q-CALIM	Btu/sec.	PRHR/IRWST heat transfer calculated on tube side
3.7-20	IRWST/PRHR	FLOWTUBE	lbm/sec.	Measured outlet flow from PRHR tube
3.7-21	IRWST/PRHR	VOID-FRC		Calculated PRHR inlet void fraction
3.7-22	Accumulator	MACCA, MACCB	lbm	Mass of fluid in accumulators
3.7-23	Accumulator	LACCA, LACCB	ft.	Collapsed liquid level in accumulators
3.7-24	Accumulator	MEASFLWA, MEASFLWB	lbm/sec.	Measured flow from accumulators
3.7-25	Accumulator	MOUTACCA, MOUTACCB	lbm	Integrated mass out of accumulators
3.7-26	Accumulator	U-TOT-A, U-TOT-B	Btu	Energy of fluid in accumulators
3.7-27	Accumulator	AIRMASSA, AIRMASSB	lbm	Mass of air exiting accumulators
3.7-28	Steam generator	MSGAP, MSGBP	lbm	Mass of fluid in steam generators - primary side
3.7-29	Steam generator	LSGAH, LSGAC, LSGBH, LSGBC	ft.	Collapsed liquid levels in steam generators - primary side - hot and cold sides of U-tubes

TEST ANALYSIS STANDARD PLOT PACKAGE Figures 3.7-1 Through 3.7-83				
Fig. No.	**Component**	**Variables**	**Units**	**Description**
3.7-30	Steam generator	MSGAH, MSGAC, MSGBH, MSBGC	lbm	Mass of fluid in steam generators - primary side - hot and cold sides of U-tubes
3.7-31	Steam generator	LSGSA, LSGSB	ft.	Collapsed liquid levels in steam generators - secondary side
3.7-32	Steam generator	Q-TRNF-A, Q-TRNF-B, Q-CALIM	Btu/sec.	Heat transfer in steam generators heat transfer in PRHR
3.7-33	Steam generator	PRESS-PA, PRESS-PB, PREF-A, PREF-B	psia	Primary and secondary pressure in steam generators
3.7-34	Pressurizer	MPZR	lbm	Fluid mass in pressurizer
3.7-35	Pressurizer	LPZR	ft.	Collapsed liquid level in pressurizer
3.7-36	Pressurizer	MSL	lbm	Fluid mass in surge line
3.7-37	Pressurizer	LSL	ft.	Collapsed liquid level in surge line
3.7-38	Pressurizer	UPZR	Btu	Fluid energy in pressurizer
3.7-39	Power channel	MPCHN	lbm	Total fluid mass in power channel
3.7-40	Power channel	L2PHASE, LDVI, LHL, LC	ft.	Two-phase liquid level in power channel vs. DVI, hot-leg, and cold-leg elevations
3.7-41	Power channel	MANDC	lbm	Fluid mass in annular downcomer
3.7-42	Power channel	LANDC, LDVI, LHL, LCL	ft.	Collapsed liquid level in annular downcomer vs. DVI, hot-leg, and cold-leg elevations

TEST ANALYSIS STANDARD PLOT PACKAGE Figures 3.7-1 Through 3.7-83 (Cont.)				
Fig. No.	**Component**	**Variables**	**Units**	**Description**
3.7-43	Power channel	MTDC	lbm	Fluid mass in tubular downcomer
3.7-44	Power channel	LTDC, LBOF, LTOF	ft.	Collapsed liquid level in tubular downcomer vs. top of active fuel and bottom of active fuel levels
3.7-45	Power channel	MLOWP	lbm	Fluid mass in lower plenum
3.7-46	Power channel	LLOWP	ft.	Collapsed liquid level in lower plenum
3.7-47	Power channel	MCORE	lbm	Fluid mass in core region
3.7-48	Power channel	LCORE	ft.	Collapsed liquid level in core
3.7-49	Power channel	MFOUT	lbm	Fluid mass in core outlet region
3.7-50	Power channel	LFOUT	ft.	Collapsed liquid level in core outlet region
3.7-51	Power channel	MUPPL	lbm	Fluid mass in the lower portion of the upper plenum
3.7-52	Power channel	LUPPL	ft.	Collapsed liquid level in the lower portion of the upper plenum
3.7-53	Power channel	MUPPU	lbm	Fluid mass in the upper portion of the upper plenum
3.7-54	Power channel	LUPPU	ft.	Collapsed liquid level in the upper portion of the upper plenum
3.7-55	Power channel	MHEAD	lbm	Fluid mass in the upper head
3.7-56	Power channel	LHEAD	ft.	Collapsed liquid level in the upper head

TEST ANALYSIS STANDARD PLOT PACKAGE Figures 3.7-1 Through 3.7-83 (Cont.)				
Fig. No.	**Component**	**Variables**	**Units**	**Description**
3.7-57	Power channel	UPC	Btu	Total fluid energy in power channel
3.7-58	Power channel	Q-FLUX	Btu/sec.-ft.^{2}	Average heat flux on the heated rods
3.7-59	Power channel	STM-RATE	lbm/sec.	Core steam generation rate
3.7-60	Power channel	FLOWCOR	lbm/sec.	Calculated core flow
3.7-61	Power channel	VOIDOUT		Void fraction at core exit
3.7-62	Power channel	TMAX, TSAT, TMAX-TSAT	°F	Maximum clad temperature, saturation temperature and delta
3.7-63	Hot leg	MHLA, MHLB	lbm	Fluid mass in hot legs
3.7-64	Hot leg	FLA, FLB	Fraction	Fractional collapsed liquid level in hot legs
3.7-65	Cold leg	MCLA, MCLB	lbm	Fluid mass in cold legs
3.7-66	Cold leg	LCLA1, LCLA2, LPSA	ft.	Collapsed liquid levels in cold leg-A
3.7-67	Cold leg	LCLB1, LCLB2, LPSB	ft.	Collapsed liquid levels in cold leg-B
3.7-68	Total system mass	MADS1-3, MADS4, BRKMASS	lbm	Catch tank mass for ADS-1, ADS-2, ADS-3, ADS-4, and break
3.7-69	Total system mass	DMADS1-3	lbm/sec.	Calculated flow out ADS-1, ADS-2, ADS-3
3.7-70	Total system mass	DMADS4	lbm/sec.	Calculated flow out ADS-4
3.7-71	Total system mass	BRKFLOW	lbm/sec.	Calculated flow out break
3.7-72	Total system energy	UADS123, UADS4, UBREAK	Btu	Integrated fluid energy for ADS-1, ADS-2, ADS-3, ADS4, and the break

TEST ANALYSIS STANDARD PLOT PACKAGE
Figures 3.7-1 Through 3.7-83 (Cont.)

Fig. No.	Component	Variables	Units	Description
3.7-73	Total system energy	VOID		Calculated void fraction for ADS-1, ADS-2, and ADS-3
3.7-74	Total system mass	MTOTAL, MTOT0	lbm	Total system fluid mass vs. initial fluid mass
3.7-75	Total system mass	ERRLOP	lbm	Error in the mass balance (using measured and calculated flows)
3.7-76	Total system mass	ERRLOP1	lbm	Error in the mass balance (using fluid inventory)
3.7-77	Total system mass	MPCLTOT, MPCLO	lbm	Total fluid mass in power channel and loops vs. Initial fluid mass
3.7-78	Total system mass	MACOUT, MCMOUT, MIROUT	lbm	Total integrated mass discharged from accumulators, CMTs, and IRWST
3.7-79	Total system mass	MSOURCE, MSINK, MSOURIN	lbm	Total source inventory, total mass ejected from primary system, and total mass injected to primary system
3.7-80	Total system energy	UADS123, UBREAK, UADS4, UCATCH	Btu	Integrated fluid energy exiting via ADS-1, ADS-2, ADS-3, ADS-4, and the break, and the sum
3.7-81	Total system energy	USURR, UCATCH, UQIN, UFLD-UO, UMTL-UO, USG	Btu	Overall energy balance including integrated rod power, steam generator power, and heat loss to the surroundings, energy exiting via ads and break, energy input via nonsafety systems, and change in primary system fluid and metal energy relative to start of test
3.7-82	Total system energy	UERROR, ERROR-%	Btu, %	Error in overall energy balance, relative to initial fluid and metal energy
3.7-83	System pressure	--	psia	Test event phases and system pressure

The figures listed are proprietary and, therefore,
are not available in the Class 3 version of this report.

These figures are available in the Class 2 version of this report.

3.8 Analysis of the Double-Ended Guillotine Direct Vessel Injection Line Break (S00706)

This matrix test simulated a double-ended guillotine (DEG) direct vessel injection-B (DVI-B) line break without any nonsafety systems operating. The event started with the initiation of the break located on the DVI-B line. For this break, the test facility was set up such that the break flows from the CMT-B side and the vessel side of the break were measured separately; the CMT-side break flow was measured by IF040P, and the vessel side was measured by IF005P (Figure 3.8-84).

This test was performed without any nonsafety systems' pumps operating. That is, it was performed without the chemical and volume control system (CVCS) makeup pumps, steam generator startup feedwater (SFW) pumps, and normal residual heat removal (NRHR) pumps.

3.8.1 Summary of Test Observations

Figure 3.8-83 shows the plant primary system pressure during matrix test S00706 (as measured at the top of the pressurizer), with selected component actuations and plant responses shown in relation to the primary system pressure.

This event is asymmetric for the plant since the emergency core cooling injection from the B side of the plant is lost. The event started with the initiation of the break in the DVI line by opening the two break line valves (Figure 3.8-83). During the first [ ]^{a,b,c}, [ ]^{a,b,c} of subcooled water were discharged through the CMT side of the break, while draining CMT-B and accumulator-B (most of this occurred in the first [ ]^{a,b,c}) directly into the collection tank without entering the primary system. The rapid draining of CMT-B initiated the ADS-1 at [ ]^{a,b,c}.

The IDP started with the initiation of the break, which caused the pressurizer to drain. This resulted in a rapid reduction in pressure. The reactor trip (R) signal initiated at [ ]^{a,b,c}, and the safety systems actuation (S) signal initiated at [ ]^{a,b,c}. The R and the S signals initiated the following actions:

- Decay heat simulation (with heat loss compensation) initiated.
- The main steam line isolation valves (MSLIVs) closed.
- The main feedwater isolation valves (MFWIVs) shut off.
- The core makeup tank (CMT) injection valves opened.
- The passive residual heat removal (PRHR) return flow valve opened.
- The reactor coolant pumps (RCPs) shut down.

The recirculation flow through CMT-A and the PRHR flow started immediately after the CMT injection valve and the PRHR return flow valve were opened. Due to the rapid loss of pressure to the saturation pressure for the heater bundle region and upper plenum, heater bundle boiling was initiated and the upper plenum flashed while the fluid level dropped below the hot-leg elevation. The flashing slowed the rapid drop in primary system pressure. When the RCPs were shut off (at [ ]^{a,b,c}), the flow through the power channel started to oscillate. This resulted in oscillations in the heater

bundle and upper-plenum void fraction, upper-plenum temperature, and system pressure. The oscillations ended approximately [ ]^{a,b,c} into the event, when the flow through the steam generators stopped.

During the pressure decay phase (PDP), the boiling in the heater bundle increased. This resulted in an increasing void fraction in the upper plenum and the hot legs. The hot legs contained two-phase fluid that had a void fraction very close to that shown in the upper plenum. The void fraction in hot leg-A was slightly lower than hot leg-B due to the removal of vapor from hot leg-A by the PRHR.

The two-phase flow in the hot legs initiated draindown of the steam generator U-tubes since steam from the two-phase mixture collected in the top of the U-tubes, thereby draining the steam generator U-tubes. The flow through steam generator-B stopped approximately [ ]^{a,b,c} into the event, and the flow through steam generator-A approximately [ ]^{a,b,c} later.

The two-phase flow through the PRHR had an average integrated void fraction significantly greater than seen in the upper plenum. Due to boiling in the heater bundle, two-phase flow entered the hot legs from the upper plenum, and flowed through the PRHR heat exchanger (HX) in the in-containment refueling water storage tank (IRWST). The average integrated void fraction in the PRHR inlet was as high as 80 to 95 percent, which enhanced the PRHR heat removal from the primary system when compared with that obtainable with single-phase saturated or subcooled water. The PRHR flow was not a uniform two-phase mixture. Instead, it consisted of slugs of water separated by slugs of steam, depending on the level in the upper plenum. The PRHR inlet nozzle was located on the top of the horizontal pipe of hot leg-A. The hot leg was alternately filled and partially drained, responding to small level changes in the upper plenum.

When the flow stabilized after the initial flow oscillations, a heat removal rate of [ ]^{a,b,c} was calculated. This calculation was based on the average void fraction of the flow in the PRHR supply line, the flow, the temperature, and the pressure. The calculation assumed a slip coefficient of 1 between steam and water and may give slightly lower value than the actual heat transfer. It should, therefore, be used for test-to-test comparison only.

At [ ]^{a,b,c}, when draindown of the CMT-A balance line occurred (that is, when the cold legs had partially emptied), CMT-A converted from the recirculation mode to the draindown mode of injection. This increased the cold injection flow and the rate of system pressure decay. The upper head started to drain when the system pressure dropped to the saturation pressure for the upper head at [ ]^{a,b,c} and was completely drained at [ ]^{a,b,c}.

During the first [ ]^{a,b,c} (ADS-1), [ ]^{a,b,c} of water were discharged through the power channel side of the break, while draining the cold leg and the annular downcomer to the DVI nozzle elevation. A two-phase mixture existed in the hot leg up to the lower part of the steam generator U-tubes (hot side). The pressurizer and the power channel upper plenum above the hot-leg elevation were drained. CMT-B was partially drained, which initiated the ADS actuation. The core decay heat simulation reduced the heater bundle power level to approximately [ ]^{a,b,c} before ADS-1

occurred at [ ]^{a,b,c}, consisting of [ ]^{a,b,c} decay heat and [ ]^{a,b,c} heat loss compensation. The power measured for the heater bundle was approximately twice that specified for this test for the first [ ]^{a,b,c} of the event and did not reach the specified power level until approximately [ ]^{a,b,c} into the event. The break flow from the power channel side break was steady for the first [ ]^{a,b,c}, indicating that the DVI line was full of water during this period. The level on the cold-leg side reached the DVI nozzle elevation at [ ]^{a,b,c}, and the break flow was then reduced since it consisted of water and steam.

The ADS actuation at [ ]^{a,b,c} increased the rate of primary system depressurization and resulted in a high injection flow from accumulator-A. The injection of cold fluid from accumulator-A ([ ]^{a,b,c}) was insufficient to maintain the level in the annular downcomer, and it eventually decreased down into the tubular downcomer. Heater bundle boiling and the void fraction in the heater bundle and upper plenum increased. The maximum void fractions and minimum tubular downcomer level occurred at [ ]^{a,b,c}, near the end of the accumulator-A delivery. The pressurizer was partially refilled after ADS-1 occurred and stayed partially filled until approximately [ ]^{a,b,c}.

When the accumulator discharge ended (at [ ]^{a,b,c}), the CMT-A injection, which had been suppressed by the accumulator-A injection, restarted and also the IRWST-A injection started. The PRHR flow stopped at [ ]^{a,b,c} when the PRHR drained due to the low level in the upper plenum. As the CMT-A and IRWST-A injection flows started to raise the level in the tubular and annular downcomer, the void fractions for the fluid in the heater bundle gradually reduced, and the upper plenum gradually refilled to the hot-leg elevation (at approximately [ ]^{a,b,c}). At [ ]^{a,b,c}, the level in the hot leg-A was sufficient to restart the flow through the PRHR. At about [ ]^{a,b,c}, the heated rod bundle became subcooled and that steady-state condition existed for the rest of the event.

The fluid discharge from the power channel side break slowed when the water level in the annular downcomer decreased to the elevation of the DVI line ([ ]^{a,b,c}) and converted to steam when the level dropped into the tubular downcomer ([ ]^{a,b,c}). When the injection flows from CMT-A and IRWST-A refilled the system, the level increased to the DVI nozzle elevation at [ ]^{a,b,c} and liquid discharge from the break restarted.

The CMT side of the break was steadily discharging fluid from the IRWST-B, starting at approximately [ ]^{a,b,c}. At this time, both CMT-B and accumulator-B were drained. The discharge from ADS-1, ADS-2, and ADS-3, contained very little mass since the pressurizer never filled completely. For this reason, it consisted of essentially pure steam.

This test demonstrated that the heater bundle (active core) was fully covered by water or a two-phase mixture above the top of the active fuel level at all times during this event, and there was no indication of heater rod temperatures increasing due to lack of cooling.

3.8.2 Analysis of the S00706 Test Data

The analysis of the SPES-2 test was performed using the SPESAN computer code. The code performs a detailed accounting of the coolant inventory in all parts of the system from the start to the end of the test. Also, the internal energy of all components and parts of the facility, including the energy losses from the break and ADS flows, are calculated throughout the event. The mass balance and the energy transfer calculations are performed in much greater detail than was performed in WCAP-14309, *Final Data Report.*[1] The results of the test data analysis are presented in Figures 3.8-1 through 3.8-82. Mass balance snapshots for all the major primary system components, at various points of interest throughout the transition, are presented in Table 3.8-1.

Mass Balance

Overall Mass Balance

The uncertainty in the overall mass balance is an indication of the overall quality of the test. The total water inventory is tracked from the start until the end of the test. Figures 3.8-74, 3.8-75, and 3.8-76 show the overall mass and the mass balance error (uncertainty) for S00706.

The total system mass during S00706 (shown in Figure 3.8-74) indicated a [ ]^{a,b,c} variation of water inventory during the first [ ]^{a,b,c}, and a steady [ ]^{a,b,c} for the rest of the event. This variation resulted from the overall uncertainty in the instrumentation and the assumptions of the mass balance model used to determine the total water inventory. Figure 3.8-75 shows the difference between the total mass during the event and the initial mass (mass balance error) when the inventory was calculated by integrating the flows. Figure 3.8-76 shows the mass balance error when inventory was calculated based on the catch tank weight and component level measurements. The mass balance error in both cases indicated a gain of approximately [ ]^{a,b,c} of water during the event.

Water Inventory for the Power Channel and the Loop

Maintenance of the coolant coverage of the heater bundle was the most critical issue for the power channel. The heater bundle coverage during a loss-of-coolant accident (LOCA) often consists of two-phase fluid, which can have a very high void fraction. Figure 3.8-40 shows the true level of two-phase fluid in the power channel as measured from the elevation of the top of the core (TAF). Since this represents the true two-phase level, it will be different than the collapsed liquid level measured in the power channel.

For S00706, the two-phase level in the upper plenum decreased below the hot-leg elevation, by approximately [ ]^{a,b,c}, then recovered temporarily before decreasing toward the low inventory level of about [ ]^{a,b,c} above TAF for this test at [ ]^{a,b,c}. The accumulator-A injection ([ ]^{a,b,c}) was sufficient to keep the heater rod bundle covered by two-phase fluid, but the void fraction of the fluid exiting the rod bundle (Figure 3.8-61) exceeded [ ]^{a,b,c}. The IRWST-A injection, starting at approximately [ ]^{a,b,c} (Figure 3.8-15), gradually refilled

the inventory and the two-phase level in the power channel to the hot-leg elevation by the end of the event. The void fraction of the fluid exiting the rod bundle showed that boiling continued in the heater rod bundle to the end of the test.

The level on the cold side of the power channel is shown in Figures 3.8-42 (annular downcomer) and 3.8-44 (tubular downcomer). The collapsed level in the annular downcomer dropped to the DVI nozzle elevation approximately [ ]^{a,b,c} into the event. From then until the annular downcomer drained at [ ]^{a,b,c}, the level stayed near the DVI nozzle elevation. However, flashing of the downcomer fluid affected the level. The collapsed level in the tubular downcomer started to decrease at approximately [ ]^{a,b,c} due to flashing of the fluid and reached a minimum level at approximately [ ]^{a,b,c}. This corresponded to the time of minimum water inventory in the power channel shown in Figure 3.8-39. Figure 3.8-62 shows the maximum cladding temperature during the event and compares this temperature with the saturation temperature. After an initial peak up to approximately [ ]^{a,b,c} above saturation temperature, the cladding temperature dropped below ([ ]^{a,b,c}) and remained there for the duration of the test. There were no indications of loss of cooling for the heater rods during this event.

The collapsed fluid level in the rod bundle (Figure 3.8-48), and the rod bundle exit void fraction (Figure 3.8-61) show that the rod bundle was water solid before the break was initiated. The rod bundle exit void fraction was determined from DP-014P, which covers the span from the rod bundle near the TAF elevation to the lower part of the upper plenum. Two-phase flow with an increasing void fraction, which reached approximately [ ]^{a,b,c} existed in the rod bundle during the accumulator-A injection. When the accumulator-A injection ended at approximately [ ]^{a,b,c}, the collapsed level again started to increase due to the IRWST injection. The rod bundle exit void fraction decreased to approximately [ ]^{a,b,c} by the end of the test.

The upper plenum collapsed level (Figures 3.8-52 and 3.8-54) decreased rapidly below the hot leg elevation due to flashing of the upper plenum fluid, and was drained by approximately [ ]^{a,b,c}. Figure 3.8-50 shows that the collapsed level above the rod bundle dropped into the fuel exit region above the TAF, and reached a minimum level at approximately [ ]^{a,b,c} of [ ]^{a,b,c} (minimum inventory) before the level recovery started due to the initiation of IRWST injection.

The water inventory in the power channel (Figure 3.8-39) had a minimum at approximately [ ]^{a,b,c} before the IRWST injection started to affect the level recovery. The minimum power channel water inventory was approximately [ ]^{a,b,c}, or [ ]^{a,b,c} of starting inventory. The total primary system inventory (power channel, pressurizer, and loops), shown in Figure 3.8-77, reaches approximately [ ]^{a,b,c} ([ ]^{a,b,c} of starting inventory).

Water Injection/Ejection

The injected fluid mass from all injection sources is shown in Figure 3.8-78. Figure 3.8-79 shows the total source inventory and the injected and ejected masses during the event. The source inventory started with a total of [ ]^{a,b,c}; [ ]^{a,b,c} ([ ]^{a,b,c} of available source water) was used by the end of the event.

Energy Balance

PRHR Heat Transfer

The heat transfer from the PRHR to the IRWST offered a unique possibility to compare heat transfer on the primary and the secondary side. A method of calculating the heat rejection by the PRHR HX into the IRWST is described in Section 2.0, and a comparison of three heat transfer calculations are given in Section 4.0. The PRHR primary-side heat transfer was calculated based on the measured exit flow rate, and the difference in enthalpy of the inlet and exit flows. The S00706 test had two-phase flow conditions in the hot legs and PRHR. The PRHR inlet flow void fraction for S00706 could not be calculated since the differential pressure instrument of the inverted U-tube in the inlet line did not function properly. The SPESAN code for these conditions sets the void fraction to 0 (Figure 3.8-21) and consequently used the enthalpy of saturated water as the effective enthalpy of the two-phase inlet flow. The outlet flow from the PRHR HX was always subcooled water. The primary-side two-phase heat transfer for S00706 (shown in Figure 3.8-19) represents the heat transfer for single-phase flow through the PRHR, and accordingly underpredicts the heat transfer. Figure 3.8-18 shows the calculated heat transfer from the PRHR external tube surface to the water in the IRWST by the three-tube section of the heat exchanger. The top part of the PRHR HX acted as a condenser, where the steam of the two-phase fluid extracted from hot leg-A was condensed. The top horizontal tube transfers the greatest amount of heat. The condensation process on the inside effectively heated this tube wall temperature above the boiling point for the water in the IRWST, resulting in very effective nucleate boiling heat transfer from the outside surface. The vertical and the bottom horizontal sections of the heat exchanger remained, for the most part, subcooled with a less effective free convection heat transfer to the IRWST water and contributed less to the overall heat transfer of the PRHR.

Figure 3.8-17 shows the internal energy of the IRWST water, the integrated power from the primary side of the PRHR HX, and the heat transfer from the PRHR HX external surfaces. The internal energy in the IRWST water was calculated based on thermocouples located at various elevations in the IRWST tank, which were allocated different control volumes to arrive at an effective average temperature. Due to the severe temperature stratification in the IRWST tank, this technique only produced good results until the IRWST started to drain.

For S00706, there was good correlation between the IRWST internal energy and the PRHR HX tubes external surface heat transfer calculations. However, the PRHR overall heat transfer indicated significantly less energy transfer due to the assumption made regarding the inlet flow conditions by the code. Based on the tests where the inlet void fraction could be calculated for the PRHR, it was

concluded that the calculated increase in IRWST internal energy gives a reasonably accurate value for the PRHR total heat transfer until the IRWST draindown starts.

Steam Generator Heat Transfer

Figure 3.8-32 shows the heat transfer in the steam generators for S00706, and Figure 3.8-33 shows the pressures on the primary side and the secondary side of the steam generators. Heat transfer is sharply lower after the pumps are tripped due to reduced flow in the tubes. The pressures show that the steam generators were available as heat sinks until approximately [ ]^{a,b,c} into the event, at which time the primary-side pressure dropped below the secondary making the steam generators a potential heat source for the primary system. Figure 3.8-28 shows the water inventory in the steam generators primary side, which includes inlet and outlet plena and U-tubes. When full, the steam generator inlet and outlet plena contained approximately [ ]^{a,b,c} lbm of water. When the primary-side pressure dropped below the secondary-side pressure (approximately [ ]^{a,b,c}), the steam generators U-tubes were essentially drained of water and contained trapped steam, which became more and more superheated as the primary-side pressure decayed.

The heat transfer calculated for the steam generators decreased rapidly after the pumps are tripped and disappears after approximately [ ]^{a,b,c}. Figure 3.8-32 also shows that the PRHR heat transfer that removed heat from the system after the steam generator heat transfer had ended.

Overall Energy Balance

The overall energy balance for S00706 had greater uncertainly than the other small LOCA events. The greater uncertainty is a result of several factors; the assumption the downcomer side of break flow consisting of saturated water was inaccurate, and the steam energy loss through CMT-B following its draindown was not accounted for by the code. These two factors resulted in a large unrecoverable energy balance error accumulating between [ ]^{a,b,c} and [ ]^{a,b,c} of the event. The additional recoverable energy balance error resulting from the metal energy also affected the results.

Figure 3.8-80 shows the integrated energy of the fluid streams leaving the system. The fluid from the CMT-side of the break was collected in the catch tank for ADS-4. Until CMT-B drained ([ ]^{a,b,c}) this flow consisted of cold water ejected from the CMT-B and accumulator-B. After CMT-B drained, a steam flow path from cold leg-B2 opened to the ADS-4 catch tank. However, the amount of steam leaving the system via this path was not known, and the energy loss not accounted for in the energy balance.

The fluid from the downcomer-side of the break was collected in the break flow catch tank. The energy content of the downcomer-side break flow was calculated based on the assumption that the flow consisted of saturated water. While for most of the LOCA events this assumption was good, it significantly underpredicted the energy of the break flow for S00706. Figure 3.8-42 shows the collapsed level for the annular downcomer. This level decreased to the DVI nozzle elevation in the first [ ]^{a,b,c}, and stayed there until [ ]^{a,b,c}. During this time significant flashing of

the fluid in the downcomer occurred due to the rapid depressurization of the primary system. This resulted in a two-phase break flow mixture with significantly higher effective enthalpy than the saturated fluid used in the energy balance calculations.

Figure 3.8-81 shows the components in the energy balance for the system. Throughout the event, core power was the dominant heat input to the system; and during the initial part of the event, the steam generators provided the dominant heat extraction. When the primary and secondary system pressures equalized and the steam generator U-tubes drained, the steam generator became thermally isolated from the primary system and did not affect the rest of the event.

From the initiation of the break to approximately [ ]^{a,b,c}, more energy left the system through the break and ADS flows than was generated by the heater bundle, and the overall energy stored within the system (fluid and metal mass) decreased to compensate. After approximately [ ]^{a,b,c}, the metal energy stabilized while there was still a slow decrease in the fluid energy. The rate of fluid energy leaving the system (primarily via ADS-4) and the decrease in fluid energy stored within the system after [ ]^{a,b,c} slightly exceeded the heater rod input power. This steady-state condition existed for the rest of the event.

The total mass flow rate leaving the system was steady for S00706 after the first [ ]^{a,b,c} (Figure 3.8-79). Figure 3.8-80 shows that the energy of the fluid ejection was steady at an average rate of [ ]^{a,b,c} for the rest of the event, as compared to an average power of approximately [ ]^{a,b,c} in the rod bundle. Part of this difference was compensated for by a reduction in the fluid energy in the system of about [ ]^{a,b,c}, as shown in Figure 3.8-81. However, the major part of the difference appeared to be a combination of delayed metal energy and a reduction of the accumulated error (Figure 3.8-82).

Figure 3.8-82 shows the accumulated energy balance error during the event. The energy balance error increased rapidly from [ ]^{a,b,c} as discussed earlier.

The maximum error band for Figure 3.8-82 is approximately +400000/-100000 Btu, which corresponds to [ ]^{a,b,c} of the total fluid energy ejected from the system. The error at the end of the event is approximately [ ]^{a,b,c} of the total ejected fluid energy.

Other Observations

Pressure Decay

Figure 3.8-3 shows the primary system pressure during the S00706 test. Throughout this event the pressure was controlled by the saturation pressure of the hottest fluid volume in the primary system. At the initiation of the break, the controlling fluid volume was in the pressurizer and surge line; however, this shifted within the first [ ]^{a,b,c} (after the initial blowdown phase) to the power channel upper plenum. Figure 3.8-2 shows that the temperature of the upper plenum was equal to the saturation temperature corresponding to the primary system pressure measured in the upper head

during the natural circulation phase and into the ADS phase. Due to the high break flow rate, the system continued to depressurize rapidly during the natural circulation phase. Figure 3.8-3 shows increases in the pressure decay rate occurred at approximately [ ]^{a,b,c} (ADS-1) and [ ]^{a,b,c} (ADS-2), when the system transitioned from natural circulation phase to the ADS phase. The rapid pressure decay during the ADS phase resulted in flashing occurring in the cold leg and downcomer in addition to the hot leg.

Following the actuation of ADS-4 (at approximately [ ]^{a,b,c}), the system pressure decreased sufficiently to allow gravity injection flow to start (at approximately [ ]^{a,b,c}) from the IRWST into the DVI-A nozzles. This flow was not sufficiently high to subcool the primary system, and boiling in the rod bundle continued for the rest of the event. The ADS-4 actuation decreased the system pressure to a near-atmospheric internal pressure.

Ejection Flows

The arrangements for the catch tanks for the ejection flows are shown in Figure 3.8-85. The break flow for this event consisted of two components: CMT side and downcomer side. The CMT side break flow was collected in the ADS-4 catch tank, while the downcomer side break flow was collected in the break flow catch tank.

Figure 3.8-68 shows the individual mass flows collected in the tanks for the break and the ADS. The individual flow rates are given in Figures 3.8-69, 3.8-70, and 3.8-71.

The flows being ejected from the downcomer side of the break and ADS-4 are assumed to consist of saturated water. For the CMT-side of the break, the discharge prior to ADS-4 was considered cold water from the CMT-B and the accumulator-B. After ADS-4 the code assumed water at the hot-leg temperature. For ADS-1, ADS-2, and ADS-3 it was assumed that the flow consisted of saturated water if the void fraction measured in the top of the pressurizer (Figure 3.8-73) was less than 90 percent, and saturated steam if it was greater than 90 percent.

The total mass flow rate leaving the system was steady for S00706 after the first [ ]^{a,b,c}, as seen in Figure 3.8-79.

TABLE 3.8-1
COMPONENT MASS VARIATIONS IN TEST S00706

	Start Fault	End Blowdown	CMT to Draindown	ADS-1 Starts	First Acc. Empty	ADS-4 Starts	IRWST Starts	End of Transient
Event time	0.0	50.0	130.0	199.0	570.0	504.0	700.0	3016.5
Power channel	355.5	285.1	240.1	221.2	70.2	131.0	56.4	254.8
PC: core	71.4	50.0	30.1	29.0	10.4	34.8	9.3	74.9
PC: downcomers	90.9	83.9	76.3	74.2	27.8	49.9	17.9	104.1
PC: upper plenum	69.8	29.4	12.3	17.3	10.3	18.8	3.5	33.9
Hot leg-A	49.8	30.7	20.6	24.6	1.9	4.4	0.3	26.1
Hot leg-B	49.3	31.3	18.9	19.6	2.3	0.9	0.3	28.4
Cold leg-A	79.8	74.3	3.6	2.8	0.4	1.4	0.4	0.1
Cold leg-B	79.8	75.7	3.3	2.8	0.1	0.4	0.8	0.1
SG primary-A	79.8	71.1	24.0	19.7	0.5	7.0	0.1	1.0
SG primary-B	79.8	76.3	23.4	19.1	5.6	11.8	0.5	1.0
Pressurizer+SL	92.8	17.0	17.0	16.4	44.9	41.7	40.1	11.7
CMT-A	314.1	315.2	308.8	295.1	240.0	243.6	225.1	50.1
CMT-B	310.2	299.2	204.9	57.9	0.8	1.5	0.4	0.9
Accumulator-A	259.9	259.9	259.9	260.7	0.0	63.5	0.0	0.0
Accumulator-B	248.7	166.7	68.4	35.2	0.0	0.0	0.0	0.0
IRWST	12185.6	12193.6	12193.6	12185.6	12185.6	12193.6	12149.3	10008.3

TEST ANALYSIS STANDARD PLOT PACKAGE Figures 3.8-1 Through 3.8-84				
Fig. No.	**Component**	**Variables**	**Units**	**Description**
3.8-1	Power channel	CORE-POW	kW	Core power
3.8-2	Power channel	TSAT, TAVTDC, TFOUT	°F	Core inlet/outlet temperature, saturation temperature
3.8-3	Pressurizer	PPZRTOP	psia	System pressure
3.8-4	Steam generator	PSGAS, PSGBS	psia	Primary and secondary pressure in steam generators
3.8-5	Steam generator	TAVGSGA, TAVGSGB	°F	Average fluid temperature in steam generators
3.8-6	CMT	MCMTA, MCMTB	lbm	Fluid mass in CMTs
3.8-7	CMT	CLEVELA, CLEVELB	ft.	Collapsed liquid level in CMTs
3.8-8	CMT	MOUTCMTA, MOUTCMTB, MINCMTA, MINCMTB	lbm	Integrated mass in/out of CMTs
3.8-9	CMT	FLOWOUTA, FLOWOUTB	lbm/sec.	Measured flow out of CMTs
3.8-10	CMT	FLOWINA, FLOWINB	lbm/sec.	Calculated flow into CMTs
3.8-11	CMT	BLFRACA, BLFRACB	Fraction	Fractional differential pressure in cold leg-CMT balance lines
3.8-12	CMT	UTOT-A, UTOT-B	Btu	Fluid energy in CMTs
3.8-13	IRWST/PRHR	MIRWST	lbm	Mass of fluid in IRWST
3.8-14	IRWST/PRHR	LIRWST	ft.	Collapsed liquid level in IRWST
3.8-15	IRWST/PRHR	FIRWST	lbm/sec.	Measured discharge flow from IRWST

TEST ANALYSIS STANDARD PLOT PACKAGE Figures 3.8-1 Through 3.8-84 (Cont.)				
Fig. No.	**Component**	**Variables**	**Units**	**Description**
3.8-16	IRWST/PRHR	MOUTDVIA, MOUTDVIB	lbm	Integrated mass out of DVI lines
3.8-17	IRWST/PRHR	INT-QCAL, INT-QTUB, U-UO	Btu	Comparison of energy transfer from PRHR tubes to IRWST
3.8-18	IRWST/PRHR	Q-HOR-1, Q-VERT, Q-HOR-2, QTUBEXT	Btu/sec.	Breakdown of heat transfer from different sections of PRHR tube
3.8-19	IRWST/PRHR	Q-CALIM	Btu/sec.	PRHR/IRWST heat transfer calculated on tube side
3.8-20	IRWST/PRHR	FLOWTUBE	lbm/sec.	Measured outlet flow from PRHR tube
3.8-21	IRWST/PRHR	VOID-FRC		Calculated PRHR inlet void fraction
3.8-22	Accumulator	MACCA, MACCB	lbm	Mass of fluid in accumulators
3.8-23	Accumulator	LACCA, LACCB	ft.	Collapsed liquid level in accumulators
3.8-24	Accumulator	MEASFLWA, MEASFLWB	lbm/sec.	Measured flow from accumulators
3.8-25	Accumulator	MOUTACCA, MOUTACCB	lbm	Integrated mass out of accumulators
3.8-26	Accumulator	U-TOT-A, U-TOT-B	Btu	Energy of fluid in accumulators
3.8-27	Accumulator	AIRMASSA, AIRMASSB	lbm	Mass of air exiting accumulators
3.8-28	Steam generator	MSGAP, MSGBP	lbm	Mass of fluid in steam generators - primary side
3.8-29	Steam generator	LSGAH, LSGAC, LSGBH, LSGBC	ft.	Collapsed liquid levels in steam generators - primary side - hot and cold sides of U-tubes

TEST ANALYSIS STANDARD PLOT PACKAGE Figures 3.8-1 Through 3.8-84 (Cont.)				
Fig. No.	**Component**	**Variables**	**Units**	**Description**
3.8-30	Steam generator	MSGAH, MSGAC, MSGBH, MSBGC	lbm	Mass of fluid in steam generators - primary side - hot and cold sides of U-tubes
3.8-31	Steam generator	LSGSA, LSGSB	ft.	Collapsed liquid levels in steam generators - secondary side
3.8-32	Steam generator	Q-TRNF-A, Q-TRNF-B, Q-CALIM	Btu/sec.	Heat transfer in steam generators heat transfer in PRHR
3.8-33	Steam generator	PRESS-PA, PRESS-PB, PREF-A, PREF-B	psia	Primary and secondary pressure in steam generators
3.8-34	Pressurizer	MPZR	lbm	Fluid mass in pressurizer
3.8-35	Pressurizer	LPZR	ft.	Collapsed liquid level in pressurizer
3.8-36	Pressurizer	MSL	lbm	Fluid mass in surge line
3.8-37	Pressurizer	LSL	ft.	Collapsed liquid level in surge line
3.8-38	Pressurizer	UPZR	Btu	Fluid energy in pressurizer
3.8-39	Power channel	MPCHN	lbm	Total fluid mass in power channel
3.8-40	Power channel	L2PHASE, LDVI, LHL, LCL	ft.	Two-phase liquid level in power channel vs. DVI, hot-leg, and cold-leg elevations
3.8-41	Power channel	MANDC	lbm	Fluid mass in annular downcomer
3.8-42	Power channel	LANDC, LDVI, LHL, LCL	ft.	Collapsed liquid level in annular downcomer vs. DVI, hot-leg, and cold-leg elevations
3.8-43	Power channel	MTDC	lbm	Fluid mass in tubular downcomer

TEST ANALYSIS STANDARD PLOT PACKAGE Figures 3.8-1 Through 3.8-84 (Cont.)				
Fig. No.	**Component**	**Variables**	**Units**	**Description**
3.8-44	Power channel	LTDC, LBOF, LTOF	ft.	Collapsed liquid level in tubular downcomer vs. top of active fuel and bottom of active fuel levels
3.8-45	Power channel	MLOWP	lbm	Fluid mass in lower plenum
3.8-46	Power channel	LLOWP	ft.	Collapsed liquid level in lower plenum
3.8-47	Power channel	MCORE	lbm	Fluid mass in core region
3.8-48	Power channel	LCORE	ft.	Collapsed liquid level in core
3.8-49	Power channel	MFOUT	lbm	Fluid mass in core outlet region
3.8-50	Power channel	LFOUT	ft.	Collapsed liquid level in core outlet region
3.8-51	Power channel	MUPPL	lbm	Fluid mass in the lower portion of the upper plenum
3.8-52	Power channel	LUPPL	ft.	Collapsed liquid level in the lower portion of the upper plenum
3.8-53	Power channel	MUPPU	lbm	Fluid mass in the upper portion of the upper plenum
3.8-54	Power channel	LUPPU	ft.	Collapsed liquid level in the upper portion of the upper plenum
3.8-55	Power channel	MHEAD	lbm	Fluid mass in the upper head
3.8-56	Power channel	LHEAD	ft.	Collapsed liquid level in the upper head
3.8-57	Power channel	UPC	Btu	Total fluid energy in power channel

TEST ANALYSIS STANDARD PLOT PACKAGE Figures 3.8-1 Through 3.8-84 (Cont.)				
Fig. No.	**Component**	**Variables**	**Units**	**Description**
3.8-58	Power channel	Q-FLUX	Btu/sec.-ft.^{2}	Average heat flux on the heated rods
3.8-59	Power channel	STM-RATE	lbm/sec.	Core steam generation rate
3.8-60	Power channel	FLOWCOR	lbm/sec.	Calculated core flow
3.8-61	Power channel	VOIDOUT		Void fraction at core exit
3.8-62	Power channel	TMAX, TSAT, TMAX-TSAT	°F	Maximum clad temperature, saturation temperature and Δ
3.8-63	Hot leg	MHLA, MHLB	lbm	Fluid mass in hot legs
3.8-64	Hot leg	FLA, FLB	Fraction	Fractional collapsed liquid level in hot legs
3.8-65	Cold leg	MCLA, MCLB	lbm	Fluid mass in cold legs
3.8-66	Cold leg	LCLA1, LCLA2, LPSA	ft.	Collapsed liquid levels in cold leg-A
3.8-67	Cold leg	LCLB1, LCLB2, LPSB	ft.	Collapsed liquid levels in cold leg-B
3.8-68	Total system mass	MADS1-3, MADS4, BRKMASS	lbm	Catch tank mass for ADS-1, ADS-2, ADS-3, ADS-4, and break
3.8-69	Total system mass	DMADS1-3	lbm/sec.	Calculated flow out ADS-1, ADS-2, ADS-3
3.8-70	Total system mass	DMADS4	lbm/sec.	Calculated flow out ADS-4
3.8-71	Total system mass	BRKFLOW	lbm/sec.	Calculated flow out break
3.8-72	Total system energy	UADS123, UADS4, UBREAK	Btu	Integrated fluid energy for ADS-1, ADS-2, ADS-3, ADS4, and the break
3.8-73	Total system energy	VOID		Calculated void fraction for ADS-1, ADS-2, and ADS-3

TEST ANALYSIS STANDARD PLOT PACKAGE Figures 3.8-1 Through 3.8-84 (Cont.)				
Fig. No.	**Component**	**Variables**	**Units**	**Description**
3.8-74	Total system mass	MTOTAL, MTOT0	lbm	Total system fluid mass vs. initial fluid mass
3.8-75	Total system mass	ERRLOP	lbm	Error in the mass balance (using measured and calculated flows)
3.8-76	Total system mass	ERRLOP1	lbm	Error in the mass balance (using fluid inventory)
3.8-77	Total system mass	MPCLTOT, MPCLO	lbm	Total fluid mass in power channel and loops vs. initial fluid mass
3.8-78	Total system mass	MACOUT, MCMOUT, MIROUT	lbm	Total integrated mass discharged from accumulators, CMTs, and IRWST
3.8-79	Total system mass	MSOURCE, MSINK, MSOURIN	lbm	Total source inventory, total mass ejected from primary system, and total mass injected to primary system
3.8-80	Total system energy	UADS123, UBREAK, UADS4, UCATCH	Btu	Integrated fluid energy exiting via ADS-1, ADS-2, ADS-3, ADS-4, and the break, and the sum
3.8-81	Total system energy	USURR, UCATCH, UQIN, UFLD-UO, UMTL-UO, USG	Btu	Overall energy balance including integrated rod power, steam generator power, and heat loss to the surroundings, energy exiting via ads and break, energy input via nonsafety systems, and change in primary system fluid and metal energy relative to start of test
3.8-82	Total system energy	UERROR, ERROR-%	Btu, %	Error in overall energy balance, relative to initial fluid and metal energy
3.8-83	System pressure		psia	Test event phases and system pressure
3.8-84	DVI line	--	--	Break line configuration for DEG of DVI-B

The figures listed are proprietary and, therefore,
are not available in the Class 3 version of this report.

These figures are available in the Class 2 version of this report.

3.9 Analysis of the Two-Inch Cold-Leg/Core Makeup Tank Balance Line Break without Nonsafety Systems (S01007)

This matrix test simulated a 2-in. break in cold leg-B2/CMT-B balance line. The event began with the initiation of the break of the cold-leg/core makeup tank (CMT) balance line. This break was located between the balance line isolation valve and the CMT-B. This test was performed without any nonsafety systems' pumps operating. That is, it was performed without the chemical and volume control system (CVCS) makeup pumps, steam generator startup feedwater (SFW) pumps, and normal residual heat removal system (NRHR) pumps.

3.9.1 Summary of Test Observations

Figure 3.9-83 shows plant primary system pressure during matrix test S01007 (as measured at the top of the pressurizer) during the S01007 event, with selected component actuations and plant responses shown in relation to primary system pressure.

The IDP began with the initiation of the break, which caused the pressurizer to drain. This resulted in a rapid reduction in pressure. The reactor trip (R) signal initiated at [ ]^{a,b,c} and the safety systems actuation (S) signal initiated at [ ]^{a,b,c} The R and the S signals initiated the following actions:

- Decay heat simulation (with heat loss compensation) initiated.
- The main steam line isolation valves (MSIVs) closed.
- The main feedwater isolation valves (MFWIVs) shut off.
- The CMT injection valves opened.
- The passive residual heat removal (PRHR) return flow valve opened.
- The reactor coolant pumps (RCPs) shut down.

The recirculation flow through the CMT-A and PRHR flow started immediately after the CMT injection valve and the PRHR isolation valve opened. Boiling in the rod bundle was initiated by the reduction of the system pressure to saturation level. The upper plenum flashed while the fluid level in the upper plenum dropped to hot-leg elevation. The flashing on the hot-leg side of the rod bundle stopped the rapid drop in primary system pressure. When the RCPs shut down (at [ ]^{a,b,c}), the flow through the rod bundle began to oscillate (approximately [ ]^{a,b,c} oscillation period). This resulted in oscillations in the core and upper-plenum void fraction, upper-plenum temperature, and system pressure.

During the initial stages of the PDP, the rod bundle void fraction increased. This resulted in an increasing void fraction in the upper plenum and the hot legs. The hot leg-B fluid had a void fraction close to that observed in the upper plenum. The void fraction in hot leg-A was much lower due to the selective removal of vapor from the hot leg by the PRHR inlet line.

Two-phase flow in the hot legs initiated the draindown of the steam generator U-tubes. Steam from the two-phase mixture collected in the top of the U-tubes, thereby draining the steam generator U-tubes. This stopped the flow through the primary system. The void fraction oscillations through the core and in the upper plenum terminated when the break of the siphon occurred in the steam generators. Approximately [ ]^{a,b,c} into the event, flow through steam generator-B stopped due to the higher void fraction in hot leg-B. Approximately [ ]^{a,b,c} later, the flow through steam generator-A stopped.

The two-phase flow through the PRHR had an average integrated void fraction significantly greater than that seen in the upper plenum. Due to boiling in the rod bundle, two-phase flow entered the hot leg from the upper plenum and flowed through the PRHR heat exchanger (HX) located in the in-containment refueling water storage tank (IRWST). The average void fraction in the PRHR inlet was as high as [ ]^{a,b,c} percent, which enhanced the PRHR heat transfer from the primary system when compared with that obtainable with single-phase saturated or subcooled water. When the flow stabilized after the initial flow oscillations, a heat removal rate of [ ]^{a,b,c} was calculated. This calculation was based on the average void fraction of the flow in the PRHR supply line, the flow rate, the temperature, and the pressure. This calculation assumes a slip coefficient of 1 between steam and water and may give a slightly lower value than the actual heat transfer. It should, therefore, be used for test-to-test comparison only.

When the cold legs had partially emptied, CMT-A converted from the recirculation mode to the draindown mode of injection. This increased the cold injection flow and the rate of system pressure decay. This occurred at approximately [ ]^{a,b,c} for CMT-A and [ ]^{a,b,c} for CMT-B. When system pressure dropped to saturation pressure for the upper head, the upper head began to drain (at [ ]^{a,b,c}).

During the first [ ]^{a,b,c} of this event, [ ]^{a,b,c} of water were expelled through the break while draining the pressurizer, the steam generator U-tubes, the power channel upper head, the power channel upper plenum above the hot leg, most of the cold legs, and approximately [ ]^{a,b,c} of the CMTs. The heated rods in the power channel that simulated the core decay heat reduced the power level to approximately [ ]^{a,b,c} at [ ]^{a,b,c} This value consisted of [ ]^{a,b,c} decay heat and [ ]^{a,b,c} heat loss compensation. The break flow was steady, indicating that cold leg-B2 was not totally empty.

The ADS phase began with the actuation of ADS-1 (at approximately [ ]^{a,b,c}). ADS-2 and ADS-3 occurred within the next [ ]^{a,b,c} The heat loss compensation was terminated from the decay heat simulation during ADS-1, and the core power level was reduced to approximately [ ]^{a,b,c}

The ADS actuation increased the rate of primary system depressurization and resulted in a high level of injection flow from the accumulators. The rapid injection of cold fluid from the accumulators ([ ]^{a,b,c}) subcooled the whole primary system, temporarily refilling the power

channel upper plenum and the pressurizer. When the accumulator discharge ended, boiling occurred again in the heater bundle. Two-phase flow occurred again in hot leg-A, the PRHR HX, and the ADS via the pressurizer.

The liquid discharge through the break was replaced by saturated steam at approximately [ ]^{a,b,c} During the ADS period, approximately [ ]^{a,b,c} of subcooled water were discharged from ADS-1, ADS-2, and ADS-3. This water was supplied primarily by the accumulator discharge and was followed by an increase in rod bundle void fraction after the accumulators had drained and only the CMTs provided core injection.

The post-ADS phase began when ADS-4 was actuated at [ ]^{a,b,c} and the pressurizer water level fell. The fluid discharge through ADS-1, ADS-2, and ADS-3 ended, and fluid was discharged through ADS-4. The pressurizer drained again, and a small amount of CMT flow still entered the direct vessel injection (DVI) line. When system pressure had been reduced below the pressure corresponding to the water elevation head of the IRWST, flow from the IRWST entered the DVI line, and shortly thereafter the CMT flow ended. The flow from the IRWST cooled the primary system, the rod bundle boiling slowly ended, and the upper plenum partially refilled. The PRHR drained approximately [ ]^{a,b,c} into the event and was no longer effective. A steady flow of subcooled water then flowed from the IRWST into the DVI line, through the power channel, and left the primary system through ADS-4.

3.9.2 Analysis of the S01007 Test Data

The analysis of the SPES-2 test was performed using the SPESAN computer code. The code performs a detailed accounting of the coolant inventory in all parts of the system from the start to the end of the test. Also, the internal energy of all components and parts of the facility, including the energy losses from the break and ADS flows, are calculated throughout the event. The mass balance and the energy transfer calculations are performed in much greater detail than were performed in WCAP-14309, *Final Data Report.*[1] The results of the test data analysis are presented in Figures 3.9-1 through 3.9-82. Mass balance snapshots, for key times during the transient, are presented in Table 3.9-1 for all the major primary system components.

Mass Balance

Overall Mass Balance

The uncertainty in the overall mass balance is an indication of the overall quality of the test. The total water inventory was tracked from the start until the end of the test. Figures 3.9-74, 3.9-75, and 3.9-76 show the overall mass balance and the error (uncertainty) in mass balance for S01007.

The overall mass balance for S01007 (Figure 3.9-74) shows a small variation of water inventory during the event, resulting from the overall uncertainty in the instrumentation and the assumptions of the mass balance model used to determine the total water inventory. The average total inventory

during the test was indicated to be approximately [ ]^{a,b,c} higher than the initial system mass, and a final mass was indicated to be approximately [ ]^{a,b,c} above the initial mass. Figure 3.9-75 shows the difference between the total mass during the event and the initial mass (mass balance error) when the inventory was calculated by integrating the flows. Figure 3.9-76 shows the mass balance error when inventory was calculated based on the catch tank weight and component level measurements. The mass balance error, based on flow measurements, varied from [ ]^{a,b,c} and final error of [ ]^{a,b,c} at the end of the event; the weight and level measurements resulted in an average error of approximately [ ]^{a,b,c} during the event and a final error of [ ]^{a,b,c} at the end of the event.

Water Inventory for the Power Channel and the Loop

Maintenance of the coolant coverage of the heater bundle was the most critical issue for the power channel. The heater bundle coverage during a loss-of-coolant accident (LOCA) event often consisted of two-phase fluid, which can have a very high void fraction. Figure 3.9-40 shows the level of two-phase fluid in the power channel as calculated from the measured pressure drop data, which was then used to infer a void fraction and two-phase level. Since this represents the true two-phase level, it will be different than the collapsed liquid level in the heater bundle.

For S01007, the calculated two-phase fluid level in the upper plenum decreased to the hot-leg elevation and remained at this elevation for most of the event. The accumulator injection ([ ]^{a,b,c}) partially condensed the steam bubble in the upper plenum causing the level to rise before the end of the accumulator injection. After the end of the accumulator injection, the two-phase level again decreased, this time to approximately [ ]^{a,b,c} below the hot-leg elevation. This occurred at the time of minimum power channel water inventory, before the IRWST injection started (at [ ]^{a,b,c}) to refill the power channel. The IRWST injection also partially condensed the steam bubble in the upper plenum causing the level to rise above the hot leg elevation once more.

The collapsed level in the annular downcomer and tubular downcomer are shown in Figures 3.9-42 (annular downcomer) and 3.9-44 (tubular downcomer). The annular downcomer was full until approximately [ ]^{a,b,c} into the event. At that time, the level started to decrease, but it was maintained above the elevation of the hot leg until after the end of the accumulator injection (approximately [ ]^{a,b,c}). The level then decreased and drained the annular downcomer by [ ]^{a,b,c} and reached a minimum level in the tubular downcomer at approximately [ ]^{a,b,c} This corresponded to the time of minimum water inventory in the power channel (Figure 3.9-39). Figure 3.9-62 shows the maximum cladding temperature during the event and compares this temperature with the saturation temperature. There were no indications of loss of cooling for the heater rods during this event, which confirms the estimated two-phase level in the power channel.

The collapsed fluid level in the rod bundle (Figure 3.9-48), and the rod bundle exit void fraction (Figure 3.9-61) show that the rod bundle was water solid before the break was initiated. The rod bundle exit void fraction was determined from DP-014P, which covers the span from the rod bundle

near the TAF elevation to the lower part of the upper plenum. Two-phase flow with approximately [ ]^{a,b,c} percent average void fraction existed in the rod bundle prior to the accumulator injection. During the accumulator injection, the rod bundle became essentially water solid. However, when the accumulator injection ended, the collapsed level again started to decrease. The rod bundle exit void fraction reached approximately [ ]^{a,b,c} percent prior to the start of the IRWST injection phase, at approximately [ ]^{a,b,c}

The collapsed level in the upper plenum (Figures 3.9-52 and 3.9-54) decreased to approximately [ ]^{a,b,c} below the hot leg before the accumulator injection, followed by a period when the level in the upper plenum increased above the hot leg during the accumulator injection. This period was followed by a drop in the collapsed level to approximately [ ]^{a,b,c} below the hot leg at the time of minimum water inventory before the IRWST injection started.

The water inventory in the power channel (Figure 3.9-39) had two minima: before the accumulator injection and before the IRWST injection. The second minimum was more severe showing a total power channel inventory of approximately [ ]^{a,b,c} ([ ]^{a,b,c} percent of starting inventory) at that time. The total primary system inventory (power channel, pressurizer, and loops), shown in Figure 3.9-77, reached approximately [ ]^{a,b,c} ([ ]^{a,b,c} percent of starting inventory) for this minimum.

Water Injection/Ejection

The injected fluid mass from all injection sources is shown in Figure 3.9-78. Figure 3.9-79 shows the total source inventory and the injected and ejected masses during the event. Starting with a total of approximately [ ]^{a,b,c} source inventory, only [ ]^{a,b,c} ([ ]^{a,b,c} percent of available source water) was used by the end of the event.

Energy Balance

PRHR Heat Transfer

The heat transfer from the PRHR to the IRWST gives a unique possibility of comparing heat transfer on the primary and the secondary side. A method of calculating the heat rejection by the PRHR heat exchanger into the IRWST is described in Section 2.2-2, and a comparison of three heat transfer calculations is given in Section 4.0. The PRHR primary-side heat transfer was calculated based on the measured exit flow rate, and the difference in enthalpy of the inlet and exit flows. Since the S01007 test had two-phase flow conditions in the hot legs and PRHR, the inlet flow void fraction was determined (Figure 3.9-21) and used to establish the effective enthalpy of the two-phase inlet flow. The outlet flow from the PRHR HX was always subcooled water. The primary-side two-phase heat transfer for S01007, shown in Figure 3.9-19, was considerably greater than the heat transfer measured for single-phase flow through the PRHR during the hot preoperational testing (see WCAP-14309, *Final Data Report.*)[1] Figure 3.9-18 shows the calculated heat transfer from the PRHR external tube surface to the water in the IRWST by the three-tube section of the heat exchanger. The top part of the

PRHR HX acted as a condenser, where the steam of the two-phase fluid extracted from hot leg-A was condensed. The top horizontal tube transfers the greatest amount of heat. The condensation process on the inside effectively heated this tube wall temperature above the boiling point for the water in the IRWST, resulting in very effective nucleate boiling heat transfer from the outside surface. The vertical and the bottom horizontal sections of the HX remain, for the most part, subcooled the fluid with a less effective free-convection heat transfer to the IRWST water, and contributed less to the overall heat transfer of the PRHR.

Figure 3.9-17 shows the internal energy of the IRWST water, the integrated power from the primary side of the PRHR HX, and the heat transfer from the PRHR HX external surfaces. The internal energy in the IRWST water was calculated based on thermocouples located at various elevations in the IRWST tank, which were allocated different control volumes to arrive at an effective average temperature. Due to the severe temperature stratification in the IRWST tank, this technique only produced good results until the IRWST started to drain.

For S01007 up to [ ]^{a,b,c} the PRHR primary-side calculation and the IRWST internal energy calculation were very close. After [ ]^{a,b,c} the IRWST internal energy appeared to increase significantly due to the effect of draindown on the thermocouple readings. However, since there is very little energy being provided by the PRHR after [ ]^{a,b,c} this apparent increase does not reflect an actual increase in the average water temperature and IRWST internal energy. The comparison shown in Figure 3.9-17 indicates that the calculated heat transfer from the PRHR HX external surfaces for test S01007 is higher then the PRHR heat transfer calculated for primary side.

Steam Generator Heat Transfer

Figure 3.9-32 shows the heat transfer in the steam generators for S01007, and Figure 3.9-33 shows the pressures on the primary side and the secondary side of the steam generators. Heat transfer is sharply reduced after the pumps trip due to low flow in the steam generator tubes. The pressures show that the steam generators were available as heat sinks until approximately [ ]^{a,b,c} into the event, at which time the primary-side pressure dropped below the secondary making the steam generators a potential heat source for the primary system. Figure 3.9-28 shows the water inventory in the steam generators primary side, which includes inlet and outlet plena and U-tubes. When full, the steam generator inlet and outlet plena contains approximately [ ]^{a,b,c} of water. When the primary-side pressure dropped below the secondary-side pressure (approximately [ ]^{a,b,c}), the steam generators U-tubes are essentially drained of water and contain trapped steam, which becomes more and more superheated as the primary side pressure decays.

The heat transfer calculated for the steam generators decreased rapidly after pumps trip and disappeared after approximately [ ]^{a,b,c}. Also shown in Figure 3.9-32 is the PRHR heat transfer, which removed heat from the system after the steam generators' heat transfer had ended.

Overall Energy Balance

Figure 3.9-80 shows the integrated energy of the fluid streams leaving the system. The energy content of the break flow was greatly reduced when ADS-1 occurred since, although the break flow converted to steam, the mass flow rate became very low. For ADS-1, ADS-2, and ADS-3 the same happened when ADS-4 occurred.

Figure 3.9-81 shows all the energy components in the heat balance for the system. Throughout the event, core power was the dominant heat input to the system, and during the initial part of the event the steam generators provided the dominant heat extraction. When the primary and secondary system pressures equalize, and the steam generator U-tubes drain (about [ ]^{a,b,c}), the steam generator becomes thermally isolated from the primary system, and does not affect the rest of the event. Figure 3.9-80 shows the energy loss from the break and the ADS flows as calculated based on assumptions described in Section 2.8. The average energy loss from the fluids ejected from the system during the first [ ]^{a,b,c} of the event was approximately [ ]^{a,b,c} which was reduced to approximately [ ]^{a,b,c} from about [ ]^{a,b,c} to the end of the test.

From approximately [ ]^{a,b,c} more energy left the system through the break and ADS flows than was generated by the heater bundle, and the overall energy stored within the system (fluid and metal mass) decreased to compensate. The average loss of the metal thermal energy for the first [ ]^{a,b,c} was approximately [ ]^{a,b,c} which was greater than the heated rod power for most of this period. After approximately [ ]^{a,b,c} the metal and fluid energy stabilized in the system, and the rate of the fluid energy leaving the system (primarily via ADS-4) matched the core input power well. This steady-state condition existed for the rest of the event.

Figure 3.9-82 shows that the accumulated error in the energy balance increased rapidly from [ ]^{a,b,c} to [ ]^{a,b,c} (during the accumulator discharge into the primary system). This error was a consequence of the rapid drop in the metal energy seen in Figure 3.9-81, which was calculated based on fluid temperatures. In reality, the calculated decrease of metal energy occurs at a slower rate than indicated by the fluid thermocouples due to the large thermal inertia of the heavy-walled components. The increasing error and the error peak shown in Figure 3.9-82 at [ ]^{a,b,c} are, therefore, a consequence of taking credit for metal heat too fast during the event, and this error largely disappears within the following [ ]^{a,b,c} when the metal temperatures catch up with the fluid temperatures. In evaluating the overall error in the accuracy of the energy balance, this peak was disregarded. On this basis, the maximum error band for Figure 3.9-82 is approximately 0 to +150000 Btu, which corresponds a maximum error of [ ]^{a,b,c} percent of the total fluid energy ejected from the system. The error at the end of the event is approximately [ ]^{a,b,c} percent of the total ejected fluid energy.

Other Observations

Pressure Decay

Figure 3.9-3 shows the primary system pressure during the S01007 test. Throughout this event the pressure was controlled by the saturation pressure of the hottest fluid volume in the primary system. At the initiation of the break the controlling fluid volume is in the pressurizer and surge line, however, this shifted within the first [ ]^{a,b,c} (after the initial blowdown phase) to the power channel upper plenum. Figure 3.9-2 shows that the temperature of the upper plenum was equal to the saturation temperature corresponding to the primary system pressure measured in the upper head during the natural circulation phase and into the ADS phase. The pressure stabilized at the saturation pressure for the upper plenum, and then continued a slow pressure decay responding to the CMTs injection. Figure 3.9-3 shows that an increase in the pressure decay rate occurred at approximately [ ]^{a,b,c} when the CMT-A transitioned from natural circulation injection to draindown injection, which essentially increased the injection rate of cold water into the DVI. The higher injection rate resulted in a more rapid temperature drop in the upper plenum (fuel exit in Figure 3.9-2), which was reflected in a more rapid pressure decay. With the actuation of ADS-1 at approximately [ ]^{a,b,c} the pressure dropped rapidly due to the increased rate of mass ejection from the system (Figure 3.9-68), and the increased flow of cold water being injected into the annular downcomer and flowing through the core. This continued to reduce the power channel inlet plenum temperature, and subcool the heated rod bundle due to the higher flow. Since the power channel outlet plenum became subcooled at approximately [ ]^{a,b,c} the hottest fluid in the system at this time was in the pressurizer, the cold legs, and the CMTs, and the pressure was partially supported by the flashing of the fluid in one or several of these locations. When the accumulator discharge ended (approximately [ ]^{a,b,c}), the lower-plenum temperature increased due to the metal heat, and the upper plenum temperature increased to the saturation temperature and again took control of the system pressure for the rest of the event. It is noted here that at the end of the accumulator injection, a large amount of nitrogen from the accumulators were injected into the primary system. This injection had very little immediate effect on the primary system, but as will be discussed in Section 4.0, affects the upper plenum, the PRHR HX, and the CMT at later stages of the event.

The actuation of ADS-4 (at approximately [ ]^{a,b,c}) lowered the system pressure sufficiently to allow gravity injection flow from the IRWST into the DVI nozzles. This flow was sufficiently high to subcool the primary system, ending core boiling and partially collapsing the steam bubble in the upper plenum, and bringing the system to a near atmospheric internal pressure.

Ejection Flows

Figure 3.9-68 shows the individual mass flows leaving the system via the break and the ADS. The individual flow rates are given in Figures 3.9-69, 3.9-70, and 3.9-71. The break and ADS-4 flows were assumed to consist of saturated water. For ADS-1, ADS-2, and ADS-3 it was assumed that the flow consisted of saturated water if the void fraction measured in the top of the pressurizer (Figure 3.9-73) was less than [ ]^{a,b,c} percent, and saturated steam if it was greater than [ ]^{a,b,c} percent.

The total mass flow rate leaving the system was reasonably steady for S01007, as seen in Figure 3.9-79. Figure 3.9-80 shows that the energy of the fluid ejection was steady at an average rate of [ ]^{a,b,c} for the first [ ]^{a,b,c} and then decreased to [ ]^{a,b,c} for the rest of the event. The change in energy ejection rate was related to actuation of ADS-4, which caused the pressurizer to drain, converted the ADS-1, ADS-2, and ADS-3 flow to steam with a low-mass flow rate, and simultaneously started fluid ejection through ADS-4.

ADS-1 opened at approximately [ ]^{a,b,c} followed by ADS-2 and ADS-3 within the next [ ]^{a,b,c} The break flow changes from saturated water to steam, but due to the low mass flow rate (Figure 3.9-68), the energy removal by the break flow (Figure 3.9-80) became very low. The energy leaving the system through ADS-1, ADS-2, and ADS-3 was greater than for break and ADS-4 and provided an effective means of removing the stored metal energy from the system, as seen in Figure 3.9-81.

The mass leaving the system via ADS-1, ADS-2, and ADS-3 during the next 1000 seconds was greater than the break flow, and also the energy loss through the ADS-1, ADS-2, and ADS-3 exceeded the energy loss by the break flow (Figure 3.9-80).

ADS-4 opened at approximately [ ]^{a,b,c} and the ADS-1, ADS-2, and ADS-3 flows converted to steam with a very low mass flow rate and energy loss rate. The ADS-4 flow stabilized at a rate that matched the injection rate from the IRWST (Figure 3.9-79), and the energy removal via ADS-4 was comparable to the heated rod power (Figure 3.9-81).

TABLE 3.9-1
COMPONENT MASS VARIATIONS IN TEST S01007

	Start Fault	End Blowdown	CMT to Draindown	ADS-1 Starts	First Acc. Empty	ADS-4 Starts	IRWST Starts	End of Transient
Event time								
Power channel								
PC: core								
PC: downcomers								
PC: upper plenum								
Hot leg-A								
Hot leg-B								
Cold leg-A								
Cold leg-B								
SG primary-A								
SG primary-B								
Pressurizer + SL								
CMT-A								
CMT-B								
Accumulator-A								
Accumulator-B								
IRWST								

a,b,c

TEST ANALYSIS STANDARD PLOT PACKAGE Figures 3.9-1 Through 3.9-83				
Fig. No.	**Component**	**Variables**	**Units**	**Description**
3.9-1	Power channel	CORE POW	kW	Core power
3.9-2	Power channel	TSAT, TAVTDC, TFOUT	°F	Core inlet/outlet temperature, saturation temperature
3.9-3	Pressurizer	PPZRTOP	psia	System pressure
3.9-4	Steam generator	PSGAS, PSGBS	psia	Primary and secondary pressure in steam generators
3.9-5	Steam generator	TAVGSGA, TAVGSGB	°F	Average fluid temperature in steam generators
3.9-6	CMT	MCMTA, MCMTB	lbm	Fluid mass in CMTs
3.9-7	CMT	CLEVELA, CLEVELB	ft.	Collapsed liquid level in CMTs
3.9-8	CMT	MOUTCMTA, MOUTCMTB, MINCMTA, MINCMTB	lbm	Integrated mass in/out of CMTs
3.9-9	CMT	FLOWOUTA, FLOWOUTB	lbm/sec.	Measured flow out of CMTs
3.9-10	CMT	FLOWINA, FLOWINB	lbm/sec.	Calculated flow into CMTs
3.9-11	CMT	BLFRACA, BLFRACB	Fraction	Fractional differential pressure in cold leg-CMT balance lines
3.9-12	CMT	UTOT-A, UTOT-B	Btu	Fluid energy in CMTs
3.9-13	IRWST/PRHR	MIRWST	lbm	Mass of fluid in IRWST
3.9-14	IRWST/PRHR	LIRWST	ft.	Collapsed liquid level in IRWST
3.9-15	IRWST/PRHR	FIRWST	lbm/sec.	Measured discharge flow from IRWST

TEST ANALYSIS STANDARD PLOT PACKAGE Figures 3.9-1 Through 3.9-83 (Cont.)				
Fig. No.	**Component**	**Variables**	**Units**	**Description**
3.9-16	IRWST/PRHR	MOUTDVIA, MOUTDVIB	lbm	Integrated mass out of DVI lines
3.9-17	IRWST/PRHR	INT-QCAL, INT-QTUB, U-UO	Btu	Comparison of energy transfer from PRHR tubes to IRWST
3.9-18	IRWST/PRHR	Q-HOR-1, Q-VERT, Q-HOR-2, QTUBEXT	Btu/sec.	Breakdown of heat transfer from different sections of PRHR tube
3.9-19	IRWST/PRHR	Q-CALIM	Btu/sec.	PRHR/IRWST heat transfer calculated on tube side
3.9-20	IRWST/PRHR	FLOWTUBE	lbm/sec.	Measured outlet flow from PRHR tube
3.9-21	IRWST/PRHR	VOID-FRC		Calculated PRHR Inlet void fraction
3.9-22	Accumulator	MACCA, MACCB	lbm	Mass of fluid in accumulators
3.9-23	Accumulator	LACCA, LACCB	ft.	Collapsed liquid level in accumulators
3.9-24	Accumulator	MEASFLWA, MEASFLWB	lbm/sec.	Measured flow from accumulators
3.9-25	Accumulator	MOUTACCA, MOUTACCB	lbm	Integrated mass out of accumulators
3.9-26	Accumulator	U-TOT-A, U-TOT-B	Btu	Energy of fluid in accumulators
3.9-27	Accumulator	AIRMASSA, AIRMASSB	lbm	Mass of air exiting accumulators
3.9-28	Steam generator	MSGAP, MSGBP	lbm	Mass of fluid in steam generators - primary side
3.9-29	Steam generator	LSGAH, LSGAC, LSGBH, LSGBC	ft.	Collapsed liquid levels in steam generators - primary side - hot and cold sides of U-tubes

TEST ANALYSIS STANDARD PLOT PACKAGE Figures 3.9-1 Through 3.9-83 (Cont.)				
Fig. No.	**Component**	**Variables**	**Units**	**Description**
3.9-30	Steam generator	MSGAH, MSGAC, MSGBH, MSBGC	lbm	Mass of fluid in steam generators - primary side - hot and cold sides of U-tubes
3.9-31	Steam generator	LSGSA, LSGSB	ft.	Collapsed liquid levels in steam generators – secondary side
3.9-32	Steam generator	Q-TRNF-A, Q-TRNF-B, Q-CALIM	Btu/sec.	Heat transfer in steam generators heat transfer in PRHR
3.9-33	Steam generator	PRESS-PA, PRESS-PB, PREF-A, PREF-B	psia	Primary and secondary pressure in steam generators
3.9-34	Pressurizer	MPZR	lbm	Fluid mass in pressurizer
3.9-35	Pressurizer	LPZR	ft.	Collapsed liquid level in pressurizer
3.9-36	Pressurizer	MSL	lbm	Fluid mass in surge line
3.9-37	Pressurizer	LSL	ft.	Collapsed liquid level in surge line
3.9-38	Pressurizer	UPZR	Btu	Fluid energy in pressurizer
3.9-39	Power channel	MPCHN	lbm	Total fluid mass in power channel
3.9-40	Power channel	L2PHASE, LDVI, LHL, LCL	ft.	Two-phase liquid level in power channel vs. DVI, hot-leg, and cold-leg elevations
3.9-41	Power channel	MANDC	lbm	Fluid mass in annular downcomer
3.9-42	Power channel	LANDC, LDVI, LHL, LCL	ft.	Collapsed liquid level in annular downcomer vs. DVI, hot-leg, and cold-leg elevations

TEST ANALYSIS STANDARD PLOT PACKAGE Figures 3.9-1 Through 3.9-83 (Cont.)				
Fig. No.	**Component**	**Variables**	**Units**	**Description**
3.9-43	Power channel	MTDC	lbm	Fluid mass in tubular downcomer
3.9-44	Power channel	LTDC, LBOF, LTOF	ft.	Collapsed liquid level in tubular downcomer vs. top of active fuel and bottom of active fuel levels
3.9-45	Power channel	MLOWP	lbm	Fluid mass in lower plenum
3.9-46	Power channel	LLOWP	ft.	Collapsed liquid level in lower plenum
3.9-47	Power channel	MCORE	lbm	Fluid mass in core region
3.9-48	Power channel	LCORE	ft.	Collapsed liquid level in core
3.9-49	Power channel	MFOUT	lbm	Fluid mass in core outlet region
3.9-50	Power channel	LFOUT	ft.	Collapsed liquid level in core outlet region
3.9-51	Power channel	MUPPL	lbm	Fluid mass in the lower portion of the upper plenum
3.9-52	Power channel	LUPPL	ft.	Collapsed liquid level in the lower portion of the upper plenum
3.9-53	Power channel	MUPPU	lbm	Fluid mass in the upper portion of the upper plenum
3.9-54	Power channel	LUPPU	ft.	Collapsed liquid level in the upper portion of the upper plenum
3.9-55	Power channel	MHEAD	lbm	Fluid mass in the upper head
3.9-56	Power channel	LHEAD	ft.	Collapsed liquid level in the upper head

TEST ANALYSIS STANDARD PLOT PACKAGE Figures 3.9-1 Through 3.9-83 (Cont.)				
Fig. No.	**Component**	**Variables**	**Units**	**Description**
3.9-57	Power channel	UPC	Btu	Total fluid energy in power channel
3.9-58	Power channel	Q-FLUX	Btu/sec.-ft.^{2}	Average heat flux on the heated rods
3.9-59	Power channel	STM-RATE	lbm/sec.	Core steam generation rate
3.9-60	Power channel	FLOWCOR	lbm/sec.	Calculated core flow
3.9-61	Power channel	VOIDOUT		Void fraction at core exit
3.9-62	Power channel	TMAX, TSAT. TMAX-TSAT	°F	Maximum clad temperature, saturation temperature and delta
3.9-63	Hot leg	MHLA, MHLB	lbm	Fluid mass in hot legs
3.9-64	Hot leg	FLA, FLB	Fraction	Fractional collapsed liquid level in hot legs
3.9-65	Cold leg	MCLA, MCLB	lbm	Fluid mass in cold legs
3.9-66	Cold leg	LCLA1, LCLA2, LPSA	ft.	Collapsed liquid levels in cold leg-A
3.9-67	Cold leg	LCLB1, LCLB2, LPSB	ft.	Collapsed liquid levels in cold leg-B
3.9-68	Total system mass	MADS1-3, MADS4, BRKMASS	lbm	Catch tank mass for ADS-1, ADS-2, ADS-3, ADS-4, and break
3.9-69	Total system mass	DMADS1-3	lbm/sec.	Calculated flow out ADS-1, ADS-2, ADS-3
3.9-70	Total system mass	DMADS4	lbm/sec.	Calculated flow out ADS-4
3.9-71	Total system mass	BRKFLOW	lbm/sec.	Calculated flow out break
3.9-72	Total system energy	UADS123, UADS4, UBREAK	Btu	Integrated fluid energy for ADS-1, ADS-2, ADS-3, ADS4, and the break

TEST ANALYSIS STANDARD PLOT PACKAGE
Figures 3.9-1 Through 3.9-83 (Cont.)

Fig. No.	Component	Variables	Units	Description
3.9-73	Total system energy	VOID		Calculated void fraction for ADS-1, ADS-2, and ADS-3
3.9-74	Total system mass	MTOTAL, MTOT0	lbm	Total system fluid mass vs. initial fluid mass
3.9-75	Total system mass	ERRLOP	lbm	Error in the mass balance (using measured and calculated flows)
3.9-76	Total system mass	ERRLOP1	lbm	Error in the mass balance (using fluid inventory)
3.9-77	Total system mass	MPCLTOT, MPCLO	lbm	Total fluid mass in power channel and loops vs. Initial fluid mass
3.9-78	Total system mass	MACOUT, MCMOUT, MIROUT	lbm	Total integrated mass discharged from accumulators, CMTs, and IRWST
3.9-79	Total system mass	MSOURCE, MSINK, MSOURIN	lbm	Total source inventory, total mass ejected from primary system, and total mass injected to primary system
3.9-80	Total system energy	UADS123, UBREAK, UADS4, UCATCH	Btu	Integrated fluid energy exiting via ADS-1, ADS-2, ADS-3, ADS-4, and the break, and the sum
3.9-81	Total system energy	USURR, UCATCH, UQIN, UFLD-UO, UMTL-UO, USG	Btu	Overall energy balance including integrated rod power, steam generator power, and heat loss to the surroundings, energy exiting via ads and break, energy input via nonsafety systems, and change in primary system fluid and metal energy relative to start of test
3.9-82	Total system energy	UERROR, ERROR-%	Btu, %	Error in overall energy balance, relative to initial fluid and metal energy
3.9-83	System pressure	--	psia	Test event phases and system pressure

The figures listed are proprietary and, therefore,
are not available in the Class 3 version of this report.

These figures are available in the Class 2 version of this report.

3.10 Analysis of the Steam Generator Tube Rupture with Nonsafety Systems Operational and Operator Action for Mitigation (S01309)

This matrix test simulated a steam generator tube rupture (SGTR) with both the passive and nonsafety systems operational and with operator action for mitigation. There were two operator actions simulated for this test: cooldown of the primary system by dumping steam through the intact steam generator power-operated relief valve (PORV) to obtain hot-leg subcooling (while limiting the overall cooldown rate of the primary system) and subsequent controlled depressurization of the primary system to terminate primary-to-secondary leakage using an ADS-1 valve. There was no core makeup tank (CMT) draindown during this transient. Therefore, there was no actuation of the automatic depressurization system (ADS) primary system depressurization function, no in-containment refueling water storage tank (IRWST) injection, and no significant accumulator injection. The chemical and volume control system (CVCS) and startup feedwater system (SFWS) were automatically initiated and controlled throughout this test.

As in test run S01110, the single steam generator tube rupture was simulated via a line connected from the primary side (coolant pump B suction piping) to the secondary side of steam generator-B (approximately [ ]^{a,b,c} above the tube sheet), with a break orifice diameter scaled to simulate [ ]^{a,b,c} the area of a single AP600 steam generator tube diameter.

Non-loss-of-coolant accident (non-LOCA) events in the AP600 SPES-2 test, including SGTRs and main steam line break (MSBL), did not result in ADS actuation and, therefore, include only the first two event phases observed in LOCA recovery. The event phases identified for the purpose of detailed evaluation of the thermal-hydraulic phenomena occurring within the primary and safety systems for non-LOCA events are shown in Figure 3.10-83 and are as follows:

- Initial depressurization phase (IDP)
- Pressure decay phase (PDP)

3.10.1 Summary of Test Observations

This test simulated an SGTR with nonsafety systems operating and with the operator performing manual actions. Therefore, specific actuation setpoints and anticipated operator actions were performed that impacted the facility response and made this test different from S01110 (an SGTR with nonsafety systems inoperable and no operator actions).

Figure 3.10-83 shows the facility primary system pressure during matrix test S01309 (as measured at the top of the pressurizer) with selected component actuations shown in relation to the primary system pressure.

The IDP began with the opening of the SGTR break valve at time zero seconds and ended at approximately [ ]^{a,b,c} when the primary system pressure had stabilized and when operator actions to control the primary system heat removal and depressurization began. The pressurizer

pressure did not begin to decrease upon initiation of the SGTR because the pressurizer internal heaters and pressure control remained on until [ ]^{a,b,c}. Pressurizer level (shown in Figure 3.10-32) began to decrease immediately upon break initiation. The reactor trip (R) signal and the safety systems actuation (S) signal were actuated at [ ]^{a,b,c} when the pressurizer level reached [ ]^{a,b,c} These actuations, combined with the 16-second delay in the reactor coolant pump (RCP) trip, caused an expected sudden cooldown and shrinkage of the primary system inventory. This was evidenced by the rapid draining of the pressurizer from [ ]^{a,b,c}, and the rapid depressurization from approximately [ ]^{a,b,c} to [ ]^{a,b,c} after the typical small repressurization due to reheating of the hot-leg side fluid as natural circulation takes hold. The pressurizer pressure and overall temperature decreased smoothly at a rate dictated by the break flow and the net primary system cooldown effects. Primary system heat removal was provided by the CMT recirculation; CVCS and startup feedwater injection; and passive residual heat removal (PRHR) heat exchanger (HX) and heat losses offset. During the IDP, the water in the reactor vessel and hot legs remained subcooled.

At [ ]^{a,b,c}, the pressurizer pressure rapidly decreased from approximately [ ]^{a,b,c} to approximately [ ]^{a,b,c}. This was caused by opening of the ADS-1 valve by the facility control computer. After the ADS actuation, there was little or no subcooling present. The time of this event corresponded to the S signal + 7 minutes [ ]^{a,b,c} specified for the automatic functions to start. The combined effect of both the steam generator-A PORV and the ADS-1 valve actuation was to rapidly reduce the hot leg-A temperature from [ ]^{a,b,c} and to reduce the primary system pressure to (or near) the hot-leg saturation pressure.

During the initial portion of the PDP (from [ ]^{a,b,c}), the primary system depressurized from [ ]^{a,b,c} and the hot-leg temperature decreased from [ ]^{a,b,c} that is, the pressure essentially equaled the hot-leg saturation pressure. The hot-leg temperature decrease closely matched the desired [ ] cooldown rate, and the steam generator-A PORVs were not actuated. After [ ]^{a,b,c}, the cooldown rate of hot leg-A dropped below [ ]^{a,b,c}, apparently due to the automatic isolation of the startup feedwater flow to the steam generator-A.

The test personnel cycled one of the two ADS-1 valves (the orifice was sized to simulate one of two ADS-1 valves at 50 percent open) at approximately [ ]^{a,b,c}. (ADS-1 functioned as the primary-side PORV.) This caused a reduction in primary system pressure and a loss of hot-leg subcooling. At approximately [ ]^{a,b,c}, the steam generator-A PORV operation was initiated. From the time the ADS-1 valve was opened until approximately [ ]^{a,b,c}, hot-leg subcooling margin was lost, although the break flow continued to decrease. Approximately [ ]^{a,b,c} into the event, the CMTs were fully heated. This resulted in hotter injection flow to the vessel and effectively reduced the primary system heat removal rate. Opening the steam generator-A PORV for 10-second intervals was insufficient to maintain the desired [ ]^{a,b,c} cooldown rate. Therefore, at approximately [ ]^{a,b,c}, the steam generator-A PORV was left in the open position. This resulted in a cooldown rate of approximately [ ]^{a,b,c}, which established a [ ]^{a,b,c} hot-leg subcooling margin at approximately [ ]^{a,b,c}. The ADS-1 valve was then cycled opened and

closed to reduce primary system pressure. This resulted in the termination of break flow from the primary to secondary side.

During the entire PDP of this event, the heater bundle region and hot legs remained near or below saturation temperature, as evidenced by the collapsed level in the rod bundle and PRHR HX supply line differential pressure (dP) instruments, which showed no voiding.

3.10.2 Analysis of the S01309 Test Data

The analysis of the SPES-2 test was performed using the SPESAN computer code. The code performs a detailed accounting of the coolant inventory in all parts of the system from the start to the end of the test. Also, the internal energy of all components and parts of the facility, including the energy losses from the break and ADS flows, are calculated throughout the event. The mass balance and the energy transfer calculations are performed in much greater detail than were performed in WCAP-14309, *Final Data Report.*[1] The results of the test data analysis are presented in Figures 3.10-1 through 3.10-82. Mass balance snapshots, for key times during the transient, are presented in Table 3.10-1 for all the major primary system components.

Mass Balance

Overall Mass Balance

The uncertainty in the overall mass balance was an indication of the overall quality of the test. The total water inventory was tracked from the start to the end of the test. Figures 3.10-74, 3.10-75, and 3.10-76 show the overall mass balance and the error in mass balance for S01309.

The overall mass balance for S01309 (Figure 3.10-74) shows that the total inventory varies during the event. The primary side loses inventory to the secondary side immediately after initiation of the break. The mass input to the primary system from the operation of the CVCS was not sufficient to make up for the mass lost to the secondary side. A maximum of [ ]^{a,b,c} lbm was lost to the steam generator secondary side until the primary-side pressure equalized with the secondary side-B pressure (approximately [ ]^{a,b,c} sec.). Note that the secondary side was depressurized (above [ ]^{a,b,c} using steam generator A PORV causing flow to the ADS-4/steam generator catch tank. The computer code was developed to include the steam generator-A discharged mass with the system mass (Figure 3.10-74). Figure 3.10-75 shows the difference between the total mass during the event and the initial mass (mass balance error) when the inventory was calculated by integrating the flows to determine the injected mass. Figure 3.10-76 shows the mass balance error when inventory was calculated based on the component mass calculation. The mass balance error, based on flow measurements varied from [ ]^{a,b,c} throughout the event. The component mass calculation results in a very similar mass balance error. A final error was [ ]^{a,b,c} at the end of the event. Mass balance error was affected by the break flow (not included) and ADS-4 mass flow (included into the system mass inventory). Mass injected by the CVCS cancels in the mass balance error.

Water Inventory for the Power Channel and the Loop

Maintenance of the coolant coverage of the heater bundle was the most critical issue for the power channel. The heater bundle coverage during a loss-of-coolant accident (LOCA) event often consists of two-phase fluid, which can have a very high void fraction. However, during a non-LOCA event, such as a SGTR or steam line break (SLB), the heater bundle typically remains well covered with water or two-phase fluid, and if there is any voiding at all, the void fraction is usually low. Figure 3.10-40 shows the level of two-phase fluid in the power channel as calculated from the measured pressure drop data, which was then used to infer a void fraction and two-phase level. Since this represents the true two-phase level, it will be different than the collapsed liquid level in the heater bundle. For S01309, the two-phase level dropped gradually throughout the event beginning at about [ ]^{a,b,c} seconds. However, the level never falls below the cold-leg elevation and is well above the heater bundle.

The collapsed levels in the annular downcomer and tubular downcomer are shown in Figures 3.10-42 (annular downcomer) and 3.10-44 (tubular downcomer). The annular downcomer remains full throughout the event. Figure 3.10-62 shows the maximum cladding temperature during the event and compares this temperature with the saturation temperature. There were no indications of loss of cooling for the heater rods during this event, which confirms the estimated two-phase level in the power channel.

The collapsed fluid level in the rod bundle (Figure 3.10-48) and the rod bundle exit void fraction (Figure 3.10-61) show that the core is water solid before the break was initiated. The rod bundle exit void fraction was determined from DP-014P, which covers the span from the rod bundle near the TAF elevation to the lower part of the upper plenum. Upon reactor trip and the subsequent RCP trip at [ ]^{a,b,c}, the collapsed level falls minimally to [ ]^{a,b,c} with a void fraction of about [ ]^{a,b,c} percent. The collapsed level slowly recovered for the remainder of the event ending at approximately [ ]^{a,b,c} (void fraction about [ ]^{a,b,c}).

The collapsed level in the upper plenum (Figures 3.10-52 and 3.10-54) is essentially unchanged throughout the transient, except for the end of the test. From about [ ]^{a,b,c} until the end, the level began showing the effects of the depressurization of the primary side when the ADS-1 valve is cycled open for [ ]^{a,b,c} and then closed at [ ]^{a,b,c} intervals. By the end of the test, the collapsed level has fallen to about [ ]^{a,b,c} in the upper upper plenum, which is still well above the hot leg elevation.

The water inventory in the power channel is shown in Figure 3.10-39. The mass inventory falls slowly to a minimum of about [ ]^{a,b,c} by the end of the test, which was only [ ]^{a,b,c} less than the initial mass inventory of [ ]^{a,b,c}. The total primary-system inventory (power channel, pressurizer, and loops) is shown in Figure 3.10-77. It reached a minimum of about [ ]^{a,b,c} ([ ]^{a,b,c} of the initial mass of [ ]^{a,b,c}) immediately following RCP trip. It climbed by about [ ]^{a,b,c} to about [ ]^{a,b,c} until the ADS-3 valve was mistakenly cycled opened from [ ]^{a,b,c} to [ ]^{a,b,c} instead of the steam generator-A PORV. This resulted in a reduction of primary system pressure and a loss of hot-leg subcooling. Consequently, this resulted in

the total mass inventory falling from [ ]^{a,b,c} to about [ ]^{a,b,c} until hot-leg subcooling was restored at about [ ]^{a,b,c}. Then the mass increases again to [ ]^{a,b,c} which was within [ ]^{a,b,c} ([ ]^{a,b,c}) of the initial mass inventory.

Water Injection/Ejection

The injected fluid mass from all injection sources is shown in Figure 3.10-78. Figure 3.10-79 shows the total source inventory and the injected and ejected masses during the event. Starting with a total of approximately [ ]^{a,b,c}, only [ ]^{a,b,c} ([ ]^{a,b,c}) of available source water was used by the end of the event.

Energy Balance

PRHR Heat Transfer

The heat transfer from the PRHR to the IRWST gives a unique possibility of comparing heat transfer on the primary and secondary side. A method of calculating the heat rejection by the PRHR heat exchanger into the IRWST is described in Section 2.0, and a comparison of three heat transfer calculations is given in Section 4.0. The PRHR primary-side heat transfer was calculated based on the measured exit flow rate, and the difference in enthalpy of the inlet and exit flows. Since the S01309 test had single-phase flow conditions in the hot legs and PRHR, the inlet flow void fraction was essentially, zero (Figure 3.10-21) making it simple to establish the effective enthalpy of the inlet flow. The outlet flow from the PRHR heat exchanger was always subcooled water as well. The primary-side heat transfer for S01309, shown in Figure 3.10-19, was nearly identical to the heat transfer measured for single-phase flow through the PRHR during the hot pre-operational testing (see WCAP-14309, *Final Data Report*[1]). Figure 3.10-18 shows the calculated heat transfer from the PRHR external tube surface to the water in the IRWST by the three-tube section of the heat exchanger. For the first [ ]^{a,b,c} of the event, the vertical tube transfers the greatest amount of heat, and the top and bottom horizontal sections of the heat exchanger, for the most part, subcooled the fluid with a less effective free-convection heat transfer to the IRWST water, and contributed less to the overall heat transfer of the PRHR. Above [ ]^{a,b,c}, the heat transfer on the inside tube wall at the PRHR inlet effectively heated the outer tube wall temperature above the boiling point for the water in the IRWST, resulting in very effective nucleate boiling heat transfer from the outside surface. Then the top horizontal tube section transferred at the greatest amount of heat.

Figure 3.10-17 shows the internal energy of the IRWST water, the integrated power from the primary side of the PRHR Hx and the heat transfer from the PRHR heat exchanger external surfaces. The internal energy in the IRWST water was calculated based on thermocouples located at various elevations in the IRWST tank, which were allocated different control volumes to arrive at an effective average temperature. A comparison between all three integrated calculations shows good correlation between the PRHR heat transfer (plot line A) and the IRWST heat pickup (plot line C). The calculation for Q_{TUBE} (plot line B) doesn't compare as well since the calculation is based on boiling and free convection heat transfer coefficients, and no boiling occurred at the PRHR Hx inlet walls of

the IRWST for the first [ ]^{a,b,c} of the event making the calculation somewhat inaccurate for this SGTR test.

Steam Generator Heat Transfer

Figure 3.10-32 shows the heat transfer in the steam generators for S01309, and Figure 3.10-33 shows the pressures on the primary side and the secondary side of the steam generators. SFW is initiated after the S signal to maintain steam generator narrow range level. Heat transfer is sharply reduced after the pumps are tripped due to the reduction of flow in the tubes and SFW flow. The pressure plot shows that steam generator-A was available as a heat sink for the entire event. After [ ]^{a,b,c}, steam generator-A was cycled opened and closed for [ ]^{a,b,c} at [ ]^{a,b,c} intervals in order to depressurize the secondary side, specifically for the intent of primary-side cooling. As shown in Figure 3.10-32, this resulted in an increase in the heat transfer rate for steam generator-A from [ ]^{a,b,c}. The steam generator-B pressure nearly follows the primary-side pressure due to the SGTR. The total heat transfer from the primary side to the secondary side, after pumps were tripped, was small. Figure 3.10-28 shows the water inventory in the steam generators primary side, which includes inlet and outlet plena and U-tubes. When full at normal operating temperatures, the steam generator inlet and outlet plena contain approximately [ ]^{a,b,c} of water. Despite the steam generator tube rupture, both steam generators remained full for the entire event. The apparent increase is due to the density changes during the event.

Overall Energy Balance

Figure 3.10-80 shows the integrated energy of the fluid streams leaving the system. The energy content of the SGTR break flow is not indicated in this figure. The flow through the steam generator-A PORV is indicated as UADS4. Note that the only source of fluid leaving the primary system is via the ADS-1 valve (UADS123). The integrated energy of this fluid is very low, only 30000 Btu, compared to the LOCA events when it is on the order of 10^5 Btu.

Figure 3.10-81 shows all the energy components in the heat balance for the system. Throughout the event, core power is the dominant heat input to the system and during the initial part of the transient the steam generators provide the dominant heat extraction. After the RCPs trip at [ ]^{a,b,c}, the heat transfer to the steam generators secondary side became very small. The discharged fluid energy (Figure 3.10-81) is incorrect (actually it is energy discharged from secondary side to the ADS-4 catch tank). The energy related to the break flow and CVCS injection, which was very small, was not included into the energy inventory.

Figure 3.10-82 shows the accumulated heat balance error during the event. During the initial part of the transient, an increasing negative error is produced by a greater than actual transfer through the steam generator. This was a consequence of an assumed overall heat transfer coefficient (HTC) for the steam generator, which was calculated from full-power/full-flow conditions (before time 0) which is higher than the actual HTC at the lower flow conditions existing after the pumps have shut down. The overall error in the heat balance is within [ ]^{a,b,c}

Other Observations

Pressure Decay

Figure 3.10-3 shows the primary system pressure during the S01309 test. Throughout this event the pressure was controlled by the saturation pressure of the hottest fluid volume in the primary system. At the initiation of the break, the controlling fluid volume was in the pressurizer and surge line. Figure 3.10-2 shows that the temperature of the upper plenum was close to the saturation temperature corresponding to the primary system pressure measured in the upper head during the natural circulation phase until about [ ]^{a,b,c} After that time, the primary system pressure was controlled by the steam generator primary-side fluid temperature.

Ejection Flows

Figure 3.10-68 shows the individual mass flows leaving the system via the ADS-1/2/3 and ADS-4/steam generator-A PORV. The individual flow rates are given in Figures 3.10-69, 3.10-70, and 3.10-71. The ADS-1, ADS-2, and ADS-3 flows are very small. The ADS-4 flow (MADS4) represents fluid mass discharged from steam generator-A secondary side through PORV.

TABLE 3.10-1 COMPONENT MASS VARIATIONS IN TEST S01309			
	Start Fault	**End Blowdown**	**End of Transient**
Event time	[		] a,b,c
Power channel			
PC: core			
PC: downcomers			
PC: upper plenum			
Hot leg-.\			
Hot leg-B			
Cold leg-A			
Cold leg-B			
Steam generator primary-A			
steam generator primary-B			
Pressurizer+SL			
CMT-A			
CMT-B			
Accumulator-A			
Accumulator-B			
IRWST	[		]

TEST ANALYSIS STANDARD PLOT PACKAGE Figures 3.10-1 Through 3.10-83				
Fig. No.	**Component**	**Variables**	**Units**	**Description**
3.10-1	Power channel	CORE-POW	kW	Core power
3.10-2	Power channel	TSAT, TAVTDC, TFOUT	°F	Core inlet/outlet temperature, saturation temperature
3.10-3	Pressurizer	PPZRTOP	psia	System pressure
3.10-4	Steam generator	PSGAS, PSGBS	psia	Primary and secondary pressure in steam generators
3.10-5	Steam generator	TAVGSGA, TAVGSGB	°F	Average fluid temperature in steam generators
3.10-6	CMT	MCMTA, MCMTB	lbm	Fluid mass in CMTs
3.10-7	CMT	CLEVELA, CLEVELB	ft.	Collapsed liquid level in CMTs
3.10-8	CMT	MOUTCMTA, MOUTCMTB, MINCMTA, MINCMTB	lbm	Integrated mass in/out of CMTs
3.10-9	CMT	FLOWOUTA, FLOWOUTB	lbm/sec.	Measured flow out of CMTs
3.10-10	CMT	FLOWINA, FLOWINB	lbm/sec.	Calculated flow into CMTs
3.10-11	CMT	BLFRACA, BLFRACB	Fraction	Fractional differential pressure in cold leg-CMT balance lines
3.10-12	CMT	UTOT-A, UTOT-B	Btu	Fluid energy in CMTs
3.10-13	IRWST/PRHR	MIRWST	lbm	Mass of fluid in IRWST
3.10-14	IRWST/PRHR	LIRWST	ft.	Collapsed liquid level in IRWST
3.10-15	IRWST/PRHR	FIRWST	lbm/sec.	Measured discharge flow from IRWST

TEST ANALYSIS STANDARD PLOT PACKAGE (Cont.) Figures 3.10-1 Through 3.10-83				
Fig. No.	**Component**	**Variables**	**Units**	**Description**
3.10-16	IRWST/PRHR	MOUTDVIA, MOUTDVIB	lbm	Integrated mass out of DVI lines
3.10-17	IRWST/PRHR	INT-QCAL, INT-QTUB, U-UO	Btu	Comparison of energy transfer from PRHR tubes to IRWST
3.10-18	IRWST/PRHR	Q-HOR-1, Q-VERT, Q-HOR-2, QTUBEXT	Btu/sec.	Breakdown of heat transfer from different sections of PRHR tube
3.10-19	IRWST/PRHR	Q-CALIM	Btu/sec.	PRHR/IRWST heat transfer calculated on tube side
3.10-20	IRWST/PRHR	FLOWTUBE	lbm/sec.	Measured outlet flow from PRHR tube
3.10-21	IRWST/PRHR	VOID-FRC		Calculated PRHR Inlet void fraction
3.10-22	Accumulator	MACCA, MACCB	lbm	Mass of fluid in accumulators
3.10-23	Accumulator	LACCA, LACCB	ft.	Collapsed liquid level in accumulators
3.10-24	Accumulator	MEASFLWA, MEASFLWB	lbm/sec.	Measured flow from accumulators
3.10-25	Accumulator	MOUTACCA, MOUTACCB	lbm	Integrated mass out of accumulators
3.10-26	Accumulator	U-TOT-A, U-TOT-B	Btu	Energy of fluid in accumulators
3.10-27	Accumulator	AIRMASSA, AIRMASSB	lbm	Mass of air exiting accumulators
3.10-28	Steam generator	MSGAP, MSGBP	lbm	Mass of fluid in steam generators - primary side
3.10-29	Steam generator	LSGAH, LSGAC, LSGBH, LSGBC	ft.	Collapsed liquid levels in steam generators - primary side - hot and cold sides of U-tubes

TEST ANALYSIS STANDARD PLOT PACKAGE (Cont.) Figures 3.10-1 Through 3.10-83				
Fig. No.	**Component**	**Variables**	**Units**	**Description**
3.10-30	Steam generator	MSGAH, MSGAC, MSGBH, MSBGC	lbm	Mass of fluid in steam generators - primary side - hot and cold sides of U-tubes
3.10-31	Steam generator	LSGSA, LSGSB	ft.	Collapsed liquid levels in steam generators - secondary side
3.10-32	Steam generator	Q-TRNF-A, Q-TRNF-B, Q-CALIM	Btu/sec.	Heat transfer in steam generators heat transfer in PRHR
3.10-33	Steam generator	PRESS-PA, PRESS-PB, PREF-A, PREF-B	psia	Primary and secondary pressure in steam generators
3.10-34	Pressurizer	MPZR	lbm	Fluid mass in pressurizer
3.10-35	Pressurizer	LPZR	ft.	Collapsed liquid level in pressurizer
3.10-36	Pressurizer	MSL	lbm	Fluid mass in surge line
3.10-37	Pressurizer	LSL	ft.	Collapsed liquid level in surge line
3.10-38	Pressurizer	UPZR	Btu	Fluid energy in pressurizer
3.10-39	Power channel	MPCHN	lbm	Total fluid mass in power channel
3.10-40	Power channel	L2PHASE, LDVI, LHL, LCL	ft.	Two-phase liquid level in power channel vs. DVI, hot-leg, and cold-leg elevations
3.10-41	Power channel	MANDC	lbm	Fluid mass in annular downcomer
3.10-42	Power channel	LANDC, LDVI, LHL, LCL	ft.	Collapsed liquid level in annular downcomer vs. DVI, hot-leg, and cold-leg elevations

TEST ANALYSIS STANDARD PLOT PACKAGE (Cont.) Figures 3.10-1 Through 3.10-83				
Fig. No.	**Component**	**Variables**	**Units**	**Description**
3.10-43	Power channel	MTDC	lbm	Fluid mass in tubular downcomer
3.10-44	Power channel	LTDC, LBOF, LTOF	ft.	Collapsed liquid level in tubular downcomer vs. top of active fuel and bottom of active fuel levels
3.10-45	Power channel	MLOWP	lbm	Fluid mass in lower plenum
3.10-46	Power channel	LLOWP	ft.	Collapsed liquid level in lower plenum
3.10-47	Power channel	MCORE	lbm	Fluid mass in core region
3.10-48	Power channel	LCORE	ft.	Collapsed liquid level in core
3.10-49	Power channel	MFOUT	lbm	Fluid mass in core outlet region
3.10-50	Power channel	LFOUT	ft.	Collapsed liquid level in core outlet region
3.10-51	Power channel	MUPPL	lbm	Fluid mass in the lower portion of the upper plenum
3.10-52	Power channel	LUPPL	ft.	Collapsed liquid level in the lower portion of the upper plenum
3.10-53	Power channel	MUPPU	lbm	Fluid mass in the upper portion of the upper plenum
3.10-54	Power channel	LUPPU	ft.	Collapsed liquid level in the upper portion of the upper plenum
3.10-55	Power channel	MHEAD	lbm	Fluid mass in the upper head
3.10-56	Power channel	LHEAD	ft.	Collapsed liquid level in the upper head

TEST ANALYSIS STANDARD PLOT PACKAGE (Cont.) Figures 3.10-1 Through 3.10-83				
Fig. No.	**Component**	**Variables**	**Units**	**Description**
3.10-57	Power channel	UPC	Btu	Total fluid energy in power channel
3.10-58	Power channel	Q-FLUX	Btu/sec.-ft.^{2}	Average heat flux on the heated rods
3.10-59	Power channel	STM-RATE	lbm/sec.	Core steam generation rate
3.10-60	Power channel	FLOWCOR	lbm/sec.	Calculated core flow
3.10-61	Power channel	VOIDOUT		Void fraction at core exit
3.10-62	Power channel	TMAX, TSAT, TMAX-TSAT	°F	Maximum clad temperature, saturation temperature and delta
3.10-63	Hot leg	MHLA, MHLB	lbm	Fluid mass in hot legs
3.10-64	Hot leg	FLA, FLB	Fraction	Fractional collapsed liquid level in hot legs
3.10-65	Cold leg	MCLA, MCLB	lbm	Fluid mass in cold legs
3.10-66	Cold leg	LCLA1, LCLA2, LPSA	ft.	Collapsed liquid levels in cold leg-A
3.10-67	Cold leg	LCLB1, LCLB2, LPSB	ft.	Collapsed liquid levels in cold leg-N
3.10-68	Total system mass	MADS1-3, MADS4, BRKMASS	lbm	Catch tank mass for ADS-1, ADS-2, ADS-3, ADS-4, and break
3.10-69	Total system mass	DMADS1-3	lbm/sec.	Calculated flow out ADS-1, ADS-2, ADS-3
3.10-70	Total system mass	DMADS4	lbm/sec.	Calculated flow out ADS-4
3.10-71	Total system mass	BRKFLOW	lbm/sec.	Calculated flow out break
3.10-72	Total system energy	UADS123, UADS4, UBREAK	Btu	Integrated fluid energy for ADS-1, ADS-2, ADS-3, ADS-4, and the break

TEST ANALYSIS STANDARD PLOT PACKAGE (Continued) FIGURES 3.10-1 Through 3.10-82				
Fig. No.	**Component**	**Variables**	**Units**	**Description**
3.10-73	Total system energy	VOID		Calculated void fraction for ADS-1, ADS-2, and ADS-3
3.10-74	Total system mass	MTOTAL, MTOTO	lbm	Total system fluid mass vs. initial fluid mass
3.10-75	Total system mass	ERRLOP	lbm	Error in the mass balance (using measured and calculated flows)
3.10-76	Total system mass	ERRLOPI	lbm	Error in the mass balance (using fluid inventory)
3.10-77	Total system mass	MPCLTOT, MPCLO	lbm	Total fluid mass in power channel and loops vs. Initial fluid mass
3.10-78	Total system mass	MACOUT, MCMOUT, MIROUT	lbm	Total integrated mass discharged from accumulators, CMTs, and IRWST
3.10-79	Total system mass	MSOURCE, MSINK, MSOURIN	lbm	Total source inventory, total mass ejected from primary system, and total mass injected to primary system
3.10-80	Total system energy	UADS123, UBREAK, UADS4, UCATCH	Btu	Integrated fluid energy exiting via ADS-1, ADS-2, ADS-3, ADS-4, and the break, and the sum
3.10-81	Total system energy	USURR, UCATCH, UQIN, UFLD-UO, UMTL-UO, USG	Btu	Overall energy balance including integrated rod power, steam generator power, and heat loss to the surroundings, energy exiting via ads and break, energy input via nonsafety systems, and change in primary system fluid and metal energy relative to start of test
3.10-82	Total system energy	UERROR, ERROR-%	Btu, %	Error in overall energy balance, relative to initial fluid and metal energy
3.10-83	System pressure	--	psia	Test event phases and system pressure

The figures listed are proprietary and, therefore,
are not available in the Class 3 version of this report.

These figures are available in the Class 2 version of this report.

3.11 Analysis of the Steam Generator Tube Rupture without Nonsafety Systems (S01110)

This matrix test simulated a steam generator tube rupture (SGTR) with only the automatic passive safety systems being used for accident mitigation (no nonsafety systems operating nor operator actions). The pressurizer internal heaters were shut-off at break initiation and the chemical and volume control system (CVCS), normal residual heat removal (NRHR) function and startup feedwater system (SFWS) were shut-off for this test. During mitigation of the SGTR, there was no core makeup tank (CMT), accumulator, or in-containment refueling water storage tank (IRWST) injection throughout the transient. The single SGTR is simulated via a line connected from the primary side (reactor coolant pump-B (RCP-B) suction piping) to the secondary side of steam generator-A (approximately [ ]^{a,b,c} above the tube sheet), with a break orifice diameter scaled to a single AP600 steam generator tube diameter.

Since this SGTR event did not result in automatic depressurization system (ADS) actuation, only the first two event phases observed in loss-of-coolant accident (LOCA) recovery occurred. The event phases selected for the purpose of detailed evaluation of the non-LOCA events are as follows:

- Initial depressurization phase (IDP)
- Pressure decay phase (PDP)

3.11.1 Summary of Test Observations

Figure 3.11-1 shows the plant primary system pressure during matrix test S01110 (as measured at the top of the pressurizer) with selected component actuations and plant responses shown in relation to the primary system pressure.

The IDP began with the opening of the break valve between the primary and secondary side, causing the pressurizer to drain. Because the control grade pressurizer heaters were not on after break initiation, there was a reduction in pressure due to pressurizer steam expansion.

When the pressurizer level dropped to [ ]^{a,b,c} at [ ]^{a,b,c}, the reactor trip (R) and safety system actuation (S) signals were actuated. Two seconds later, the main steam line isolation valves (MSLIVs) and main feedwater isolation valves (MFWIVs) were closed, the CMTs and passive residual heat removal (PRHR) heat exchanger (HX) return line isolation valves were opened, and the RCPs coasted down with a [ ]^{a,b,c} delay (at [ ]^{a,b,c} into the event). Power in the heated rod bundle was reduced to [ ]^{a,b,c} percent of full-power and heat decay began with [ ]^{a,b,c} delay (at [ ]^{a,b,c}). The rod bundle power was maintained at [ ]^{a,b,c} above the scaled decay heat, starting at approximately [ ]^{a,b,c} after trip, to compensate for heat losses.

The recirculation flow through the CMTs and the PRHR flow began immediately after the CMT injection valves and the PRHR return flow valve were opened. The power-to-flow ratio was changing when the RCPs were tripped and coasted down, during the onset of natural circulation flow. This caused a reduction, followed by an increase, in the hot-leg temperature, and a rapid decrease in

pressurizer pressure from [ ]^{a,b,c} psia followed by a slight increase in pressure. Primary pressure then dropped toward the steam generator saturation pressure while transferring heat to the steam generators, and the break flow stabilized at approximately [ ]^{a,b,c}. The IDP ended at [ ]^{a,b,c}, when hot-leg/upper-plenum temperature ([ ]^{a,b,c}) started to control the primary system pressure. The level of the upper plenum, which was above the hot legs, began to decrease.

During the initial portion of the PDP (up to [ ]^{a,b,c}), the primary system, with the exception of the top of the upper plenum and upper head, remained water solid. Primary system cooling was provided by the PRHR HX, CMT recirculation, break flow, and facility heat losses. The primary and secondary system temperature and pressure slowly decreased throughout the PDP. The PRHR HX heat removal rate was calculated to be [ ]^{a,b,c} at [ ]^{a,b,c}, based on essentially single-phase flow in the PRHR supply line, the PRHR flow rate, temperature, and pressure.

At approximately [ ]^{a,b,c}, the upper portion of the reactor vessel upper plenum and the reactor vessel upper head began to drain at a significant rate. This resulted in an increasing pressurizer level. The upper plenum drained rapidly to the hot-leg elevation starting at approximately [ ]^{a,b,c} and was completely drained at approximately [ ]^{a,b,c}.

At this time, primary and secondary pressures were essentially equalized and several events occurred almost simultaneously:

- The break flow to steam generator-B decreased from approximately [ ]^{a,b,c} at [ ]^{a,b,c} and to approximately 0 at [ ]^{a,b,c}.
- The steam generator-B tubes began to drain at approximately [ ]^{a,b,c}.
- The loop-B cold leg flows decreased and loop-A flows increased momentarily.
- The upper plenum, below the hot legs, PRHR supply line, etc., all became voided.
- The pressurizer level rapidly increased in response to the draining steam generator-B U-tubes and primary system voiding.

This resulted in oscillations of temperature, void fraction, tubular downcomer flow, and system pressure, all of which continued throughout the rest of test. The pressurizer was completely filled at [ ]^{a,b,c} and remained filled for the rest of the test. The CMT's natural recirculation flow continued, but the flow rate decreased. The upper head was completely drained at [ ]^{a,b,c} into the event, and the level never recovered. The primary system pressure oscillated about the secondary system pressure and there was a small alternating flow in the break line.

Due to periodic boiling in the rod bundle, an oscillating two-phase flow entered the hot leg from the upper plenum and flowed through the steam generators and PRHR HX in the IRWST. When the level in the hot leg dropped below the PRHR inlet (top of the horizontal hot leg), steam from the upper

plenum flowed into the PRHR inlet line to the PRHR HX where it condensed. When the hot leg filled to the PRHR inlet, a slug of water flowed to the PRHR HX.

Hot leg-B fluid had a void fraction close to that shown in the upper plenum. The void fraction in hot leg-A was lower due to the selective removal of vapor from the hot leg by the PRHR inlet line. The void fraction in the PRHR supply at the IRWST oscillated and reached high peaks, which enhanced the PRHR from the primary system when compared with single-phase saturated or subcooled water before [ ]^{a,b,c}.

As stated above, the natural circulation flow ended in steam generator-B (by voiding U-tubes) approximately [ ]^{a,b,c} into the event. At the end of the event, the steam generator-B U-tubes were drained, thereby partly draining the pump B suction. The natural circulation flow in steam generator-A continued through this test; however, there was a high oscillating void fraction in the upper section of the U-tubes.

3.11.2 Analysis of the S01110 Test Data

The analysis of the SPES-2 test was performed using the SPESAN computer code. The code performs a detailed accounting of the coolant inventory in all parts of the system from the start to the end of the test. Also, the internal energy of all components and parts of the facility, including the energy losses from the break and ADS flows, are calculated throughout the event. The mass balance and the energy transfer calculations are performed in much greater detail than were performed in WCAP-14309, *Final Data Report*.[1] The results of the test data analysis are presented in Figures through 3.11-82. Mass balance snapshots, for key times during the transient, are presented in Table 3.11-1, for all the major primary system components.

Mass Balance

Overall Mass Balance

The uncertainty in the overall mass balance was an indication of the overall quality of the test. The total water inventory is tracked from the start until the end of the test. Figures 3.11-74, 3.11-75, and 3.11-76 show the overall mass balance and the error (uncertainty) in mass balance for S01110.

The overall mass balance for S01110 (Figure 3.11-74) shows that the total inventory falls moderately during the event. The primary side loses inventory to the secondary side immediately after initiation of the break. The slope was relatively linear for the first [ ]^{a,b,c} seconds of the transient, but flattens out around [ ]^{a,b,c} seconds. A maximum of [ ]^{a,b,c} lbm was lost to the steam generator secondary side until the primary-side pressure equalizes with the secondary side pressure at about [ ]^{a,b,c} seconds. The final mass loss on the primary side was approximately [ ]^{a,b,c} lbm. Figure 3.11-75 shows the difference between the total mass during the event and the initial mass (mass balance error) when the inventory was calculated by integrating the flows. Figure 3.11-76 shows the mass balance error when inventory was calculated based on the catch tank weight and level

measurements. The mass balance error, based on flow measurements, shows that the error increases negatively as the event progresses with the final result being -110 lbm. The weight and level measurements result in a similar error. This mass balance error matched well with fluid mass lost to the secondary side, not included into the mass inventory calculation by the computer code.

Water Inventory for the Power Channel and the Loop

Maintenance of the coolant coverage of the heater bundle was the most critical issue for the power channel. The heater bundle coverage during a LOCA event often consisted of two-phase fluid, which can have a very high void fraction. However, during a non-LOCA event such as an SGTR or steam line break (SLB), the heater bundle typically remains well covered with water or two-phase fluid, and if there is any voiding at all, the void fraction is usually low. Figure 3.11-40 shows the true level of two-phase fluid in the power channel as measured from the elevation of the top of the core (TAF). Since this represents the true two-phase level, it will be different than the collapsed liquid level in the heater bundle. For S01110, the two-phase level was relatively unchanged for the first [ ]^{a,b,c} of the event, but then dropped suddenly from about [ ]^{a,b,c} It remained at the [ ]^{a,b,c} level for the remainder of the event which was well above the heater bundle.

The level on the cold side of the power channel is shown in Figures 3.11-42 (annular downcomer) and 3.11-44 (tubular downcomer). The annular downcomer remained full throughout the event. Figure 3.11-62 shows the maximum cladding temperature during the event and compares this temperature with the saturation temperature. There were no indications of loss of cooling for the heater rods during this event, which confirms the estimated two-phase level in the power channel.

The collapsed fluid level in the core (Figure 3.11-48) and the core exit void fraction (Figure 3.11-61) show that the core is water solid when the event starts. Upon reactor trip and the subsequent RCP trip at [ ]^{a,b,c} seconds, the collapsed core level fell minimally to [ ]^{a,b,c} ft. with a low void fraction of about [ ]^{a,b,c} percent. It remained at these conditions up to about [ ]^{a,b,c} seconds. Then there were large oscillations in the core exit void fraction and the collapsed fluid level. The average core exit void fraction was about [ ]^{a,b,c} percent, and the average collapsed fluid level was about [ ]^{a,b,c} ft.

The collapsed level in the upper plenum (Figures 3.11-54 and 3.11-52) decreased to about [ ]^{a,b,c} ft. below the hot-leg elevation at about [ ]^{a,b,c} seconds into the event. Then the collapsed level in the upper plenum oscillated and had an oscillating range from [ ]^{a,b,c} ft. below the hot leg to [ ]^{a,b,c} ft. above the hot leg. The average by the end of the test was about [ ]^{a,b,c} ft., or [ ]^{a,b,c} inches below the hot leg.

Figure 3.11-39 shows the water inventory in the power channel. Initially, the mass inventory increased slightly to a maximum of approximately [ ]^{a,b,c} lbm around [ ]^{a,b,c} seconds. Then the mass inventory fell rapidly to about [ ]^{a,b,c} lbm just prior to the initiation of the oscillations at [ ]^{a,b,c} seconds. When the oscillations began, the power channel mass inventory flattened out at an average of [ ]^{a,b,c} lbm with minimum and maximum oscillations ranging from [ ]^{a,b,c} lbm to [ ]^{a,b,c} lbm, respectively. The total primary system inventory (power channel, pressurizer, and loops)

is shown in Figure 3.11-77. It reached a minimum of about [ ]^{a,b,c} lbm ([ ]^{a,b,c} percent of the initial mass of [ ]^{a,b,c} lbm) by the end of the event.

Water Injection/Ejection

The injected fluid mass from all injection sources is shown in Figure 3.11-78. Figure 3.11-79 shows the total source inventory and the injected and ejected masses during the event. Starting with a total of approximately [ ]^{a,b,c} inventory, only [ ]^{a,b,c} lbm ([ ]^{a,b,c} percent) of available source water was used by the end of the event (Figure 3.11-6).

Energy Balance

PRHR Heat Transfer

The heat transfer from the PRHR to the IRWST gave a unique possibility of comparing heat transfer on the primary and secondary side. A method of calculating the heat rejection by the PRHR HX into the IRWST is described in Section 2.2.2, and a comparison of three heat transfer calculations is given in Section 4.0. The PRHR primary-side heat transfer was calculated based on the measured exit flow rate and the difference in enthalpy of the inlet and exit flows. Since the S01110 test had two-phase flow conditions in the PRHR after [ ]^{a,b,c} seconds, the inlet flow void fraction was determined (Figure 3.11-21) and used to establish the effective enthalpy of the inlet flow. The outlet flow from the PRHR HX was always subcooled water. For the first [ ]^{a,b,c} seconds of the event, the primary-side heat transfer for S01110 (shown in Figure 3.11-19), was nearly identical to the heat transfer measured for single-phase flow through the PRHR during the hot pre-operational testing (see WCAP-14309, *Final Data Report*).[1] After [ ]^{a,b,c} seconds, the two-phase heat transfer was considerably greater than the single-phase-flow heat transfer.

Figure 3.11-18 shows the calculated heat transfer from the PRHR external tube surface to the water in the IRWST by the three tube sections of the HX. For the first [ ]^{a,b,c} seconds, S01110 was similar to the other SGTR test S01309. The void fraction was near zero so that the vertical tube transferred the greatest amount of heat, and the top and bottom horizontal sections of the heat exchanger contributed less to the overall heat transfer of the PRHR for the first [ ]^{a,b,c} seconds of the event which averaged about [ ]^{a,b,c} Btu/sec. After [ ]^{a,b,c} seconds, two-phase fluid flow began through the PRHR HX, and the void fraction oscillated at an average of about [ ]^{a,b,c} percent. Then the top horizontal tube transfers the greatest amount of heat. The condensation process on the inside effectively heated this tube wall temperature above the boiling point for the water in the IRWST, resulting in very effective nucleate boiling heat transfer from the outside surface. The heat transfer rate correspondingly increases to an average of about [ ]^{a,b,c} Btu/sec. This was similar to the typical LOCA event which has a high heat transfer rate due to a high void fraction. Due to the oscillating slugs of steam and water in the PRHR supply line, there are large fluctuations in the heat transfer rate and the void fraction. The void fraction ranges from zero to [ ]^{a,b,c} percent after [ ]^{a,b,c} seconds, and the heat transfer rate correspondingly ranges from zero to [ ]^{a,b,c} Btu/sec.

Figure 3.11-17 shows the internal energy of the IRWST water, the integrated power from the primary side of the PRHR HX, and the heat transfer from the PRHR HX external surfaces. The internal energy in the IRWST water was calculated based on thermocouples located at various elevations in the IWRST tank, which were allocated different control volumes to arrive at an effective average temperature. A comparison between all three integrated calculations shows good correlation between the PRHR heat transfer (plot line A) and the IRWST heat pickup (plot line C). The calculation for Q_{TUBE} (plot line B) doesn't compare as well initially since the calculation is based on boiling and free convection heat transfer coefficients, and no boiling occurs at the PRHR HX inlet walls of the IRWST for the first [ ]^{a,b,c} seconds of the event. Beyond that time, boiling of the IRWST fluid near the PRHR Hx tube walls begins making the Q_{TUBE} calculation more accurate so that Plot line B has nearly the same slope as plot lines A and B.

Steam Generator Heat Transfer

Figure 3.11-32 shows the heat transfer in the steam generators for S01110, and Figure 3.11-33 shows the pressures on the primary side and the secondary side of the steam generators. Heat transfer was sharply reduced after the pumps are tripped due to the reduction of flow in the tubes. The pressures show that the steam generators were available as heat sinks until approximately [ ]^{a,b,c} seconds into the event, at which time primary-and secondary-side pressures nearly equalize and heat transfer rate for steam generators dropped to nearly zero.

Figure 3.11-28 shows the water inventory in the steam generators primary side, which includes inlet and outlet plena and U-tubes. When full, the steam generator inlet and outlet plena contains approximately 80 lbm of water. After oscillations started in the primary system, the steam generator-B U-tubes started to drain (at approximately [ ]^{a,b,c} seconds) and contain trapped steam, which became more and more superheated as the primary-side pressure decays. The steam generator-A U-tubes were water solid, but fluid void fraction was oscillated above [ ]^{a,b,c} seconds, as seen in the oscillations of mass (Figure 3.11-28).

Overall Energy Balance

Figure 3.11-80 shows the integrated energy of the fluid streams leaving the system. For test S01110, the only fluid stream leaving the system was the SGTR break flow, which was very small and not accounted for by the computer code.

Figure 3.11-81 shows all the energy components in the heat balance for the system. Throughout the event, core power was the dominant heat input to the system and during the initial part of the transient the steam generators provide the dominant heat extraction until about [ ]^{a,b,c} seconds, after which time heat transfer to the secondary side was very small. Then the sum of the other integrated energies for the surroundings, system fluid, discharged fluids, and metal mass matches the heat input by the power channel heater rods reasonably well.

Figure 3.11-82 shows the accumulated error in the energy balance during the event. The maximum error band in the heat balance is approximately [ ]^{a,b,c} The error at the end of the event was approximately [ ]^{a,b,c} Energy associated with the break flow, which was very low, was not included into the energy balance.

Other Observations

Pressure Decay

Figure 3.11-3 shows the primary system pressure during the S01110 test. Throughout this event the pressure was controlled by the saturation pressure of the hottest fluid volume in the primary system. At the initiation of the break, the controlling fluid volume was in the pressurizer and surge line. Figure 3.11-2 shows that the temperature of the upper plenum was nearly at the saturation temperature corresponding to the primary system pressure measured in the upper head after [ ]^{a,b,c} seconds during the natural circulation phase.

Ejection Flows

Figure 3.11-68 shows the individual mass flows leaving the system via the ADS 1/2/3 and ADS-4/SG A PORV. The individual flow rates are given in Figures 3.11-69, 3.11-70, and 3.11-71. The ADS 1/2/3 flow was zero. The ADS-4 mass flow (from steam generator-A PORV) was low and the total mass is less than [ ]^{a,b,c} lbm. The total mass flow leaving the system (Figure 3.11-79) as well as the energy of fluid ejection (Figure 3.11-80) were very low for S01110.

a,b,c

TABLE 3.11-1
COMPONENT MASS VARIATIONS IN TEST S01110

	Start Fault	End Blowdown	End of Transient
Event time			
Power channel			
PC: core			
PC: downcomers			
PC: upper plenum			
Hot leg-A			
Hot leg-B			
Cold leg-A			
Cold leg-B			
SG primary-A			
SG primary-B			
Pressurizer + SL			
CMT-A			
CMT-B			
Accumulator-A			
Accumulator-B			
IRWST			

TEST ANALYSIS STANDARD PLOT PACKAGE Figures 3.11-1 Through 3.11-83				
Fig. No.	**Component**	**Variables**	**Units**	**Description**
3.11-1	Power channel	CORE-POW	kW	Core power
3.11-2	Power channel	TSAT, TAVTDC, TFOUT	°F	Core inlet/outlet temperature, saturation temperature
3.11-3	Pressurizer	PPZRTOP	psia	System pressure
3.11-4	Steam generator	PSGAS, PSGBS	psia	Primary and secondary pressure in steam generators
3.11-5	Steam generator	TAVGSGA, TAVGSGB	°F	Average fluid temperature in steam generators
3.11-6	CMT	MCMTA, MCMTB	lbm	Fluid mass in CMTs
3.11-7	CMT	CLEVELA, CLEVELB	ft.	Collapsed liquid level in CMTs
3.11-8	CMT	MOUTCMTA, MOUTCMTB, MINCMTA, MINCMTB	lbm	Integrated mass in/out of CMTs
3.11-9	CMT	FLOWOUTA, FLOWOUTB	lbm/sec.	Measured flow out of CMTs
3.11-10	CMT	FLOWINA, FLOWINB	lbm/sec.	Calculated flow into CMTs
3.11-11	CMT	BLFRACA, BLFRACB	Fraction	Fractional differential pressure in cold leg-CMT balance lines
3.11-12	CMT	UTOT-A, UTOT-B	Btu	Fluid energy in CMTs
3.11-13	IRWST/PRHR	MIRWST	lbm	Mass of fluid in IRWST
3.11-14	IRWST/PRHR	LIRWST	ft.	Collapsed liquid level in IRWST
3.11-15	IRWST/PRHR	FIRWST	lbm/sec.	Measured discharge flow from IRWST

TEST ANALYSIS STANDARD PLOT PACKAGE Figures 3.11-1 Through 3.11-83 (Cont.)				
Fig. No.	**Component**	**Variables**	**Units**	**Description**
3.11-16	IRWST/PRHR	MOUTDVIA, MOUTDVIB	lbm	Integrated mass out of DVI lines
3.11-17	IRWST/PRHR	INT-QCAL, INT-QTUB, U-UO	Btu	Comparison of energy transfer from PRHR tubes to IRWST
3.11-18	IRWST/PRHR	Q-HOR-1, Q-VERT, Q-HOR-2, QTUBEXT	Btu/sec.	Breakdown of heat transfer from different sections of PRHR tube
3.11-19	IRWST/PRHR	Q-CALIM	Btu/sec.	PRHR/IRWST heat transfer calculated on tube side
3.11-20	IRWST/PRHR	FLOWTUBE	lbm/sec.	Measured outlet flow from PRHR tube
3.11-21	IRWST/PRHR	VOID-FRC		Calculated PRHR Inlet void fraction
3.11-22	Accumulator	MACCA, MACCB	lbm	Mass of fluid in accumulators
3.11-23	Accumulator	LACCA, LACCB	ft.	Collapsed liquid level in accumulators
3.11-24	Accumulator	MEASFLWA, MEASFLWB	lbm/sec.	Measured flow from accumulators
3.11-25	Accumulator	MOUTACCA, MOUTACCB	lbm	Integrated mass out of accumulators
3.11-26	Accumulator	U-TOT-A, U-TOT-B	Btu	Energy of fluid in accumulators
3.11-27	Accumulator	AIRMASSA, AIRMASSB	lbm	Mass of air exiting accumulators
3.11-28	Steam generator	MSGAP, MSGBP	lbm	Mass of fluid in steam generators - primary side
3.11-29	Steam generator	LSGAH, LSGAC, LSGBH, LSGBC	ft.	Collapsed liquid levels in steam generators - primary side - hot and cold sides of U-tubes

TEST ANALYSIS STANDARD PLOT PACKAGE Figures 3.11-1 Through 3.11-83 (Cont.)				
Fig. No.	**Component**	**Variables**	**Units**	**Description**
3.11-30	Steam generator	MSGAH, MSGAC, MSGBH, MSBGC	lbm	Mass of fluid in steam generators - primary side - hot and cold sides of U-tubes
3.11-31	Steam generator	LSGSA, LSGSB	ft.	Collapsed liquid levels in steam generators - secondary side
3.11-32	Steam generator	Q-TRNF-A, Q-TRNF-B, Q-CALIM	Btu/sec.	Heat transfer in steam generators heat transfer in PRHR
3.11-33	Steam generator	PRESS-PA, PRESS-PB, PREF-A, PREF-B	psia	Primary and secondary pressure in steam generators
3.11-34	Pressurizer	MPZR	lbm	Fluid mass in pressurizer
3.11-35	Pressurizer	LPZR	ft.	Collapsed liquid level in pressurizer
3.11-36	Pressurizer	MSL	lbm	Fluid mass in surge line
3.11-37	Pressurizer	LSL	ft.	Collapsed liquid level in surge line
3.11-38	Pressurizer	UPZR	Btu	Fluid energy in pressurizer
3.11-39	Power channel	MPCHN	lbm	Total fluid mass in power channel
3.11-40	Power channel	L2PHASE, LDVI, LHL, LCL	ft.	Two-phase liquid level in power channel vs. DVI, hot-leg, and cold-leg elevations
3.11-41	Power channel	MANDC	lbm	Fluid mass in annular downcomer
3.11-42	Power channel	LANDC, LDVI, LHL, LCL	ft.	Collapsed liquid level in annular downcomer vs. DVI, hot-leg, and cold-leg elevations

TEST ANALYSIS STANDARD PLOT PACKAGE Figures 3.11-1 Through 3.11-83 (Cont.)				
Fig. No.	**Component**	**Variables**	**Units**	**Description**
3.11-43	Power channel	MTDC	lbm	Fluid mass in tubular downcomer
3.11-44	Power channel	LTDC, LBOF, LTOF	ft.	Collapsed liquid level in tubular downcomer vs. top of active fuel and bottom of active fuel levels
3.11-45	Power channel	MLOWP	lbm	Fluid mass in lower plenum
3.11-46	Power channel	LLOWP	ft.	Collapsed liquid level in lower plenum
3.11-47	Power channel	MCORE	lbm	Fluid mass in core region
3.11-48	Power channel	LCORE	ft.	Collapsed liquid level in core
3.11-49	Power channel	MFOUT	lbm	Fluid mass in core outlet region
3.11-50	Power channel	LFOUT	ft.	Collapsed liquid level in core outlet region
3.11-51	Power channel	MUPPL	lbm	Fluid mass in the lower portion of the upper plenum
3.11-52	Power channel	LUPPL	ft.	Collapsed liquid level in the lower portion of the upper plenum
3.11-53	Power channel	MUPPU	lbm	Fluid mass in the upper portion of the upper plenum
3.11-54	Power channel	LUPPU	ft.	Collapsed liquid level in the upper portion of the upper plenum
3.11-55	Power channel	MHEAD	lbm	Fluid mass in the upper head
3.11-56	Power channel	LHEAD	ft.	Collapsed liquid level in the upper head

TEST ANALYSIS STANDARD PLOT PACKAGE Figures 3.11-1 Through 3.11-83 (Cont.)				
Fig. No.	**Component**	**Variables**	**Units**	**Description**
3.11-57	Power channel	UPC	Btu	Total fluid energy in power channel
3.11-58	Power channel	Q-FLUX	Btu/sec.-ft.^{2}	Average heat flux on the heated rods
3.11-59	Power channel	STM-RATE	lbm/sec.	Core steam generation rate
3.11-60	Power channel	FLOWCOR	lbm/sec.	Calculated core flow
3.11-61	Power channel	VOIDOUT		Void fraction at core exit
3.11-62	Power channel	TMAX, TSAT, TMAX-TSAT	°F	Maximum clad temperature, saturation temperature and delta
3.11-63	Hot leg	MHLA, MHLB	lbm	Fluid mass in hot legs
3.11-64	Hot leg	FLA, FLB	Fraction	Fractional collapsed liquid level in hot legs
3.11-65	Cold leg	MCLA, MCLB	lbm	Fluid mass in cold legs
3.11-66	Cold leg	LCLA1, LCLA2, LPSA	ft.	Collapsed liquid levels in cold leg-A
3.11-67	Cold leg	LCLB1, LCLB2, LPSB	ft.	Collapsed liquid levels in cold leg-B
3.11-68	Total system mass	MADS1-3, MADS4, BRKMASS	lbm	Catch tank mass for ADS-1, ADS-2, ADS-3, ADS-4, and break
3.11-69	Total system mass	DMADS1-3	lbm/sec.	Calculated flow out ADS-1, ADS-2, ADS-3
3.11-70	Total system mass	DMADS4	lbm/sec.	Calculated flow out ADS-4
3.11-71	Total system mass	BRKFLOW	lbm/sec.	Calculated flow out break
3.11-72	Total system energy	UADS123, UADS4, UBREAK	Btu	Integrated fluid energy for ADS-1, ADS-2, ADS-3, ADS4, and the break

TEST ANALYSIS STANDARD PLOT PACKAGE Figures 3.11-1 Through 3.11-83 (Cont.)				
Fig. No.	**Component**	**Variables**	**Units**	**Description**
3.11-73	Total system energy	VOID		Calculated void fraction for ADS-1, ADS-2, and ADS-3
3.11-74	Total system mass	MTOTAL, MTOT0	lbm	Total system fluid mass vs. initial fluid mass
3.11-75	Total system mass	ERRLOP	lbm	Error in the mass balance (using measured and calculated flows)
3.11-76	Total system mass	ERRLOP1	lbm	Error in the mass balance (using fluid inventory)
3.11-77	Total system mass	MPCLTOT, MPCLO	lbm	Total fluid mass in power channel and loops vs. initial fluid mass
3.11-78	Total system mass	MACOUT, MCMOUT, MIROUT	lbm	Total integrated mass discharged from accumulators, CMTs, and IRWST
3.11-79	Total system mass	MSOURCE, MSINK, MSOURIN	lbm	Total source inventory, total mass ejected from primary system, and total mass injected to primary system
3.11-80	Total system energy	UADS123, UBREAK, UADS4, UCATCH	Btu	Integrated fluid energy exiting via ADS-1, ADS-2, ADS-3, ADS-4, and the break, and the sum
3.11-81	Total system energy	USURR, UCATCH, UQIN, UFLD-UO, UMTL-UO, USG	Btu	Overall energy balance including integrated rod power, steam generator power, and heat loss to the surroundings, energy exiting via ads and break, energy input via nonsafety systems, and change in primary system fluid and metal energy relative to start of test
3.11-82	Total system energy	UERROR, ERROR-%	Btu, %	Error in overall energy balance, relative to initial fluid and metal energy
3.11.83	System Pressure	—	psia	Test event phases and system pressure

3.12 Steam Generator Tube Rupture without Nonsafety Systems, with Inadvertent ADS (S01211)

Test S01211 was a blind test; therefore, this section has been intentionally left blank and will be provided later.

3.13 Large Steam Line Break at Hot Standby Conditions without Nonsafety Systems (S01512)

Test S01512 was a blind test; therefore, this section has been intentionally left blank and will be provided later.

4.2 Behavior of Core Makeup Tanks

A unique feature of the AP600 design is the use of passive safety systems to enhance reactor protection following postulated accidents. The core makeup tank (CMT) is one component of the AP600 passive safety systems. Each tank stores 2000 $ft.^3$ of cold borated water at reactor coolant system (RCS) pressure that can be gravity-injected into the RCS to provide reactivity control and core cooling. The CMTs provide the same function as the high-pressure safety injection system in existing pressurized water reactors (PWRs), with the difference being that current plants require the availability of ac power to perform their safety function, whereas the CMTs achieve this with gravity-driven flows.

A brief description of the AP600 CMT is presented, along with a description of the SPES-2 representation.

An examination of the CMT behavior for the range of test conditions is presented. These include the following:

- Fluid temperature distributions and fluid-wall temperature differences, including the effects of air in the CMT
- Flashing and liquid level swell for larger breaks
- Steam/water mixing
- CMT refill (after IRWST actuation)

These topics are discussed in Sections 4.2.3 and 4.2.4.

4.2.1 AP600 Core Makeup Tank

In the AP600, the CMTs are connected to the RCS, by normally open isolation valves on the cold leg balance line and normally closed isolation valves and check valves on the CMT discharge line. The CMT discharge valves open on a safety systems actuation (S) signal and remain open. The tanks are maintained at full-system pressure by the cold leg balance lines. During normal operation, the CMTs and the cold-leg balance lines are completely filled with water.

In addition to adding coolant and boron to the reactor systems, the CMTs have an additional safety function. Continued draining of the tank indicates an unrecoverable loss-of-coolant (LOCA). When approximately 33 percent of the tank liquid has drained, the CMT level sensing device activates the first stage of the automatic depressurization system (ADS), and the plant begins a controlled blowdown through the ADS valves into the in-containment refueling water storage tank (IRWST). The second- and third-stage ADS valves open based on timers that are started with the opening of ADS-1. If the CMTs continue to drain and the volume reaches 20 percent, then the fourth-stage ADS valves (located on the hot legs) open, providing a large vent path directly to containment to

4.0 PHENOMENOLOGICAL MODELING RESULTS

4.1 Introduction

The analysis results presented in Section 3.0 provide an in-depth understanding of each of the SPES-2 tests. The purpose of this section is to compare these results for several tests and to provide additional understanding of the passive safety system components unique to the AP600.

A test-to-test comparison for the SPES-2 tests is included in WCAP-14309, *SPES-2 Tests: Final Data Report.*[1] Additional comparisons are made that make use of insights into the tests, which were not available in the previous report. These include the following:

- Component mass inventory and overall system mass balance
- Component energy inventory and overall system energy balance
- Timing of events that occur in the course of each test as the AP600 safety systems respond

These topics are discussed in detail in this section.

Two components, the core makeup tank (CMT) and the passive residual heat removal (PRHR) system, are unique to the AP600 design. The phenomena observed in the tests for these components are discussed in detail in this section.

depressurize the RCS to containment pressure. As the RCS depressurizes by opening the ADS valves on the pressurizer and hot legs, the CMTs continue to add coolant to the RCS to maintain continued core cooling during the depressurization.

Each AP600 CMT is a [ ]^{a,b,c} tank, consisting of hemispherical heads and a cylindrical shell. The hemispherical heads are stainless-steel-clad carbon steel ([ ]^{a,b,c} stainless cladding) with a total thickness of [ ]^{a,b,c} The cylindrical portion of the tank is also stainless-steel clad and is a total of [ ]^{a,b,c} thick. The top of the tank is located 28 ft. above the RCS cold legs, providing a gravity head to drive the flow into the reactor vessel downcomer. The drain line is connected from the bottom of the CMT through an isolation valve and two check valves to the direct vessel injection line (DVI). The cold-leg balance line between the top of a cold-leg and the top of a CMT is an 8-in. schedule 160 pipe with an inside diameter of [ ]^{a,b,c} There is a normally open isolation valve near the top of the balance line.

There are two modes of operation for the CMTs: recirculation and draining. During the initial phase of a small-break LOCA, steam line break, or steam generator tube rupture event, the RCS inventory remains at or near its steady-state value. When an S signal occurs (typically low pressurizer pressure), the reactor coolant pumps trip, and the CMT isolation valves open. With the valves open, buoyancy-driven flow from the CMT to the reactor vessel and return flow from the cold leg to the top of the CMT is initiated, beginning the recirculation phase of operation for the CMTs. The colder, denser CMT water drives flow into the reactor vessel because of the density difference between the CMT water and that in the cold leg balance line. This flow will continue and steadily decrease as the colder CMT water is replaced by hotter water from the balance line, thereby decreasing the thermal driving head.

As the break continues to drain the RCS, the cold-leg balance line begins to void, the recirculation flow path is broken, and the CMT drains as the water volume is replaced by steam from the cold leg, beginning the draining mode of the CMT. The CMT injection flow rate is larger in this mode because of the greater density difference between the colder CMT water and the steam or two-phase mixture in the balance line.

For a small break, the CMT is in the recirculation mode for an extended period, and there is the potential for a large portion of the top of the CMT to be hot. This hot liquid layer will reduce the steam condensation when the CMT transitions into the draining mode. The hot liquid layer can also flash as the RCS depressurizes, causing mixing and reducing the effects of condensation in the CMT. These effects are discussed in Section 4.2-4.

For a larger break, the recirculation period is reduced because the cold-leg balance line will void sooner, breaking natural circulation. In these cases, the hot liquid layer in the CMT, and its associated effects may be less significant.

Separate effects tests of the core makeup tank were conducted to determine the operating characteristics of the CMT during simulated large and small break accidents. The analysis of these tests is summarized in WCAP-14215, *AP600 Core Makeup Tank Test Analysis Report.*[10]

4.2.2 SPES-2 Representation of the Core Makeup Tanks

As has been shown in WCAP-14073, *SPES-2 Facility Description,*[2] the CMTs in the SPES-2 facility are designed to maintain the AP600 elevation, with a [ ]^{a,b,c} volume scaling. Thus, the CMTs in SPES-2 are [ ]^{a,b,c} from top to bottom, with a total volume of [ ]^{a,b,c} The heat capacity scaling of the CMT walls has also been preserved, resulting in walls that are [ ]^{a,b,c} thick. To maintain these thin-walled tanks at high pressure, the CMTs are located within thick walled ([ ]^{a,b,c} thick) guard vessels which are unique to SPES-2. The heat transfer models which are used in this analysis (Section 2.2) account for the heat transfer from the CMT walls to the guard vessel walls, the heat capacity of the CMT and guard vessel walls, and the heat transfer from the uninsulated guard vessel to the environment.

4.2.3 CMT Performance for Selected Tests

As discussed previously, the behavior of the CMTs is dependent on the accident sequence which is simulated (that is, type of accident; small-break LOCA (SBLOCA), steam generator tube rupture (SGTR), or main steam line break (MSLB); break size; break location; and availability of nonsafety protection systems). Four tests are examined; the 2-in. cold-leg break (S00303), the 2-in. cold-leg break with nonsafety systems available (S00504), the double-ended guillotine DVI line break (S00706), and the steam generator tube rupture (S01110).

A discussion of the CMT performance is provided for each of these tests.

2-in. Cold Leg Break (S00303)

For the 2-in. cold leg break (S00303), the CMT isolation valves opened at [ ]^{a,b,c} initiating the recirculation mode for both CMTs. The liquid level in the CMTs is shown in Figure 4.2-1. The CMT in the break loop, CMT-B, transitioned into the draining mode at approximately [ ]^{a,b,c} while the CMT in the unbroken loop, CMT-A, transitioned into the draining mode at approximately [ ]^{a,b,c} Drainage was slowed by accumulator flow at approximately [ ]^{a,b,c}

The axial fluid temperature distributions for both CMTs at discrete points in time are shown in Figures 4.2-2 and 4.2-3. The inlet temperature is plotted at the top of the tank. Both CMTs show similar behavior as the heated liquid region grows at the top of the CMT during the recirculation phase. At this time, nearly [ ]^{a,b,c} of the CMT is heated as the tanks begin to drain. As the tanks drain, the walls at the top of the tank reach thermal equilibrium with the hot water, cooling the water layer. Thus, as the steam enters the CMT from the cold leg balance line, and little condensation occurs either at the CMT walls, or at the steam/water interface.

The fluid-to-wall axial temperature difference for both CMTs at discrete points in time are shown in Figures 4.2-4 and 4.2-5. These figures indicate that the temperature difference from the fluid to the walls is highest well below the water level when the hot water layer passes the colder wall as the tanks drain down. The slow rate of draining indicates that the walls are sufficiently heated by the hot liquid layer such that condensation of steam entering the top of the CMT is minimized.

Figures 4.2-6 and 4.2-7 show the fluid superheat (the difference between the fluid temperature and the saturation temperature) for both CMTs at discrete points in time. This value is plotted as a function of elevation relative to the steam/water interface (plus elevation is above interface). The superheating of the inlet pipe temperature relative to the CMT pressure is indicated at the top of the tank. At the start of the event, the fluid in the tanks is highly subcooled. During the recirculation phase, the fluid closest to the interface is heated to near the saturation temperature. Then, as the tanks drain, the steam temperatures in the top of the CMT are at the saturation temperature or slightly superheated, while the liquid temperatures range from saturation at the steam/water interface to highly subcooled at the bottom of the tank.

Late in the event, the steam temperatures exhibit superheating at the top of the tanks, then remain at or near the saturation temperature to a point approximately half-way down the tank wall. Below this point, the steam temperature becomes subcooled, indicating the presence of non-condensible gas in the CMTs. From Figure 4.2-6, the first evidence of subcooling of steam occurs at approximately [ ]^{a,b,c} for CMT-A. The introduction of non-condensible gas occurs immediately after the accumulators have emptied, and, as is shown in Figure 4.2-8, the cold leg balance line had previously drained sufficiently to allow a path for gas to enter the CMTs. Figure 4.2-8 also shows the start of CMT refill after the initiation of IRWST injection (>[ ]^{a,b,c}).

Two-in. Cold Leg Break with Nonsafety Systems Available (S00504)

For the 2-in. cold leg break with nonsafety systems available (S00504), the CMT isolation valves opened at [ ]^{a,b,c} initiating the recirculation mode for both CMTs. The liquid level in the CMTs is shown in Figure 4.2-9. The CMT in the break loop, CMT-B, transitioned into the draining mode at approximately [ ]^{a,b,c} The CMT in the unbroken loop, CMT-A, transitioned into the draining mode at approximately [ ]^{a,b,c}

The axial fluid temperature distribution for CMT-A at discrete points in time is shown in Figure 4.2-10 (Note: fluid thermocouples for CMT-B failed for S00504). CMT-A shows behavior similar to S00303 as the heated liquid region grows at the top of the CMT during the recirculation phase.

The tank drains more slowly than in test S00303 due to the added RCS inventory from the nonsafety systems and stops draining at approximately [ ]^{a,b,c} At this time, the fluid in the cold-leg balance line is cooled due to the effects of accumulator injection and the nonsafety systems, which results in a reduction in the thermal driving head. In addition, the nonsafety systems cause a reduction in the system pressure which decreases flow out of the break and ADS to a point where the cold legs refill. At this time, the cold leg balance lines refill and introduced liquid into the top of the CMTs.

This results in condensation of steam in the top of the CMTs and results in rapid refilling at the CMTs. Refill stops short of completely filling the tanks due to noncondensible gas occupying the top of the CMTs.

The fluid-wall axial temperature difference for CMT-A at discrete points in time is shown in Figures 4.2-11. Figure 4.2-12 shows the fluid superheat (the difference between the fluid temperature and the saturation temperature) for CMT-A.

The steam space temperatures remain saturated despite the introduction of fluid at a higher temperature, until about [ ]^{a,b,c} At that time subcooling indicates the introduction of non-condensibles which essentially fill the tank above the water level as the level rises. This implies condensation of most of the steam in this region despite the low fluid-wall temperature difference.

Double-Ended Guillotine DVI Line Break (S00706)

For the DEG DVI line break (S00706), the CMT isolation valve opened at [ ]^{a,b,c} for CMT-A, and [ ]^{a,b,c} for CMT-B, initiating the recirculation mode for both CMTs. The liquid level in the CMTs is shown in Figure 4.2-13. Since the CMT empties into the DVI line, the CMT in the break loop, CMT-B, drains through the break within [ ]^{a,b,c} The CMT in the unbroken loop, CMT-A, transitioned into the draining mode at approximately [ ]^{a,b,c} CMT-A drains at a constant rate until approximately [ ]^{a,b,c} when ADS-4 is activated. At this time, the level remains nearly constant for approximately [ ]^{a,b,c} then resumes draining. CMT-A is [ ]^{a,b,c} full at the end of the test.

The fluid temperatures in CMT-B quickly reach the system saturation temperature. The axial fluid temperature distribution for CMT-A at discrete points in time is shown in Figure 4.2-14. CMT-A behavior is similar to the results observed in S00303, except that the recirculation phase is much shorter due to the larger break. The heated liquid region grows at the top of the CMT during the recirculation phase [ ]^{a,b,c} At this time, only [ ]^{a,b,c} of the CMT is heated above the initial temperature as the tank begins to drain.

Since the tank drains quickly, the walls at the top of the tank do not reach thermal equilibrium with the hot water, and there is considerable condensation at the relatively cold walls. Thus, the fluid-wall temperature differences for CMT-A, shown in Figure 4.2-15, indicate higher heat transfer than observed in S00303. Condensation is even more apparent in the fluid-wall temperature differences for CMT-B, shown in Figure 4.2-16. Rapid draining of CMT-B exposes cold walls to incoming steam resulting in significant temperature differences.

Figures 4.2-17 and 4.2-18 show the fluid superheat (the difference between the fluid temperature and the saturation pressure) for both CMTs at discrete points in time. This value is calculated as a function of elevation relative to the steam/water interface. At the start of the event, the fluid in the tanks is highly subcooled. For CMT-A, during the short recirculation phase, the fluid at the top is replaced with water near the saturation temperature. As the tanks drain, the steam temperatures in the

top of the CMT are more significantly superheated than for S00303 due to the rapidly decaying system pressure. The hot water deposited at the top cools down as it moves down the cold tank. The liquid temperatures range from saturation at the steam/water interface to highly subcooled at the bottom of the tank.

Late in the event, the steam temperatures exhibit superheating at the top of both CMTs, then remain at or near the saturation temperature along most of the exposed length. The lack of non-condensible gas in this test can be attributed to the break being located in the DVI line, which causes the gas from one accumulator to be completely discharged to the environment. In addition, accumulator-A empties after Stage 4 ADS actuation, and it is likely that most of the gas injected into the intact DVI line will exit the system before passing into the CMTs.

Figure 4.2-19 shows that the CMTs do not refill during the test for this size break, as no increase in the cold leg balance line liquid levels are observed.

Steam Generator Tube Rupture (S01110)

For the steam generator tube rupture (S01110), the CMT isolation valves do not open until nearly [ ]^{a,b,c} The recirculation mode of operation prevails for this event as the CMTs do not drain. The discharge flow rate for both CMTs is shown in Figure 4.2-20. The flows decrease at a nearly constant rate as hot liquid replaces the cold liquid in the tanks. The rate drops at about [ ]^{a,b,c} and [ ]^{a,b,c} for CMT-A and -B respectively, as hot water enters the drain line and further reduces the buoyancy driving head.

The axial fluid temperature distributions for both CMTs at discrete points in time are shown in Figures 4.2-21 and 4.2-22. Both CMTs show similar behavior as the heated liquid region grows during the event. By the end of the event, the tanks reach a nearly steady state temperature distribution with an axial temperature gradient ranging from [ ]^{a,b,c} at the top of the tanks to [ ]^{a,b,c} at the bottom.

The fluid-wall axial temperature differences for both CMTs at discrete points in time are shown in Figures 4.2-23 and 4.2-24. As was observed in S00303, the heat transfer from the fluid to the walls is highest when the hot water layer passes the colder wall as the tanks drain down. At the end of the event, a nearly constant temperature difference of approximately [ ]^{a,b,c} is observed along the entire length of the CMTs. This indicates that the heat loss to the surrounding is nearly constant along the length of the tanks.

Since the CMTs never drain for this event, the effects of non-condensible gas and CMT refill are not observed.

4.2.4 Flashing, Swell, and Steam-Water Mixing

Summary

Flashing of core makeup tank (CMT) liquid into steam during decompression could effect water level indications and flow of fluid in the balance line. In the scaling logic for the CMT test,[11] this phenomenon was rated as being of high importance to study for small-break loss-of-coolant (SBLOCA) events. This section reviews two possible indicators of the extent of flashing and swell (that is, the raising of the actual water level or mixture level above the inferred collapsed water due to the presence of steam below the mixture level). Although flashing occurred in several tests, significant level swell occurred in both CMTs only for tests S00401 and S01613.

The phenomenon of direct or contact condensation was also rated of high importance for large and SBLOCAs. There was no evidence of rapid contact condensation as observed in the rapid draindown CMT tests.

Flashing and Swell

Level swell was calculated as the difference between the calculated mixture level and the calculated collapsed mixture level. As explained in Section 2.1.1, the collapsed liquid level was calculated based on the sum of pressure drops within four [ ]^{a,b,c} pressure difference (dP) measurement spans in a CMT. Mixture level was calculated within each of the individual spans. Thus, when steam exists within a span below the actual mixture level, the inferred mixture level in the next higher span will be higher than the calculated collapsed level. Furthermore, within the span containing the mixture level, the vapor fraction is assumed to be at least as high as the vapor fraction in the span below it. On this basis, the calculated mixture level was raised above what would be inferred assuming pure liquid below the mixture level within this span (Section 2.1.1).

A mixture level was calculated in each dP span. Typically, the mixture level will be within three spans, at or near the upper or lower poind of the span; that is, they were full of liquid or had none; and the actual mixture existed within one span. The actual mixture level was within the highest span location having a collapsed liquid level above 1 percent from the bottom of the span.

With this method, significant swell was detected if subsurface steam existed within the mixture in more than one of the four dP spans. Significant swell indicated that there was steam below the pressure drop measurement span that contained the liquid surface. (Up to one or two inches of swell showed up in obviously subcooled condition. This was attributed to measurement and calculational errors). The actual swell was expected to be a fairly smooth continuous function of time; due to the measurement limitations, the calculated swell tended to drop to zero when the mixture level dropped below the bottom of each dP span, and it remained there until a void is calculated in the second span below that. Mixture level swell cannot be calculated by this method when the mixture level is in the bottom dP span.

Figures 4.2-25 through 4.2-34 are plots of mixture level swell vs. time as the solid line with the scale on the left side. Also shown are plots of the calculated mixture level for each pressure difference range, using the right-hand scale. These indicate the level transient and help to gage the possible effect of level proximity to the range bound on the swell mixture level calculation.

In tests S00401 and S01613 (1-inch cold-leg breaks; Figures 4.2-28 and 4.2-29), there was evidence of significant swell, starting at the time of the opening of ADS-2 ([ ]^{a,b,c} respectively). The same plots, showing only the flashing time periods, are shown in Figures 4.2-35 and 4.2-36, respectively. Swell of the mixture is expected to occur when there has been a large balance line flow into the CMT to heat the liquid, when pressure decrease was greater; and when the pressure decrease occurred at low pressure, which caused greater steam volume per unit of pressure decrease. Figures 4.2-37 through 4.2-39 show CMT-A pressure transients and integrated mass inlet flow for all tests reviewed in groups of similar tests. The test number for each curve is shown in the legend. From surveying these plots, one would expect mixture level swell in CMT-A to occur for the 1-inch cold-leg break.

In test S00706, a double-ended break of the direct vessel injection (DVI) line, (Figure 4.2-31 there appears to be significant mixture level swell in CMT-B, as it rapidly blows down to the atmosphere through the DVI line. This time period is shown in more detail in Figure 4.2-40. In this test, in CMT-B, there was an apparent bias of up to [ ]^{a,b,c} in the measured fluid temperatures for the first [ ]^{a,b,c} which covers the period of the indicated swell. This caused an underestimate of both the collapsed level and the mixture level. For S08706, apparently, there were problems with the fluid thermocouples in CMT-B, postulating a multiplier of [ ]^{a,b,c} (Figure 4.2-40) on the thermocouples and recalculating removes of all but three or four inches of calculated mixture level swell during this time period. Since the pressure was essentially constant at this time, it can be concluded that there was no clear indication of mixture level swell for test S00706.

Figure 4.2-32 for test S01007, a 2-inch break in the CMT-B balance line, shows very noisy calculated levels in CMT-A when the level is around [ ]^{a,b,c} and in CMT-B before draining starts. Closer inspection shows a very noisy signal on the bottom dP tap on both CMTs and on the top dP cell on CMT-B during this period. This results in short-duration spikes in the calculated swell. Because the duration of these spikes is so short compared to the swell evidenced in other tests, we conclude that there is no clear indication of the existence of significant swell for this test.

The indication of measurable level swell in a few tests can be compared with the indications of saturated regions below the mixture level, discussed in Section 4.2.3. Those figures imply that flashing occurred during decompression in more cases than those in which mixture level swell was observed. This is expected, since slow decompression of saturated liquid, and decompression at high pressure, results in the formation of steam within the liquid at a volume rate, which is small enough that individual bubbles can escape to the surface without a measurable volume being present.

Direct Contact Steam Condensation

In the CMT separate effects test,[11] rapid contact condensation of steam was observed when steam was introduced into the CMT before the initially cold CMT liquid had been heated. During this period, a low CMT drain flow was observed, because of the lower pressure at the top of the CMT, which was limited because most of the CMT elevation head was consumed in the flow losses in the steam line and steam distributor. The steam/water mixing continued until the top region of the CMT liquid nas been heated to near saturation by the steam, after which the direct condensation stopped. At that time the CMT drain rate increased, with most of the elevation head being consumed in flow losses in the drain line. In CMT tests in which the introduction of steam was preceded by recirculation of hot liquid, no rapid condensation occurred. A fairly high drain flow rate was observed during liquid circulation, and when steam was introduced the drain flow increased.

In all of the SPES-2 tests reviewed, the steam flow into the CMT was preceded by hot liquid flow. Thus, significant direct condensation was not expected.

On indicator of significant direct condensation would be a drop in discharge (CMT injection) rate when the flow balance line flow into the CMT changes from liquid to steam. This would be followed by a sharp increase when the direct condensation ended. In most cases, we see a recirculation discharge rate of about [ ]^{a,b,c}, followed by increase to a higher rate when steam starts to enter and emptying of the CMT starts. In only one test, S00504, a 2-inch cold-leg break, and only a CMT-A, does a pronounced drop in discharge flow rate appear before the switch to the drain mode. In this case, the flow drops from [ ]^{a,b,c} between [ ]^{a,b,c}, then rises sharply starting at about [ ]^{a,b,c} to [ ]^{a,b,c}, eventually hitting a maximum of [ ]^{a,b,c} at [ ]^{a,b,c} Various parameters are shown for this period in Figure 4.2-41. Examination of the fluid temperature traces for this time in Figure 4.2-42 show no sharp rise in temperatures near the CMT top, which would be expected in the case of vigorous contact condensation. We interpret the balance line dP signal as indicating that the balance line was filled with liquid until about [ ]^{a,b,c}, and that voiding initiated more rapid discharge flow, accompanied by more rapid liquid flow in, until [ ]^{a,b,c} when CMT drain started and discharge flow increased further. The drop in flow from [ ]^{a,b,c} is attributed to a shift in coolant system pressure drops between the DVI line and the cold-leg B1, coincident with the draining of the vertical cold-leg B sections below the steam generator.

A second indicator of rapid direct condensation would be the sudden appearance of a region of uniform fluid temperature at the top of the CMT just prior to the start of draindown. A review of the superheat curves shows no such event.

The conclusion is that there is no period of rapid condensation due to mixing of the incoming steam with CMT liquid. This is consistent with the expectation that such phenomena would not exist for cases when steam injection is preceded by significant liquid circulation.

The figures listed are proprietary and, therefore,
are not available in the Class 3 version of this report.

These figures are available in the Class 2 version of this report.

4.3 Passive Residual Heat Removal Heat Exchanger

As discussed in Section 2.2, the passive residual heat removal (PRHR) is designed to remove core decay heat in the event that the active safety systems are not available. The heat exchanger (HX) consists of a series of tubes in the in-containment refueling water storage tank (IWRST), which are connected to the hot leg (inlet) and pump suction (outlet). The tubes enter the tank a few feet below the surface and exit the tank near the bottom. At normal operating conditions, the PRHR is isolated from the primary system. In the event of an accident, the isolation valves are opened and natural circulation flow is established, driven by the density difference between the hot fluid entering the PRHR and the cold fluid exiting the PRHR. Heat is transferred from the tubes to the IRWST water by either subcooled boiling or free convection.

This section will determine the heat transfer characteristics of the SPES-2 representation of the PRHR/IRWST. Three methods of quantifying the heat transfer were identified:

1. Heat loss by the primary (tube-side) fluid between the PRHR inlet and outlet

2. Heat transfer from the outside of the PRHR HX tubes to the IRWST water

3. Increase in the internal energy of the IRWST water

Ideally, the energy transfer calculated by each of these methods should yield the same results.

4.3.1 Primary-Side Heat Balance

The primary-side heat balance is defined as

$$Q_{cal} = \dot{m} \, (h_{in} - h_{out}) \tag{4.3-1}$$

where:

Q_{cal} = heat loss from the primary fluid between the PRHR inlet and outlet
$\dot{m}$ = mass flow rate as determined by the flow meter in the PRHR outlet
h_{in} = fluid-specific enthalpy in the PRHR inlet
h_{out} = fluid-specific enthalpy in the PRHR outlet

For all cases, the PRHR outlet flow will be single-phase liquid. However, the PRHR inlet flow could be either a single-phase liquid or a two-phase liquid (steam/water mixture). To determine the inlet enthalpy, the quality of the inlet flow must be determined. To do this, the SPES-2 tests used an inverted U-tube with two differential pressure cells in series. As discussed in Section 2.2, the differential pressure cell readings were used to approximate the average void fraction of the inlet flow. Then, a homogeneous flow model was used to calculate the quality from the void fraction, and this quality was used to determine the inlet enthalpy.

Applying the ΔP reading to determine the void fraction eliminates the friction drops resulting in a calculated static void fraction based on the elevation pressure. The flowing void is assumed to be the same as the predicted static void fraction from the ΔP cells. This is a fair assumption, since the flow oscillates at the PRHR inlet, the alternating vapor and liquid plugs or mixture are forced into the PRHR, and the results are time averaged. The oscillatory flow also assumes a slip of unity; this is a reasonable assumption, since low-and high-quality fluid will be pushed, by the steam, into the PRHR tube. With these assumptions, a time-averaged inlet quality and enthalpy can be calculated for the PRHR.

For test S00303, the inlet void fraction and quality are shown in Figure 4.3-1. This figure shows that a two-phase mixture was observed at the PRHR inlet during much of the test. The resulting primary fluid heat loss is shown in Figure 4.3-2, and the integrated heat loss is shown in Figure 4.3-3. Figure 4.3-2 also shows the timing for ADS actuation and accumulator injection. For this test, the heat loss increased to a maximum of [ ]^{a,b,c}, which remained relatively constant until [ ]^{a,b,c} into the test. This corresponded to the time of accumulator injection, after ADS actuation, which reduced primary system temperature and thereafter the buoyancy head for PRHR flow, and introduced nitrogen into the primary system at the end of the accumulator injection (approximately [ ]^{a,b,c}). These factors caused a rapid reduction in the PRHR flow rate, and heat loss decreased to less than [ ]^{a,b,c}. After [ ]^{a,b,c}, ADS-4 actuated, and the heat loss in the PRHR dropped further. The PRHR was no longer a factor in removing the decay heat beyond this point to the end of the test.

4.3.2 Energy Transfer from the Tubes to the IRWST

In SPES-2, the PRHR tube walls are instrumented to determine the relative fraction of energy transfer that occurs in the three sections of tube:

1. **PRHR inlet** - [ ]^{a,b,c} of horizontal tube near the top of the IRWST. High-temperature fluid enters this section from the hot leg and cools rapidly. The combination of high tube wall temperatures and the locally low saturation temperature of the IRWST water can result in subcooled boiling and high heat flux.

2. **PRHR vertical section** - [ ]^{a,b,c} of vertical tube extending from the elevation of the PRHR inlet to the PRHR outlet. At the top of the vertical section, the fluid inside the tubes may still be hot enough to result in subcooled boiling off the outer tube wall. However, the local saturation temperature increases as the hydrostatic pressure increases with increasing depth. Thus, the lower section of the tubes experience free convection heat transfer with the IRWST water, resulting in much lower heat fluxes.

3. **PRHR outlet** - [ ]^{a,b,c} of horizontal tube near the bottom of the IRWST. At this point, the fluid temperature inside the tube is very low, and the local saturation temperature in the IRWST is at a maximum. Heat transfer from the tube walls to the IRWST is due to free

convection. The combination of the small surface area in this section, and low heat flux limits the contribution to the overall heat transfer.

The total heat transfer from the external PRHR tube wall to the IRWST is summed for the three sections and is given by the following equation:

$$Q_{tube} = \Sigma h_i A_i (T_w - T_\infty) \quad (4.3\text{-}2)$$

where:

h_i = heat transfer coefficient (either subcooled boiling or free convection) for each section
A_i = surface area of the tube for each section
T_w = tube wall temperature
T_∞ = bulk fluid temperature

Temperature measurements were made at the midpoint of the three sections. The local wall temperatures were interpolated between these three measurements. Thus, the local temperature can be estimated for the inlet tube wall between midpoint and the corner with confidence. However, the highest heat fluxes occurred at the point where the PRHR inlet tube first entered the IRWST, and no wall temperature measurements were available at this location. It was assumed that the inlet wall temperature must be higher than the midpoint temperature by some ΔT_{inlet}. Several values of ΔT_{inlet} were tested, and one was chosen to fit the overall heat transfer rate calculated for the primary side. This value was found to be

$$\Delta T_{inlet} = [\quad]^{a,b,c}$$

This value was used to analyze all ten tests and, in most cases, resulted in excellent agreement with both the PRHR primary-side heat transfer calculation and the IRWST internal energy calculation.

Figure 4.3-4 shows the breakdown in the heat transfer between the PRHR inlet, PRHR vertical, and PRHR outlet sections. During peak operation, the inlet horizontal section is responsible for [ ]^{a,b,c} or nearly [ ]^{a,b,c} of the total heat transfer, the vertical section is responsible for [ ]^{a,b,c} and the heat transfer in the outlet section is essentially negligible. After ADS actuation, the heat transfer on the outside of the PRHR tubes at the inlet transition from subcooled boiling to free convection, and the heat transfer from this section falls to [ ]^{a,b,c} which is [ ]^{a,b,c} of the total heat transfer. The vertical section heat transfer during this period is [ ]^{a,b,c} (or [ ]^{a,b,c} of the total), and the outlet section heat transfer is less than [ ]^{a,b,c} This heat transfer breakdown is specific for LOCA tests when PRHR inlet fluid void fraction is high (two-phase fluid) and condensation occurs mainly in the horizontal inlet tube. For SGTR tests S01309 and S01110 [ ]^{a,b,c} when PRHR inlet fluid void fraction was low (single-phase fluid), the heat transfer occurred throughout the horizontal and vertical tube surfaces. However, because the vertical tube surface was greater, the most heat was transferred through the vertical tube surface. Figures 4.3-11 and 4.3-12 show that the model used for heat transfer through the PRHR external wall calculation better matches the two-phase fluid in the PRHR inlet.

4.3.3 Increase in the IRWST Internal Energy

The water temperature in the IRWST was measured at five locations from the top to the bottom of the tank. By associating a volume with each of these measurements, a total fluid internal energy was calculated for each time step. The difference between this value and the internal energy of the tank at the start of the test is an excellent measure of the heat transfer from the PRHR to the IRWST. The ADS does not interact with the IRWST in SPES-2 such that all energy addition is due to the PRHR.

The thermocouples used to evaluate the tank temperature are located near the PRHR tubes. Thus, the measured temperature was somewhat higher than the actual tank temperature at a given elevation. To account for this difference, the measured temperature are adjusted by 2.5°F during the time when the PRHR is operating. The calculation was useful for comparison to the other heat transfer calculations up to the point of IRWST draindown. No evaporative heat loss from the IRWST was considered.

The difference between the initial internal energy and the internal energy at any point in time is shown in Figure 4.3-5 for the S00303 test. Also shown is the integrated PRHR primary-side heat transfer (Equation 4.3-1) and the integrated total heat transfer from the outside of the PRHR tubes. These results indicate that assumptions that were made to perform these calculations give good agreement with the change in the IRWST internal energy, which is the most accurate measure of the PRHR/IRWST heat transfer.

4.3.4 Calculation of the PRHR/IRWST Heat Transfer for Other Tests

Comparisons of the three methods of calculating the PRHR/IRWST heat transfer are shown for the other nine tests in Figures 4.3-6 to 4.3-14. There is good agreement for most of the tests, with some notable exceptions. Tests S00605 (Figure 4.3-8) and S00706 (Figure 4.3-9) show a large deficit for the primary PRHR heat transfer calculation. The primary-side heat transfer calculation was not performed for these tests. This was due to a malfunction in the differential pressure cells used to determine the inlet void fraction.

Test S01703 (Figure 4.3-14) is a repeat of test S00303. Analysis of the test shows that the integrated heat transfer calculated from the PRHR external tube wall was much higher than the other two methods. This was due to a [ ]^{a,b,c} increase in the tube wall temperature for this test as compared to S00303, which effectively doubled the temperature difference between the tube wall and the bulk fluid. The subcooled boiling heat transfer coefficient was proportional to this temperature difference raised to the power of 2.5. Thus, a doubling of the temperature difference corresponds to a six-fold increase in the heat transfer coefficient. It is likely that the wall temperature for this test, the last in the sequence, is inaccurate.

The other SBLOCA tests show the same behavior as S00303; the heat transfer was constant until the accumulators emptied and then decreased. The smaller breaks (that is, test S00401; Figure 4.3-6) showed approximately the same heat transfer rate ([ ]^{a,b,c}) as the larger breaks. However, the heat transfer continued at a nearly constant level for a much longer period of time. The PRHR

flow rate decreased slowly after the CMT draindown started (approximately [ ]^{a,b,c} for S00401), slowly decreasing heat transfer. After ADS-1 was actuated and accumulator high injection started reducing the primary system temperature and as a consequence the PRHR flow rate, the PRHR/IRWST heat transfer rate decreased similarly to the S00303. Conversely, for the larger break (that is, test S00706, Figure 4.4-9), the period of maximum PRHR/IRWST heat transfer was much shorter due to the rapid decrease in pressure, and subsequent early ADS actuation accumulator discharge.

The SGTR tests show similar behavior, with two important differences:

1. The heat transfer rate remained constant over the entire test because of slow primary system pressure and temperature decay.

2. The heat transfer rate was somewhat lower than the LOCA cases ([ ]^{a,b,c}) due to the lower PRHR inlet void fraction. The overall integrated heat transfer was much higher for the SGTR cases, since the PRHR kept flowing throughout the test.

The time during the LOCA transient when the PRHR is effective is determined by the interaction of the PRHR and the other safety systems. Figure 4.3-15 shows the energy which is added to the primary system by the heated rods, and the energy removed from the primary system by the break, ADS, steam generators, and the PRHR. In this simplified analysis, the change in the energy of the primary system fluid and the component metal mass is neglected.

At the start of the test (0 to [ ]^{a,b,c} seconds),

1. The rod power is quickly reduced to decay heat levels (including the heat loss compensation).

2. The pumps are tripped, an the steam generator heat transfer drops to zero.

3. Energy is lost out the break at a rate which decreases slowly due to the falling system pressure.

When the steam generator heat transfer drops off (approximately [ ]^{a,b,c} seconds),

1. The core begins to produce steam.

2. The PRHR removes heat from the primary system.

When the ADS is actuated (approximately [ ]^{a,b,c} seconds),

1. The break flow and associated energy is sharply reduced.

2. The PRHR heat transfer is reduced.

3. The ADS energy removal increases to make up for the break and the PRHR, and to match the core decay heat level.

When ADS-4 is actuated (approximately [ ]^{a,b,c} seconds),

1. The break and ADS1-1, ADS-2, and ADS-3 energy renewal rate is essentially zero.

2. The ADS-4 energy removal matches the core decay heat level.

Thus, the PRHR is effective for removing energy from the time when the steam generator heat transfer ceases, until the time of ADS actuation. After this time, the core decay heat is removed by the ADS-1, ADS-2, and ADS-3 until ADS-4 is actuated.

4.3.5 Effect of Multiple PRHR Tubes on PRHR Performance

The purpose of test S01613 is to determine the effect of multiple PRHR tubes on the PRHR performance. The test is the same as S00401, the one-inch cold leg break without non-safety systems, except that three PRHR tubes are used, as opposed to one for S00401. The PRHR/IRWST heat transfer for the two tests is shown in Figure 4.3-16, and the PRHR flow rate is shown in Figure 4.3-17.

Several comparisons can be made between the tests to evaluate the increased PRHR capacity.

1. Tripling the heat transfer area of the PRHR tubes results in a [ ]^{a,b,c} percent increase in the heat transfer rate.

2. The increase in the heat transfer is due in part to the increased flow through the PRHR tubes for the multiple tube case. Figure 4.3-17 shows an increase in the PRHR flow of [ ]^{a,b,c} percent for test S01613 over S00401. The remainder of the increase is due to the lower outlet enthalpy resulting from the increased heat transfer area.

3. The [ ]^{a,b,c} percent increase in PRHR performance results in a faster pressure decay rate which hastens the actuation of the accumulator injection (see Table 4.5-2). In addition, the increased heat removal delays the onset of ADS by about [ ]^{a,b,c} seconds, and results in a higher minimum two-phase level and liquid mass in the core compared to the single tube case (see Table 4.6-12).

The results of these tests indicate that the PRHR heat rejection is close to optimum for the single tube case, and increasing the number of tubes does not significantly increase performance.

The figures listed are proprietary and, therefore,
are not available in the Class 3 version of this report.

These figures are available in the Class 2 version of this report.

4.4 Accumulator Air Injection and Migration in SPES-2

Each of the two accumulators in SPES-2 were precharged with approximately [ ]^{a,b,c} of air at a pressure of [ ]^{a,b,c} When the primary system pressure decreased below the accumulator gas pressure, the gas volume expanded and injected the water stored in the accumulator into the primary system. When the water was totally ejected, the air gas volume continued to expand, injecting most of the air (approximately [ ]^{a,b,c} from each accumulator) into the primary system. For the reference loss-of-coolant accident (LOCA) event S00303, the air injection into the power channel annular downcomer started at approximately [ ]^{a,b,c} into the event and continued for nearly [ ]^{a,b,c} (Figure 3.2-27).

The initial distribution of air in the system was assessed based on the flow paths available during the initial injection. During the initial injection for test S00303, some air left the system via the cold-leg break and ADS-1, ADS-2, and ADS-3, while the rest was distributed in the system. The effect of the processes in the system (specifically the steam flow and condensation) by the distribution of the air in the system was assessed. The air will be transported by steam flow to the locations where steam condensation takes place such as the core makeup tanks (CMTs) and the passive residual heat removal heat exchanger (PRHR HX), and the partial pressure of air will build up in these locations. The higher partial pressure of air reduce the partial pressure of the steam in these locations and, therefore, could affect the saturation temperature.

During the initial air injection for S00303, which started at [ ]^{a,b,c} the levels in the annular downcomer and the hot leg decreased momentarily. Since the downcomer still had water, no air could enter the core from the cold-leg side. The air propagated through the system by flowing from the annular downcomer through the cold legs, the steam generator U-tubes, and into the hot legs. The air swept residual water into the steam generator U-tubes, this water flashed and caused a momentary pressure increase in the system. The hot legs drained momentarily at [ ]^{a,b,c} thereby opening a path for air to enter the upper plenum via the hot legs (Figure 4.4-1). The upper-plenum level at this time was above the hot-leg nozzle (Figure 4.4-2). The air entered the upper plenum and collected in the top of the upper plenum above the free-water surface. During this process, which took place from [ ]^{a,b,c} the level in the upper plenum decreased approximately [ ]^{a,b,c} corresponding to a partial air pressure of [ ]^{a,b,c} in the upper plenum (Figure 4.4-2). Some air may have reached the upper head via the annular downcomer/upper-head bypass line. However, due to the small capacity of this line and the pressure decay in the system causing a general flow of superheated steam out of the upper head, only a small amount of air is likely to have reached the upper head via this path.

The level in hot leg-A dropped to or below the elevation of the surge line nozzle (corresponding to approximately [ ]^{a,b,c}) and stayed at this elevation until ADS-4 actuation (Figure 4.4-1). This opened a direct flow path for air from the annular downcomer into the pressurizer. Air entering the pressurizer was ejected via ADS-1, ADS-2, and ADS-3, leaving the system.

When the air injection from the accumulators started, the flow through the CMT balance lines (A and B) consisted of steam since the cold legs had already drained (Figure 3.2-11). Steam was flowing from the cold leg through the balance lines into the CMTs and condensing on the coldest metal surfaces above the water level in the vessels and on the water surface. This steam flow also swept air from the cold leg into the CMTs, resulting in a significant amount of air in the CMTs. The temperatures above the water surface in the CMTs dropped below TSAT based on the CMT pressure due to a high partial pressure of air (Figure 4.4-3).

For the time during a LOCA event when there was two-phase flow in the upper plenum and the hot leg-A, two-phase flow with much higher void fraction occurred in the PRHR. In the PRHR HX, the upper horizontal tube and the upper part of the vertical tube, contained a steam volume and acted as a condenser for the steam/water mixture coming from the hot leg.

During the accumulator water injection period ([ ]^{a,b,c}) the PRHR supply line and the HX gradually became water-solid. During the initial air injection, a short period of flow reversal occurred (at [ ]^{a,b,c}), filling the inverted U-tube in the inlet line with subcooled water from the heat exchanger. When hot leg-A drained, the lower part of the PRHR supply line drained and filled with air. When forward flow was re-established, a steam/air volume established in the top part of the heat exchanger (Figure 4.4-1). This occurred during a time when the core and the upper plenum were still subcooled. Flow through the PRHR started increasing (Figure 4.4-4) when the core again discharged two-phase flow starting between [ ]^{a,b,c}

From approximately [ ]^{a,b,c} until [ ]^{a,b,c} the level in the upper plenum stayed at the hot-leg elevation. Air stored in the upper-plenum steam bubble gradually was transported to the PRHR HX by the steam in the two-phase fluid. The decreasing level in the HX from [ ]^{a,b,c} (Figure 4.4-1) was probably a result of an increasing buildup of air in the top of HX. There was a small but noticeable affect on the measured heat transfer between [ ]^{a,b,c}, which was probably caused by the increasing amount of air in the HX. Figure 4.4-5 shows that the temperature at the PRHR HX inlet corresponds to TSAT based on the pressure at this location, indicating that there was no significant affect of the partial pressure of air at this location. The affect of air on the saturation temperature would be expected where the condensation process takes place near the free water surface inside the HX. At [ ]^{a,b,c} the steam bubble in the upper plenum started to collapse caused by the IRWST flow subcooling the upper plenum (Figure 4.4-2). The water from the IRWST injection was insufficient to supply the upper plenum at the rate of steam bubble collapse, and water was being pulled from the rest of the primary system. The level dropped in the PRHR HX and inlet line (Figure 4.4-1), and the pressure in the ADS-4 header dropped below atmospheric, and air was pulled into the PRHR inlet line through ADS-4. This ended natural circulation for the PRHR loop, the flow stopped, and the PRHR heat transfer ended. The first significant injection of air into the PRHR for S00303 occurred after ADS-4, and was a result of backflow of air through ADS-4 and not the flow of air around the system following the end of accumulator injection caused by the collapse of the steam bubble in the upper plenum.

During the initial air injection, most of the air was leaving the system via ADS-1, ADS-2, and ADS-3. The residual air was stored in the CMTs, the cold legs, the steam generator U-tubes, the hot leg, the

pressurizer, and the upper plenum. There was a noticeable affect of air on the temperature distribution in the CMTs (Figure 4.4-3).

Only a small amount of air from the initial injection from the accumulators ended directly in the PRHR HX. Air injected into the upper head was transported to the PRHR HX by the two-phase flow going to the PRHR; however, the amount was insufficient to affect the saturation temperature at the PRHR HX inlet. Air was clearly present in the PRHR HX after the collapse of the steam bubble in the upper plenum, which pulled sufficient air into the PRHR inlet line to break the recirculation in the PRHR loop.

The effects of the air injection from the accumulators are not consistent from event to event. The consequences of the air injection appear to be dependent on several factors, the most important factors being the water inventory in the system at the time of the injection, and the location and size of the break.

The differences in system response S00303 is compared with S00401, which was a 1-inch cold-leg break (smaller than S00303), and S00706, which was a double-ended guillotine break (much larger than S00303).

The 1-inch cold-leg break (S00401) showed indications of a large amount of air in the PRHR, sufficient to end the natural circulation immediately after the air injected from the accumulators (at [ ]^{a,b,c}), and the PRHR heat transfer stopped. This was different from S00303, which showed indication of a small amount of air reaching the PRHR heat exchanger having little effect on the PRHR flow. The difference between the S00401 and S00303 may be related to the water inventory and the break size, since significantly more air was lost through the break for S00303 than for S00401. With more air left in the system for S00401, combined with the lower water inventory in the system when the air injection occurred, PRHR natural circulation was broken for S00401 while this did not occur for S00303.

For the double-ended guillotine break of the direct vessel injection (DVI) line, S00706, PRHR natural circulation stopped when the injection of air from accumulator-A occurred (approximately [ ]^{a,b,c}), and the PRHR flow and heat transfer stopped. This was primarily due to the low water inventory in the system at this time. However, ADS-4 occurring at [ ]^{a,b,c} when the system pressure was still high, appears to have ejected a large amount of the air which halted flow in the PRHR. As the IRWST injection raised the water level in the primary system to the hot-leg elevation, the PRHR partially refilled and the flow restarted.

The air injection from the accumulators affected primarily the performance of the PRHR although the air was noticed in the CMTs. For many of the events performed in SPES-2 the PRHR heat transfer ended when the accumulator air stopped natural circulation in the PRHR. Unfortunately, the system response for each event was sufficiently different to make generalization difficult. It is clear, however, that one must assume loss of PRHR heat transfer at the end of the accumulator injection, although for some events PRHR heat transfer continued after the injection.

The figures listed are proprietary and, therefore,
are not available in the Class 3 version of this report.

These figures are available in the Class 2 version of this report.

4.5 Behavior of Other Components

Several interesting observations were made during the course of testing. The behavior of the components unique to AP600—the core make up tanks and the passive residual heat removal system—are discussed in Sections 4.2 and 4.3. In addition, characteristic primary system flow oscillation was observed for the loss-of-coolant accident (LOCA) tests. These oscillations, along with the primary system behavior up to the loss of natural circulation, are discussed in this section.

Also included in this section is a summary of events that occur during the test. These events included the actuation of safety systems, such as reactor trip, pump trip, steam generator isolation, core makeup tank (CMT) draining, accumulator discharge, automatic depressurization system (ADS) initiation, and in-containment refueling water storage tank (IRWST) draining. Included are the timing of the events relative to the initiation of the test and the system pressure at this time.

4.5.1 Core Behavior - Oscillations After Reactor Coolant Pump Trip

Oscillations in the primary system flow, temperature, and pressure occurred for LOCA events when the reactor coolant pumps (RCPs) were shut down, and two-phase fluid conditions existed in the primary system.

When the RCPs were stopped, the power-to-flow (P/F) ratio for the heated rod bundle increased. As a result of the loss of system pressure down to the saturation pressure for hot-leg temperature, boiling in the heated rod bundle and flashing in the upper plenum occurred and produced sufficient steam to control the system pressure, and both temperature and pressure increased. This increased the void fraction in the power channel and, consequently, reduced the density of the two-phase liquid being fed into the hot legs.

The two-phase mixture in the steam generators left the steam generators as saturated water. Some of the steam was being condensed in the U-tubes (the primary-side pressure was higher than the secondary-side pressure at this time, allowing some heat to be transferred to the secondary-side fluid), while the rest of the steam was separated from the two-phase mixture in the high point of the U-tubes. Since the driving head for the natural circulation flow was determined by the density difference between the single-phase fluid in the cold side of the primary system and the two-phase mixture in the hot side of the primary system, the flow through the heated rod bundle increased, reducing boiling intensity, primary system pressure and temperature, void fraction, and as a consequence, the driving head for flow through the power channel. When flow through the heated rod bundle subsequently decreased, the boiling intensity again increased, increasing the driving head for flow in the primary system. The cycle was repeated and the flow through the power channel started to oscillate, resulting in oscillations in the heated rod bundle and upper-plenum void fraction, upper-plenum temperature, and system pressure.

Since a part of steam was separated from the two-phase mixture in the high point of the U-tubes, it eventually broke the flow path through the U-tubes when the free surface had fallen too low to be

overcome by the buoyancy head. The oscillations were sustained as long as there was flow through the steam generators. When the steam generator U-tubes started to drain, these oscillations stopped. For steam generator-B, the flow stopped earlier than the flow for steam generator-A due to the higher void fraction in the fluid from hot leg-B.

These oscillations were observed in all tests where boiling occurred in the power channel after RCPs are shut off until the flow path through the steam generator U-tubes was broken. In steam generator tube rupture (SGTR) test S01110, oscillations in the primary system started at about 3000 seconds when CMTs and passive residual heat removal (PRHR) natural circulation flows decreased and were not sufficient to subcool the power channel.

Primary system pressure (upper-head pressure and hot-leg pressure) and the upper-plenum temperature, and the void fraction in the heated rod bundle oscillated in phase (see Figures 4.5-1 and 4.5-2). The amplitudes of these oscillations was about [ ]^{a,b,c} respectively. The fluid void fraction in the steam generator U-tubes oscillated approximately in opposite phase with the primary system pressure. When the void fraction in the heated rod bundle and the saturation temperature for primary system pressure (see Figure 4.5-3) decreased, they reached minima at about [ ]^{a,b,c} after the tubular downcomer (TDC) flow rate had reached a maximum at [ ]^{a,b,c} and started to decrease. The fluid void fraction in the upper part of the hot legs and the steam generator U-tubes increased in this period because of flashing, caused by the lower saturation temperature (system pressure). The fluid void fraction in the steam generator U-tubes reached maxima at about [ ]^{a,b,c}. At the same time [ ]^{a,b,c} the TDC flow rate dropped, and due to the low flow rate, the core void fraction started to increase due to boiling. As the saturation temperature increased (the system pressure increased) the void fraction in the steam generator U-tubes hot-side decreased. The calculated steam generator U-tube cold-side void fraction stayed higher, compared to the hot-side void fraction, because of lower fluid level on the cold side due to the lower temperature. In this time period, condensation occurred predominantly on the cold side of the steam generator U-tubes. At about [ ]^{a,b,c} the PRHR heat exchanger (HX) return flow rate (oscillating) started to increase, thereby reducing liquid temperature in cold leg-A.

At about [ ]^{a,b,c} when the void fraction in the heated rod bundle approached its maximum and the hot-leg void fraction increased (Figure 4.5-5), the driving head for flow in the primary system increased increasing the TDC flow rate (Figure 4.5-3). The fluid void fraction in the steam generator U-tubes decreased with the increasing saturation temperature for system pressure, the void fraction in the heated rod bundle peaked at about [ ]^{a,b,c} and then decreased while the TDC flow rate increased, reaching the maximum at about [ ]^{a,b,c} The high flow through the power channel reduced boiling in the power channel. The void fraction in the heated rod bundle as well as the hot leg void fraction decreased reducing the driving head for primary system flow (flow rate decreased), and the cycle was completed.

The TDC flow rate lags primary system pressure (core void fraction) by about 1/4 of the oscillation period.

The minimum fluid void fraction in the steam generator U-tubes gradually increased (Figure 4.5-6) indicating that a part of steam was separated in the high point of the U-tubes where temperature (metal) was the highest and steam was superheated.

The fluid void fraction in the hot leg-B is higher than in the hot leg-A and more steam is separated in the high point of the steam generator-B U-tubes. This resulted in a break of the flow path through the steam generator-B earlier (at [ ]^{a,b,c}) than in the steam generator-A. After break of the flow path in the steam generator-B flow through it was stopped, the TDC flow reduced to about one half, and oscillation period increased from about [ ]^{a,b,c} (Figure 4.5-7). The oscillations in the primary system continued until [ ]^{a,b,c} when flow stopped through the steam generator-A U-tubes. The liquid level in the U-tubes gradually decreased thereby draining the steam generators. The TDC flow rate decreased to about the total PRHR HX and the CMTs natural recirculation flow rate at about [ ]^{a,b,c}

The fluid void fraction in the top of the PRHR HX inlet line (Figure 4.5-8) changed due to the oscillation of the saturation temperature for system pressure (intensity of flashing oscillates in the inlet line or even condensation occurred in the inlet line) as well as separation of steam at the top of the hot leg into the PRHR HX inlet line. The fluid maximum void fraction in the top of the PRHR inlet line was significantly higher than in the heated rod bundle ([ ]^{a,b,c} percent in the rod bundle versus [ ]^{a,b,c} percent in the PRHR HX inlet line). The increasing system pressure (increasing saturation temperature) stopped flashing in the inlet line and condensation occurred in it (Figure 4.5-9); that produced vacuum in the inlet line and caused the low void fraction fluid from the hot leg to fill the the top of the inlet line (Figure 4.5-8), which was followed by the higher void fraction fluid; the fluid void fraction in the top of the inlet line dropped, then increased due to high void fraction fluid entering from the hot leg, and at that time the PRHR HX return flow peaked (Figure 4.5-8). Then decreasing system pressure again caused flashing in the inlet line resulting in the high fluid void fraction in the top of the PRHR HX inlet line and the next cycle started.

4.5.2 Timing of Events During Accident Sequences

Tables 4.5-1 to 4.5-2 list the timing of the major events during the ten SPES-2 tests being analyzed, referenced to a time zero, which corresponds to the time of the initiating event. Table 4.5-1 presents data for the 2-inch LOCA tests. Table 4.5-2 covers the 1-inch and double-ended guillotine breaks. Table 4.5-3 covers the steam generator tube ruptures. For each event, the time it occurs and the associated system pressure (that is, the top of pressurizer pressure) is presented. Some of these results are discussed further in the following text. Timings for the CMTs are discussed in Section 4.2; and timings for the PRHR are discussed in Section 4.3.

Reactor Trip (R) Signals and Related Events

All of the LOCA events were conservatively tripped on a low-pressure signal when the pressurizer pressure reached [ ]^{a,b,c} (that is, the power was reduced to simulate control rod entry into the core and transition to decay heat levels). For the 1-inch break, this occurred at around [

[ ]^{a,b,c} For the 2-inch breaks, the trip signal was issued between [ ]^{a,b,c} with the cold-leg breaks being the earliest and the direct vessel injection (DVI) line break being the latest. The very rapid depressurization experienced in the double-ended guillotine break of the DVI line (S00706) leads to a trip signal in [ ]^{a,b,c} In all cases, the main steam isolation signal was detected two to three seconds after the reactor trip (R) signal was issued.

For the steam generator tube rupture tests, the reactor trip was initiated on low pressurizer level. For test S01110, signals were issued at [ ]^{a,b,c} when the level decreased to [ ]^{a,b,c} for test S01309, the signal was issued at [ ]^{a,b,c} when the pressurizer level was [ ]^{a,b,c} (WCAP-14309, *Final Data Report*).[1] The main steam isolation signal was detected [ ]^{a,b,c} later.

Safety Systems Actuation (S) Signals and Related Events

In the LOCA simulations, the safety systems actuation (S) signal was issued when the pressurizer pressure reached [ ]^{a,b,c} For the 1-inch breaks, this was about [ ]^{a,b,c} after the trip signal; for the 2-inch breaks, the delay was about [ ]^{a,b,c} In the case of the double-ended guillotine break, the delay was only three seconds. Following the S signal, main feedwater isolation, PRHR actuation, and CMT injection signals occurred approximately [ ]^{a,b,c} later. Reactor coolant pumps (RCP) trips were detected within [ ]^{a,b,c} of the signal, which is consistent with the [ ]^{a,b,c} design delay.

For the steam generator tube ruptures, the S signal occurred at the same time as the reactor trip. Main feedwater isolation, PRHR actuation, and CMT injection were detected [ ]^{a,b,c} after the signal. RCP trips were again detected within [ ]^{a,b,c} of the signal.

Accumulator Injection

The start times for accumulator injections are listed in Tables 4.5-1 to 4.5-3 together with the system pressure at the time of actuation. The start time and the time at which all the water has been ejected are listed in Table 4.5-4.

In general, for the LOCA events, accumulator injection began when the system pressure reached approximately 700 psi. The only exceptions to this appeared to be accumulator-B in tests S00706 and S00401. The former was a result of the initiating event, which was a break of the associated DVI line, and this water injection was collected in the CMT-side break catch tank. The latter is an artifact of the way in which the accumulator injection was detected. That is, for three consecutive time steps, the measured accumulator flow must exceed [ ]^{a,b,c} In this test (as discussed further below), there was a period of sporadic outflow that made the initial injection difficult to detect by this method. In reality, a small level of outflow will have occurred from around [ ]^{a,b,c} onward.

The rate of initial accumulator injection depends on whether the ADS phase has been initiated. This is illustrated in Figures 4.5-10 to 4.5-12. For the double-ended direct vessel injection (DVI) line break, ADS-1 actuation occurred [ ]^{a,b,c} before accumulator injection started, and ADS-2 began eight

seconds later. There was, therefore, a very rapid initial rate of water discharge. At the other extreme, for the 1-inch cold-leg breaks, ADS actuation was [ ]^{a,b,c} after the start of the accumulator injection. Until the ADS stage began, the accumulator discharge was very sporadic; however, once the rate of system depressurization increased, so did the accumulator discharge. For the 2-inch cold-leg to CMT balance line and cold-leg breaks, there were shorter delays ([ ]^{a,b,c}) between accumulator injection starting and ADS actuation, so the sporadic outflow phase was much shorter. For the 2-inch DVI line break, accumulator injection and ADS-1 actuation were almost coincidental. It is interesting to note that in test S00504, the effect of the nonsafety systems was to delay the onset of rapid accumulator injection by approximately [ ]^{a,b,c} relative to the equivalent tests without these systems. Figures 4.5-10 to 4.5-12 show that the actuation of ADS-2 and ADS-3 leads to further increases in the rate of accumulator discharge.

Comparing Tables 4.5-1, 4.5-2, and 4.5-3 shows that the accumulators take between [ ]^{a,b,c} to empty from the time of ADS-1 actuation, for all but S00706, which is very rapid and takes [ ]^{a,b,c} to discharge. The discharge time for the 1-inch breaks was slightly less than in the 2-inch breaks because there had been a significant loss of water during the prolonged sporadic outflow phase. Averaged over the time for the accumulators to empty, in all tests the air expansion is near isothermal. However, during the initial discharge there is a reduction in air temperature which is followed by a reheat as the walls supply energy to the air.

Figures 4.5-10 to 4.5-12 show that, following the emptying of the accumulators, the rapid outflow continued as the discharge lines emptied. Following the fall in discharge flow, there was another burst of lower flow. This is likely to be a result of the passage of the air discharged from the accumulators. The consequences of this air discharge is discussed further in Section 4.4-1. In all tests with ADS-4 actuation, except S00706, there was a further small pulse at the time ADS-4 began.

In the two steam generator tube rupture tests, CMT draindown did not occur and ADS was not activated. However, in test S01309, the primary system depressurized enough for sporadic accumulator outflow to occur during the last [ ]^{a,b,c} of the transient (Figure 3.10-24).

ADS Actuation

ADS actuation occurred when CMT level decreased to the actuation points. These are as follows:

ADS-1	CMT level of [	]^{a,b,c}
ADS-2	CMT level of [	]^{a,b,c}
ADS-3	CMT level of [	]^{a,b,c}
ADS-4	CMT level of [	]^{a,b,c}

For the steam generator tube ruptures, these conditions were never met and ADS actuation did not occur. For the LOCA events, there was a spread of initiating times–depending on the rate of CMT emptying. The higher the system pressure at the time of the actuation, the greater the effect of the ADS. The system pressures pertinent to the time of ADS actuation are listed in Tables 4.5-1 and 4.5-2.

For the SGTRs, the loss of water from the primary system was not enough to lead to CMT draindown, and thus, ADS actuation did not occur. For all the LOCA events, except S00504, all four stages of ADS were activated. In test S00504, the water injected from the nonsafety systems—chemical volume and control system (CVCS) and normal residual heat removal (NRHR)—prevented the complete draindown of the CMTs and, hence, ADS-4 actuation. The nonsafety system injection also delayed the onset of ADS-1, ADS-2, and ADS-3 actuation by [ ]^{a,b,c} relative to the equivalent tests without these systems (S00303 and S01703). The lower the elevation of the break, the more rapid the draindown of the CMTs, and ADS-1 actuation occurred approximately [ ]^{a,b,c} earlier in the 2-inch DVI line break relative to the 2-inch cold leg break, which was an additional [ ]^{a,b,c} earlier than in the 2-inch cold-leg to CMT balance line break. Halving the size of the cold-leg break delays the onset of ADS actuation by nearly [ ]^{a,b,c}

IRWST Injection

Gravity fed water injection from the IRWST began when the primary system had depressurized to near atmospheric conditions (that is, in the region of [ ]^{a,b,c} in these tests). The time of initiation was, therefore, dependent on both the severity of the initial depressurization and the effectiveness of the ADS phase. For the steam generator tube ruptures, there was no ADS actuation, the primary system did not fully depressurize, and therefore, there was no IRWST injection. For all the LOCA events, except S00504, IRWST injection was achieved. In test S00706 (the double-ended guillotine break of the DVI line), the IRWST line on the unbroken side began to feed water [ ]^{a,b,c} after ADS-1 actuation. For the one-and two-inch breaks, ADS depressurization led to IRWST injection, approximately [ ]^{a,b,c} after ADS-1 actuation. In test S00504, ADS-4 actuation was not achieved and the system pressure remained above that at which IRWST injection can begin.

TABLE 4.5-1
EVENT TIMINGS AND SYSTEM PRESSURES FOR 2-INCH LOCAs

Event	Test Number				
	S00303 2-in. CL (sec/psi)	S01703 2-in. CL (sec/psi)	S00504 2-in. CL (w/NS Systems) (sec/psia)	S00605 2-in. DVI (sec/psia)	S01007 2-in. CL/CMT BL (sec/psia)
Reactor trip signal (R)					
Main steam line isolation (A/B)					
Safety systems actuation signal (S)					
Main feedwater isolation (A/B)					
CMT injection (A/B)					
PRHR supply actuation					
RCP trip (A/B)					
Accumulator injection (A/B)					
ADS-1					
ADS-2					
ADS-3					
ADS-4 (A/B)					
IRWST injection (A/B)					

a,b,c

TABLE 4.5-2
EVENT TIMINGS AND SYSTEM PRESSURES FOR 1-INCH AND DEG LOCAs

Event	Test Number			
	[			a,b,c]
Reactor trip (R) signal				
Main steam line isolation (A/B)				
Safety systems actuation (S) signal				
Main feedwater isolation (A/B)				
CMT injection (A/B)				
PRHR supply actuation				
RCP trip (A/B)				
Accumulator injection (A/B)				
ADS-1				
ADS-2				
ADS-3				
ADS-4 (A/B)				
IRWST injection (A/B)				

TABLE 4.5-3
EVENT TIMINGS AND SYSTEM PRESSURES FOR SGTRs

Event	Test Number		a,b,c
Reactor trip low pressurizer level signal (R)			
Main steam line isolation (A/B)			
Safety systems actuation (S) Signal			
Main feedwater isolation (A/B)			
CMT injection (A/B)			
PRHR supply actuation			
RCP tip (A/B)			
Accumulator injection (A/B)			
ADS-1			
ADS-2			
ADS-3			
ADS-4 (A/B)			
IRWST injection (A/B)			

TABLE 4.5-4
ACCUMULATOR INJECTION START AND END TIMINGS COEFFICIENT

Test	Accumulator	Injection Start Time (sec.)	Accumulator Empty Time (sec.)
S00401 1-in. CL LOCA	A	[ ] a,b,c	
	B		
S01613 1-in. CL LOCA	A		
	B		
S00303 2-in. CL LOCA	A		
	B		
S01703 2-in. CL LOCA	A		
	B		
S00504 2-in. CL LOCA with nonsafety systems	A		
	B		
S00605 2-in. DVI LOCA	A		
	B		
S01007 2-in. CL-CMT Balance line LOCA	A		
	B		
S00706 DEG DVI LOCA	A		
	B		
S01110 1 tube SGTR	A		
	B		
S01309 1 tube SGTR	A		
	B	[ ]	

The figures listed are proprietary and, therefore,
are not available in the Class 3 version of this report.

These figures are available in the Class 2 version of this report.

4.6 Overall Mass Balance

The total system mass inventory, at each point in each transient, is shown in Figures 4.6-1 to 4.6-10 with the initial value. These figures represent the total water inventory in the SPES-2 facility that is included in the mass model. Certain piping lengths have not been included in the model because of their small volume and the lack of suitable differential pressure measurements in many cases. The amount of mass neglected by omitting these piping lengths was estimated based on temperature and pressure measurements for time 0 in test S00303. This missing mass is listed in Table 4.6-1 along with the volume of the components (data from WCAP-14073, *SPES-2 Facility Description*).[2]

The majority of this additional mass will appear within the total measured system inventory when the relevant safety system is utilized, although the precise amount included at any time depends on what systems have been used and how much water mass remains within the pipes. Figures 4.6-1 to 4.6-10 show that, in most tests, there was an apparent gain in total system water that is consistent with a total additional water mass of up to [ ]^{a,b,c} lbm. The following tests are not bounded by this missing mass figure:

- **Test S00504**

  In this test, the final system mass inventory was approximately [ ]^{a,b,c} lbm higher than the initial value. This is a test in which the nonsafety systems—chemical volume control system (CVCS) and normal residual heat removal (NRHR)—were used and these injected nearly [ ]^{a,b,c} lbm of water during the test. In this test, the in-containment refueling water storage tank (IRWST) injection did not occur and there was a considerable level of water in the core makeup tank (CMT) to cold-leg balance line (CLBL) at the end of the test, so not all the neglected mass will be included in the system inventory.

- **Test S01110**

  This is a steam generator tube rupture (SGTR) in which the end inventory was approximately [ ]^{a,b,c} lbm less than at the start. The mass of water transferred from the primary to secondary side of the system was not included in the mass balance, since this focused on the primary system components. The amount of mass transferred was small, amounting to a total of [ ]^{a,b,c} lbm. In this test, the CMTs did not enter the draindown phase and accumulator injection and IRWST injection did not occur. The majority of the additional mass (listed in Table 4.6-1), therefore, did not enter the system being modeled.

- **Test S01309**

  This is the other steam generator tube rupture; however, in this case, there was the additional complication that the CVCS also injected water throughout the test and the ADS-4 catch tank was used to collect water from the power-operated relief valve (PORV) cycled by the operator. There is, therefore, a loss from and injection to the modeled system that is not included in the

initial mass balance that is shown by the mass increase shown in Figure 4.6-9. The total transfer from the primary to the secondary side is [ ]^{a,b,c} lbm. The total mass of water injected from the CVCS is [ ]^{a,b,c} lbm and the total collected in the ADS-4 catch tank was [ ]^{a,b,c} lbm. Due to problems with CVCS flow measurements, a constant flow of [ ]^{a,b,c} lbm/sec was assumed for the entire transient. This led to an overestimate of 100 lbm. inserted mass relative to WCAP-14309, *Final Data Report.*[1]

4.6.1 Component Masses: A Test-by-Test Comparison

Tables 4.6-2 through 4.6-12 provide test-by-test component mass comparisons for both loss-of-coolant accident (LOCA) and non-LOCA tests (where appropriate) at the following times in the transient:

- Start of transient
- End of initial blowdown phase
- Start of first CMT draindown
- Automatic depressurization system (ADS-1) actuation
- Point at which first accumulator empties
- ADS-4 initiation
- Start of IRWST injection start
- End of transient

The following observations can be made:

- At the initiation of the transient, all tests have essentially the same mass inventory distribution.

- At the end of the initial blowdown phase, the mass inventory in the power channel is unchanged in the 1-in. LOCA and SGTR events. In the 2-in. LOCA events, the core and upper plenum have lost mass. As expected, the double-ended guillotine break of the direct vessel injection (DVI) line shows the most severe power channel and heated rod bundle water loss during this phase of the transient.

- By the time the first CMT goes into draindown mode, cold leg-B is essentially empty in all the LOCA tests. Due to the more prolonged system draindown, the power channel mass inventory is now lower in the 1-in. LOCA events than the 2-in. events.

- At ADS-1 initiation, the power channel mass inventories lie between [ ]^{a,b,c} and [ ]^{a,b,c} lbm in all LOCA tests except those involving DVI line breaks and the mass distribution between the heated rod bundle, downcomers and upper plenum is similar. The DVI line breaks show more severe reductions in inventory up to this point in the transient. The 2-in. break of the DVI line has a lower power channel inventory at this point than is the case for the double-ended break; however, this is only a temporary situation.

- Accumulator injection refills the power channel in all the LOCA tests, except the DVI breaks, where not all the initial accumulator inventory reaches the core. In the case of the 2-in. DVI line break, there is a partial refilling of the power channel by the time the first accumulator empties; but in the case of the double-ended break, the power channel inventory has further reduced to this point.

- Following the emptying of the accumulators, all tests show a further reduction in power channel and rod bundle water inventory until the IRWST injection starts. In all the LOCA events, the minimum power channel inventory is just before IRWST injection takes effect. As noted below, this is not necessarily the time of minimum water inventory. In the case of the double-ended guillotine break of the DVI line (S00706), the end of the accumulator injection is later than ADS-4 actuation. Thus, the apparent increase in inventories between these two events actually represents a continuing temporal reduction.

- By the end of the transients, the power channel is water-solid up to the hot-leg elevation in all LOCA tests, except the double-ended break of the DVI line in which heated rod bundle voidage still persists.

Table 4.6-13 shows the minimum power channel (that is, span of DP-000P) inventory and the time at which it occurs.

One-in. LOCA Events: The minimum power channel inventory arises just before IRWST injection takes effect. The minimum inventory is [ ]^{a,b,c} lower in the test with only one passive residual heat removal (PRHR) heat exchanger (HX) tube (S00401). The minimum inventory in that test is about [ ]^{a,b,c} higher than that achieved in the 2-in LOCA events.

Two-in. LOCA Events: The minimum power channel inventory is about [ ]^{a,b,c} lbm, and it occurs [ ]^{a,b,c} seconds into the transient during the core oscillation phase.

Double-Ended Guillotine Break of DVI Line: A minimum power channel inventory of only [ ]^{a,b,c} lbm occurs [ ]^{a,b,c} seconds into the transient, during the accumulator injection.

SGTRs: With the nonsafety systems operating (S01309), the minimum power channel inventory occurs during the initial blowdown; in test S01110 the minimum occurs during the flashing in the heated rod bundle, which occurred from [ ]^{a,b,c} seconds to the end of the transient. For this period, the core inventory oscillates between around [ ]^{a,b,c} lbm.

In all the tests undertaken on the SPES-2 facility, there is no evidence for uncovery of the heated rod bundle. The maximum clad temperature shown in Figures 3.x-62 (x = 2,3....11) clearly shows that there is no dramatic clad temperature increase. This demonstrates that the rod bundle always remain sufficiently wet to maintain adequate cooling.

TABLE 4.6-1 MASS OMITTED FROM THE MASS BALANCE MODEL				
Component	**Volume ($ft.^3$)**		**Initial Mass (lbm)**	
CMT-A injection line	[	]	[	]a,b,c
CMT-B injection line	[	]	[	]
CMT to cold-leg balance line	[	]	[	]
PRHR supply line	[	]	[	]
PRHR return line	[	]	[	]
IRWST to DVI-A injection line	[	]	[	]
IRWST to DVI-B injection line	[	]	[	]
Accumulator-B injection line	[	]	[	]
Direct vessel injection line A	[	]	[	]
Direct vessel injection line B	[	]	[	]
Total	[	]	[	]

The total missing mass represents less than 1 percent of the initial inventory.

TABLE 4.6-2
COMPONENT MASS COMPARISON AT START OF TRANSIENT IN LOCA TESTS

	S00401 1-in CL	S01613 1-in CL	S00303 2-in CL	S01703 2-in CL	S00504 2-in CL+NS	S00605 2-in DVI	S01007 2-in BL	S00706 DEG of DVI
Event time								
Power channel (PC)								
PC: heated rod bundle								
PC: downcomers								
PC: upper plenum								
Hot leg-A								
Hot leg-B								
Cold leg-A								
Cold leg-B								
SG primary-A								
SG primary-B								
Pressurizer + SL								
CMT-A								
CMT-B								
Accumulator-A								
Accumulator-B								
IRWST								

a,b,c

TABLE 4.6-3
COMPONENT MASS COMPARISON AT START OF TRANSIENT IN NON-LOCA TESTS

	S01110 1 SGTR	S01309 1 SGTR+NS
Event time	[	] a,b,c
Power channel (PC)		
PC: heated rod bundle		
PC: downcomers		
PC: upper plenum		
Hot leg-A		
Hot leg-B		
Cold leg-A		
Cold leg-B		
SG primary-A		
SG primary-B		
Pressurizer + SL		
CMT-A		
CMT-B		
Accumulator-A		
Accumulator-B		
IRWST	]	]

TABLE 4.6-4
COMPONENT MASS COMPARISON AT END OF BLOWDOWN IN LOCA TESTS

	S00401 1-in CL	S01613 1-in CL	S00303 2-in CL	S01703 2-in CL	S00504 2-in CL+NS	S00605 2-in DVI	S01007 2-in BL	S00706 DEG of DVI
Event time	[							] a,b,c
Power channel (PC)								
PC: heated rod bundle								
PC: downcomers								
PC: upper plenum								
Hot leg-A								
Hot leg-B								
Cold leg-A								
Cold leg-B								
SG primary-A								
SG primary-B								
Pressurizer + SL								
CMT-A								
CMT-B								
Accumulator-A								
Accumulator-B								
IRWST	[							]

TABLE 4.6-5
COMPONENT MASS COMPARISON AT END OF BLOWDOWN IN NON-LOCA TESTS

	S01110 1 SGTR	S01309 1 SGTR+NS
Event time	[	] a,b,c
Power channel (PC)		
PC: heated rod bundle		
PC: downcomers		
PC: upper plenum		
Hot leg-A		
Hot leg-B		
Cold leg-A		
Cold leg-B		
SG primary-A		
SG primary-B		
Pressurizer + SL		
CMT-A		
CMT-B		
Accumulator-A		
Accumulator-B		
IRWST	[	]

TABLE 4.6-6
COMPONENT MASS COMPARISON AT START OF CMT DRAINDOWN IN LOCA TESTS

	S00401 1-in CL	S01613 1-in CL	S00303 2-in CI	S01703 2-in CL	S00504 2-in CL+NS	S00605 2-in DVI	S01007 2-in BL	S00706 DEG of DVI
Event time	[							] a,b,c
Power channel (PC)								
PC: heated rod bundle								
PC: downcomers								
PC: upper plenum								
Hot leg-A								
Hot leg-B								
Cold leg-A								
Cold leg-B								
SG primary-A								
SG primary-B								
Pressurizer + SL								
CMT-A								
CMT-B								
Accumulator-A								
Accumulator-B								
IRWST	[							]

TABLE 4.6-7
COMPONENT MASS COMPARISON AT TIME OF ADS-1 INITIATION IN LOCA TESTS

	S00401 1-in CL	S01613 1-in CL	S00303 2-in CL	S01703 2-in CL	S00504 2-in CL+NS	S00605 2-in DVI	S01007 2-in BL	S00706 DEG of DVI
Event time	[							] a,b,c
Power channel (PC)								
PC: heated rod bundle								
PC: downcomers								
PC: upper plenum								
Hot leg-A								
Hot leg-B								
Cold leg-A								
Cold leg-B								
SG primary-A								
SG primary-B								
Pressurizer + SL								
CMT-A								
CMT-B								
Accumulator-A								
Accumulator-B								
IRWST	[							]

TABLE 4.6-8
COMPONENT MASS COMPARISON AT TIME FIRST ACCUMULATOR EMPTIES IN LOCA TESTS

	S00401 1-in CL	S01613 1-in CL	S00303 2-in CL	S01703 2-in CL	S00504 2-in CL+NS	S00605 2-in DVI	S01007 2-in BL	S00706 DEG of DVI
Event time	[							] a,b,c
Power channel (PC)								
PC: heated rod bundle								
PC: downcomers								
PC: upper plenum								
Hot leg-A								
Hot leg-B								
Cold leg-A								
Cold leg-B								
SG primary-A								
SG primary-B								
Pressurizer + SL								
CMT-A								
CMT-B								
Accumulator-A								
Accumulator-B								
IRWST	[							]

TABLE 4.6-9
COMPONENT MASS COMPARISON AT TIME ADS-4 INITIATION IN LOCA TESTS

	S00401 1-in CL	S01613 1-in CL	S00303 2-in CL	S01703 2-in CL	S00504 2-in CL+NS	S00605 2-in DVI	S01007 2-in BL	S00706 DEG of DVI
Event time	[							] a,b,c
Power channel (PC)								
PC: heated rod bundle								
PC: downcomers								
PC: upper plenum								
Hot leg-A								
Hot leg-B								
Cold leg-A								
Cold leg-B								
SG primary-A								
SG primary-B								
Pressurizer + SL								
CMT-A								
CMT-B								
Accumulator-A								
Accumulator-B								
IRWST	[							]

TABLE 4.6-10
COMPONENT MASS COMPARISON AT START OF IRWST INJECTION IN LOCA TESTS

	S00401 1-in CL	S01613 1-in CL	S00303 2-in CL	S01703 2-in CL	S00504 2-in CL+NS	S00605 2-in DVI	S01007 2-in BL	S00706 DEG of DVI
Event time								
Power channel (PC)								
PC: heated rod bundle								
PC: downcomers								
PC: upper plenum								
Hot leg-A								
Hot leg-B								
Cold leg-A								
Cold leg-B								
SG primary-A								
SG primary-B								
Pressurizer + SL								
CMT-A								
CMT-B								
Accumulator-A								
Accumulator-B								
IRWST								

a,b,c

TABLE 4.6-11
COMPONENT MASS COMPARISON AT END OF TRANSIENT IN LOCA TESTS

	S00401 1-in CL	S01613 1-in CL	S00303 2-in CL	S01703 2-in CL	S00504 2-in CL+NS	S00605 2-in DVI	S01007 2-in BL	S00706 DEG of DVI
Event time	[							] a,b,c
Power channel (PC)								
PC: heated rod bundle								
PC: downcomers								
PC: upper plenum								
Hot leg-A								
Hot leg-B								
Cold leg-A								
Cold leg-B								
SG primary-A								
SG primary-B								
Pressurizer + SL								
CMT-A								
CMT-B								
Accumulator-A								
Accumulator-B								
IRWST	[							]

TABLE 4.6-12
COMPONENT MASS COMPARISON AT END OF TRANSIENT IN NON-LOCA TESTS

	S01110 1 SGTR	S01309 1 SGTR+NS
Event time	[	] a,b,c
Power channel (PC)		
PC: heated rod bundle		
PC: downcomers		
PC: upper plenum		
Hot leg-A		
Hot leg-B		
Cold leg-A		
Cold leg-B		
SG primary-A		
SG primary-B		
Pressurizer + SL		
CMT-A		
CMT-B		
Accumulator-A		
Accumulator-B		
IRWST	[	]

TABLE 4.6-13
MINIMUM HEATED ROD BUNDLE MASS INVENTORIES

Test	Test Description	Minimum Heated Rod Bundle Mass (lbm)	Percent of Initial Heated Rod Bundle Mass	Time (sec.)
S00401	1-in. cold-leg LOCA	[		] a,b,c
S01613	1-in. cold-leg LOCA			
S00303	2-in. cold-leg LOCA			
S01703	2-in. cold-leg LOCA			
S00504	2-in. cold-leg LOCA + nonsafety system			
S00605	2-in. DVI LOCA			
S01007	2-in. cold-leg to CMT balance line LOCA			
S00706	Double-ended DVI break			
S01110	1 tube SGTR			
S01309	1 tube SGTR + nonsafety systems	]		]

The figures listed are proprietary and, therefore,
are not available in the Class 3 version of this report.

These figures are available in the Class 2 version of this report.

4.7 Overall Energy Balance

As discussed in Section 2.9, the error in the total system energy inventory was determined by considering the SPES-2 facility (primary system, core makeup tanks [CMTs], accumulators, and in-containment refueling water storage tank [IRWST]) as a control volume. The energy balance on this control volume is defined as

$$U_{error} = U_{rods} - U_{fl\text{-}out} - U_{surr} - U_{sg} + \Delta U_{fluid} + \Delta U_{metal} + U_{NS} \qquad (4.7\text{-}1)$$

where:

U_{error} = error in the overall energy balance
U_{rods} = integrated power in the heated rods
$U_{fl\text{-}out}$ = energy of the fluid leaving the control volume
U_{surr} = integrated heat loss to the surroundings
U_{sg} = integrated heat transfer in the steam generators
ΔU_{fluid} = change in the energy of the fluid in the control volume
ΔU_{metal} = change in the energy of the metal in the control volume
U_{NS} = energy of the fluid entering the control volume through nonsafety systems—chemical and volume control system (CVCS) and normal residual heat removal (NRHR)—when operating

As discussed previously, several assumptions are necessary to calculate the components of the energy balance. These include the following:

1. Determination of the enthalpy of the fluid leaving the break is made by assuming saturated liquid at all times during the tests.

   This assumption is expected to be reasonably valid, since the break is at the bottom of the pipe for break sequences located on predominantly water solid piping (that is, cold-leg breaks) and for smaller breaks that exhibit slower depressurization to preclude flashing in the break location.

2. Determination of the enthalpy of the fluid leaving ADS-1, ADS-2, and ADS-3 is made assuming saturated vapor when the calculated void fraction in the top of the pressurizer is greater than 0.9 and assuming saturated liquid when the calculated void fraction is less than 0.9.

   This assumption is used as a switch between fluid and steam discharge through the automatic depressurization system (ADS). It is expected to be a good approximation for most times during the test.

3. Determination of the enthalpy of the fluid leaving ADS-4 is made assuming saturated liquid at the hot-leg temperatures.

   This assumption is expected to be valid for most tests, since the ADS-4 is actuated when the system pressure is low. Thus, approximating the ADS-4 flow as saturated liquid, even when two-phase, is a good approximation due to the large density difference at lower pressures, such that the majority of the mass flow is liquid.

4. Determination of the energy transfer in the steam generators is made assuming a constant overall heat transfer coefficient until the pumps are tripped. At this time the overall heat transfer drop dramatically due to the lower flow through the tubes.

   This assumption results in a constant level of energy transfer from the primary side to the secondary side until the pumps trip. After this time, the heat transfer drops to a very small value. This result is the same for all tests. For the loss-of-coolant accident (LOCA) tests, the energy transfer is set to zero when the primary system pressure is less than the secondary-side pressure. This assumption results in a small negative energy error before the pumps are tripped, as more energy transfer is predicted than actually occurs. After the pumps are tripped, the model accurately predicts the energy transfer.

5. The total fluid energy at the start of the test neglects approximately 100 lbm of fluid due to several small diameter piping runs not being included.

   Section 4.6 showed that just over 100 lbm of liquid is initially omitted from the mass inventory from various piping runs including the CMT discharge lines, CMT to cold-leg balance lines, passive residual heat removal (PRHR) tubing and lines, direct vessel injection (DVI) lines, and accumulator injection lines. This results in an amount of energy which is equal to the neglected mass times the saturated liquid enthalpy at operating conditions. This results in approximately [50,000 Btu][abc] of energy that is not accounted for by the energy balance and is included in the overall error when these pipes are discharged into the primary system.

6. The energy content of the metal in a given component is calculated from the average fluid temperature for that component.

   The effects of this assumption is to force the thick metal components to thermally react as quickly as the fluid temperature. In reality, there is a time lag associated with the metal temperature change. Typically, the error in the overall energy balance increases when the primary system temperature is being reduced rapidly, and it decreases when the primary system temperature reaches equilibrium and the actual metal temperatures catch up.

7. Uncertainties associated with measurements.

   The errors in the data from uncertainties in the instrumentation are accumulated over the test. They affect the overall heat balance and are included in the overall mass and energy error.

The energy balance error is shown for each test in Figures 4.7-1 to 4.7-10.

4.7.1 Loss-of-Coolant Accident (LOCA) Tests

The energy balance error curves show similar behavior from test to test. From the initiation of the test until the primary system pumps shut down, the error was slightly negative. This indicates that the energy transfer at the steam generators was slightly overpredicted. The rapid increase in the error, which occurred shortly after the initiation of the event, was caused by the lack of thermal lag in the metal energy calculation. The error peaked and was reduced as the actual metal temperature approached that of the primary system. The resulting accumulated energy at the end of the test resulted from the missing fluid mass in the piping (about 50,000 Btu), the accumulated uncertainties in the measurements, and the accumulated error associated with the assumptions of the break and ADS discharge enthalpy. The error was larger for the larger breaks (test S0706, Double-Ended Guillotine (DEG) DVI Line Break, Figure 4.8-5). This indicates that the break flow is single-phase saturated liquid, was less valid for the larger breaks where the steeper pressure gradients may result in flashing.

4.7.2 Steam Generator Tube Rupture (SGTR) Tests

The energy balance error curves for the two SGTR tests (Figures 4.7-8 and 4.7-9) show the same slightly negative behavior during the first 500 seconds due to the approximations in the steam generator heat transfer calculation. However, unlike the LOCA tests, no large peak associated with the metal time lag was observed for these tests. This is due to the slow cool-down rate of the primary system associated with these tests. At the end of the test, the accumulated error was similar to that observed in the LOCA tests and resulted from the neglected fluid mass in the piping (about 50,000 Btu) and the accumulated uncertainties in the measurements.

For test S01309, the ADS-4 catch tank was used to measure mass from the affected steam generator power-operated relief valve (PORV) which was cycled by the operation. This mass includes both the break flow associated with the tube ruptures (140 lbm) and the feedwater flow to the steam generator (260 lbm), and it is reflected in the energy balance error in Figure 4.7-9.

Overall, with the exception of test S0706, the error associated with the energy balance was generally within 10 percent of the total energy out the ADS and/or breaks. This is considered to be an acceptable result, given the approximate nature of the assumptions used to generate the energy balance.

The figures listed are proprietary and, therefore,
are not available in the Class 3 version of this report.

These figures are available in the Class 2 version of this report.

5.0 CONCLUSIONS

The data from the SPES-2 integral systems experiments have been analyzed. These experiments used a scaled test facility to investigate the performance of the AP600 passive safety systems. It was observed that, in all experiments, the heater rod bundle remained in a coolable state and no temperature excursions were observed. The passive safety systems provided ample injection flow to the heater rod bundle over the full transient. It was also observed that the intrusion and operation of the nonsafety injections systems did not degrade the overall safety performance of the passive systems. The tests with the active systems were able to terminate with the heater rod bundle in a coolable state with the bundle covered with a two-phase mixture. The observed performance of the test facility with and without the application of the active charging systems should resolve any concerns regarding possible active and passive system interaction.

The results of these analyses, coupled with the results summarized in the *Final Data Report*,[1] demonstrate the acceptability of the SPES-2 tests.

The analysis of the SPES-2 test data has indicated the relative importance of the passive residual heat removal (PRHR) as a heat removal system. As the reactor system depressurizes and the steam generators drain, the amount of heat removal from the PRHR increases and is sufficient to decrease the primary pressure below the steam generator secondary-side pressure such that the generators are not a heat sink but rather a weak heat source.

The SPES-2 tests were performed simulating the nitrogen release from the accumulators. The effects of the noncondensible gas release was found to have a negligible effect on the system response for the small-break loss-of-coolant accidents (SBLOCAs). Tracing the flow path for the noncondensibles indicates that some of the nitrogen will migrate to the PRHR, which will decrease its effectiveness. However, in the time frame that this occurs, the PRHR is not the predominate heat removal path, since ADS-2 and ADS-3 have opened, ADS-4 is about to open, and most of the energy leaves the system through the automatic depressurization system (ADS) flow paths. Noncondensible gases will also accumulate in the CMTs after the CMTs are empty.

An overall energy and mass balance was performed for the experiments that indicated that both mass and energy were preserved over the test duration. The assumptions used to estimate the break and ADS energy flows, while approximate, were found to be adequate such that energy closure could be obtained with reasonable accuracy. The mass of liquid was accurately characterized throughout the test facility such that the mass storage and distribution can be determined and used to validate the computer models of the test facility.

The SPES-2 experiments provided valid integral systems effects data that captured the key thermal-hydraulic phenomena identified in the phenomena identification ranking table (PIRT) for the AP600 small break loss-of-coolant accident (LOCA), steam generator tube rupture (SGTR) transients, and the steam line break transients (SLB). By performing computer code validation against the SPES-2 experiments, the ability of the codes to predict the key thermal-hydraulic phenomena can be assessed. The computer codes will be validated so that they can be used, in confidence, to assess the performance of the AP600 passive safety systems.

6.0 REFERENCES

1. Conway, L., R. Hundal, M. Loftus, V. Merritt, and M. Ogrinish, *AP600 Design Certification Program, SPES-2 Tests: Final Data Report*, WCAP-14309, March 1995.

2. Rigamonti, M., *SPES-2 Facility Description*, WCAP-14073, Revision 0, May 1994.

3. *NOTRUMP Code Applicability Document*, WCAP-14206.

4. Carlin, E. L., *LOFTRAN and LOFTR2 AP600 Code Applicability Document*, WCAP-14234, November 1994.

5. *AP600 Standard Safety Analysis Report*, DE-AC03-905F18495, Revision 1, June 1992.

6. Holman, J. P., *Heat Transfer*, McGraw-Hill, 1976.

7. Lahey, R. T., and F. J. Moody, *The Thermal-Hydraulics of a Boiling Water Reactor*, American Nuclear Society, 1977.

8. *SPES-2 Hot Pre-Operational Tests Results*, AP600 Doc. No. PXS-TZR-027, Revision 0, 1994.

9. *SPES-2 AP600 FHFP Integral Systems Test Specification*, AP600 Doc. No. PXS-T1P-002, Revision 0, November 8, 1993.

10. *AP600 Core Makeup Tank Test Analysis Report*, WCAP-14215.

11. Hochreiter, L. E., et al., *Scaling Logic for the Core Makeup Tank Test*, WCAP-1963, Revision 1, January 1995.